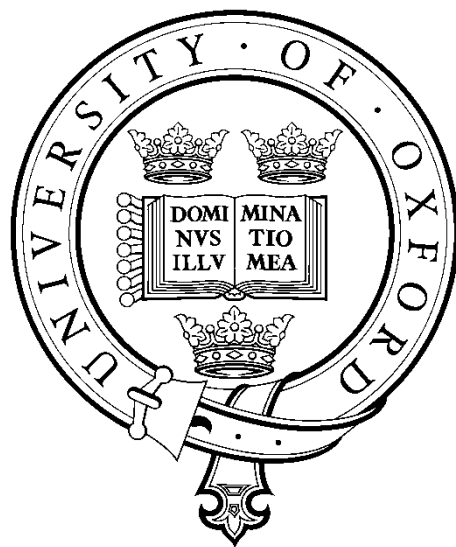


# Thin-walled Tubes with Pre-folded Origami Patterns as Energy Absorption Devices



**Jiayao Ma**

Balliol College Oxford

A dissertation submitted for the degree of Doctor of Philosophy

in the Department of Engineering Science

at the University of Oxford

Hilary Term, 2011

*To my parents.*

# ABSTRACT

## Thin-walled Tubes with Pre-folded Origami

### Patterns as Energy Absorption Devices

Jiayao Ma, Balliol College, Oxford

A dissertation submitted for the degree of Doctor of Philosophy  
in the Department of Engineering Science at the University of Oxford

Hilary Term, 2011

This dissertation is concerned with a type of energy absorption device made of thin-walled tubes. The tubes will undergo plastic deformation when subjected to an impact loading, and therefore absorb kinetic energy. It has been found that, if the surface of a tube is pre-folded according to an origami pattern, the failure mode of the tube can be altered, leading to a noticeable increase in energy absorption while at the same time, reducing the force needed to initiate plastic deformation within the tube. The main work is presented in four parts.

First of all, an experimental study of a type of previously reported thin-walled square tube with pre-manufactured pyramid patterns on the surface has been conducted. Quasi-static axial crushing tests show that the octagonal mode, although numerically proven to be efficient in terms of energy absorption, cannot be consistently triggered.

Secondly, a new type of thin-walled tubular energy absorption device, known as the origami tube, which has origami pattern pre-fabricated on the surface, has been studied. A family of origami patterns has been designed for tubes with different profiles. The performances of a series of origami tubes with various configurations subjected to quasi-static axial crushing have been investigated numerically. It is found that a new failure mode, referred to as the complete diamond mode, can be triggered, and both over 50% increase in the mean crushing force and about 30% reduction in the peak force can be achieved in a single tube design in comparison with those of a conventional square tube with identical surface area and wall thickness. A theoretical study of the axial crushing of square origami tubes has been conducted and a mathematical formula has been derived to calculate the mean crushing force. Comparison between theoretical prediction and numerical results shows a good agreement. Quasi-static axial crushing experiments on several square origami tube samples have been carried out. The results show that the complete diamond mode is formed in the samples and both peak force reduction and mean crushing force increase are attained.

Thirdly, a new type of curved thin-walled beam with pre-manufactured origami pattern on the surface, known as the origami beam, has been designed and analyzed. A numerical study of a series of origami beams with a variety of configurations subjected

to quasi-static lateral bending has been conducted. The results show that two new failure modes, namely, the longitudinal folding mode and the mixed mode, can be induced, and both reduced peak force and increased energy absorption are achieved.

Finally, a number of automobile frontal bumpers, which have the origami tube and the origami beam as key components, have been designed and analyzed. Three impact tests have been conducted on each bumper. The numerical results show that both types of origami structures can perform well in realistic loading scenarios, leading to improved energy absorption of the bumpers.

**Keywords:** Thin-walled tube, thin-walled beam, origami pattern, energy absorption device, axial crushing, lateral bending, finite element analysis.

# ACKNOWLEDGEMENTS

The work described in this dissertation was conducted by the author in the Department of Engineering Science at the University of Oxford. I received great help from a lot of people during my time there, without whom I would not have completed my study.

The first and most important one I would like to thank is my supervisor, Dr. Zhong You who introduced me into the area of deployable structures and inspired, advised, and supported me from the beginning to the end. His broad knowledge in the area of deployable structures, unique views to different problems, and sparkling imaginations benefited me enormously during every meeting with him.

My special appreciation also goes to my co-supervisor, Prof. Martin Williams, regular meeting with whom greatly broadened and enhanced my understanding of the area of structural dynamics, which contributed a lot to my research project, and my college advisor, Dr. Dominic O'Brien, who advised and helped me both academically and in everyday life.

I would also like to thank Dr. Igor Dyson in the Department of Engineering Science for his help on heat treatment and axial crushing tests of square tube samples, Mr. Bob Sawala for his help on constructing tube samples, Mr. Clive Baker for his suggestions on various machining related issues, and the Workshop in the Department of Engineering Science for machining a lot of moulds for me. My peers in the Civil Engineering Group, particularly Dr. Xiang Zhou, Dr. Weina Wu, Dr. James Eaton Evans, Mr. Jason Crabtree, and Mr. Jiewen Deng from the deployable structures group, also contributed in various ways to my study and life in Oxford, to whom I would also like to express my deep appreciation.

Financial support from the Clarendon Scholarship of University of Oxford and the Jason Hu Scholarship of Balliol College is gratefully acknowledged. I would also like to thank Balliol College and the Department of Engineering Science for financially supporting me to attend the AIAA conference in US.

Finally, I would like to thank my parents, brother, sister and the whole family for their tremendous support and encouragement.

# CONTENTS

<b>ABSTRACT .....</b>	<b>ii</b>
<b>ACKNOWLEDGEMENTS .....</b>	<b>iv</b>
<b>LIST OF FIGURES.....</b>	<b>ix</b>
<b>LIST OF TABLES.....</b>	<b>xiii</b>
<b>NOTATION .....</b>	<b>xv</b>
<b>CHAPTER 1 INTRODUCTION .....</b>	<b>1</b>
1.1 Thin-Walled Energy Absorption Devices.....	1
1.2 Origami Patterns.....	4
1.3 Aim and scope.....	5
1.4 Layout of dissertation .....	6
<b>CHPATER 2 REVIEW OF PREVIOUS WORK .....</b>	<b>9</b>
2.1 Axial Crushing of Circular and Square Tubes .....	9
2.1.1 Static buckling .....	9
2.1.2 Static axial crushing .....	12
2.1.3 Dynamic axial crushing .....	19
2.2 Thin-Walled Tubular Energy Absorption Devices .....	21
2.2.1 Circular and square tubes with geometric discontinuity.....	21
2.2.2 Polygonal Tubes.....	23
2.2.3 Cellular Tubes.....	24
2.2.4 Tapered tubes.....	26
2.2.5 Foam-filled tubes .....	27
2.2.6 Composite tubes.....	28
2.3 Thin-Walled Beam Designs .....	30
2.4 Deployable Cylinders.....	31
<b>CHAPTER 3 SQUARE TUBES WITH PYRAMID PATTERNS .....</b>	<b>35</b>
3.1 Sample Preparation and Experimental Setup.....	35
3.1.1 Sample preparation.....	36
3.1.2 Experimental setup.....	38

3.2 Numerical Simulation of the Axial Crushing .....	40
3.2.1 Finite element modelling .....	40
3.2.2 Results and discussions.....	44
3.3 Axial Crushing Tests.....	46
3.3.1 Conventional square tubes .....	46
3.3.2 Patterned square tubes .....	48
3.3.3 Modified patterned square tubes .....	50
3.3.4 Discussions.....	51
3.4 Summary.....	51
<b>CHAPTER 4 THE ORIGAMI TUBE: GEOMETRY AND NUMERICAL ANALYSIS.....</b>	<b>53</b>
4.1 Theoretical Basis of the New Design Approach .....	53
4.2 Design and Geometric Analysis of Origami Patterns .....	60
4.3 Design of Origami Tubes and Finite Element Modelling.....	65
4.3.1 Design of origami tubes.....	65
4.3.2 Finite element modelling .....	67
4.4 Results and Discussions .....	69
4.4.1 Axial crushing of conventional square tube.....	70
4.4.2 Axial crushing of square origami tube .....	71
4.4.3 Effects of geometric parameters .....	72
4.4.4 Effects of tube profile.....	79
4.5 Other Factors Influencing the Performance of the Origami Tube .....	86
4.5.1 Boundary condition .....	86
4.5.2 Material mechanical properties.....	87
4.5.3 Reinforcement.....	91
4.5.4 Bending capacity and torsion capacity .....	93
4.5.5 Dynamic axial crushing .....	97
4.6 Summary.....	100
<b>CHAPTER 5 THE ORIGAMI TUBE: THEORETICAL ANALYSIS AND EXPERIMENTS.....</b>	<b>104</b>
5.1 Theoretical Prediction of the Mean Crushing Force.....	104
5.1.1 Basic folding element .....	105
5.1.2 Energy Absorption at Stage I .....	108

5.1.3 Energy Absorption at Stage II .....	110
5.1.4 Mean crushing force .....	110
5.2 Axial Crushing Tests.....	113
5.2.1 Sample preparation and experimental setup.....	113
5.2.2 Material tensile tests.....	116
5.2.3 Experimental results .....	116
5.2.4 Numerical simulation of the axial crushing tests.....	119
5.2.2 Refined manufacturing approach .....	121
5.3 Summary.....	123
<b>CHAPTER 6 THE ORIGAMI BEAM.....</b>	<b>125</b>
6.1 Origami Pattern Geometry .....	126
6.2 Numerical Modelling .....	127
6.2.1 Arrangement of origami modules.....	127
6.2.2 Finite element modelling .....	130
6.3 Results and Discussions .....	131
6.3.1 Crushing of conventional beam .....	131
6.3.2 Crushing of origami beam.....	133
6.3.3 The dihedral angle.....	134
6.3.4 The number of modules .....	136
6.3.5 Arrangement of origami modules.....	138
6.4 Summary.....	141
<b>CHAPTER 7 THE COMPLETE BUMPER.....</b>	<b>144</b>
7.1 Introduction of Automobile Frontal Bumpers.....	145
7.2 Design of Bumpers and Finite Element Modelling .....	147
7.2.1 Design of bumpers .....	147
7.2.2 Design of impact tests .....	149
7.2.3 Finite element modelling .....	149
7.3 Results and Discussions .....	150
7.3.1 Full overlap impact at 5 m/s.....	150
7.3.2 40% overlap impact at 5 m/s .....	156
7.3.3 40% overlap impact at 20 m/s .....	161
7.4 Summary.....	165
<b>CHAPTER 8 FINAL REMARKS.....</b>	<b>169</b>



8.1 Main achievements .....	169
8.2 Future work.....	173
<b>APPENDIX I.....</b>	<b>175</b>
<b>APPENDIX II .....</b>	<b>184</b>
<b>REFERENCES.....</b>	<b>185</b>

# LIST OF FIGURES

1.1	An automobile bumper .....	2
1.2	(a) Primary energy absorbers in a train, and (b) crash tube in a helicopter landing gear .....	3
1.3	A guardrail system.....	4
1.4	Origami models .....	5
2.1	(a) The bellows buckling mode, and (b) the diamond buckling mode .....	11
2.2	(a) The concertina mode, and (b) the diamond mode .....	12
2.3	(a) Idealized concertina mode proposed by Alexander (1960), and (b) realistic concertina mode.....	13
2.4	(a) Initial basic folding element for the diamond lobe, and (b) modified basic folding element for the diamond mode.....	15
2.5	(a) The non-compact mode, (b) the symmetric mode, and (c) crushing process of a quarter of a square tube in the symmetric mode.....	16
2.6	(a) Inextensional folding element, and (b) extensional folding element..	17
2.7	(a) Corrugated circular tube, (b) grooved circular tube, (c) square tubes with full dents and half dents, and (d) square tube with a type of buckling initiator .....	22
2.8	(a) Double-cell, (b) triple-cell, and (c) new multi-cell .....	25
2.9	Crushed configurations of (a) a CFRP tube, and (b) a steel-CFRP tube..	28
2.10	Sandwich tube local reinforcement designs.....	29
2.11	(a) Reinforced beam, (b) beam integrated with energy absorbers, and (c) beam with tension a component .....	31
2.12	Deployment processes of (a) AST, and (b) RST .....	32
2.13	(a) A triangulated cylinder, (b) folded and deployed configurations of an inflatable tube, and (c) a 6-sided deployable cylinder .....	33
2.14	Fully deployed and folded configurations of an origami stentgraft .....	33
3.1	(a) Basic pyramid element, and (b) a square tube with pyramid pattern .....	36
3.2	Moulds for pattern stamping .....	37
3.3	(a) Conventional tube, (b) patterned tube, and (c) modified patterned tube .....	38
3.4	(a) Pinned boundary conditions, and (b) a block with channels .....	39
3.5	Material engineering stress vs strain curves.....	39
3.6	AE/IE vs displacement curves for three mesh densities .....	43
3.7	KE/IE vs displacement curves for three analysis times .....	44

3.8	Crushing processes of (a) Conventional, (b) Patterned2, and (c) Modified .....	45
3.9	Crushing processes of (a) C2, (b) P1, (c) P4, and (d) M2 .....	47
3.10	Crushed configurations of (a) C1, (b) P2, (c) P3, and (d) M1 .....	47
3.11	Force vs displacement curves of C1 and C2 .....	48
3.12	Force vs displacement curves of P1 - P4.....	49
3.13	Force vs displacement curves of M1 and M2 .....	50
4.1	Configuration of the pre-folded strut.....	55
4.2	Deflection vs axial force curves of the pre-folded strut.....	59
4.3	(a) A module of the origami pattern for square tubes, and (b) a module of a square origami tube .....	62
4.4	(a) A module of the origami pattern for rectangular tubes, and (b) a module of a rectangular origami tube .....	63
4.5	(a) A module of the origami pattern for hexagonal tubes, and (b) a module of a square origami tube .....	63
4.6	(a) A module of the origami pattern for type I tapered tubes, and (b) a module of a type I tapered origami tube .....	64
4.7	(a) A module of an origami pattern for type II tapered tubes, and (b) a module of a type II tapered origami tube .....	64
4.8	Force vs displacement curves of the whole-tube model and the half-tube model.....	69
4.9	Material engineering stress vs strain curve .....	69
4.10	Crushing processes of (a) A0, and (b) A1_1.....	70
4.11	Force vs displacement curves of A0 and A1_1 .....	71
4.12	Partially crushed configurations of (a) a square origami tube, and (b) a conventional square tube .....	72
4.13	Crushed configurations of (a) A1_2, (b) A1_3, (c) A1_5, (d) A2_1, (e) A2_2, (f) A2_3, (g) A2_4, (h) A2_5, (i) A3_1, (j) A3_4, (k) A3_5, (l) A4_1, (m) A4_4, (n) A5_1, (o) A5_2, and (p) A6_1 .....	75
4.14	Crushing process of A1_4 .....	76
4.15	Mean crushing force vs dihedral angle curves of A1_1 - A6_1.....	76
4.16	Force vs displacement curves of A1_1, A1_2 and A1_3 .....	77
4.17	Force vs displacement curves of A2_1, A3_1 and A4_1 .....	78
4.18	Crushing process of B2 .....	80
4.19	Crushing processes of (a) C1, and (b) C3.....	81
4.20	Force vs displacement curves of C1, C2, C3 and A2_1 .....	82
4.21	Crushing processes of (a) D1, (b) D3, (c) D5, and (d) D7 .....	83
4.22	Crushed configurations of (a) D2, (b) D4, (c) D5, (d)D6, and (e) D8 .....	84

4.23	Force vs displacement curves of D1 - D4.....	85
4.24	Force vs displacement curves of D5 - D8.....	86
4.25	(a) Range Rover crashcan, and (b) BMW crashcan.....	87
4.26	Crushed configurations of A1_1 under different boundary conditions. (a) Free, (b) fixed, and (c) with supporter.....	88
4.27	Force vs displacement curves of A1_1 under different boundary conditions .....	88
4.28	Material engineering stress vs strain curves of high strength steel and aluminium alloy .....	89
4.29	Crushed configurations of A1_1 made of (a) high strength steel, and (b) aluminium alloy.....	89
4.30	Force vs displacement curves of A0 and A1_1 made of high strength steel.....	90
4.31	Force vs displacement curves of A0 and A1_1 made of aluminium alloy .....	90
4.32	Crushed configurations of (a) A0_R, and (b) A3_1_R .....	91
4.33	Force vs displacement curves of A0_R and A3_1_R.....	92
4.34	The “imperfect” square tube .....	94
4.35	Loading scenarios of (a) bending analysis, and (b) twisting analysis .....	94
4.36	Force vs displacement curves of the tubes under bending .....	95
4.37	Torque vs rotation curves of the tubes under twisting.....	96
4.38	Crushed configurations of (a) C <sub>c</sub> ,and (b) O <sub>c</sub> under conditions I - IV (from left to right) .....	98
4.39	Force vs displacement curves of (a) C <sub>c</sub> , and (b) O <sub>c</sub> under four conditions .....	99
5.1	Crushing process of a quarter of A2_2. (a) Front view, (b) side view, and (c) PEEQ contour .....	106
5.2	Crushing process of the basic folding element. (a) side view of the initial configuration, (b) side view of the configuration at the end of stage I, (c) side view of a partially crushed configuration at stage II, and (d) top view of the fully crushed configuration .....	107
5.3	Comparison of theoretical prediction of $P_m$ and numerical results .....	112
5.4	(a) Moulds for stamping, and (b) a stamped steel sheet.....	114
5.5	A half-tube folded out of a stamped sheet.....	115
5.6	Material engineering stress vs strain curve .....	116
5.7	Crushing processes of (a) N, (b) O1, and (c) O2.....	117
5.8	Force vs displacement curves of N, O2, and O2 .....	118
5.9	Crushing processes of (a) half-tube model, and (b) whole-tube model .....	120

5.10	Moulds to form a half-tube .....	122
5.11	(a) Steel moulds, and (b) prototype origami tube.....	122
6.1	A module of the origami pattern for curved thin-walled beams. (a) Perspective view, (b) projection on y-z plane, and (c) projection on x-z plane.....	127
6.2	Configuration and loading scenario of P0 .....	128
6.3	Arrangements of origami modules on (a) P1_2, (b) P1_3, (c) P1_4, (d) P1_5, (e) P1_6, and (f) P1_7.....	129
6.4	Crushing processes of (a) P0, and (b) P1_1.....	132
6.5	Force vs displacement curves of P0 and P1_1 .....	132
6.6	Crushing processes of (a) P3_1, and (b) P4_1 .....	134
6.7	Force vs displacement curves of P1_1, P2_1, P3_1 and P4_1.....	135
6.8	Crushed configurations of (a) P3_2, (b) P3_3, and (c) P3_4.....	137
6.9	Crushing process of P3_5 .....	137
6.10	Force vs displacement curves of P3_1 - P3_5 .....	138
6.11	Crushed configurations of (a)P1_2, (b) P1_3, and (c) P1_4.....	138
6.12	Force vs displacement curves of P1_2, P1_3, and P1_4 .....	139
6.13	Crushing process of P1_6 .....	140
6.14	Crushed configurations of (a) P1_5, and (b) P1_7 .....	141
6.15	Force vs displacement curves of P1_1, P1_5, P1_6, and P1_7.....	141
7.1	(a) Front view of CC, (b) front view of OO, and (c) perspective view of CC .....	147
7.2	Full overlap crushing processes at 5 m/s of (a) CC, (b) CO, (c) OC, and (d) OO .....	152
7.3	Force vs displacement curves of the bumpers subjected to the full overlap impact at 5 m/s .....	153
7.4	40% overlap crushing processes at 5 m/s of (a) CC, (b) CO, (c) OC, and (d) OO .....	158
7.5	Force vs displacement curves of the bumpers subjected to the 40% overlap impact at 5 m/s .....	159
7.6	40% overlap crushing processes at 20 m/s of (a) CC, (b) CO, (c) OC, and (d) OO .....	163
7.7	Force vs displacement curves of the bumpers subjected to the 40% overlap impact at 20 m/s .....	164

# LIST OF TABLES

2.1	Comparison of tubes with different cross section profiles .....	26
3.1	Material mechanical properties .....	40
3.2	Mesh convergence test results.....	43
3.3	Analysis time convergence test results .....	44
3.4	Numerical results of the tube models.....	45
3.5	Experimental results of the tube samples .....	48
4.1	Summary of the geometric design parameters for origami tubes with five profiles.....	65
4.2	Configurations of tubes in Group A and numerical results .....	66
4.3	Configurations of tubes in groups B, C, D and numerical results.....	67
4.4	Mechanical properties of high strength steel and aluminium alloy .....	89
4.5	Numerical results of A0 and A1_1 made of high strength steel and aluminium alloy.....	91
4.6	Numerical results of A0_R and A3_1_R.....	93
4.7	Ranking of the bending capacity and torsion capacity of the origami tubes.....	96
4.8	Configurations of the tubes.....	97
4.9	Axial crushing conditions of the tubes.....	97
4.10	Numerical results of the tubes under four conditions .....	99
5.1	Axial crushing test results of N, O1, and O2.....	119
5.2	Numerical simulation results .....	120
6.1	Configurations of the beams and numerical results.....	129
7.1	Configurations of the cross beams.....	148
7.2	Configurations of the crashcans .....	148
7.3	Configurations of the bumpers.....	149
7.4	Numerical results of the bumpers subjected to the full overlap impact at 5 m/s .....	153
7.5	Numerical results of CC and OC subjected to the full overlap impact at 5 m/s at Stage I.....	155
7.6	Numerical results of the bumpers subjected to the 40% overlap impact at 5 m/s .....	159
7.7	Numerical results of the bumpers subjected to the 40% overlap impact at 20 m/s .....	164

7.8 Performances of the origami crashcan subjected to the three impact tests .....	166
7.9 Performances of the origami beam subjected to the three impact tests..	167
7.10 Mean crushing forces of the bumpers subjected to the three impact tests .....	167

# NOTATION

$A$	Strut cross section area
$A_1, A_2, A_3, A_4$	Constants of integration
$C$	Width of the tubular components of the new multi-cell tube
$C_r, q_r$	Material constants in the Cowper-Symonds equation
$C_1, C_2$	Two constants in Eq. (2.10)
$D$	Diameter of a circular tube
$E$	Young's modulus
$E_{CA_1}$	Energy absorption of travelling plastic hinge line $CA_1$
$E_b$	Energy absorption of the beam in a bumper
$E_c$	Energy absorption of the crashcan in a bumper
$E_e$	Energy absorption of the in-plane deformation in one intersecting point
$E_1$	Total energy absorption of the travelling plastic hinge lines
$E_2$	Total energy absorption of the in-plane deformation
$E_3$	Total energy absorption of the circumferential stationary plastic hinge lines
$E_4$	Total energy absorption of the inclined stationary plastic hinge lines
$E_5$	Total energy absorption of the vertical stationary plastic hinge lines
$I$	Moment of inertia of a cross section
$I_1$	Numerical integral
$H$	Tube height
$L$	Length of the member
$L_b$	Beam length
$M$	Number of modules
$M_p$	Full plastic bending moment per unit length
$N$	Number of sides of a tube
$N_a, N_t$	Numbers of basic pyramid elements in the axial and the transverse directions
$NSEA$	Normalized specific energy absorption
$NSEA_i$	Normalized specific energy absorption of beam $i$
$P$	Axial force
$P_{cr}$	Critical buckling load



$P_E$	Euler buckling load
$P_m$	Mean crushing force
$P_{m,i}$	Mean crushing force of beam $i$
$P_{m,0}$	Mean crushing force of beam P0
$P_{max}$	Peak force
$P_u$	Ultimate load
$R_b$	Radius of curvature of a curved beam
$S$	Beam surface area
$S_i$	Surface area of beam $i$
$S_0$	Surface area of beam P0
$S_{ACA_1}$	Area of triangle $ACA_1$
$V$	Potential energy
$a$	Length of a rectangular cross section
$a_1, a_2$	Lengths of the upper and the lower bottoms of the trapezoid surface of a tapered tube
$b$	Tube width
$c$	Corner width of an origami pattern
$d_1, d_2, d_3, d_4$	Crease lengths of the origami pattern for curved beams
$h$	Height of the basic pyramid element
$k$	Integer constant
$l$	Module length of an origami pattern
$l_i$	Total length of the inclined stationary plastic hinge lines
$l_v$	Total length of the vertical stationary plastic hinge lines
$m$	Number of lobes circumferentially in a circular tube
$n$	Material power law exponent
$p$	Width of the basic pyramid element
$p_m$	Ratio of the mean crushing force of square origami tubes to that of conventional square tubes
$q$	Length of the basic pyramid element
$r$	Radius of curvature of a travelling plastic hinge line
$t$	Wall thickness
$z$	Maximum distance on a cross section from its neutral axis
$\alpha, \beta$	Two angles in the basic folding element for square origami tubes
$\gamma$	Barrier angle
$\delta$	Final crushing distance
$\delta_1, \delta_2$	Amplitudes of the half sine and the full sine components of the curve pre-folded on a strut

$\delta_m$	Maximum deflection in a strut
$\delta_y$	Deflection to cause yielding in a strut
$\epsilon_u$	Ultimate strain
$\dot{\epsilon}$	Strain rate
$\theta$	Half dihedral angle
$\mu$	Friction coefficient
$\nu$	Poisson ratio
$\xi$	End shortening of a strut
$\rho$	Material density
$\sigma_u$	Tensile strength
$\sigma_y$	Yield stress
$\sigma_0$	Static plastic flow stress
$\sigma_0^d$	Dynamic plastic flow stress
$\chi$	Curvature of a strut

# CHAPTER 1

## INTRODUCTION

### 1.1 Thin-walled Energy Absorption Devices

Impact accidents are unfortunate but common occurrences. An astonishing increase in traffic accidents has been witnessed accompanying the rapid development of the transportation vehicle industry. A report from the World Health Organization (WHO, 2004) pointed out that around 1.2 million people were killed and up to 50 million injured in road accidents each year. In addition, it was predicted that road traffic injuries could be the third leading cause of disease and injury by 2020 due to the expansion of car markets especially in less developed countries. Apart from severe injuries to human beings, an impact, once happens, often leads to catastrophic damages to the structures of the vehicles involved and the surrounding environment.

A most common approach of minimizing the loss of life and property in an impact accident is to install energy absorption devices in the structures, which are designed to convert, totally or partially, kinetic energy into another form of energy during the accident so that damages to the important main structures are mitigated (Alghamdi, 2001). An ideal energy absorption device should meet the following requirements (Lu and Yu, 2003):

- Irreversible energy conversion to avoid a second impact caused by energy release.
- Long stroke to allow space for plastic deformation.

- Stable and repeatable deformation mode to ensure predictable performance in each impact.
- Restricted and constant reactive force so that no excessive force is transmitted to the main structure to be protected.
- Light weight and high energy absorption to absorb as much energy as possible.
- Low cost and easy installation as it is a one-shot device and needs replacement after an impact accident.

Practically, two parameters are extensively applied to evaluate the energy absorption performance of a device: the specific energy absorption (SEA), defined as the energy absorption per unit mass, and the load uniformity, defined as the ratio of the peak force to the mean crushing force. Here the peak force is the highest reaction force during the crushing process and the mean crushing force is the total energy absorption dividing the final crushing distance.

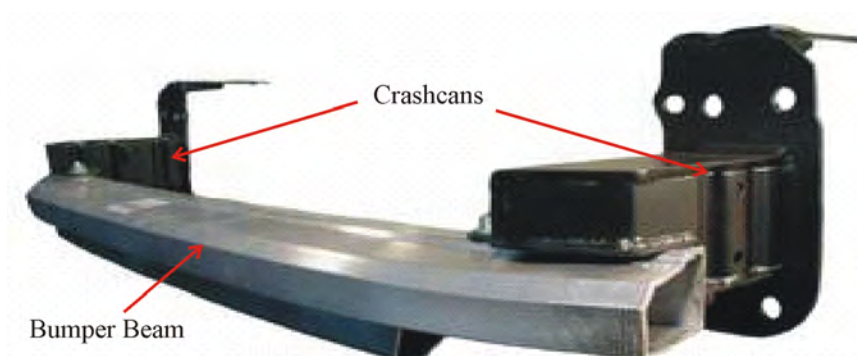


Fig. 1.1 An automobile bumper (source: <http://www.suspa.com/index.php?id=1284>).

Thin-walled tubes are among the most commonly used energy absorption devices due to their high manufacturability and low cost. The main deformation modes of thin-walled tubes include axial compression (Abramowicz and Jones, 1986), lateral compression (Reddy and Reid, 1980), lateral indentation (Lu, 1993), tube inversion (Miscow F and Al-Qureshi, 1997), and tube splitting (Reddy and Reid, 1986). Lateral compression and lateral indentation of tubes can lead to a smooth force vs displacement curve, but the SEA is relatively low because the stroke length is small. Tube inversion and tube splitting can generate a quite high SEA, but requires special

dies for the deformation modes to be induced. Axial compression of tubes has the merits of a relatively long stroke length, high SEA, and mechanical simplicity, and is therefore widely applied in practice. The main energy dissipation mechanism of this type of device is material plastic deformation. In automobiles such devices, Fig. 1.1, also known as crashcans, are mounted between the bumper beam and the main frame of a vehicle. They are designed to absorb energy during a low speed collision. The primary energy absorbers in trains, Fig. 1.2(a), are similar thin-walled tubes with a square cross section (Mayville *et al.*, 2003; Martinez *et al.*, 2004; Tyrell *et al.*, 2006). Tubular devices are also found in helicopter landing gears, Fig. 1.2(b), except that they generally have a circular cross section (Airoidi and Janszen, 2005; Airoidi *et al.*, 2006). Because different designs result in different performances, it remains a challenge to achieve both high SEA and low load uniformity while reducing cost.

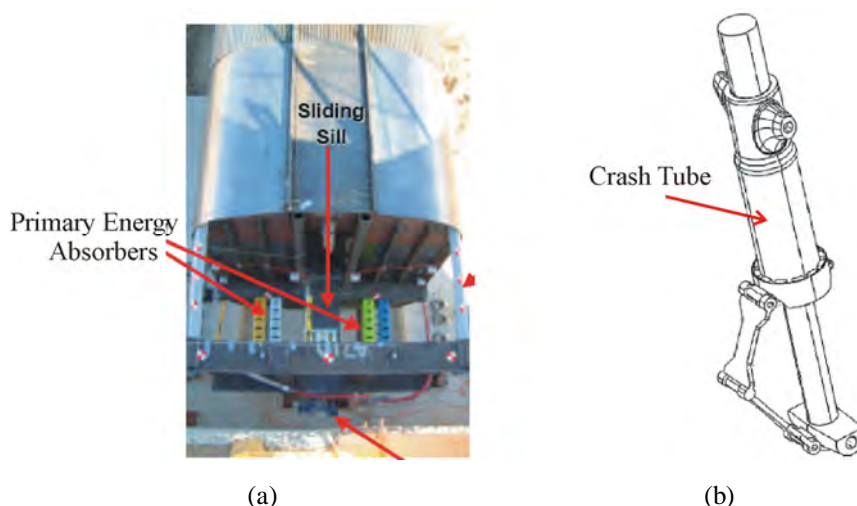


Fig. 1.2 (a) Primary energy absorbers in a train (source: Martinez *et al.*, 2004), and (b) crash tube in a helicopter landing gear (source: Airoidi and Janszen, 2005).

Thin-walled beams are another type of commonly used energy absorption device. A typical example is a bumper beam, Fig. 1.1. It usually adopts a curved profile with a box cross section and is designed to absorb kinetic energy as well as to transmit the impact loading to the two crashcans in a frontal collision. Thin-walled beams are also seen in roadside guardrail systems (Reid *et al.*, 2002), Fig. 1.3, designed to contain and re-direct out-of-control vehicles in order to reduce injuries to the occupants and damages to the vehicles themselves (AASHTO, 1995). Unlike the axial compression of

thin-walled tubes which generates extensive material plastic deformation, the lateral bending collapse of thin-walled beams features localized plastic deformation, leading to relatively low energy absorption efficiency. Therefore despite having practical applications, thin-walled beams have not received much attention from researchers and engineers.

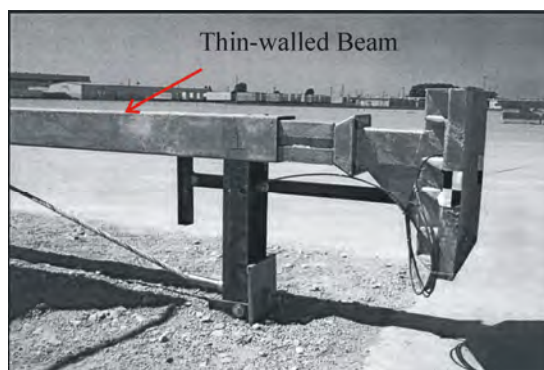


Fig. 1.3 A guardrail system (source: Reid *et al.*, 2002).

## 1.2 Origami Patterns

Origami is an ancient Japanese art of producing intricate 2D or 3D models through folding paper or cards. In its traditional form, a piece of paper is formed into an endless variety of shapes following a pattern design. Figure 1.4 shows a number of origami models made out of different patterns. The basic technique of origami is folding with two types of folding creases, namely the valley and the mountain creases. A folding pattern is produced by combining and arranging those creases.

An obvious yet significant application of origami is to use it to control the deformation process and final configuration of a thin sheet of material. This shape changing property of origami makes it possible to be applied in a variety of engineering fields in which configuration design and control are vital. Current applications of origami can be classified into two categories. One involves the design of arbitrary shapes. For instance, a technique known as “DNA-Origami” manages to fold long, single-stranded DNA molecules into arbitrary 2D shapes in order to create nanostructure shapes of

high complexity (Rothmund, 2006). The other is for packaging structures so that they can be conveniently stored or transported. Deployable cylinders, mainly used as inflatable deployable booms in aerospace engineering, fall into this category (Guest, 1994; Guest and Pellegrino, 1994a, 1994b, 1996; Barker and Guest, 1998; Sogame and Furuya, 1998; Tsunoda and Senbokuya, 2002; You and Cole, 2006).



Fig. 1.4 Origami models.

In both categories of applications, structures with origami patterns are required to be deployed and folded with minimum effort, implying a small variation in strain energy during the folding process. At the other end of the spectrum, some origami objects may induce large deformation in thin-walled materials. This feature has never been fully explored.

### 1.3 Aim and Scope

Comparison of the behaviour of thin-walled tubular energy absorption devices and deployable cylinders clearly demonstrates the strong correlation between collapse mode and energy absorption capability. A normal tube requires a great deal of energy to be crushed axially because it follows a particular failure mode, whereas a tube with a type of origami pattern on the surface can be folded with ease if the pattern is carefully selected and its folding follows the given pattern. Therefore if we can use origami patterns to direct a thin-walled tube to collapse in a failure mode that involves extensive material plastic deformation, high energy absorption could be achieved.

The aim of the work is to explore the possibility of designing high-performance thin-walled tubular energy absorption devices by means of innovative application of origami patterns. Specifically, a family of novel origami patterns are developed to design thin-walled tubes subjected to axial compression and thin-walled beams subjected to lateral bending, referred to as the *origami tube* and the *origami beam*, respectively, in the dissertation due to the fact that they have origami patterns on the surface. This dissertation concentrates on the structural design and analysis of the origami tube and the origami beam, in which numerical, analytical and experimental approaches are employed. Since the concepts developed here are purely structural, they can be applied to energy absorption devices with various dimensions and material types.

The main contents of the dissertation are as follows:

- Structural design of the origami tube as an energy absorption device.
- Numerical, analytical, and experimental analyses of the quasi-static axial crushing of the origami tube.
- Manufacturing of the origami tube.
- Structural design of the origami beam.
- Numerical analysis of the quasi-static lateral bending of the origami beam.
- Structural design of automobile bumpers with the origami tube and the origami beams as key components.
- Numerical analysis of the frontal impacts of the automobile bumpers.

## **1.4 Layout of Dissertation**

A brief review of previous work relevant to thin-walled tubular structures is provided in Chapter 2. Emphasis is placed on the static and dynamic axial crushing of circular and square tubes, i.e., thin-walled tubes with circular and square cross sections, as well as existing designs of thin-walled tubes and beams for the purpose of energy dissipation. A number of deployable cylinder designs are also reviewed in this chapter.



In Chapter 3 an experimental study of a type of previously reported thin-walled square tube with pyramid patterns on the surface is presented. A simple manufacturing approach is developed to construct the geometrically complicated patterned tubes. Eight physical tube samples are axially crushed quasi-statically and their failure modes and energy absorption properties are compared with the numerical results obtained from finite element analysis. The study provides useful insight for the main work in the dissertation.

Chapters 4 and 5 address the design and analysis of the origami tube.

Chapter 4 focuses on the numerical study of the origami tube. The theoretical basis of applying origami patterns in the design of thin-walled tubes is first presented. Following are the design and geometric analysis of a family of novel origami patterns for origami tubes with square, rectangular, polygonal cross sections, and two types of tapered shape. Subsequently four groups of origami tubes with varying configurations are designed and analyzed to investigate the failure mode and energy absorption properties of the origami tube subjected to quasi-static axial crushing. Finally, several important factors influencing the performance of the origami tube as a practical energy absorption device, the dependence of the performance on boundary condition and material, the effect of reinforcing the origami tube with a centre web, the bending capacity and torsion capacity, and the response under dynamic axial crushing, are discussed.

The analytical and experimental studies of the origami tube are given in Chapter 5. Analytically, a basic folding element is established to describe the folding process of the origami tube, and a theoretical formula is derived to estimate the mean crushing force of square origami tubes. Experimentally, a simple manufacturing approach is developed to fabricate square origami tubes. Three physical tube samples are axially crushed quasi-statically and the experimental data are compared with the numerical results. A refined manufacturing approach is also proposed to overcome the drawbacks of the simple one and prototypes with high quality are attained.

Chapter 6 addresses the design and analysis of the origami beam. An origami pattern is proposed and a pattern geometry definition is developed. A series of origami beams with various configurations are designed and their failure modes and energy absorption properties when subjected to quasi-static lateral bending are numerically analyzed.

Chapter 7 deals with the design and analysis of automobile bumpers which have the origami tube and the origami beam as key components. Three impact tests, the full overlap impact at 5 m/s, the 40% overlap impact at 5 m/s, and the 40% overlap impact at 20 m/s, are conducted on the bumpers to comprehensively evaluate the performances of the origami tube and the origami beam when subjected to practical complex loading.

The main achievements of the current research and suggestions of work to be conducted in the future are given in Chapter 8, which concludes the dissertation.

# **CHAPTER 2**

## **REVIEW OF PREVIOUS WORK**

Reviews of four topics are presented in this chapter. The first is a survey of previous work on the axial crushing of circular and square tubes most relevant to the origami tube developed in this dissertation. Static buckling, static axial crushing, and dynamic axial crushing of the two types of tubes are covered in this part. The second is a review of previous thin-walled tubular energy absorption devices with various structural designs and material types. The merits and drawbacks of each design are discussed. The third is a summary of existing thin-walled beam designs. Beams with various structural profiles and those integrated with energy absorption components are presented. And finally a series of deployable cylinder designs are reviewed.

### **2.1 Axial Crushing of Circular and Square Tubes**

#### **2.1.1 Static buckling**

The buckling of thin-walled tubes has always been a very important topic of research. Relatively long tubes tend to buckle globally, which phenomenon is called the Euler buckling. The critical buckling load of a simply supported long and slim member can be calculated by the well-known formula (Timoshenko, 1961)

$$P_{cr} = \frac{\pi^2 EI}{L^2} \quad (2.1)$$

in which  $E$  is the Young's modulus,  $I$  is the moment of inertia of the cross section, and  $L$  is the length of the member.

For circular tubes not long and slim enough for the Euler buckling to occur, the classical theory (Timoshenko, 1961) predicted the bellows buckling mode, Fig. 2.1(a), and the critical buckling load was found to be

$$P_{cr} = \frac{2\pi Et^2}{\sqrt{3(1-\nu^2)}} \quad (2.2)$$

in which  $t$  is the wall thickness of the tube and  $\nu$  is the Poisson ratio.

Experimental results (Robertson, 1928; Lundquist, 1933) revealed that the bellows buckling mode only appeared in relatively thick tubes and Eq. (2.2) severely overestimated the critical buckling load. To account for this discrepancy, Yoshimura (1955) carried out a series of tests and observed the diamond buckling mode in relatively thin circular tubes, Fig. 2.1(b), which was later referred to as the *Yoshimura pattern*. He subsequently proposed a new approach to calculate the critical buckling load of circular tubes buckling in the diamond mode, which agreed well with experimental data.

Allan (1968) later experimentally investigated the buckling of circular tubes with a wide range of diameter to wall thickness ratio,  $D/t$ , and observed two basic modes of buckling failure: relatively thick tubes failed by material yielding which led to the bellows mode and relatively thin tubes failed elastically in the diamond mode. The maximum load that a circular tube could support without failure due to local buckling was also proposed.

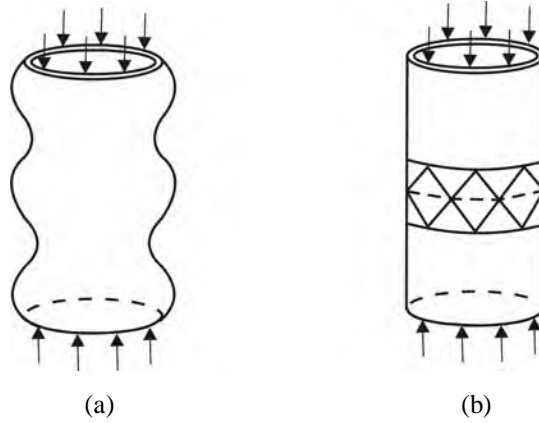


Fig. 2.1 (a) The bellows buckling mode, and (b) the diamond buckling mode.

When it comes to square tubes, it has been found from experiments that when a square tube buckles, each side of the tube deforms into several half-waves axially. Moreover, the corners of the tube remain at right angles, indicating that there is no bending moment at the corners and therefore each side of the tube can be treated as a rectangular plate simply supported at its edges (Meng *et al.*, 1983).

The critical buckling load of relatively thin square tubes which buckle elastically can be expressed as (Timoshenko, 1961)

$$P_{cr} = \frac{4\pi^2 Et^2}{3(1-\nu^2)} \left( \frac{t}{b} \right) \quad (2.3)$$

in which  $b$  is the width of the tube.

Relatively thick square tubes buckle plastically. It is usually assumed that the load is finally carried by two strips on each side of the tube, and the load is uniformly distributed across those strips. The ultimate load is (Timoshenko, 1961)

$$P_u = \frac{4\pi t^2}{\sqrt{3(1-\nu^2)}} \sqrt{E\sigma_y} \quad (2.4)$$

in which  $\sigma_y$  is the yield stress.

### 2.1.2 Static axial crushing

From the perspective of energy absorption, the post-buckling stage at which a tube is axially folded and undergoes large plastic deformation is of more interest because it is when a major portion of the energy dissipation occurs. Due to the complexity of the post-buckling behaviour of thin-walled tubes, it is quite difficult to trace theoretically the entire crushing process of a tube and to obtain the corresponding force vs displacement history. Usually only the mean crushing force can be derived analytically following a three-step procedure commonly used by previous researchers such as Wierzbicki and Abramowicz (1983). First of all, a basic folding element is extracted from the crushing process of a tube, which captures the main features of the folding of the tube. Subsequently the sources of energy dissipation in the basic folding element are identified and the energy absorption from each source is calculated. Finally the balance between external work done by the axial force and internal energy dissipated in the basic folding element is applied and the mean crushing force is obtained by dividing the total energy dissipation by the final crushing distance.

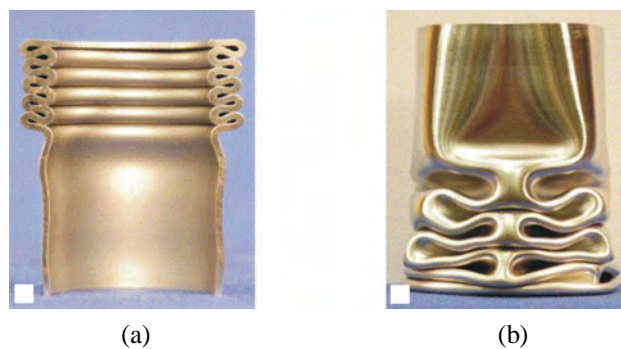


Fig. 2.2 (a) The concertina mode, and (b) the diamond mode (source: Bardi and Kyriakides, 2006).

Axial crushing of circular tubes has been extensively studied. Depending on  $D/t$  ratio, circular tubes could be crushed in the *concertina mode* or the *diamond mode* or a mixture of the two. Generally, circular tubes with  $D/t < 50$  deform in the concertina mode shown in Fig. 2.2(a), whilst those with  $D/t > 80$  deform in the diamond mode shown in Fig. 2.2(b). For the rest, the *mixed mode* usually takes place (Lu and Yu, 2003).

Alexander (1960) was among the pioneer researchers on the theoretical study of circular tubes failing in the concertina mode. In his basic folding element illustrated in Fig. 2.3(a), the folds were assumed to move completely inward or outward and the material was taken as rigid-perfectly plastic. Energy was dissipated through plastic bending of the hinges and membrane stretching in between. The mean crushing force derived from this model was

$$P_m = 6\sigma_y t^{3/2} D^{1/2} \quad (2.5)$$

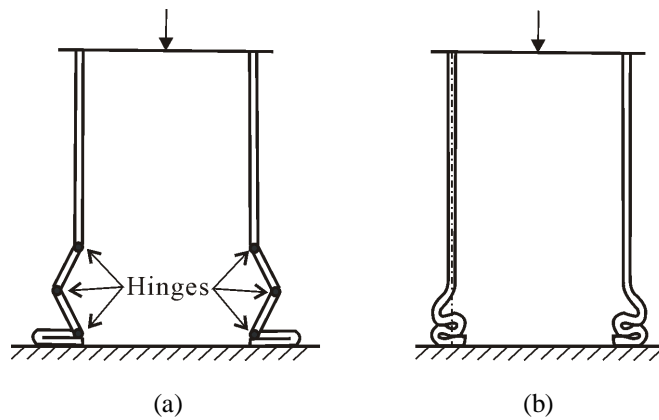


Fig. 2.3 (a) Idealized concertina mode proposed by Alexander (1960), and (b) realistic concertina mode.

Abramowicz (1983) later found that a tube could not be completely squashed to zero height because of finite folding radius and wall thickness. To account for it, he introduced the concept of effective crushing distance which denoted the maximum length of a tube that could be crushed without causing excessively large reaction force. Subsequently Abramowicz and Jones (1984b) used the effective crushing distance to modify Alexander's model and obtained the following expression for the mean crushing force

$$P_m = \sigma_y \frac{6t^{3/2}D^{1/2} + 3.44t^2}{0.86 - 0.57(t/D)^{1/2}} \quad (2.6)$$

A further improvement (Abramowicz and Jones, 1986) in which the effective plastic flow stress  $\sigma_0$  replaced the yield stress  $\sigma_y$  to account for material strain hardening yielded the following formula for the mean crushing force

$$P_m = \sigma_0 \frac{6.31t^{3/2}D^{1/2} + 3.77t^2}{0.86 - 0.57(t/D)^{1/2}} \quad (2.7)$$

Wierzbicki *et al.* (1992) observed from experiments that the folds actually did not go completely inward or outward, a phenomenon shown in Fig. 2.3(b). They introduced a parameter called the eccentricity factor which was defined as the ratio of the outward fold length to the total fold length. However, the eccentricity factor could only be obtained empirically. Taking the eccentricity factor into account, the mean crushing force became

$$P_m = 7.94\sigma_0 t^{3/2} D^{1/2} \quad (2.8)$$

Singace *et al.* (1995) later derived a theoretical value for the eccentricity factor and proposed a new expression for the mean crushing force as follows

$$P_m = \sigma_0 (5.57t^{3/2}D^{1/2} + 1.41t^2) \quad (2.9)$$

Theoretical study of circular tubes failing in the diamond mode was not as successful. Pugsley (1960) observed that when a circular tube was axially crushed, after the initial buckling in the Yoshimura pattern, there were usually 3 or 4 diamond shaped lobes left around any circumference of the tube. Based on that observation, he proposed a basic folding element, Fig. 2.4(a), and derived the corresponding mean crushing force

$$P_m = \sigma_y (C_1 t^2 + C_2 Dt) \quad (2.10)$$

in which  $C_1$  and  $C_2$  are two constants to be determined when the number of lobes circumferentially is known.



Equation (2.10) was found to underestimate considerably the mean crushing force. To improve the accuracy of the theoretical prediction, Pugsley (1979) proposed a modified basic folding element, Fig. 2.4(b), and obtained the following formula for the mean crushing force which agreed much better with experiment data

$$P_m = \frac{\pi m [1 + \cos(\pi / 2m)] \csc(\pi / 2m)}{2} \sigma_y t^2 \quad (2.11)$$

in which  $m$  is the number of lobes circumferentially.

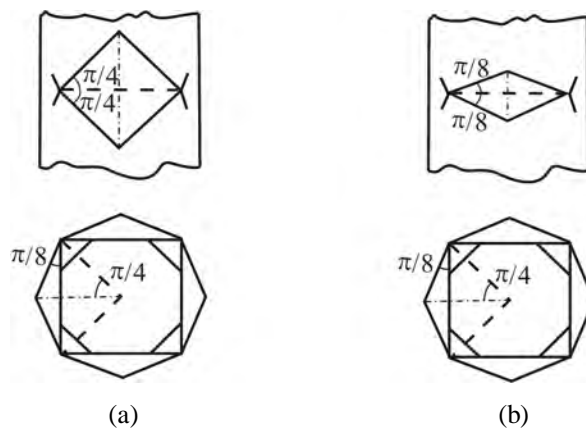


Fig. 2.4 (a) Initial basic folding element for the diamond lobe, and (b) modified basic folding element for the diamond mode.

Singace (1999) later observed that the eccentricity factor also existed in the diamond mode. He defined the eccentricity factor for the diamond mode as the ratio of the inward fold length to the total fold length, in contrast to that for the concertina mode. The mean crushing force derived in this way was

$$P_m = \frac{\sigma_y}{2\sqrt{3}} \left[ \frac{2\pi^2}{m} \tan\left(\frac{\pi}{2m}\right) Dt - \frac{\pi m}{3} t^2 \right] \quad (2.12)$$

It should be mentioned that the value of  $m$  in the above two formulae can only be determined from experiments.

Like circular tubes, square tubes also exhibit various failure modes depending on  $b/t$ . Very thin tubes, e.g., one with  $b/t = 100$ , usually fail in the *non-compact mode* (Reid *et al.*, 1986), Fig. 2.5(a). This mode is undesirable from the perspective of energy absorption because Euler buckling could result, and this would considerably reduce the energy absorption capability.

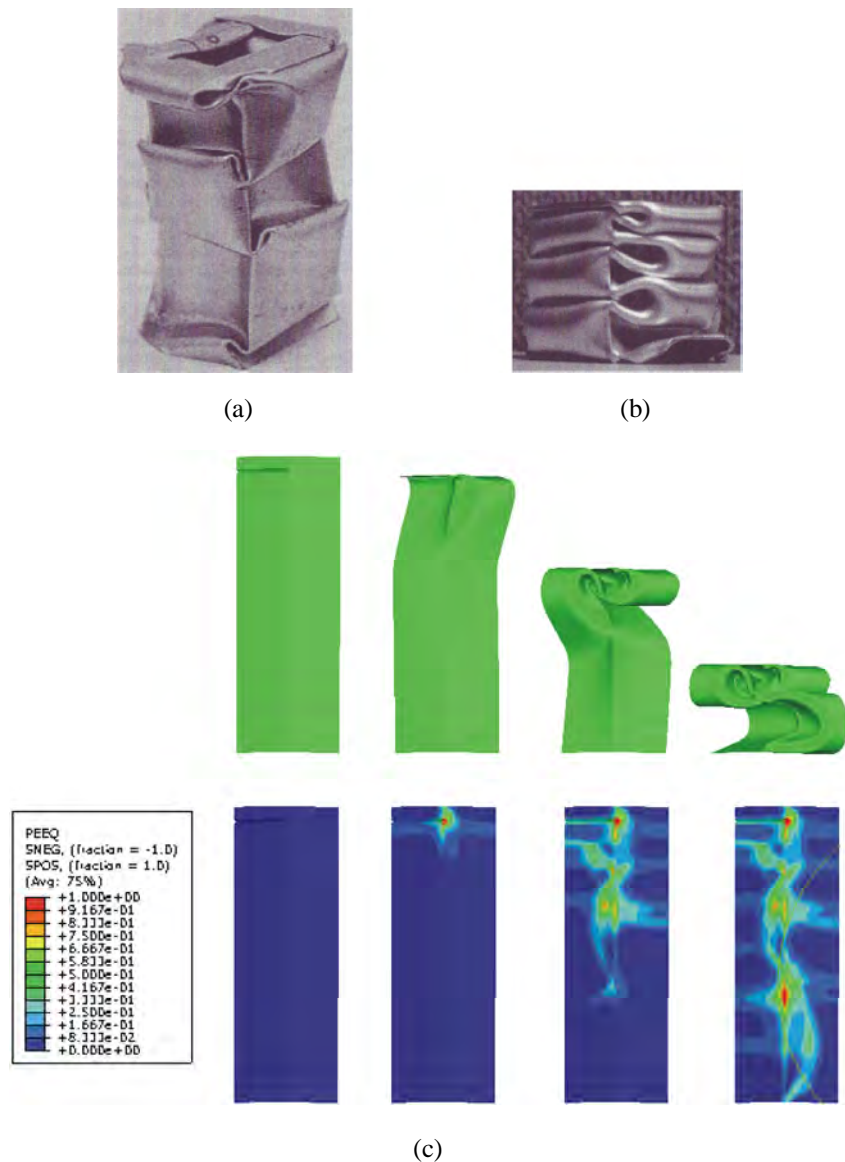


Fig. 2.5 (a) The non-compact mode, (b) the symmetric mode (source: Reid *et al.*, 1986), and (c) crushing process of a quarter of a square tube in the symmetric mode.

Tubes with moderate thickness normally fail in the *symmetric mode*, Fig. 2.5(b). The crushing process of a quarter of a square tube in the symmetric mode, which is made of mild steel and has tube width 60 mm, height 120 mm, and wall thickness 1.0 mm, and

the corresponding equivalent plastic strain (PEEQ) contours are shown in Fig. 2.5(c) as an example. It can be seen that the tube is crushed progressively from the top end. In addition, large plastic strain concentrates on the horizontal folds and the corner areas, whereas the remaining panels undergo very small plastic deformation. Wierzbicki and Abramowicz (1983) established a kinematically admissible and circumferentially inextensional basic folding element shown in Fig. 2.6(a), also known as *super folding element*, which consisted of trapezoidal, cylindrical, conical, and toroidal surfaces. Two types of plastic hinge lines, i.e., stationary plastic hinge lines which stayed in the same place throughout folding and travelling plastic hinge lines which moved as the element collapsed, were considered in the element. The energy dissipation of the element came from three main sources, i.e., folding along stationary plastic hinge lines, propagation of travelling plastic hinge lines, and localized in-plane stretching in the toroidal surface which was associated with travelling plastic hinge lines in order to satisfy the condition of kinematical continuity of the element. Assuming that this folding element could be crushed to zero height, they derived the following formula to calculate the mean crushing force for the symmetric mode

$$P_m = 9.56\sigma_0 t^{5/3} b^{1/3} \quad (2.13)$$

The folding wavelength determined in this way was  $1.966t^{1/3}b^{2/3}$ . Another important conclusion drawn from the study was that the three sources dissipated the same amount of energy. This result indicates that travelling plastic hinge lines, which account for two-thirds of the total energy absorption caused by the propagation of themselves and the associated in-plane stretching, are most effective at dissipating energy.

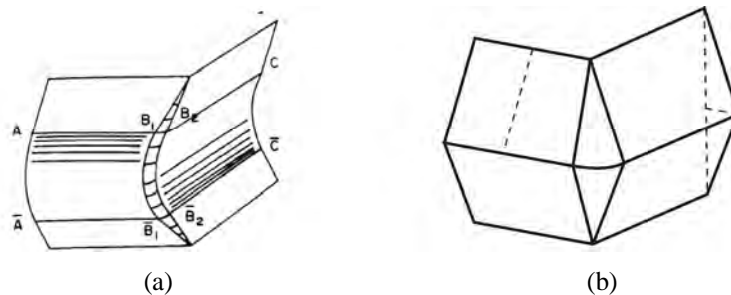


Fig. 2.6 (a) Inextensional folding element, and (b) extensional folding element.

Abramowicz and Jones (1984a, 1986) conducted a series of axial crushing tests on steel square tubes and observed three failure modes: the symmetric mode consisting of four inextensional elements within one folding wavelength, asymmetric mode A consisting of six inextensional and two extensional elements within two folding wavelengths, and asymmetric mode B consisting of seven inextensional and one extensional elements within two folding wavelengths. Using the super folding element theory and taking into consideration of the effective crushing distance, they calculated the mean crushing forces for the three modes as follows

- The symmetric mode

$$P_m = 13.06\sigma_0 t^{5/3} b^{1/3} \quad (2.14)$$

- Asymmetric mode A

$$P_m = 10.73\sigma_0 t^{5/3} b^{1/3} + 0.79\sigma_0 t^{4/3} b^{2/3} + 0.51\sigma_0 t^2 \quad (2.15)$$

- Asymmetric mode B

$$P_m = 11.48\sigma_0 t^{5/3} b^{1/3} + 0.44\sigma_0 t^{4/3} b^{2/3} + 0.26\sigma_0 t^2 \quad (2.16)$$

These three expressions give very close results to each other for the practical range of  $b / t$ , so Eq. (2.14) is usually used to estimate the mean crushing force of square tubes with moderate thickness.

Chen and Wierzbicki (2001) simplified the super folding element theory and derived an expression for the mean crushing force as follows

$$P_m = 6.68\sigma_0 t^{3/2} b^{1/2} \quad (2.17)$$

Very thick tubes usually fail in an *extensional mode*. This failure mode involves circumferential extension of a large magnitude and folding along stationary plastic hinge lines. Abramowicz and Jones (1984a) derived the mean crushing force based on the extensional folding element shown in Fig. 2.6(b) as

$$P_m = 8.16\sigma_0 t^{3/2} b^{1/2} + 2.04\sigma_0 t^2 \quad (2.18)$$

The mean crushing force associated with the extensional mode is higher than those of the other three modes until  $b/t < 7.5$ , indicating that large circumferential membrane deformation requires much more energy to be activated than bending in tubes with medium thickness which usually have  $b/t$  much larger than 7.5. For this reason, commonly used thin-walled square tubes as energy absorption devices tend to assume an inextensional failure mode.

### 2.1.3 Dynamic axial crushing

In the real world, axial crushing of energy absorption tubes occurs dynamically because they are always subjected to impact loading. Dynamic effects stemming from both structure and material substantially complicate the analysis. However, many conclusions drawn from a quasi-static analysis can be slightly modified for a dynamic analysis provided that dynamic effects such as inertia effects and strain rate effects are properly taken into consideration. Here quasi-static analysis refers to an approach in which a physical event is accelerated so that it occurs in less time as long as the solution remains nearly identical to the true static solution and dynamic effects remain insignificant. This approach has the advantage of yielding a nearly static solution in a much shorter time, and is therefore widely used in the study of thin-walled energy absorption devices.

In low velocity impacts (up to tens of metres per second), dynamic progressive buckling, referring to a buckling phenomenon that a tube buckles progressively from one end as the crushing proceeds, takes place. In this case the failure mode of a tube

under dynamic loading is virtually identical to that under quasi-static loading. Inertia effects, which tend to preserve the unbuckled shape of a tube, is not strong enough to change the way the tube buckles, and therefore can be neglected. Material strain rate effects, which can raise the initial and subsequently yield stress of a material, are significant for strain-rate-sensitive materials and thus should be taken into account. In practice, strain rate effects are usually included in the analysis by replacing the static plastic flow stress  $\sigma_0$  mentioned in Section 2.1.2 with the dynamic plastic flow stress  $\sigma_0^d$  which was calculated from the Cowper-Symonds equation as follows (Abramowicz and Jones, 1984a, 1984b, 1986; Jones and Abramowicz, 1985):

$$\frac{\sigma_0^d}{\sigma_0} = 1 + \left( \frac{\dot{\epsilon}}{C_r} \right)^{1/q_r} \quad (2.19)$$

where  $C_r$  and  $q_r$  are material constants, and  $\dot{\epsilon}$  is the strain rate which is taken as constant here although it varies both spatially and temporally during an impact event.

If the impact velocities are high enough, e.g., when explosive loading is applied (Karagiozova *et al.*, 2005), inertia forces would play a crucial role. In this circumstance, dynamic plastic buckling, which denotes a buckling phenomenon that small amplitude wrinkles are developed simultaneously along the entire length of a tube at the beginning of the loading process, occurs. Both inertia effects and strain rate effects should be considered on this occasion, and therefore the analytical results obtained under quasi-static loading are no longer able to suit this case through simple modifications.

Considerable attention has been paid to understanding the transition from dynamic progressive buckling to dynamic plastic buckling, which is believed to be influenced by the following factors: tube dimensions, material properties, impact velocities, tube end boundary conditions, and the magnitude and shape of the initial deformation profile (Murase and Wada, 2004). Due to the complexity of this phenomenon, it is almost impossible to obtain analytical solutions in the general case. Therefore a

common approach is to develop simplified analytical models combining some preliminary analytical work together with further numerical study to identify the effects of various factors.

Karagiozova *et al.* (2000) and Karagiozova and Jones (2001; 2002) studied the dynamic plastic buckling of circular tubes from the viewpoint of stress wave propagation and drew the following conclusions:

- Dynamic plastic buckling only occurs within a sustained plastic flow under the condition of almost constant stress and strain along the entire length of the tube, whereas strain localization leads to local buckling and development of progressive buckling.
- Three main factors influencing strain localization are inertia, strain hardening, and strain rate sensitivity.
- Dynamic plastic buckling usually occurs in relative thick tubes made of strain rate insensitive materials with large strain hardening ratios.

Karagiozova (2004) and Karagiozova and Jones (2004) used similar theory to study the dynamic plastic buckling of square tubes. It was found that plastic stress waves propagated at higher speeds along square tubes than along circular tubes. Furthermore, sufficiently high plastic wave speeds in combination with the inertia properties of a shell could cause different types of buckling to develop in geometrically equivalent square and circular shells made of identical material and subjected to identical dynamic loading.

## **2.2 Thin-Walled Tubular Energy Absorption Devices**

### **2.2.1 Circular and square tubes with geometric discontinuity**

Circular and square tubes are the most commonly used tubular energy absorption devices due to their ready availability and low cost. A vast amount of work has been

dedicated to improving the performance of circular and square tubes. The main challenge in the design is how to eliminate effectively the high initial buckling force while maintaining or even enhancing the energy absorption capability.

A simple but effective method of removing the high initial buckling force is to introduce some sort of geometric imperfection on the tube. Singace and El-Sobky (1997) stamped corrugations, Fig. 2.7(a), on the surface of circular tubes and found from experiments that the high initial buckling force was eliminated and the force vs displacement curve became more uniform. However, the energy absorption of the corrugated tubes was also considerably lower than that of the corresponding straight tubes. Another type of commonly used geometric imperfection is dents on circular tubes (Mamalis *et al.*, 1986c; Daneshi and Hosseinipour, 2002; Hosseinipour, 2003; Hosseinipour and Daneshi, 2003; Mamalis *et al.*, 2003c), Fig. 2.7(b), and on square tubes (Lee *et al.*, 1999), Fig. 2.7(c). Similar to corrugations, the presence of dents reduces the initial buckling force and leads to smoother force vs displacement curve, at the cost of reduced overall energy absorption capability.

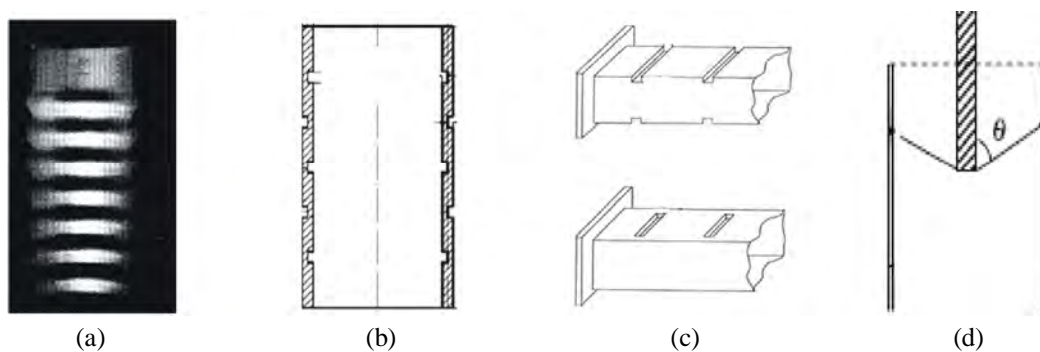


Fig. 2.7 (a) Corrugated circular tube (source: Singace and El-Sobky, 1997), (b) grooved circular tube (source: Hosseinipour and Daneshi, 2003), (c) square tubes with full dents and half dents (source: Lee *et al.*, 1999), and (d) square tube with a type of buckling initiator (source: Zhang *et al.*, 2009).

To overcome the disadvantage of corrugations and dents, Zhang *et al.* (2009) designed a type of buckling initiator, Fig. 2.7(d), which was composed of a pre-hit column and pulling strips installed near the impact end of a tube. Both initial buckling force reduction and preservation of energy absorption capability were achieved by the design.



Research has also been conducted on improving the energy absorption of circular and square tubes. Adachi *et al.* (2008) introduced ribs along circular tubes to induce the concertina mode which was known to be more efficient in terms of energy absorption than the diamond mode (Andrews *et al.*, 1983). As much as about 30% energy absorption increase was observed from experiments. Lee *et al.* (2008) used a controller to improve the energy absorption of square tubes and reported about 15% - 20% energy absorption increase. The gains of the above two devices, however, are offset by their mechanical complexity and high initial buckling force.

An interesting attempt to achieve both initial buckling force reduction and energy absorption increase is to pre-manufacture a kind of pyramid pattern on the surface of square tubes (Zhang *et al.*, 2007). Numerical results showed that a new failure mode named the *octagonal mode*, which was very similar in configuration to the diamond mode of circular tubes, was triggered and both low initial buckling force and high energy absorption were obtained. However, it will be shown in Chapter 3 that this desirable failure mode cannot be consistently triggered, which is in contradiction to the requirement of stable failure mode for energy absorption devices.

### **2.2.2 Polygonal tubes**

It is already known that the SEA of a circular tube is higher than that of a square tube with identical circumference, height, and wall thickness (Lu and Yu, 2003). But circular tubes are associated with a high initial buckling force which is not easy to be reduced without compromising the energy absorption efficiency. Therefore polygonal tubes, normally having hexagonal or octagonal cross sections, are frequently used as a trade-off between square tubes and circular tubes.

Abramowicz and Wierzbicki (1989) used the super folding element theory to study the axial crushing of multi-corner tubes and successfully derived the mean crushing forces of tubes with arbitrary number of corners. For example, they found that the approximate mean crushing force of hexagonal tubes was

$$P_m = 20.23\sigma_0 b^{0.4} t^{1.6} \quad (2.20)$$

Mamalis *et al.* (1991) conducted quasi-static axial crushing tests on octagonal tubes and observed four failure modes, i.e., the *inextensional mode*, the *extensional mode*, the *mixed mode*, and the *square mode*. Mamalis *et al.* (2003b) later did both finite element simulations and physical tests on octagonal tubes, which further confirmed the four failure modes. It was also found that the energy absorption capacity of octagonal tubes was much higher than that of square tubes and was close to that of circular tubes.

Yamashita *et al.* (2003) also examined tubes with various polygonal cross sections both numerically and experimentally and found that the SEA of a polygonal tube increased with the number of corners, but saturated when passed eleven at which point a polygonal tube behaved virtually like a circular one.

Similar to circular and square tubes, polygonal tubes also have the problem of very high initial buckling force. Little has been published to address this problem, but it is reasonable to postulate that those types of geometric imperfection for circular and square tubes can also be applied to polygonal tubes and similar effects can be achieved.

### 2.2.3 Cellular tubes

The choice of a cellular cross section over a single-cell one is based on the observation that the SEA of a square tube decreases with  $b / t$ . In other words, if two square tubes have identical height and wall thickness but different widths, the one with a small width will have a higher SEA than that of the one with a large width. This phenomenon can be explained as follows. First of all, the folding wavelength of a square tube increases with its width (Wierzbicki and Abramowicz, 1983). Therefore the tube with a small width has more folds than those of the one with a large width, resulting in higher SEA. Secondly, two-thirds of the energy absorption of a square tube come from propagation of travelling plastic hinge lines and in-plane stretching in the

corner regions whereas the contribution of folding along stationary plastic hinge lines is one-third (Wierzbicki and Abramowicz, 1983). Since corner regions take up a larger portion of the tube with a small width, a higher SEA can be expected.

The above observation has led to research on multi-cell tubes. Chen and Wierzbicki (2001) analytically and numerically studied the axial crushing of double-cell and triple-cell tubes, shown in Fig. 2.8(a) and (b), respectively, and reported a noticeable SEA increase in comparison with that of conventional square tubes. A simplified basic folding element was proposed and the mean crushing forces of the two types of tubes were obtained analytically.

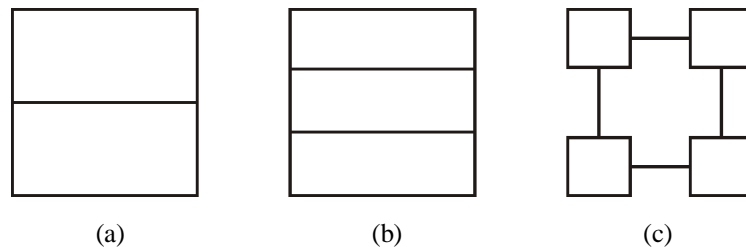


Fig. 2.8 (a) Double-cell, (b) triple-cell, and (c) new multi-cell.

Kim (2002) proposed a new multi-cell tube, Fig. 2.8(c), composed of four square tubular components connected by plates. A very short folding wavelength was observed due to the small width of the tubular components. Numerical results showed that as much as 100% SEA gain could be obtained for the new design compared with that of conventional square tubes. Based on the simplified basic folding element developed by Chen and Wierzbicki (2001), the mean crushing forces of single-cell, double-cell, triple-cell, quadruple-cell ( $2 \times 2$  cell), and the new multi-cell tubes were obtained. Table 2.1 lists those results where  $C$  denotes the width of the square tubular components of the new multi-cell tube and the SEA is calculated using  $C = b/3$ .

Zhang *et al.* (2006) looked into the energy absorption properties of multi-cell square tubes by means of numerical simulation and theoretical analysis. It was found that the SEA increased with the number of cells and about a 50% gain in SEA could be obtained when the section was divided into  $3 \times 3$  cells.

In spite of the high energy absorption, cellular tubes are not widely applied in practice mainly due to two reasons. First of all, an extrusion technique is normally needed to construct the geometrically complicated cellular tubes, resulting in high manufacturing cost. Secondly, effective reduction of the high initial buckling force of cellular tubes is quite difficult especially when the cross section profile is very complicated or the number of cells is large.

Table 2.1 Comparison of tubes with different cross section profiles (Kim, 2002)

Cross section profiles	$P_m$	Cross section area	SEA increase
Single-cell	$6.68\sigma_0 t^{3/2} b^{1/2}$	$4bt$	-
Double-cell	$9.89\sigma_0 t^{3/2} b^{1/2}$	$5bt$	18.4%
Triple-cell	$12.94\sigma_0 t^{3/2} b^{1/2}$	$6bt$	29.1%
Quadruple-cell	$14.18\sigma_0 t^{3/2} b^{1/2}$	$6bt$	41.5%
New multi-cell	$17.69\sigma_0 t^{3/2} (b + 2C)^{1/2}$	$4(b + 2C)t$	105.1%

### 2.2.4 Tapered tubes

Tapered tubes are another type of widely applied energy absorption device because of their relatively low initial buckling force (Nagel and Thambiratnam, 2005), stable force vs displacement response (Mamalis and Johnson, 1983), and high energy absorption efficiency when subjected to oblique loads, compared with that of straight tubes (Reid and Reddy, 1986). In practice, an energy absorption device is sometimes required to connect two structural components with different cross sectional dimensions, so that a tapered shape becomes a necessity.

Under axial crushing, truncated circular tubular cones, usually deform in either the concertina mode or the diamond mode depending on the geometry of the tube (Mamalis and Johnson, 1983; Mamalis *et al.*, 1986a; Mamalis *et al.*, 1986b). For capped frusta which have a closed end, inward inversion or outward flattening could also take place (Aljawi and Alghamdi, 1999, 2000).

The axial crushing behaviour of truncated square tubular cones is also similar to that of straight square tubes in that both the symmetric mode and the extensional mode could appear depending on the geometry of the tube (Mamalis *et al.*, 1989).

Because of the similarity between the failure modes of tapered tubes and those of corresponding straight ones, the theoretical study approaches for straight tubes can be slightly modified to estimate the energy absorption of tapered ones.

### **2.2.5 Foam-filled tubes**

Filling hollow tubes with foam filler has been considered as an effective approach to improving the SEA of thin-walled tubes for a long time. Upon axial crushing, the tubular envelope and the foam filler constitute a type of composite structure. The foam filler acts like an elastic-plastic foundation, which reduces the folding wavelength of the tubular envelope, whereas the tubular envelope confines the lateral expansion of the foam filler when it is compressed and thus increases its energy absorption.

Early research focused on mild steel tubes filled with polyurethane foam (Reid *et al.*, 1986; Abramowicz and Wierzbicki, 1988; Reddy and Wall, 1988). Recently, aluminium foam and honeycomb which show attractive mechanical properties from the perspective of energy absorption have been gaining practical interest. Considerable work has been carried out on this topic (Santosa and Wierzbicki, 1998; Santosa *et al.*, 2000; Hanssen *et al.*, 2000a, 2000b, 2001), from which the advantage of foam filled tubes is clearly demonstrated.

In spite of their high SEA, foam-filled tubes have several drawbacks which hinder their extensive application in practice. First of all, the effective crushing distance is reduced by the foam filler. Secondly, global rupture of the tubular envelope, which is an undesirable failure mode, could appear under certain circumstances. Finally, the material cost is relatively high.

## 2.2.6 Composite tubes

Composite materials are theoretically a very good alternative to metals due to their exceptionally high strength to weight ratio. Tubes made of composite materials can offer a SEA much higher than that of tubes made of metals.

Fibre/resin composites are commonly used materials in the design of composite tubes, e.g., fibre-reinforced tubes (Farley and Jones, 1992), fibreglass tubes (Mamalis *et al.*, 1996, 1997), and carbon fibre-reinforced polymer (CFRP) tubes (Mamalis *et al.*, 2005). While being able to achieve more than 100% SEA gain, tubes made of fibre/resin composites usually fail in brittle, unstable modes involving extensive micro-cracking development, delamination and fibre breakage, which are undesirable for an energy absorption device. Figure 2.9(a) shows the brittle failure mode of a CFRP tube as an example.

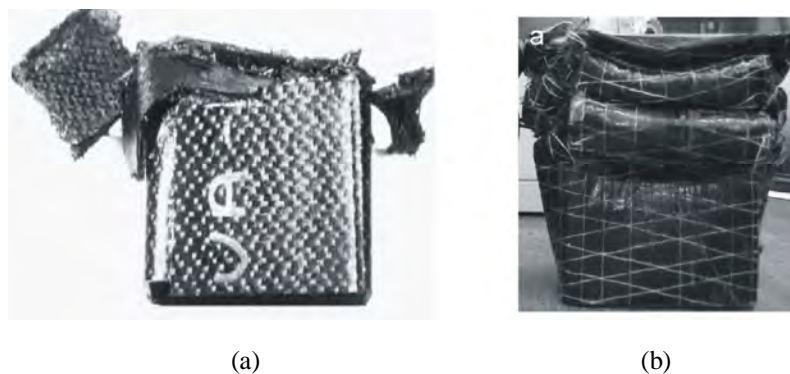


Fig. 2.9 Crushed configurations of (a) a CFRP tube (source: Mamalis *et al.*, 2005), and (b) a steel-CFRP tube (source: Bambach and Elchalakani, 2007).

To overcome the drawbacks mentioned above, attention has been paid to externally fibre-reinforced metallic tubes which combine the advantages of stable and progressive failure mode of metal and lightweight of fibre/resin composite. Axial crushing tests of metallic tubes with externally bonded glass fibre (Hanefi and Wierzbicki, 1996; Song *et al.*, 2000), and externally bonded CFRP (Bambach and Elchalakani, 2007; Bambach *et al.*, 2009a; Bambach *et al.*, 2009b) were conducted. Progressive axial folding shown in Fig. 2.9(b) was obtained and more than 50% energy absorption gain could be achieved.

However, material fracture and debonding were observed for metallic tubes with low ductility when subjected to dynamic loading.

Sandwich tubes are another type of composite tube. A typical sandwich tube is composed of two thin, stiff fibreglass facings and a lightweight polymer foam core in between. To avoid debonding of the fibreglass facings from the core, which could result in immediate loss of all load-bearing capacity and subsequent catastrophic failure, local reinforcements are frequently applied to connect the facings and the core. A variety of reinforcements, some of which are presented in Fig. 2.10, have been proposed and proved to be very effective (Mamalis *et al.*, 2000, 2001; Mamalis *et al.*, 2002a; Mamalis *et al.*, 2002b; Mamalis *et al.*, 2003a; Pitarresi *et al.*, 2007).

In spite of the superior energy absorption performance, the high cost of composite tubes limits their application to areas such as aerospace engineering and race car design. Moreover, the relatively inconsistent response of composite tubes is another obstacle to be overcome.

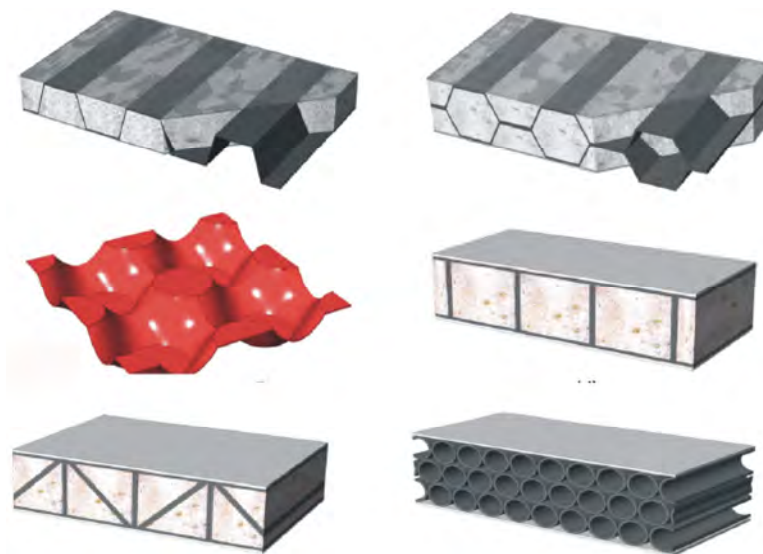


Fig. 2.10 Sandwich tube local reinforcement designs (source: Pitarresi *et al.*, 2007).

## 2.3 Thin-Walled Beam Designs

Compared with thin-walled tubes, thin-walled beams have a relatively low SEA. The low energy absorption efficiency is caused by the lateral bending collapse mode of thin-walled beams which usually features a limited number of plastic hinges during the crushing process, and therefore only a small amount of material in the neighbourhood of the hinges undergoes large plastic deformation. A typical application of this type of structure is an automobile bumper beam (Kokkula *et al.*, 2006a; Kokkula *et al.*, 2006b). Steel and aluminium alloy are commonly used materials because of high mechinability and low cost. Composite beams have also been proposed (Cheon *et al.*, 1995) but their practical use is very limited for reasons similar to those for composite tubes.

A vast number of patents on bumper beams exist. The structural design of bumper beams can be roughly divided into the following categories: box sectional beams (Jonsson, 2003; Jonsson and Juntti, 2005), cellular sectional beams (Amano *et al.*, 2005; Cumming *et al.*, 2005), reinforced beams (Roussel *et al.*, 2003) shown in Fig. 2.11(a), and beams with integrated energy absorption components (Weissenborn, 2003; Shuler and Trappe, 2006) shown in Fig. 2.11(b).

The lateral bending collapse mode of conventional beams could be altered by introducing tension components to trigger membrane deformation in curved beams (Carpenter, 1990; Schwartz and Ramoo, 1999). One of the beams of this type is shown in Fig. 2.11(c). While having higher energy absorption, this type of beam is also heavier and does not integrate well with the main structure of a vehicle. Therefore a better approach to induce the membrane deformation needs to be developed.

To summarize, it can be seen from Section 2.2 and 2.3 that despite a large amount of research having been done to develop energy absorption devices, it remains a challenge to design a system which has a low initial buckling force, high SEA, stable failure mode, integrates well with the main structure, and can be manufactured at a reasonable cost.



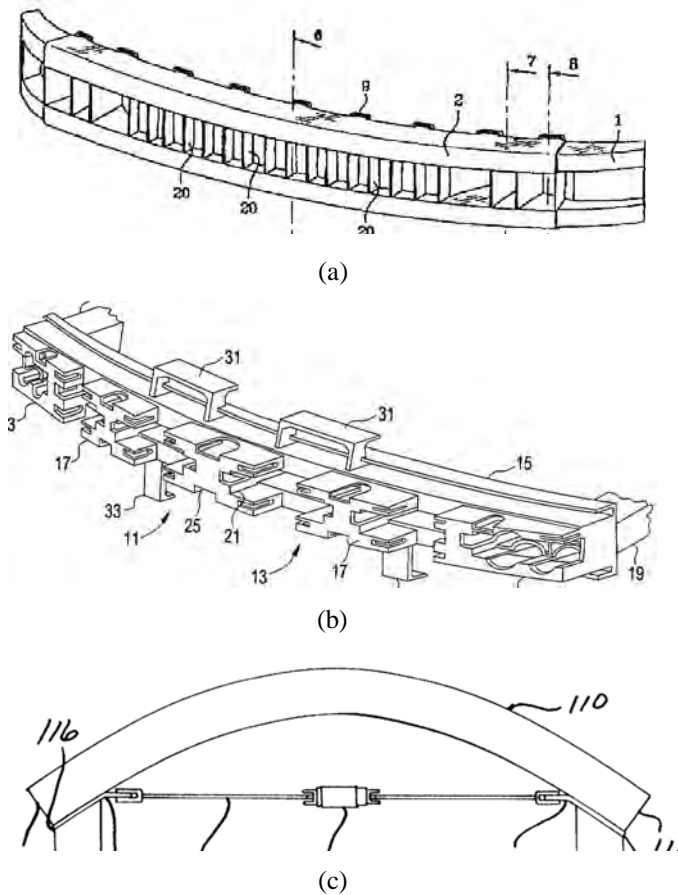


Fig. 2.11 (a) Reinforced beam (source: Roussel *et al.*, 2003), (b) beam integrated with energy absorption components (source: Shuler and Trappe, 2006), and (c) beam with a tension component (source: Schwartz and Ramoo, 1999).

## 2.4 Deployable Cylinders

Deployable cylinders are a type of deployable structure that have wide application in a variety of engineering fields owing to their remarkably high packaging efficiency, mechanical simplicity, and lightweight. Origami is extensively utilized in the design of deployable cylinders to achieve minimum strain energy variation when folded and deployed.

In the area of aerospace engineering, Sogame and Furuya (1998) developed two types of snowflake shaped deployable cylinders, namely, the Axially Symmetric Type (AST) and the Rotationally Symmetric Type (RST) shown in Fig. 2.12(a) and (b),

respectively, with potential application as dust shields or lunar base structures in caves. Each cylinder can be deployed both radially and axially to achieve a very high packaging efficiency. Barker and Guest (1998) did an initial proof-of-concept study of the application of triangulated cylinders, Fig. 2.13(a), as inflatable tubes. In contrast to those designed by Sogame and Furuya (1998), the radius of the triangulated cylinders experiences little change during the deployment process. Tsunoda and Senbokuya (2002) also introduced folding patterns to inflatable tubes, Fig. 2.13(b), for the purpose of efficient packaging. A 9.6 m long tube can be folded to about 0.2 m in length by the patterns. You and Cole (2006) proposed a self-locking bi-stable deployable cylinder with both ends closed based on a novel origami pattern. The advantage of this design is that very small in-plane strains are generated during the deployment process.

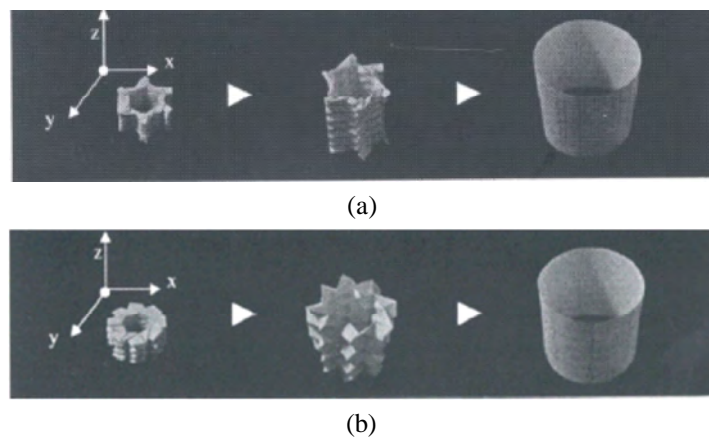


Fig. 2.12 Deployment processes of (a) AST, and (b) RST (source: Sogame and Furuya, 1998).

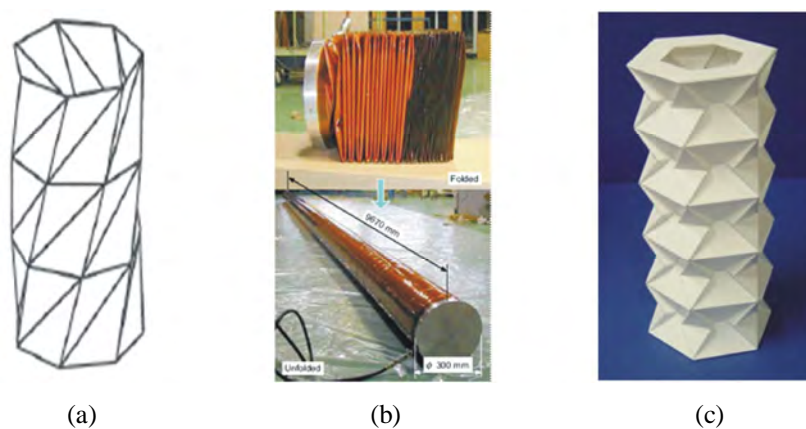


Fig. 2.13 (a) A triangulated cylinder (source: Barker and Guest, 1998), (b) folded and deployed configurations of an inflatable tube (source: Tsunoda and Senbokuya, 2002), and (c) a 6-sided deployable cylinder (source: You and Cole, 2006).

In the area of medical engineering, Kuribayashi (2004) utilized a family of origami patterns to develop a foldable tubular origami stentgraft. The device can be deployed in both radial and axial directions with very small in-plane material deformation, thus making it possible to construct a stentgraft out of a single sheet of material accurately.

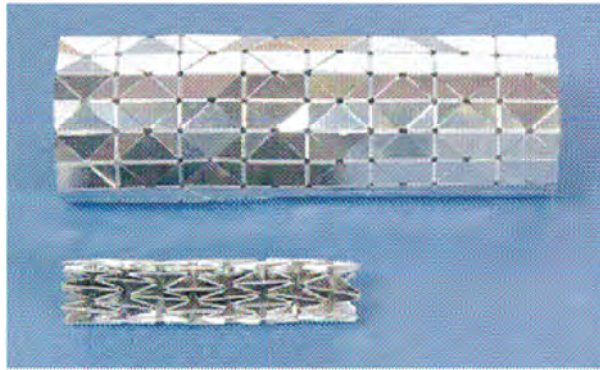


Fig. 2.14 Fully deployed and folded configurations of an origami stentgraft (source: Kuribayashi, 2004).

Compared with origami cylinders with open ends, deployable cylindrical enclosures where both ends are closed, such as the one designed by You and Cole (2006), are very difficult to design. The reason is that in the former, it is possible to create an origami pattern that keeps all panels rigid and all creases acting as rotational hinges, and therefore the resultant origami structure is strain-free during the entire folding process. In the latter, on the other hand, such a pattern does not exist because of the *bellows conjecture* proved by Connelly *et al.* (1997). This conjecture states that for a triangulated polyhedral surface forming an enclosure of a constant volume to flex as a mechanism, the volume of the enclosure must remain constant. The implication of the conjecture is that it is impossible to design a deployable cylinder with closed ends which can be folded like a perfect mechanism, provided that the volume enclosed by the cylinder varies during the process. There must be variation in strain energy during the folding of any practical deployable cylindrical enclosure. However, the magnitude of strain energy variation depends on the pattern put on a cylinder. The above examples demonstrate that a good selection of origami pattern can effectively reduce the strain energy involved in the folding of a deployable cylindrical enclosure. Following this lead, it is believed that a tube with a properly chosen pre-folded origami

pattern may lead to a structure that is hard to fold. In other words, the folding requires a large amount of energy input. This idea is extensively explored in this dissertation in design of cylindrical energy absorption devices.

# **CHAPTER 3**

## **SQUARE TUBES WITH PYRAMID PATTERNS**

It was mentioned in Chapter 2 that one approach to increase the energy consumed to fold a thin-walled square tube was to pre-manufacture a kind of pyramid shaped pattern on its surface (Zhang et al, 2007). A new failure mode called the octagonal mode was observed from the numerical analysis and substantial energy absorption increase was achieved. However, no experiments have been conducted mainly due to the difficulty in constructing the patterned tubes.

In this chapter the effectiveness of the pyramid pattern at triggering the octagonal mode in thin-walled square tubes is investigated experimentally. Section 3.1 describes a method of manufacturing the geometrically complicated patterned tube samples. Section 3.2 focuses on the finite element analysis (FEA) of the quasi-static axial crushing of the patterned tubes using Abaqus/Explicit (SIMULIA Corp., USA) prior to physical experiments. Subsequently in Section 3.3 the physical tube samples are crushed quasi-statically and the experimental results are compared with the numerical data. Finally a summary is given in Section 3.4.

### **3.1 Sample Preparation and Experimental Setup**

### 3.1.1 Sample preparation

The basic pyramid element of the pattern is shown in Fig. 3.1(a). Element width  $p$ , length  $q$ , and height  $h$ , i.e., the distance from the base to the apex, completely define the geometry of the basic pyramid element. The arrangement of the basic pyramid element on each side of the tube is determined by the number of elements in the axial direction  $N_a$  and in the transverse direction  $N_t$ . Note that the apex of the basic pyramid element can be directed outward or inward, as illustrated in Fig. 3.1(b), which affects the failure mode of the tube.

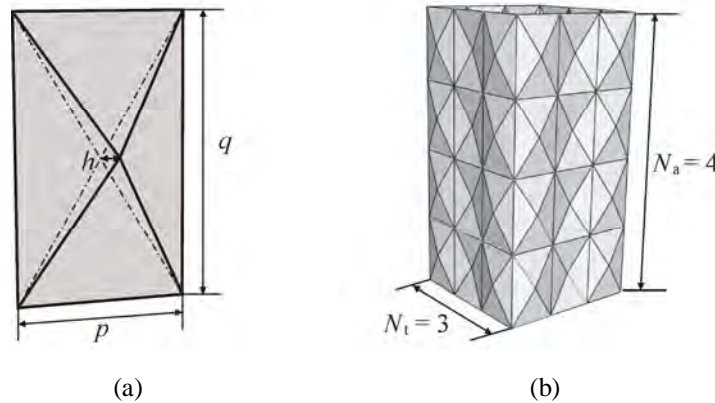


Fig. 3.1 (a) Basic pyramid element, and (b) a square tube with pyramid pattern.

As the surface of the pattern is not developable, it is impossible to produce a patterned tube out of a metal sheet without in-plane deformation. However, for thin-walled tubes, two manufacturing methods exist. One is to stamp out the pyramid pattern on a metal sheet and then to weld four sheets together to form a tube. The alternative is to stamp out the pattern directly on the sides of a conventional square tube. The tube walls would not be noticeably thinner by the stamping.

One tube with  $p = 20$  mm,  $q = 30$  mm,  $h = 2$  mm,  $N_a = 4$ , and  $N_t = 3$ , which was reported to have an energy absorption increase by 56.41%, was adopted here for prototyping. Since relatively thin steel square tubes with the suggested cross-sectional dimension were not readily available, the first manufacturing procedure was employed. A pair of male and female moulds, Fig. 3.2, was designed and manufactured for this

purpose. Steel sheets with wall thickness  $t = 1.0$  mm were used to construct tube samples. A welding technology called Gas Tungsten Arc Welding (GTAW) was applied. This technique has the following advantages

- The heat of the electric arc is centralized and the molten spot is small.
- The heat-affected zone is narrow.
- The welding process is fast.
- The welding distortion is small.
- Oxidation and absorption of noxious gas is prevented, resulting in compact weld joints.
- Weld joints with good mechanical performance are obtained.

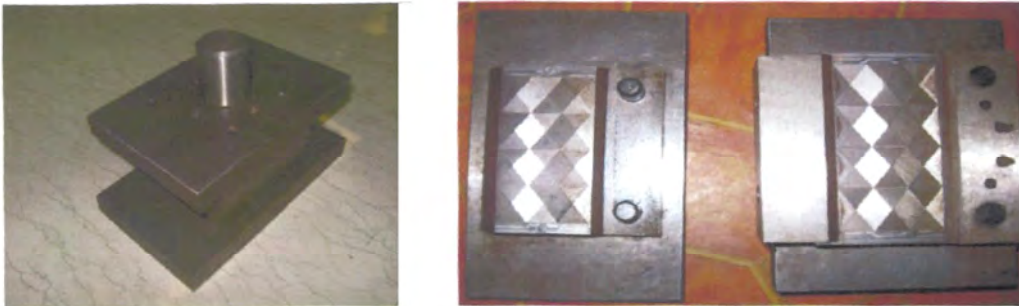


Fig. 3.2 Moulds for pattern stamping.

Two potential problems associated with this manufacturing method were also considered. One was that the corner areas of the samples might be too rigid due to the weld joints. A modified version of the prototype which had one transitional plate at each corner was designed to mitigate this problem. By applying this modification, a sharp corner line was replaced by a narrow plate with finite width, and thus the effect of the rigid weld joints was diluted and the stiffness of the tube was more even across the cross section. The other one was that residual stress existed in the samples because of the stamping process and heat effects. This problem was dealt with by means of annealing. The procedure of heating in a Carbolite furnace at  $600^{\circ}\text{C}$  for 30 minutes and then slowly cooling down in the furnace was adopted. The samples also became more ductile after annealing.

Three types, eight samples in total were manufactured, including two conventional square tubes named C1 and C2, four patterned tubes designated as P1 to P4 in which P3 and P4 were annealed, and two patterned tubes with corner modification called M1 and M2. The width and height of the conventional tubes were chosen to be identical to those of the patterned tubes, i.e., 60 mm and 120 mm, respectively. The modified patterned tubes had identical geometry with the patterned tubes except for the transitional plate at each corner which was 10 mm wide and formed identical angles with adjacent tube sides. In addition, the weld joint was located in the middle the transitional plate. Representatives of the three types of tubes are shown in Fig. 3.3.

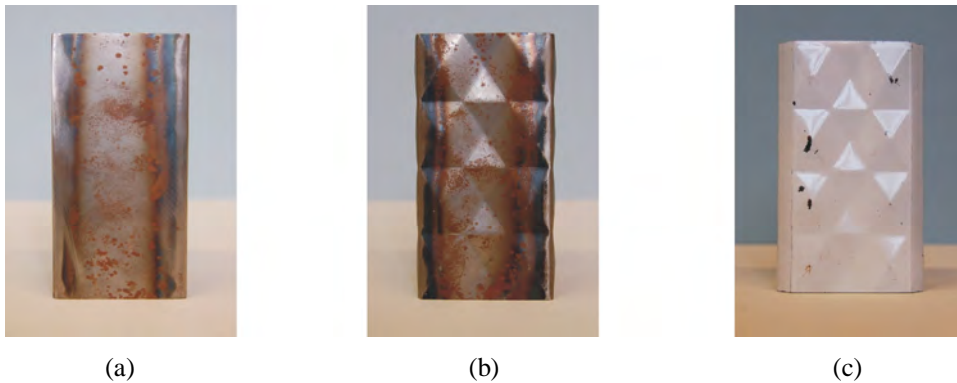


Fig. 3.3 (a) Conventional tube, (b) patterned tube, and (c) modified patterned tube.

### 3.1.2 Experimental setup

The axial crushing tests were conducted on an Instron 5582 testing machine with the upper loading limit of 100 kN. In the test a tube stood on a thick plate and the cross head connected to the load cell moved downward to compress the tube. The speed of the cross head was chosen as 1 mm / min so that material strain rate effects could be safely neglected. The final crushing distance was set to 85 mm which was about 73% of the initial length of the tubes.

Pinned boundary conditions on both ends of the tube, as shown in Fig. 3.4(a), were adopted here to eliminate the effect of arbitrary movement of the tube ends on the forming of the octagonal mode. The constraints were realized by inserting each end of



the tube into a steel block, Fig. 3.4(b), machined with 2 mm wide and 3 mm deep channels.



Fig. 3.4 (a) Pinned boundary conditions, and (b) a block with channels.

The mechanical properties of as-received material without heat treatment and annealed material subjected to identical heat treatment with the tube samples were characterized by material tensile tests. Three specimens were tested for each material. Typical engineering stress vs strain curves of the two materials are plotted in Fig. 3.5. The averaged yield stress  $\sigma_y$ , tensile strength  $\sigma_u$ , and ultimate strain  $\epsilon_u$  of the two materials are listed in Table 3.1. In addition, the density, Young's Modulus, and Poisson ratio of both materials were chosen as  $\rho = 7800 \text{ Kg/m}^3$ ,  $E = 210 \text{ GPa}$ , and  $\nu = 0.3$ .

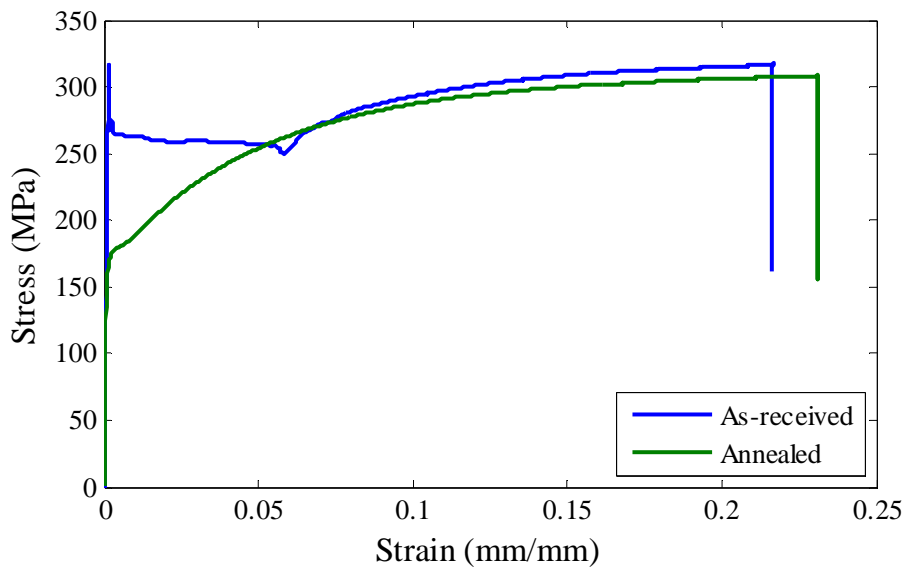


Fig. 3.5 Material engineering stress vs strain curves.

Table 3.1 Material mechanical properties

Material	$\sigma_y$ (MPa)	$\sigma_u$ (MPa)	$\epsilon_u$
As-received	278.4	322.0	21.6%
Annealed	184.3	311.0	24.9%

## 3.2 Numerical Simulation of the Axial Crushing

### 3.2.1 Finite element modelling

A series of numerical simulations of the quasi-static axial crushing of the three types of tube samples were conducted prior to the physical tests to determine whether the desired failure mode could be triggered under the experimental conditions.

A total of four tube models were analyzed, including one conventional tube named Conventional with as-received material, two patterned tubes Patterned1 with as-received material and Patterned2 with annealed material, and one modified patterned tube called Modified with as-received material. The numerical models had identical geometries with the corresponding physical samples. Moreover, a trigger in the form of a dent was introduced near the upper end of Conventional in order to generate a stable and progressive failure mode.

Commercial FEA software package Abaqus (SIMULIA Corp., USA) was applied to simulate the axial crushing process. The crushing scenario was modelled by a tube on a stationary rigid panel and subjected to compression by a moving rigid panel. The tube was mainly meshed with quadrilateral elements, with only a few triangular elements being used to avoid excessive distortion. The lower end of the tube was constrained by three translational degrees of freedom, and the upper one was coupled to the moving rigid panel by three translational degrees of freedom. All the degrees of freedom of the stationary rigid panel were fixed, whereas only the translational one of the moving rigid panel in the axial direction of the tube was free of constraint. Prescribed downward displacement of 85 mm was applied to the free translational degree of

freedom of the moving rigid panel to control the crushing distance. Two types of contacts were established: self-contact for tube walls, and surface-to-surface contact between tube walls and each rigid panel. Friction was taken into consideration and the friction coefficient  $\mu$  was taken as 0.25 (Zhang *et al.*, 2009). The constitutive behaviour of the material was assumed to be elastic-plastic and follow Von Mises yield criteria and isotropic hardening rule.

Three important points were considered in the numerical simulation in order to obtain reliable results. First of all, the axial crushing process was quasi-static due to the very slow loading rate chosen in the experiments. However, the Abaqus Standard solver, designed to solve static problems, was not effective at simulating the axial crushing of thin-walled tubes due to extensive contact and local buckling which often made numerical convergence very slow or impossible. Therefore the Abaqus Explicit solver, designed to solve dynamic problems, was applied here to simulate the crushing process quasi-statically. The key to the success of this method was to choose a proper analysis time which was long enough to guarantee that the crushing process was quasi-static but also as short as possible to be finished with reasonable computational cost. To ensure that dynamic effects were negligible in the analysis, the requirement recommended by Abaqus documentation (SIMULIA Corp., USA) that the ratio of the kinetic energy to the internal energy was below 5% during most of the analysis time was checked. The *smooth* amplitude built in Abaqus (SIMULIA Corp., USA), which guaranteed zero loading speed both at the beginning and at the end of the crushing process, was assigned to the prescribed displacement of the moving rigid panel. The second point was the choice of element. Four-node shell element with reduced integration S4R, which allowed finite membrane strains and arbitrarily large rotations, was cheap and effective to solve problems involving large deformation and complicated contacts, but it had the problem of hourglassing. To ignore safely the hourglassing effect, the requirement recommended by Abaqus documentation (SIMULIA Corp., USA) that the ratio of the artificial energy to the internal energy was below 5% was also checked. The third point was whether a whole tube, a half of a tube, or a quarter of a tube should be modelled in the numerical simulation, considering that all the tubes studied here had

symmetric properties. The quarter-tube modelling and the half-tube modelling approaches could save a lot of computational time but might lose asymmetric buckling modes. While being able to capture all possible buckling modes, the whole-tube modelling approach was not only computationally expensive but might also cause other numerical problems (Meguid *et al.*, 2007). To determine the most appropriate modelling approach, both the whole-tube modelling and the half-tube modelling approaches were used to study Patterned2. It was found out that the failure modes obtained from both approaches were symmetric and matched each other quite well. Thus only a half of each tube was modelled in the analysis here, and symmetric boundary conditions were applied to the edges on the plane of symmetry.

Convergence tests in terms of mesh density and analysis time, respectively, were also conducted. Patterned2 was selected for the tests and the two requirements recommended in Abaqus documentation (SIMULIA Corp., USA) were checked. First of all, Patterned2 was meshed with three densities, coarse with 8580 elements, medium with 18296 elements, and fine with 33752 elements, and analyzed under an identical analysis time of 0.02s. The mean crushing force for each mesh density was calculated and normalized against that for the fine mesh density. The following equation was used to calculate the mean crushing force

$$P_m = \frac{\int_0^{\delta} P(x) dx}{\delta} \quad (3.1)$$

where  $\delta$  is the final crushing distance.

The data presented in Table 3.2 showed a clear trend of convergence, and the difference between the normalized  $P_m$  for the medium mesh density and that for the fine mesh density was within 5%. It was found from Fig. 3.6, where the ratio of the artificial energy (AE) to the internal energy (IE)  $AE/IE$  was plotted against displacement, that the ratios for both the medium and the fine mesh densities were below 5%. Therefore the medium mesh density was selected.

Table 3.2 Mesh convergence test results

Mesh density	Number of elements	Normalized $P_m$
Coarse	8580	1.118
Medium	18296	1.029
Fine	33752	1

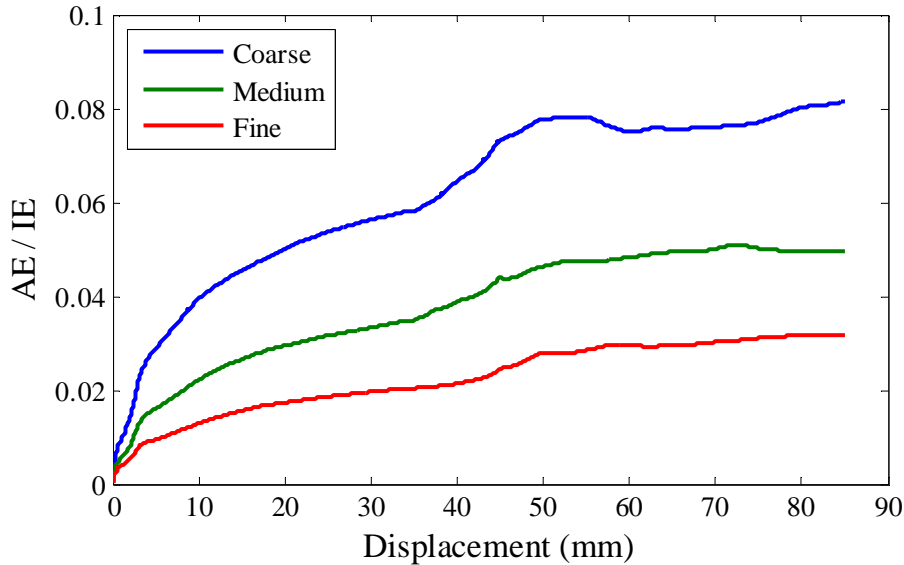


Fig. 3.6 AE / IE vs displacement curves for three mesh densities.

Subsequently Patterned2 with medium mesh density was analyzed under three different analysis times, i.e., short with 0.01s, middle with 0.02s, and long with 0.04s. A clear trend of convergence was again observed from the results shown in Table 3.3. The difference between  $P_m$  obtained from the short analysis time and that from the long analysis time was within 5%. The same is also true by comparing  $P_m$  obtained from the middle analysis time and that from the long analysis time. In addition, the ratio of the kinetic energy (KE) to the internal energy (IE)  $KE / IE$ , plotted against displacement in Fig. 3.7, was below 5% for all of the three analysis times during most of the crushing process. The reason why this ratio was rather high at the beginning of the crushing process was because the internal energy was very small due to little material deformation. Therefore the middle analysis time 0.02 s was chosen for the study here.

Table 3.3 Analysis time convergence test results

Analysis time	Duration (s)	Normalized $P_m$
Short	0.01	0.970
Middle	0.02	0.987
Long	0.04	1

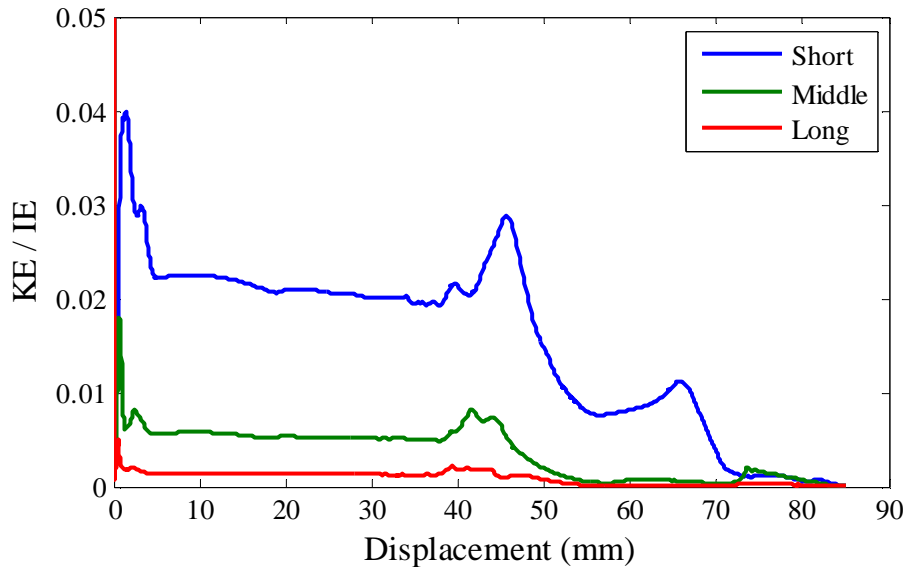


Fig. 3.7 KE / IE vs displacement curves for three analysis times.

### 3.2.2 Results and discussions

Tube model Conventional, serving as the baseline to evaluate the energy absorption improvement of the patterned tubes, is first analyzed. It can be seen from Fig. 3.8(a) that the tube collapses progressively from the upper end where the geometric trigger is placed, and the symmetric mode is eventually obtained. Three lobes are formed in the axial direction of the tube. The mean crushing force of the tube is listed in Table 3.4.

When it comes to tube models Patterned1 and Patterned2, numerical simulation results show that both collapse in a very similar manner and the octagonal mode is eventually attained. The crushing process of Patterned2 is presented in Fig. 3.8(b) as a representative. It can be seen that as the tube is being compressed, a diamond shaped lobe is formed at each corner of the tube and is gradually folded. Due to the forming of

the lobes, the cross section in the middle of the tube changes from a square to an octagon. Furthermore, comparison of  $P_m$  of Conventional and Patterned1 with identical material, also listed in Table 3.4, shows a gain of 74.0%, which further confirms the superior energy absorption of the octagonal mode.

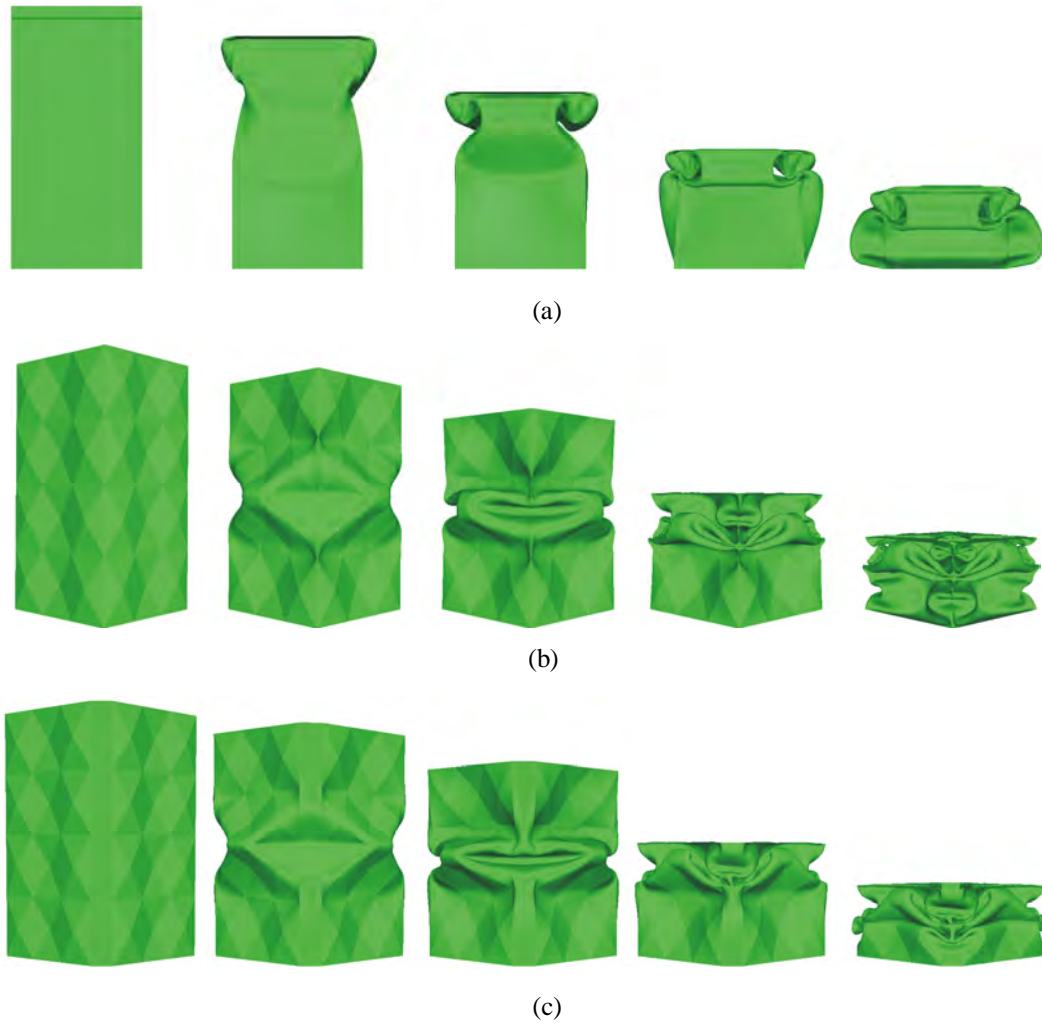


Fig 3.8 Crushing processes of (a) Conventional, (b) Patterned2, and (c) Modified.

Table 3.4 Numerical results of the tube models

Model	Material	$P_m$ (kN)	$P_m$ increase
Conventional	as-received	12.86	-
Patterned1	as-received	22.37	74.0%
Patterned2	annealed	19.37	-
Modified	as-received	22.40	74.2%

A similar crushing process is also observed in tube model Modified. As shown in Fig. 3.8(c), the octagonal mode is not noticeably affected by the transitional plates at the corners. In addition,  $P_m$  of Modified, presented in Table 3.4, is also very close to that of Patterned1, suggesting that the energy absorption of a tube is mainly determined by the failure mode it takes.

### 3.3 Axial Crushing Tests

#### 3.3.1 Conventional square tubes

Two conventional square tube samples C1 to C2 are first analyzed. The crushing process of C2 is shown in Fig. 3.9(a). As expected, the symmetric mode is observed. Comparing Fig. 3.8(a) with Fig. 3.9(a) reveals that the crushing processes of the numerical model and the physical sample agree reasonably well. Two blocks put at the ends of the tubes restrict lateral movement of the ends of the physical sample but do not change its failure mode. One difference between the numerical simulation and the physical test is that the first lobe of the numerical model is formed near the upper end whereas that of the physical sample appears near the lower end. The folding of the numerical model starts from the upper end because the dent is placed there. The location of the first lobe in the physical sample, on the other hand, is affected by geometric imperfection and therefore could be near either end. A similar failure mode is also found in C1 shown in Fig. 3.10(a).

The force vs displacement curves of C1 and C2 are plotted in Fig. 3.11 and the experimental data are listed in Table 3.5. It can be seen that  $P_m$  of the physical samples agree reasonably well with that of the numerical model. The experimental data being slightly higher than the numerical data can be attributed to the weld joints which strengthen the corner areas of the physical samples.





Fig. 3.9 Crushing processes of (a) C2, (b) P1, (c) P4, and (d) M2.

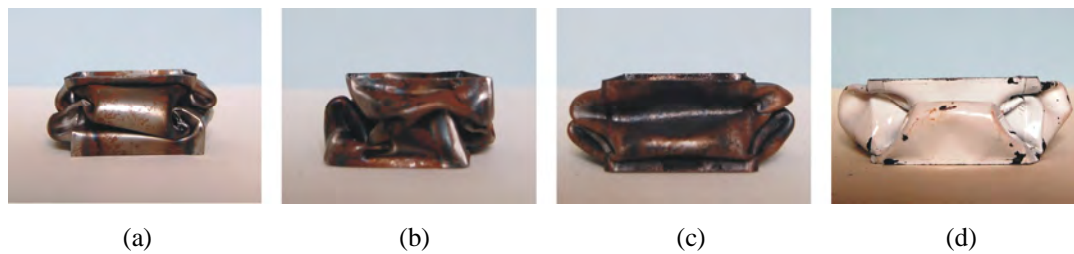


Fig. 3.10 Crushed configurations of (a) C1, (b) P2, (c) P3, and (d) M1.

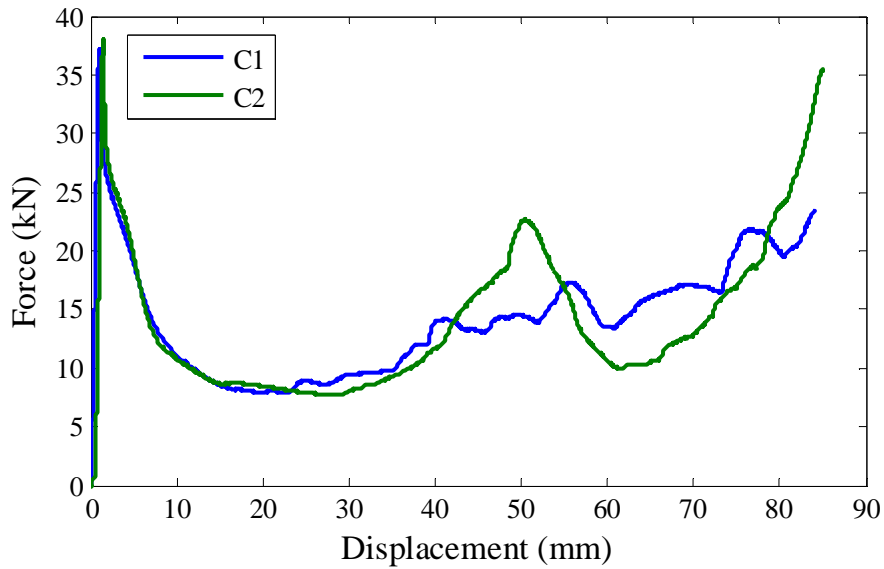


Fig. 3.11 Force vs displacement curves of C1 and C2.

Table 3.5 Experimental results of the tube samples

Model	Heat treatment	$P_m$ (kN)
C1	No	14.19
C2	No	14.09
P1	No	17.01
P2	No	16.64
P3	Yes	10.01
P4	Yes	11.96
M1	No	11.94
M2	No	12.29

### 3.3.2 Patterned square tubes

Two patterned tube samples without heat treatment, P1 and P2, are first analyzed. In contrast to the numerical results, neither sample collapses in the octagonal mode. Instead, it is seen from Fig. 3.9(b) that as P1 is being crushed, only one corner of the tube goes inward as in the case of the octagonal mode, whereas the other three behave like those in the symmetric mode. The crushed configuration of P2, Fig. 3.10(b), shows

that none of the corners folds inwards, leading to the symmetric mode. The pyramid pattern on P2 appears to make its failure mode somewhat irregular compared with those of C1 and C2.

The force vs displacement curves of P1 and P2 are plotted in Fig. 3.12 and the experimental data are compiled in Table 3.5.  $P_m$  of P1 and P2 are slightly higher than those of C1 and C2, but are far below that of the numerical model Patterned1 which has identical material with them. This relatively low energy absorption is understandable because the desired failure mode fails to be induced. It is shown from Table 3.5 that  $P_m$  of P1 is the highest among the four samples, although the improvement is not substantial due to that the desired mode is generated only at one corner. This observation suggests that the octagonal mode, once triggered, does enhance the energy absorption capability of a tube.

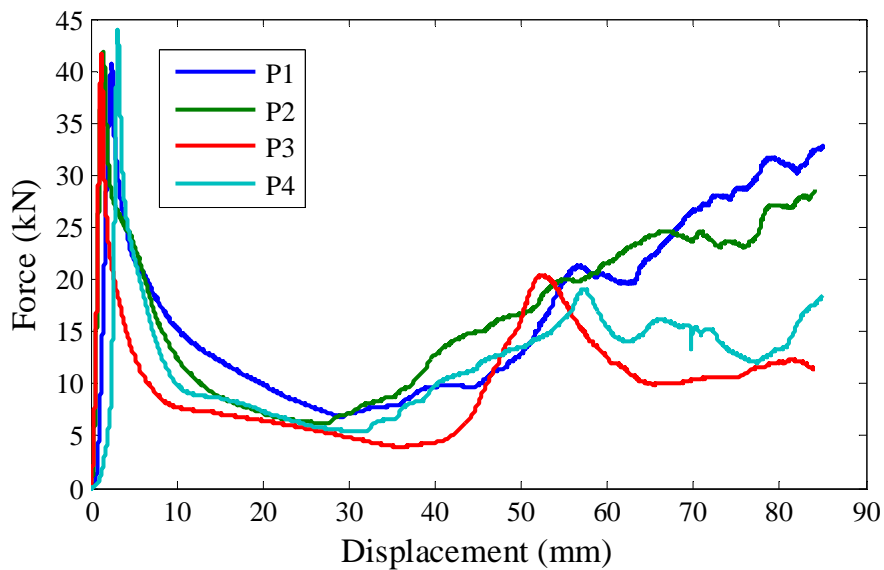


Fig. 3.12 Force vs displacement curves of P1 - P4.

Two annealed patterned tube samples P3 and P4 are analyzed subsequently. The axial crushing process of P4 is shown in Fig. 3.9(c) and the crushed configuration of P3 in Fig. 3.10(c). It can be seen that both samples fail in the symmetric mode. The only evident effect of annealing seems to be that it makes the symmetric collapse mode of P3 and P4 more regular, probably due to the fact that annealing makes the material

properties more uniform. Besides, the force vs displacement curves of P3 and P4 are also plotted in Fig. 3.12 and the experimental data are shown in Table 3.5. Since the target failure mode is not triggered,  $P_m$  of the two physical samples are found to be much lower than that of the numerical model Patterned2 with identical material.

### 3.3.3 Modified patterned square tubes

Two modified patterned tube samples with transitional plates at the corners, M1 and M2, are analyzed. The crushing process of M2 is shown in Fig. 3.9(d) and the crushed configuration of M1 in Fig. 3.10(d). The results show that the transitional plates do not help to trigger the octagonal mode. The collapse modes taken by the two physical samples are on the whole similar to the symmetric mode of conventional square tubes. The force vs displacement curves of the two samples are plotted in Fig. 3.13 and the experimental data are shown in Table 3.5. An interesting observation from the experimental data is that M1 and M2 absorb even less energy that C1, C2, P1, and P2, which appears to contradict common sense. It seems that the corners where the weld joints are located are responsible for a large portion of the total energy absorption of a tube and the transitional plates help to reduce the stiffness of the corners. Because the corners of the tubes without transitional plates are much stiffer than those of the tubes with transitional plates, more energy can be absorbed by the former.

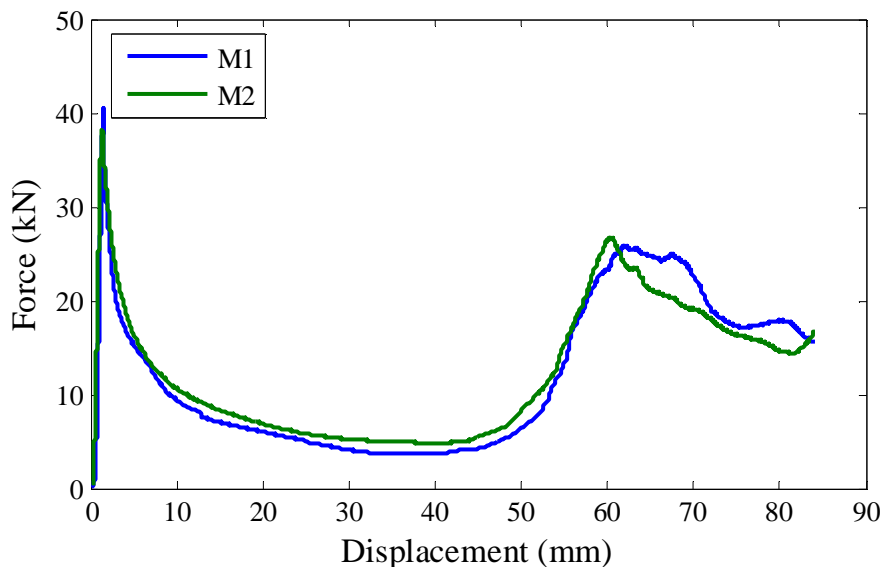


Fig 3.13 Force vs displacement curves of M1 and M2.

### 3.3.4 Discussions

The axial crushing tests on the patterned tubes present a clearly different picture from the numerical simulations. There are several possible reasons to explain the discrepancies. The first is that the octagonal mode is very sensitive to geometric and local material variations and thus difficult to be induced. From the structural point of view, the octagonal mode is actually a high order buckling mode which is unlikely to appear unless certain requirements are met. The introduction of the pyramid pattern favours the octagonal mode but other factors existing in the tube samples, e.g., geometric imperfection, prevent the mode from appearing. Moreover, the manufacturing approach currently adopted to construct the patterned tubes might be too crude. As mentioned previously, the corner zones are critical for the forming of the octagonal mode. The existence of the weld joints and the local heat effects could adversely affect the deformation mode. There are, of course, other ways of constructing tube samples of higher quality, e.g., casting, but they are not used here due to much higher cost.

### 3.4 Summary

In this chapter an experimental study has been carried out on square tube samples with pyramid patterns on the surface, which were reported to have the effect of substantial energy absorption increase when subjected to axial compression. Quasi-static axial crushing tests on eight tube samples show that in general the octagonal mode predicted by the numerical simulations fails to be induced in both the patterned tube samples and their modified version. Only a corner of one patterned tube sample exhibits an incomplete octagonal mode, which is associated with a small amount of energy absorption increase.

Three conclusions can be drawn from the work in this chapter. First of all, it confirms that it is possible to apply geometric patterns in the design of thin-walled tubes to alter

the failure mode and consequently the energy absorption. Secondly, the octagonal mode, if successfully triggered, leads to more energy absorption than the symmetric mode typical of conventional square tubes and thus is desirable from the perspective of designing an energy absorption device. And finally, the octagonal mode triggered by the pyramid pattern is not very stable and highly sensitive to geometric imperfection and local material variation. Hence a reliable and consistent performance cannot be expected from a tube with pyramid pattern.

The above conclusions are drawn from axial crushing tests of tube samples which are not of very high quality. Should a “perfect” tube like the numerical model be made by mean of other more refined approaches, e.g., casting, the octagonal mode may be obtained. However, the practical value of this ideal tube as an energy absorption device is casted into doubt due to high manufacturing cost.

Despite that the application of the pyramid pattern provides a novel way of designing thin-walled energy absorption devices, it seems not an ideal solution in itself. In the following chapters, we shall introduce a design that can consistently trigger a failure mode in a thin-walled tube which is efficient in terms of energy absorption.

# CHAPTER 4

## THE ORIGAMI TUBE: GEOMETRY AND NUMERICAL ANALYSIS

In this chapter, a type of novel thin-walled energy absorption device known as the *origami tube*, which has pre-manufactured origami pattern on the surface, is to be presented. The focus is on geometry and numerical analysis of the origami tube.

Section 4.1 illustrates the theoretical basis of the new design approach through a simple analysis of a strut with a pre-folded shape subjected to axial compression. Section 4.2 describes the design and geometric analysis of a family of origami patterns. In Section 4.3 four groups of origami tubes with a variety of configurations are given and the finite element modelling approach to simulate the quasi-static axial crushing of the tubes is established. Subsequently the numerical results are presented and discussed in Section 4.4. Section 4.5 considers several other factors that are important for the origami tube as a practical energy absorption device, i.e., the dependence of the response of the origami tube on boundary condition and material, the behaviour of the origami tube reinforced by a centre web, the bending capacity and torsion capacity of the origami tube, and the performance of the origami tube subjected to dynamic axial crushing. Finally a summary in Section 4.6 concludes this chapter.

### 4.1 Theoretical Basis of the New Design Approach

The idea of applying origami patterns to design high-performance energy absorption devices is inspired by a well-known fact in structural engineering: structural properties depend critically on structural profiles, which is most common in thin-walled structures. For instance, structural engineers have for a long time known that a “T” section will exhibit different bending stiffness from that of an “I” section. The difficulty in the design of thin-walled energy absorption devices, however, lies in that the major portion of energy absorption occurs at the post-buckling stage which is highly non-linear and thus cannot be effectively manipulated by conventional structural design approaches such as variation of cross section profiles.

To overcome this difficulty, the approach taken in this chapter is to pre-fold thin-walled tubes according to some specific origami patterns so that the buckling and post-buckling behaviour of a thin-walled tube can be controlled and adjusted. The rationale behind this approach is that, if a tube has a pre-folded pattern on it, the structure may follow this pattern during a crash. Hence, the failure mode is determined by the pattern put on. Alternation of the patterns can then change the failure modes. This approach has its theoretical basis, which can be illustrated by a simple analysis of a pin-ended strut subjected to axial compression.

Consider a slim strut of length  $L$  and bending stiffness  $EI$ , and subjected to an axial force  $P$ . The strut is assumed to be axially incompressible and the axial force is assumed to retain its magnitude and direction as the strut deforms. If perfectly straight, the strut is expected to deflect into a half sine curve when  $P$  reaches the Euler buckling load

$$P_E = \frac{\pi^2 EI}{L^2} \quad (4.1)$$

If, on the other hand, the strut, as shown in Fig. 4.1, is pre-folded into a curve as follows

$$y_0 = \delta_1 \sin \frac{\pi x}{L} + \delta_2 \sin \frac{2\pi x}{L} \quad (4.2)$$



in which  $\delta_1$  and  $\delta_2$  are the amplitudes of the half sine and the full sine components, respectively, with  $\delta_1 \ll \delta_2$  to ensure that the full sine component dominates, the buckling mode of the strut can be derived through an energy formulation.



Fig. 4.1 Configuration of the pre-folded strut.

In the linear and small deformation analysis (Timoshenko, 1961), the curvature of the strut upon compression is given by

$$\chi = \frac{d^2 y}{dx^2} - \frac{d^2 y_0}{dx^2} \quad (4.3)$$

The end shortening of the strut is

$$\xi = \int_0^L \frac{1}{2} \left[ \left( \frac{dy}{dx} \right)^2 - \left( \frac{dy_0}{dx} \right)^2 \right] dx \quad (4.4)$$

So the potential energy of the total system can be calculated as

$$V = \frac{1}{2} EI \int_0^L \left( \frac{d^2 y}{dx^2} - \frac{d^2 y_0}{dx^2} \right)^2 dx - P \int_0^L \frac{1}{2} \left[ \left( \frac{dy}{dx} \right)^2 - \left( \frac{dy_0}{dx} \right)^2 \right] dx \quad (4.5)$$

Conducting the calculus of variation on  $V$  in Eq. (4.5) leads to

$$\begin{aligned} \delta V = & \left( -P \frac{dy}{dx} \delta y \right) \Big|_0^L + \left[ EI \left( \frac{d^2 y}{dx^2} - \frac{d^2 y_0}{dx^2} \right) \delta \left( \frac{dy}{dx} \right) \right] \Big|_0^L - \left[ EI \left( \frac{d^3 y}{dx^3} - \frac{d^3 y_0}{dx^3} \right) \delta y \right] \Big|_0^L \\ & + \int_0^L \left[ EI \left( \frac{d^4 y}{dx^4} - \frac{d^4 y_0}{dx^4} \right) + P \frac{d^2 y}{dx^2} \right] \delta y dx \end{aligned} \quad (4.6)$$

The boundary conditions of the strut at  $x=0$  and  $x=L$  give

$$(y)_{x=0} = (y)_{x=L} = \left( \frac{d^2 y}{dx^2} \right)_{x=0} = \left( \frac{d^2 y}{dx^2} \right)_{x=L} = 0 \quad (4.7)$$

Substituting Eq. (4.7) into Eq. (4.6) gives

$$\delta V = \int_0^L \left[ EI \left( \frac{d^4 y}{dx^4} - \frac{d^4 y_0}{dx^4} \right) + P \frac{d^2 y}{dx^2} \right] \delta y \, dx \quad (4.8)$$

from which the equilibrium equation of the strut is attained

$$EI \left( \frac{d^4 y}{dx^4} - \frac{d^4 y_0}{dx^4} \right) + P \frac{d^2 y}{dx^2} = 0 \quad (4.9)$$

Conducting the calculus of variation on  $\delta V$  in Eq. (4.8) leads to

$$\delta^2 V = \int_0^L \left[ EI \delta \left( \frac{d^4 y}{dx^4} \right) + P \delta \left( \frac{d^2 y}{dx^2} \right) \right] \delta y \, dx \quad (4.10)$$

which can be used to determine the stability of the equilibrium path calculated from Eq. (4.9).

With all of the basic equations being obtained, we can now derive the deflection curve of the strut. First substitute Eq. (4.2) into Eq. (4.9) and solve Eq. (4.9)

$$y = A_1 \sin \sqrt{\frac{P}{EI}} x + A_2 \cos \sqrt{\frac{P}{EI}} x + A_3 x + A_4 + \frac{P_E}{P_E - P} \delta_1 \sin \frac{\pi x}{L} + \frac{4P_E}{4P_E - P} \delta_2 \sin \frac{2\pi x}{L} \quad (4.11)$$

in which  $A_1$ ,  $A_2$ ,  $A_3$ , and  $A_4$  are constants of integration to be determined.

Applying the boundary conditions in Eq. (4.7) leads to  $A_2 = A_3 = A_4 = 0$  and

$$A_1 \sin \sqrt{\frac{P}{EI}} L = 0 \quad (4.12)$$

One solution of Eq. (4.12) is

$$A_1 = 0 \quad (4.13)$$

which gives

$$y = \frac{P_E}{P_E - P} \delta_1 \sin \frac{\pi x}{L} + \frac{4P_E}{4P_E - P} \delta_2 \sin \frac{2\pi x}{L} \quad (4.14)$$

When  $|P_E - P|$  is relatively large, the second term on the right hand side of Eq. (4.14) is dominant since  $\delta_1 \ll \delta_2$ , and therefore the deflected shape of the strut is essentially a full sine curve. When, on the other hand,  $P$  is approaching  $P_E$ , the first term on the right hand side Eq. (4.14) becomes very large, resulting in that the deflection curve of the strut is practically a half sine curve.

To determine the stability of this equilibrium path, substitute Eq. (4.14) into Eq. (4.10), and the following expression can be obtained

$$\delta^2 V = \frac{\pi^4 P_E^2}{2L^3} \left( \frac{\delta_1^2}{P_E - P} + \frac{256\delta_2^2}{4P_E - P} \right) (\delta x)^2 \quad (4.15)$$

When  $P < P_E$ ,  $\delta^2 V > 0$  and therefore Eq. (4.14) represents a stable equilibrium path.

The other solution of Eq. (4.12) is

$$\sqrt{\frac{P}{EI}} L = k\pi \quad (4.16)$$

in which  $k$  is a positive integer.

The smallest value of  $k$  is 1, which gives

$$P = P_E \quad (4.17)$$

Substituting Eq. (4.17) into Eq. (4.11) leads to that term  $\frac{P_E}{P_E - P} \delta_1 \sin \frac{\pi x}{L}$  dominates

the right hand side of Eq. (4.11). In other words, the buckled shape of the strut is essentially a half sine curve.

Now consider a practical loading scenario of  $P$  slowly increasing from zero. The analysis presented above indicates that if the objective is to keep the initial full sine shape during the collapse, one approach is to make the strut yield when  $P$  is well below  $P_E$ . The first term on the right hand side of Eq. (4.14) is negligible under this circumstance because  $\delta_1 \ll \delta_2$ , so Eq. (4.14) can be rewritten as

$$\delta_m = \frac{4P_E}{4P_E - P} \delta_2 \quad (4.18)$$

where  $\delta_m$  denotes the maximum deflection of the strut, which occurs at  $x = L/4$ .

The deflection to cause material yielding in the strut can be expressed as

$$\delta_y = \frac{(\sigma_y A - P)I}{PAz} \quad (4.19)$$

in which  $A$  is the cross section area and  $z$  is the maximum distance on the section from the neutral axis.

Take a square sectional strut with  $L = 100$  mm,  $I = 1/12$  mm<sup>4</sup>,  $A = 1$  mm<sup>2</sup>,  $z = 0.5$  mm,  $E = 210$  GPa, and  $\sigma_y = 200$ MPa as an example.  $\delta_m$  and  $\delta_y$  are plotted against  $P$  in Fig. 4.2 where  $\delta_2$  varies from 0.50 mm to 1.50 mm. It can be seen that when  $\delta_2 > 1.32$ ,  $\delta_m$  and  $\delta_y$  intersect on the left hand side of  $P = P_E$ , suggesting that plastic

deformation develops in the strut before  $P$  reaches  $P_E$  and therefore the initial full sine curve is preserved upon the yielding of the strut.

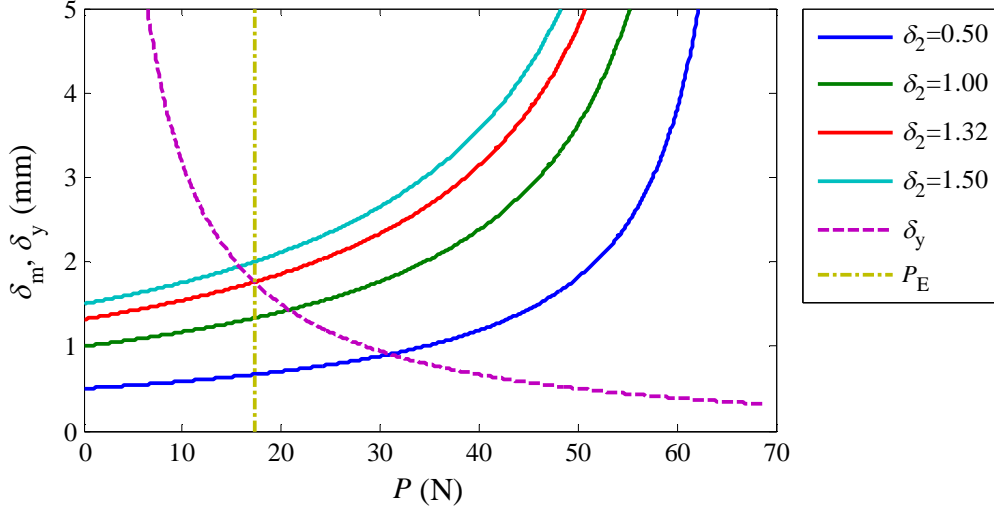


Fig. 4.2 Deflection vs axial force curves of the pre-folded strut.

Two points need to be clarified in Fig. 4.2. First of all, the  $\delta_m$  curves are calculated based on the assumption that  $\delta_1$  in the first term on the right hand side of Eq. (4.14) is very small so that the entire term is neglected. This is true when  $P$  is well below  $P_E$ . When  $P$  is very close to  $P_E$ , however, the curves have no practical meaning because now the first term on the right hand side of Eq. (4.14) can no longer be neglected. Secondly, the portions of the  $\delta_m$  curves on the right hand side of  $P_E$  can be realized if  $P$  is much larger than  $P_E$  at the beginning of the loading process. However, this type of loading scenario is not possible because the strut will have already buckled to half a sine wave when  $P$  is close to  $P_E$ .

Assuming that the material is elastic-perfectly plastic, if the full sine curve is preserved until the strut yields, a plastic hinge would appear at  $x=L/4$  or  $3L/4$ . Since the stiffness of the plastic hinge is much lower than that of the remainder of the strut, bending deformation would concentrate in the hinge, which would consequently prevent the strut from reversing back to the half sine mode. In this case the strut can be seen as two shorter parts joined by a plastic hinge. Since the two parts have different lengths, it is impossible for the strut to be completely flattened unless new plastic

hinges occur. Therefore, the energy absorption of the pre-folded strut would be higher than that of a perfect one which collapses in a half sine curve for the reason that more plastic hinges are formed in the former case.

To summarize, it has been demonstrated from the above analysis that it is possible to initiate and preserve a new buckling mode in a strut by pre-folding it into a certain shape before loading. Applying the same principle to thin-walled tubes, if a pre-folded tube can retain the specified failure mode triggered by the origami pattern on the surface, high energy absorption can be achieved provided that a correct mode is chosen.

Origami technique is selected here to create efficient failure modes in terms of energy absorption because of the following reasons. First of all, origami patterns suit this particular application well as the material that is dealt with here is thin. Secondly, most origami shapes are developable. Therefore, origami patterns can be manufactured on the surface of a tube without much distortion. Finally, mathematical modelling tools for origami are available, which facilitate the exploration of various pattern designs.

This proposed approach offers unique advantages because it can substantially improve the performance of a thin-walled structure with little additional cost; moreover, the failure mode of the structure is predictable and can be made stable, leading to reliable structural response.

## **4.2 Design and Geometric Analysis of Origami Patterns**

It is known from the review of square tubes in Chapter 2 that three main deformation mechanisms exist, i.e., stationary plastic hinge line in both the symmetric and extensional modes, travelling plastic hinge line in the symmetric mode, and circumferential extension of a large magnitude in the extensional mode. Circumferential extension is very efficient in terms of energy absorption but difficult to be activated in thin-walled tubes. This is because a sheet of thin metal is more easily

bent than stretched. One possible way of inducing large circumferential membrane deformation is to pre-manufacture a number of bulges on the surface of a square tube, as in the case of corrugations on circular tubes (Singace and El-Sobky, 1997). However, such a geometric imperfection would lead to a nondevelopable surface of the tube and thus cannot be implemented by an origami pattern out of a flat sheet of material. The approach applied here to improve the energy absorption of a square tube is to increase the number of travelling plastic hinge lines through a proper geometric trigger. Travelling plastic hinge lines are responsible for two-thirds of the total energy absorption of a square tube. Therefore if more travelling plastic hinge lines are activated in a tube, high energy absorption would be achieved. Since travelling plastic hinge lines are associated with the symmetric mode which is circumferentially inextensional, it is possible to design an origami pattern with a developable surface to implement such a trigger on a square tube. When a square tube that is folded according to an origami pattern is crushed, it can be seen as a cylindrical enclosure. Deformation mechanisms other than folding along pattern creases must exist in the tube because of the bellows conjecture, and therefore travelling plastic hinge lines are possible to be activated in theory provided that a proper pattern is designed.

To realize this objective, a basic origami pattern for square tubes, Fig 4.3(a), is designed. The solid lines in the figure stand for hill creases and the dashed ones for valley creases. If a flat sheet of material is folded along the creases and then the two opposite free edges are joined, a square origami tube, Fig. 4.3(b), can be obtained. The most important geometric feature of the origami tube that distinguishes it from a conventional square tube is the lobe at each corner. The lobe fulfils two main functions: first of all, it is a “failure mode inducer” to direct the tube to collapse following the pre-manufactured pattern, so that a new failure mode can be formed in the tube; secondly, it is also a “geometric imperfection” to reduce the initial buckling force of the tube.

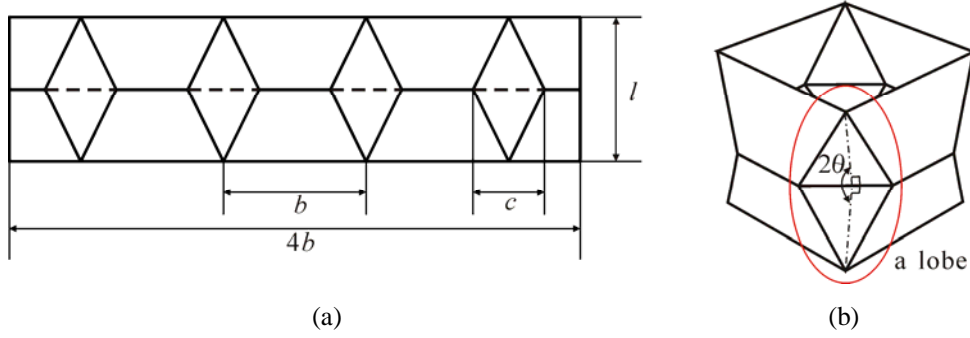


Fig. 4.3 (a) A module of the origami pattern for square tubes, and (b) a module of a square origami tube.

The basic pattern has several desirable properties. First of all, what is presented in Fig. 4.3 can be taken as a module, and longer tubes can be obtained by stacking a number of modules axially. Secondly, it can be easily modified to fit tubes with rectangular or polygonal cross sections and tapered tubes, all of which are also commonly used in practice. And finally, it has developable surface and therefore, the origami tube can be made out of a flat sheet of material with little in-plane stretching. Hence, the origami tube can be conveniently and accurately manufactured.

There are three independent geometric parameters to define the basic pattern: tube width  $b$ , corner width  $c$ , and module length  $l$ . Dihedral angle  $2\theta$  is determined by  $c$  and  $l$  through the following equation:

$$\cos \theta = (\sqrt{2} - 1) \frac{c}{l} \quad (4.20)$$

In addition, geometric constraints on  $c$  require that:

- $c \leq b$ , otherwise the pattern would not be developable.
- $c \leq (\sqrt{2} + 1)l$ , since  $\cos \theta \leq 1$ .

When  $c = 0$ , the origami tube reduces to a conventional square tube.

The basic pattern can be modified to form rectangular origami tubes. A module of the origami pattern for rectangular tubes and the corresponding module of a rectangular origami tube are shown in Fig. 4.4. Here the rectangular cross section is defined by its length  $a$  and width  $b$ , with  $a > b$ . Therefore four geometric parameters,  $a$ ,  $b$ ,  $c$ , and  $l$ ,



completely determine the configuration of the pattern. Equation (4.20) can also be applied to calculate  $2\theta$  in this case.

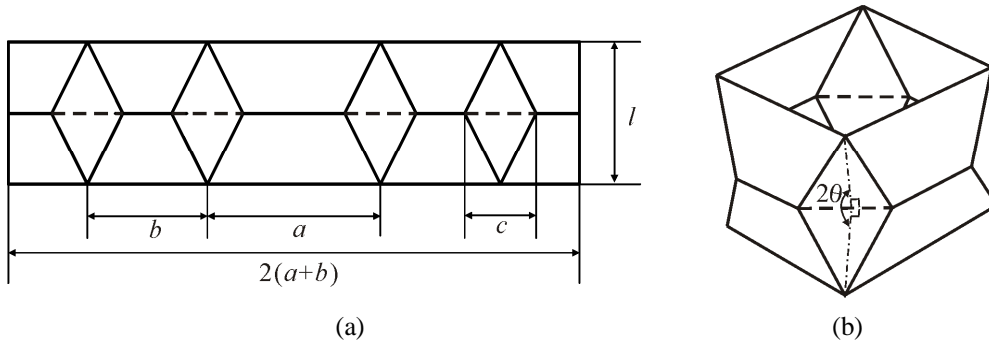


Fig. 4.4 (a) A module of the origami pattern for rectangular tubes, and (b) a module of a rectangular origami tube.

Modifying the basic pattern to design polygonal tubes can also be realized. Figure 4.5 is a module of the origami pattern for hexagonal tubes and the corresponding module of a hexagonal origami tube. Four geometric parameters,  $b$ ,  $c$ ,  $l$ , and the number of sides  $N$ , completely define the geometry of the pattern. The dihedral angle  $2\theta$  for an  $N$ -sided tube can be calculated as

$$\cos \theta = \tan\left(\frac{\pi}{2N}\right) \frac{c}{l} \quad (4.21)$$

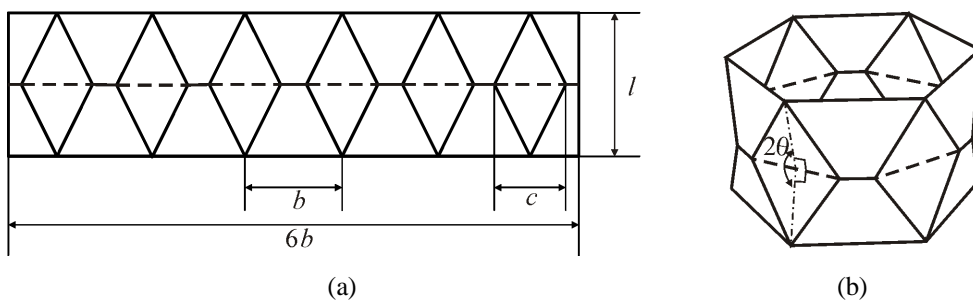


Fig. 4.5 (a) A module of the origami pattern for hexagonal tubes, and (b) a module of a hexagonal origami tube.

There is also no difficulty in designing tapered tubes by slight modification of the basic pattern. Two types of tapered tube can be attained. Type I tapered tubes have only two opposite sides inclined and the other two straight. Figure 4.6 shows a module of the origami pattern for tapered tubes of this type and the corresponding module of a

tapered origami tube of this type. Five geometric parameters determine the geometry of the pattern: the lengths of the upper bottom and lower bottom of the trapezoid surface  $a_1$  and  $a_2$ ,  $b$ ,  $c$ , and  $l$ . Type II tapered tubes have four inclined sides. A module of the origami pattern for tapered tubes of this type and the corresponding module of a tapered origami tube of this type are shown in Fig. 4.7. The geometry of this pattern is completely defined by four geometric parameters:  $a_1$ ,  $a_2$ ,  $c$ , and  $l$ . Note that no closed-form expression of  $2\theta$  can be obtained for either of the two types of tapered origami tubes. A detailed geometric analysis of the two types of tapered origami tubes is presented in Appendix I.

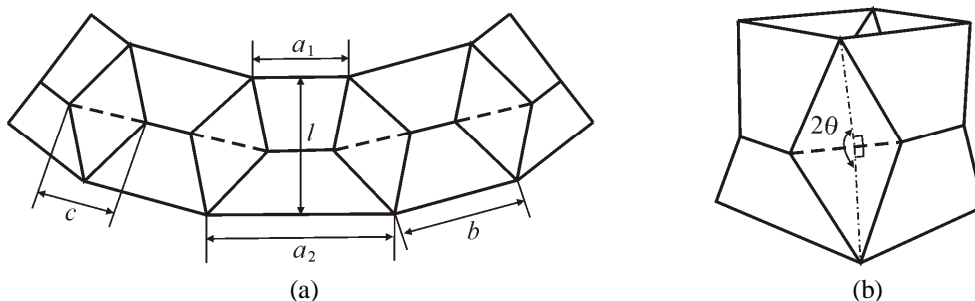


Fig. 4.6 (a) A module of the origami pattern for type I tapered tubes, and (b) a module of a type I tapered origami tube.

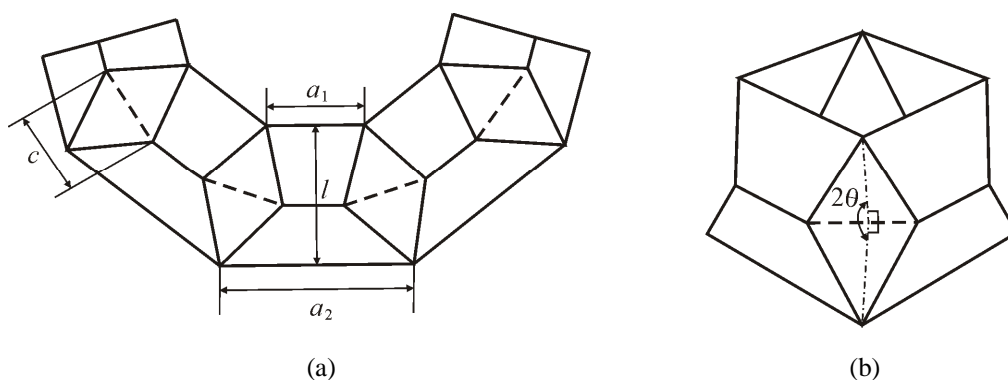


Fig. 4.7 (a) A module of the origami pattern for type II tapered tubes, and (b) a module of a type II tapered origami tube.

Finally, the number of modules in the axial direction  $M$  is another geometric parameter if long origami tubes are designed. The geometric design parameters for origami tubes with five profiles are summarized in Table 4.1. For each profile, the number of geometric design parameters is no more than 6.

Table 4.1 Summary of the geometric design parameters for origami tubes with five profiles

Tube profile	Geometric parameters
Square	$b, c, l, M$
Rectangular	$a, b, c, l, M$
Polygonal	$b, c, l, N, M$
Tapered of type I	$a_1, a_2, b, c, l, M$
Tapered of type II	$a_1, a_2, c, l, M$

### 4.3 Design of Origami Tubes and Finite Element Modelling

#### 4.3.1 Design of origami tubes

Four groups of origami tubes with various configurations were designed and analyzed to investigate the failure mode and energy absorption properties of the origami tube. Group A included one conventional square tube and twenty-nine square origami tubes. They were created to investigate the influences of nondimensional geometric parameters  $c/l$ ,  $l/b$ , and  $b/t$ . The width, height, and wall thickness of the conventional square tube A0 were  $b = 60$  mm,  $H = 120$  mm, and  $t = 1.0$  mm. The tube was vertically placed and a geometric imperfection in the form of a small dent was introduced near the upper end of the tube in order to ensure a stable and progressive collapse mode. All of the origami tubes in this group had  $b$  and surface area identical to those in A0. Parameters  $c$ ,  $l$ , and  $t$  varied from one tube to another. The configurations of all of the tubes in Group A are listed in Table 4.2.

Table 4.2 Configurations of tubes in Group A and numerical results

Model	$c$ (mm)	$l$ (mm)	$2\theta$ (°)	$M$	$t$ (mm)	$P_{\max}$ (kN)	$P_{\max}$ reduction	$P_m$ (kN)	$P_m$ increase
A0	-	-	-	-	1.0	40.17	-	11.98	-
A1_1	30	60	156	2	1.0	25.50	36.5%	18.86	57.4%
A1_2	24	60	160	2	1.0	26.20	34.8%	19.58	63.4%
A1_3	20	60	164	2	1.0	26.97	32.9%	20.38	70.1%
A1_4	15	60	168	2	1.0	26.79	33.3%	19.03	58.9%
A1_5	10	60	172	2	1.0	33.41	16.8%	18.77	56.7%
A2_1	20	40	156	3	1.0	25.00	37.8%	19.03	58.9%
A2_2	16	40	160	3	1.0	25.74	35.9%	18.73	56.3%
A2_3	13.3	40	164	3	1.0	24.41	39.2%	19.35	61.5%
A2_4	10	40	168	3	1.0	25.35	36.9%	20.12	68.0%
A2_5	6.7	40	172	3	1.0	25.37	36.8%	18.77	56.7%
A3_1	15	30	156	4	1.0	24.54	38.9%	19.49	62.7%
A3_2	12	30	160	4	1.0	27.80	30.8%	20.93	74.7%
A3_3	10	30	164	4	1.0	25.02	37.7%	21.15	76.5%
A3_4	7.5	30	168	4	1.0	24.51	39.0%	20.95	74.9%
A3_5	5	30	172	4	1.0	26.20	34.8%	19.16	59.9%
A4_1	12	24	156	5	1.0	26.46	34.1%	21.66	80.8%
A4_2	9.6	24	160	5	1.0	25.14	37.4%	22.25	85.7%
A4_3	8	24	164	5	1.0	25.39	36.8%	22.27	85.9%
A4_4	6	24	168	5	1.0	24.71	38.5%	20.28	69.3%
A5_1	10	20	156	6	1.0	31.77	20.9%	23.01	92.1%
A5_2	8	20	160	6	1.0	23.69	41.0%	21.34	78.1%
A6_1	8.6	17.2	156	7	1.0	27.19	32.3%	20.26	69.1%
A7_1	30	60	156	2	0.6	-	-	7.90	-
A7_2	30	60	156	2	0.8	-	-	12.85	-
A7_3	30	60	156	2	1.2	-	-	26.28	-
A7_4	30	60	156	2	1.4	-	-	35.00	-
A7_5	30	60	156	2	1.6	-	-	45.42	-
A7_6	30	60	156	2	1.8	-	-	56.32	-
A7_7	30	60	156	2	2.0	-	-	67.85	-

The other three groups, B, C, and D, were also built in order to examine the effects of tube profile. Group B consisted of four rectangular origami tubes with various cross section aspect ratio  $a/b$  and  $M$ , Group C included three origami tubes with triangular, pentagonal, and hexagonal cross sections, respectively, and Group D was composed of four type I and four type II tapered origami tubes. In addition, the wall thickness of all of the tubes in the three groups was chosen as 1.0 mm. The configurations of the tubes in the three groups are compiled in Table 4.3. Note that Tables 4.2 and 4.3 also contain the peak forces,  $P_{\max}$ , and mean crushing forces,  $P_m$ , of the tubes which are obtained by the finite element modelling discussed in subsequent sections.

Table 4.3 Configurations of tubes in Groups B, C, D and numerical results

Model	$N$	$a$ (mm)	$a_1$ (mm)	$a_2$ (mm)	$b$ (mm)	$c$ (mm)	$l$ (mm)	$M$	$P_{\max}$ (kN)	$P_m$ (kN)
B1	4	70	-	-	50	30	60	2	31.16	16.80
B2	4	80	-	-	40	30	60	2	24.24	13.69
B3	4	70	-	-	50	20	40	3	25.02	18.92
B4	4	80	-	-	40	20	40	3	24.37	19.42
C1	3	-	-	-	80	20	40	3	18.00	14.31
C2	5	-	-	-	48	20	40	3	32.53	25.08
C3	6	-	-	-	40	20	40	3	34.24	26.63
D1	4	-	50	70	60	30	60	2	25.57	16.79
D2	4	-	40	80	60	30	60	2	24.30	16.64
D3	4	-	50	70	60	20	40	3	23.67	18.92
D4	4	-	40	80	60	20	40	3	23.09	19.23
D5	4	-	50	70	-	30	60	2	25.55	18.37
D6	4	-	40	80	-	30	60	2	26.84	16.23
D7	4	-	50	70	-	20	40	3	24.49	18.39
D8	4	-	40	80	-	20	40	3	22.55	17.49

### 4.3.2 Finite element modelling

The quasi-static axial crushing process was simulated using Abaqus/Explicit (SIMULIA Corp., USA). The tube was placed between two rigid panels, one of which was stationary whereas the other could move to model the crushing scenario. Quadrilateral shell elements S4R were used to mesh the tube, supplemented by a few triangular elements to avoid excessively small or distorted elements. Self-contact was employed to model the contacts among different parts of the tube, and surface-to-surface contact was defined between the tube and each rigid panel. Friction was also considered and the friction coefficient  $\mu$  was taken as 0.25 (Zhang *et al.*, 2009). The lower end of the tube was pinned to the stationary rigid panel which was completely fixed in space, and the upper end was coupled to the moving rigid panel by three translational degrees of freedom. All of the degrees of freedom of the moving rigid panel were constrained except for the translational one in the axial direction of the tube. Prescribed downward displacement was assigned to the free degree of freedom of the moving rigid panel, and smooth amplitude definition built in Abaqus (SIMULIA Corp., USA) was applied to control the loading rate. The final crushing distance was so chosen that the residual height was 35 mm for all of the tubes.

All of the tubes investigated here had two mutually perpendicular vertical planes of symmetry except for C1 with a triangular cross section and C2 with a pentagonal one. The axial crushing of A1\_1 was first analyzed using the whole-tube model and the half-tube model, respectively. It was found out that the failure modes obtained from both models were symmetric and could hardly be distinguished from each other. In addition, their force vs displacement curves, plotted in Fig. 4.8, also matched very well. Therefore, the half-tube model was applied to all of the tubes with two planes of symmetry and symmetric boundary conditions were assigned to the edges on the plane of symmetry, while the whole-tube model was only applied to C1 and C2.

Furthermore, convergence tests with respect to mesh density and analysis time, respectively, were also conducted prior to the analysis. It was found out that a global mesh size of 1 mm and an analysis time of 0.02s could yield satisfactory results.

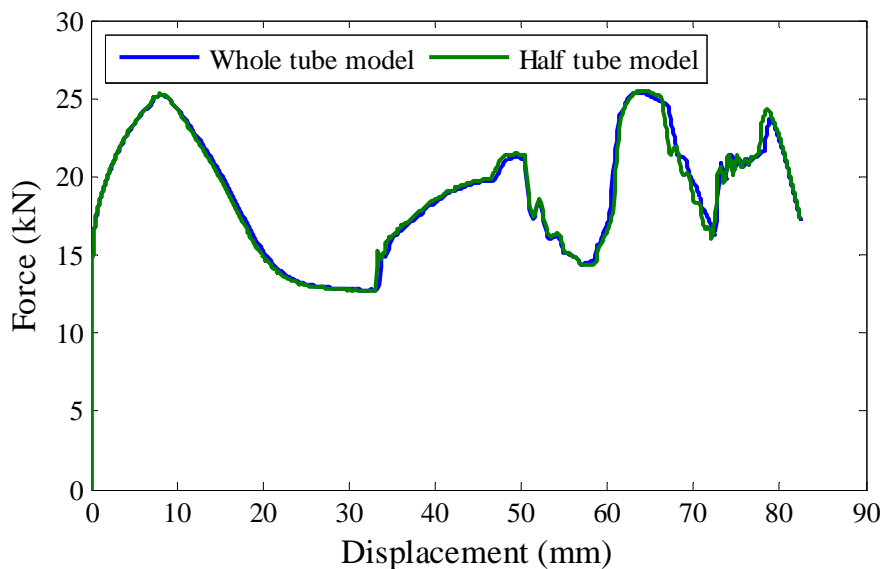


Fig. 4.8 Force vs displacement curves of the whole-tube model and the half-tube model.

Mild steel, commonly used for tubular energy absorption devices, was the material for all of the tubes. The mechanical properties are:  $\rho = 7800 \text{ Kg/m}^3$ ,  $E = 210 \text{ GPa}$ ,  $\sigma_y = 200 \text{ MPa}$ ,  $\sigma_u = 400 \text{ MPa}$ ,  $\varepsilon_u = 20.0\%$ ,  $\nu = 0.3$ , and power law exponent  $n = 0.34$ . The engineering stress vs strain curve is plotted in Fig. 4.9.

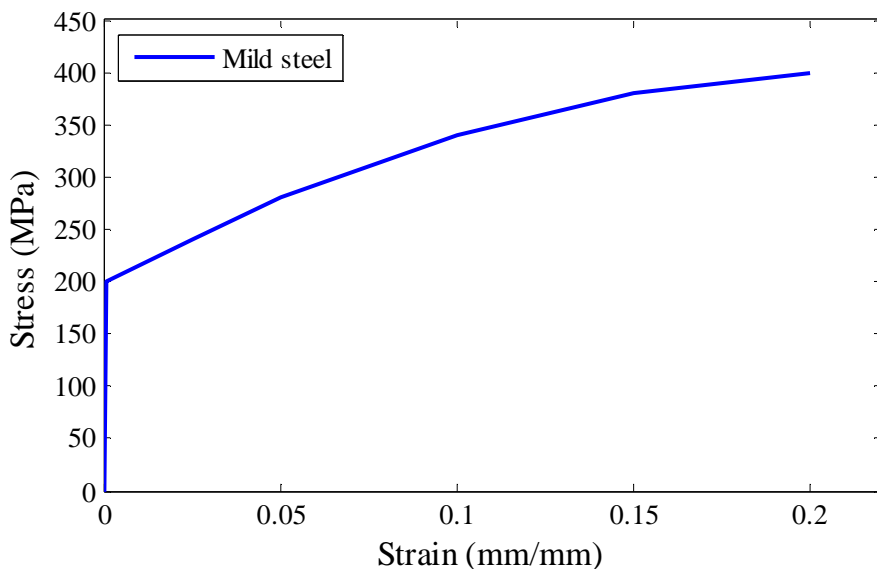


Fig. 4.9 Material engineering stress vs strain curve.

#### 4.4 Results and Discussions

### 4.4.1 Axial crushing of conventional square tube

The conventional square tube A0 is analyzed to validate the finite element modelling procedure and set a baseline to evaluate the energy absorption enhancement of the origami tube. Figure 4.10(a) shows that A0 collapses in the symmetric mode. The force vs displacement curve of A0 is plotted in Fig. 4.11. It can be seen that a very high peak occurs at the beginning, followed by a number of crests and troughs. The numerical value of  $P_m$ , shown in Table 4.2, is 11.98 kN. Note that the difference in  $P_m$  between A0 and tube model Conventional in Chapter 3, both of which have identical geometry, comes from different material properties. The theoretical value of  $P_m$ , calculated using Eq. (2.14) in Chapter 2, is found to be 12.49 kN. It can be seen that a good agreement between the numerical value and the theoretical one is obtained, indicating that the finite element modelling procedure is appropriate for the current problem. Note that the following equation is used to calculate the effective plastic flow stress  $\sigma_0$  in Eq. (2.14) (Santosa *et al.*, 2000)

$$\sigma_0 = \sqrt{\frac{\sigma_y \sigma_u}{1+n}} \quad (4.22)$$

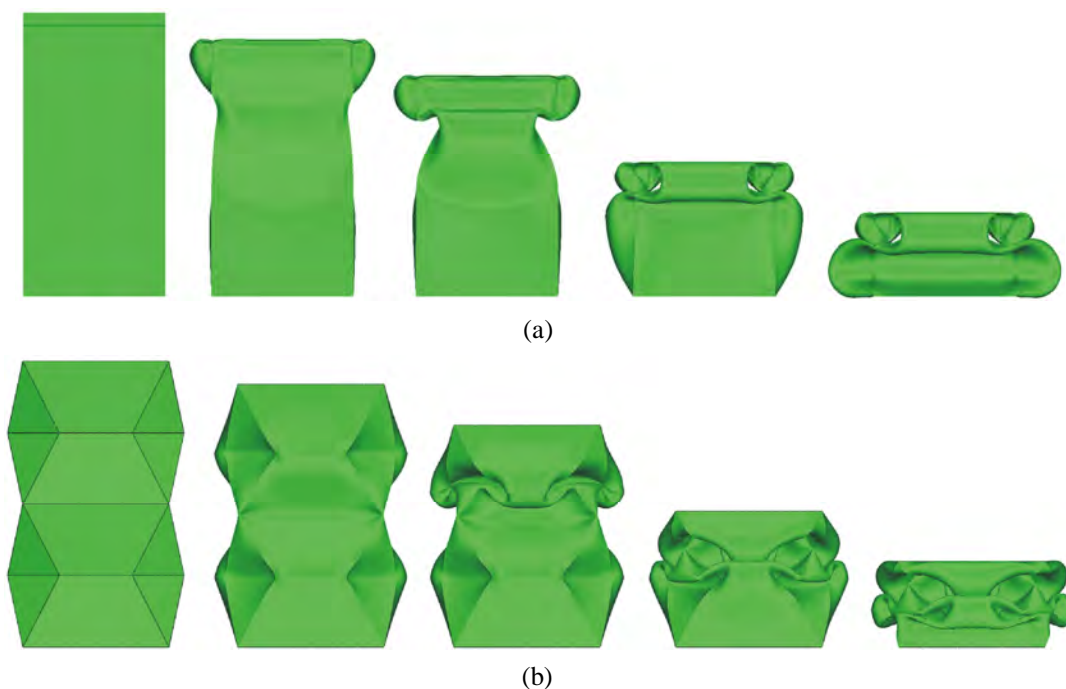


Fig. 4.10 Crushing processes of (a) A0, and (b) A1\_1.



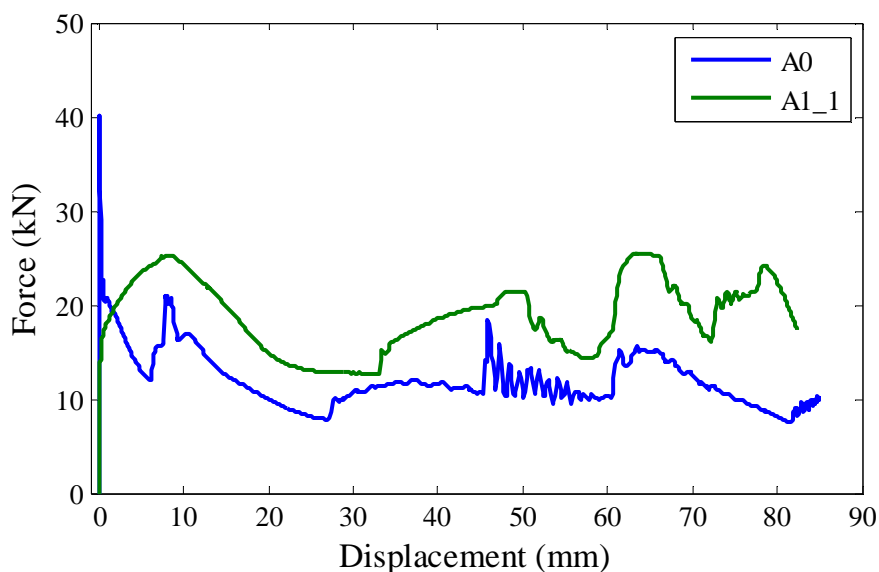


Fig. 4.11 Force vs displacement curves of A0 and A1\_1.

#### 4.4.2 Axial crushing of square origami tube

Let us take a close look at origami tube A1\_1, which is representative of the others. The crushing process of A1\_1 is shown in Fig. 4.10(b). It can be seen that the tube collapses following the pre-manufactured origami pattern on the surface in a progressive and stable manner. At the onset of the crushing process, both modules buckle simultaneously. As the tube is compressed further, two pairs of inclined plastic hinge lines are formed in each lobe and travel away from each other, sweeping across a large amount of corner areas. Comparing this collapse mode with the diamond mode of circular tubes outlined in Section 2.1.2 of Chapter 2 reveals that the two modes are quite similar in shape, with the only main difference that the origami tube is composed of flat plates instead of curved shells. Therefore the failure mode of A1\_1 is named the *complete diamond mode* in which all of the lobes develop well during the crushing process.

The force vs. displacement curve of A1\_1 is also plotted in Fig. 4.11. It can be seen that the high peak no longer exists because of the origami pattern. As a result,  $P_{\max}$  of A1\_1 is considerably lower than that of A0. The area below the forced-displacement curve of A1\_1 which indicates the energy absorption capacity, on the other hand, is

substantially larger than that of A0. Furthermore, the numerical data in Table 4.2 show that compared with those of A0,  $P_{\max}$  of A1\_1 is reduced by 36.5% while  $P_m$  is increased by 57.4%. Therefore it can be concluded that the origami pattern has successfully created a thin-walled tube with high SEA and low load uniformity.

The reason why the square origami tube is able to absorb more energy than the conventional square tube transpires when comparing the failure modes of the two tubes. Figure 4.12 shows a partially crushed square origami tube and a partially crushed conventional square tube. It can be seen that two pairs of travelling plastic hinge lines exist at each corner of the origami tube as opposed to one pair at each corner of the conventional one, leading to increased energy absorption. A detailed analysis of the deformation mechanisms of the origami tube will be presented in Chapter 5.

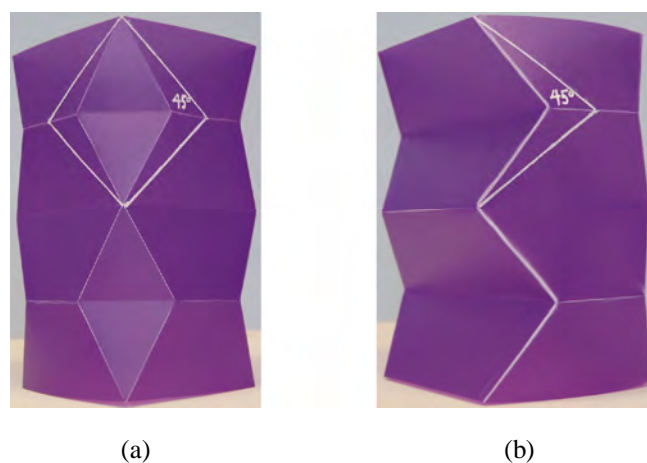


Fig. 4.12 Partially crushed configurations of (a) a square origami tube, and (b) a conventional square tube.

### 4.4.3 Effects of geometric parameters

#### 4.4.3.1 Ratios $c/l$ and $l/b$

It has been shown from the crushing of A1\_1 that the complete diamond mode is more efficient in terms of energy absorption than the symmetric mode. Therefore a key task in the design of the origami tube is to determine the range of pattern geometry that can

lead to the complete diamond mode. Among all the designs with which the complete diamond mode can be successfully induced, there must be an optimum pattern geometry that has maximum energy absorption.

Ratio  $c/l$ , which increases with decreasing  $2\theta$  following Eq. (4.20), is a crucial factor to determine whether the complete diamond mode occurs and how the plastic hinge lines travel if it does occur. It is not difficult to infer that the pattern would no longer be followed if  $c/l$  is too small, leading to impairment of the energy absorption of the origami tube. On the other hand, a very large  $c/l$  can ensure the following of the pattern, but it is also undesirable from the perspective of energy absorption as it would reduce the area swept by travelling plastic hinge lines. In addition, the amount of rotation of stationary plastic hinge lines is also reduced.

Ratio  $l/b$ , which is inversely proportional to  $M$  for a square origami tube with fixed width and surface area, is another important factor that influences the performance of the origami tube. It is intuitive that the smaller the ratio  $l/b$ , or the more the modules, the higher the energy absorption. This is because more modules lead to more horizontal plastic hinge lines. However, a very small  $l/b$  would not only make the tube geometry complicated but could also result in the pattern being overridden during the crushing process. This has been observed in tubes A3\_5, A4\_4, A5\_2, and A6\_1, which are discussed next.

Twenty-one square origami tubes, i.e., A1\_2 - A6\_1, are also analyzed. Since all of the tubes have identical width and surface area, the results are organized based on variations of  $2\theta$  and  $M$ .

Let us start with the failure modes of the tubes. Four tubes, A1\_2 - A1\_5, with  $M = 2$  but increasing  $2\theta$  are first looked into. Numerical results show that when  $2\theta \leq 164^\circ$ , the pattern is well followed and the complete diamond mode is successfully attained, as can be seen from A1\_2 and A1\_3 shown in Fig. 4.13(a) and (b), respectively. When  $2\theta$  reaches  $168^\circ$ , however, the crushing process of A1\_4, Fig. 4.14, shows that

the lobes in the upper module of the tube develop normally at the beginning, and then a sort of local folding occurs in the middle part of the tube. This local folding affects the subsequent development of the lobes, resulting in obviously different final configurations of the two modules. Further increase in  $2\theta$  leads to a failure mode close to that of A1\_4, see A1\_5 in Fig. 4.13(c). A similar transition in failure mode is also observed from A2\_1 - A2\_5 shown in Fig. 4.13(d) - (h), respectively, all of which have  $M = 3$  but with increasing  $2\theta$ . Although the pattern is still followed in each tube, the lobes in the middle module of A2\_5 with  $2\theta = 172^\circ$  show evident sign of under development.

As  $M$  reaches 4, like in the case of  $M = 2$ , the failure mode still transits from the complete diamond mode seen in A3\_1 with  $2\theta = 156^\circ$ , Fig. 4.13(i), to the mode featuring under developed lobes seen in A3\_4 with  $2\theta = 168^\circ$ , Fig. 4.13(j). But unlike in the case of  $M = 2$ , it is observed from A3\_5 with  $2\theta = 172^\circ$ , Fig. 4.13(k), that the pattern is no longer followed and the two modules at the bottom of the tube merge. As a result, only three folds are formed in A3\_5 axially instead of four as the design intended. Similar phenomena can also be observed in A4\_4, Fig. 4.13(m), and A5\_2, Fig. 4.13(o).

At  $M = 7$ , i.e., A6\_1 in Fig. 4.13(p), the pattern is not followed when  $2\theta = 156^\circ$ . No further reduction in  $2\theta$  was attempted as the results have been sufficiently clear to draw conclusions upon.

Two conclusions can be drawn from the results presented above.

- For tubes with identical  $M$ , the complete diamond mode is usually triggered when  $2\theta$  is relatively small, and then ceases to appear as  $2\theta$  surpasses a critical value where failure modes featuring either under development of the lobes or the pattern not being followed occur, see A1\_4, A1\_5, A2\_5, A3\_4, and A3\_5. Those failure modes are called the *incomplete diamond mode* here, as opposed to the complete diamond mode shown in A1\_1, A2\_1 and A3\_1. Note that there is no

rigorous method to determine whether the lobes develop “well” or not, and thus this is done based mainly on visual inspection.

- Within  $156^\circ \leq 2\theta \leq 172^\circ$ , the pattern is always followed when  $M \leq 3$ . When  $M$  goes past 3, the phenomenon that the pattern is not followed is observed, occurring at a smaller  $2\theta$  as  $M$  increases. Recall that three lobes are formed in the conventional square tube A0 axially. Therefore it is suggested that if  $M$  of a square origami tube is chosen to be identical to the number of lobes formed in the corresponding conventional square tube, the complete diamond mode would be quite stable. Note that the latter can be estimated by dividing the height of a square tube by its folding wavelength which was derived theoretically by Wierzbicki and Abramowicz (1983). On the contrary, a larger  $M$  would make it difficult for the pattern to be followed. The underlying mechanism to explain this observation warrants further investigation.

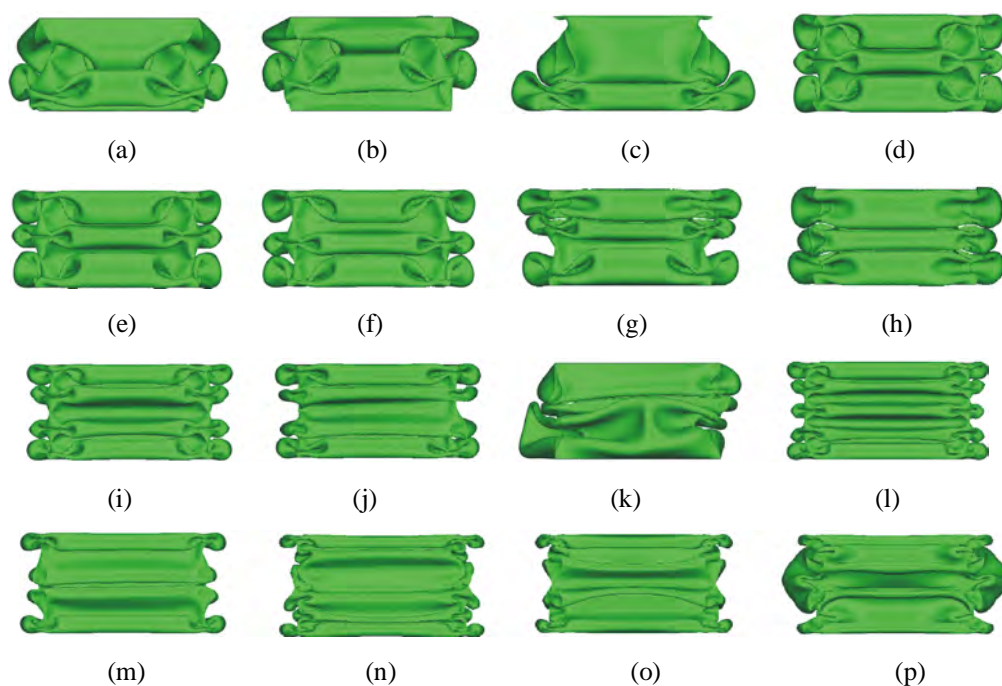


Fig. 4.13 Crushed configurations of (a) A1\_2, (b) A1\_3, (c) A1\_5, (d) A2\_1, (e) A2\_2, (f) A2\_3, (g) A2\_4, (h) A2\_5, (i) A3\_1, (j) A3\_4, (k) A3\_5, (l) A4\_1, (m) A4\_4, (n) A5\_1, (o) A5\_2, and (p) A6\_1.

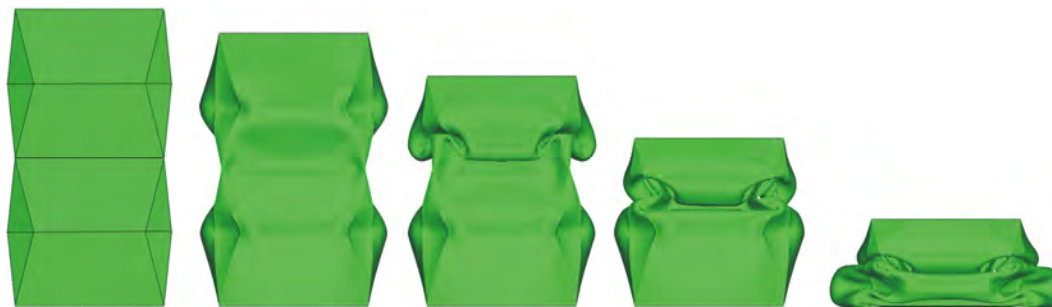


Fig. 4.14 Crushing process of A1\_4.

Now let us focus on the energy absorption properties of the tubes. The numerical data of the tubes are summarized in Table 4.2.  $P_m$  of each tube is plotted against  $2\theta$  in Fig. 4.15 and the data points associated with identical  $M$  are joined by a line. Four observations can be made from those results.

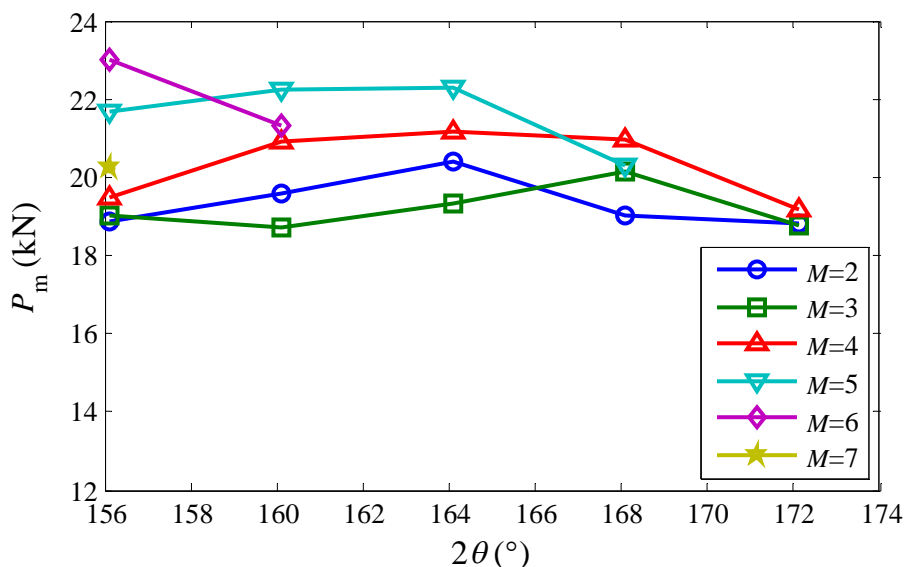


Fig. 4.15 Mean crushing force vs dihedral angle curves of A1\_1- A6\_1.

First of all, for tubes with identical  $M$ ,  $P_m$  increases with  $2\theta$  provided that the complete diamond mode is successfully triggered, but the increment is minor. For instance, at  $M = 2$ ,  $P_m$  first slightly rises from  $2\theta = 156^\circ$  to  $2\theta = 164^\circ$  within which the complete diamond mode is always obtained. Similar trends can also be observed at  $M = 3, 4,$  and  $5$ . The only exception is A2\_2 which fails in the complete diamond mode but has a lower  $P_m$  than that of A2\_1. The explanation is as follows. On one hand,  $2\theta$  determines the corner areas swept by travelling plastic hinge lines and the rotation

angles of stationary plastic hinge lines. The larger  $2\theta$ , the larger the corner areas and the rotation angles, leading to slight increase in  $P_m$ . This point can be clearly seen from the force vs displacement curves of A1\_1, A1\_2, and A1\_3 plotted in Fig. 4.16. On the other hand, the energy absorption of a tube is primarily determined by the failure mode it takes. Therefore as long as the failure mode is identical, the energy absorption is close.

Secondly,  $P_{max}$ , in contrast to  $P_m$ , shows no obvious correlation to  $2\theta$  or  $M$ . This phenomenon is also understandable because after the elimination of the very high initial buckling force, the location and magnitude of  $P_{max}$  show certain degree of randomness. Again, the variation of  $P_{max}$  is not substantial.

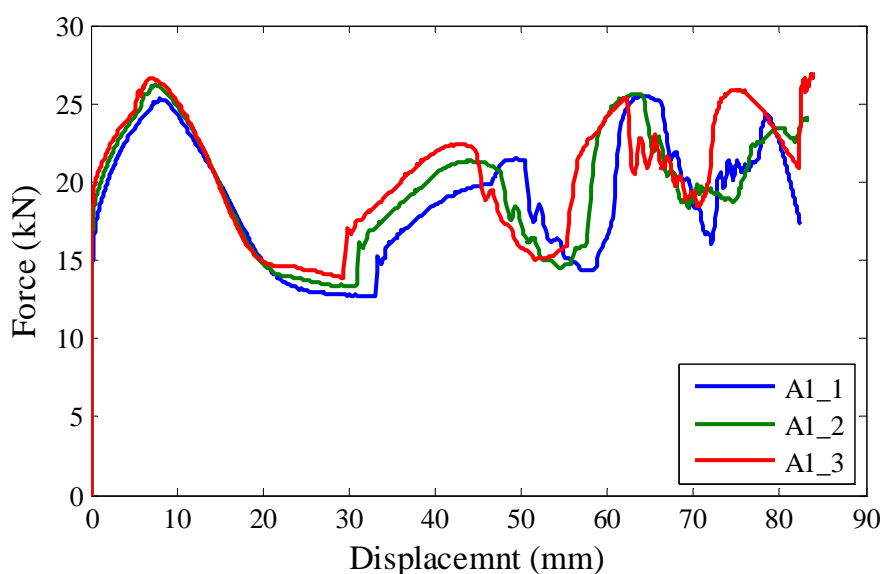


Fig. 4.16 Force vs displacement curves of A1\_1, A1\_2, and A1\_3.

Thirdly, the switch from the complete diamond mode to the incomplete diamond mode, such as from A1\_3 to A1\_4, from A2\_4 to A2\_5, and from A3\_3 to A3\_4, is usually accompanied by a drop in  $P_m$ . This observation again confirms that the new failure mode mainly accounts for the energy absorption increase. If the failure mode of a tube deviates from the complete diamond mode, the energy absorption also reduces.

Finally, for tubes with identical  $2\theta$ ,  $P_m$  increases with  $M$  when  $M > 2$  provided that the complete diamond mode is obtained. However, the increment is not large, and  $P_m$  of most tubes fall into the range of  $20 \pm 2$  kN, indicating that increasing  $M$  would not substantially improve the energy absorption of the origami tube. The force vs displacement curves of A2\_1, A3\_1, and A4\_1, which have identical  $2\theta$  but increasing  $M$ , are plotted in Fig. 4.17 as an example. It can be seen that although the curve shapes in terms of the number of crests and troughs are different from each other, the areas below remain close. A qualitative explanation to this observation involves different energy dissipation mechanisms in the collapse process. Two of the main sources of energy dissipation are the rotation of stationary plastic hinge lines and the sweeping of travelling plastic hinge lines. Although the total length of stationary plastic hinge lines increase with  $M$ , the corner areas swept by travelling plastic hinge lines shrink since the height of each module is reduced, as clearly observed by comparing A2\_1, A3\_1, and A4\_1 shown in Fig. 4.13(d), (i), and (l), respectively. The energy absorption enhancement contributed by extra stationary plastic hinge lines is comparable to the energy absorption reduction due to the shrunk corner areas swept by travelling plastic hinge lines, resulting in only minor net energy absorption difference.

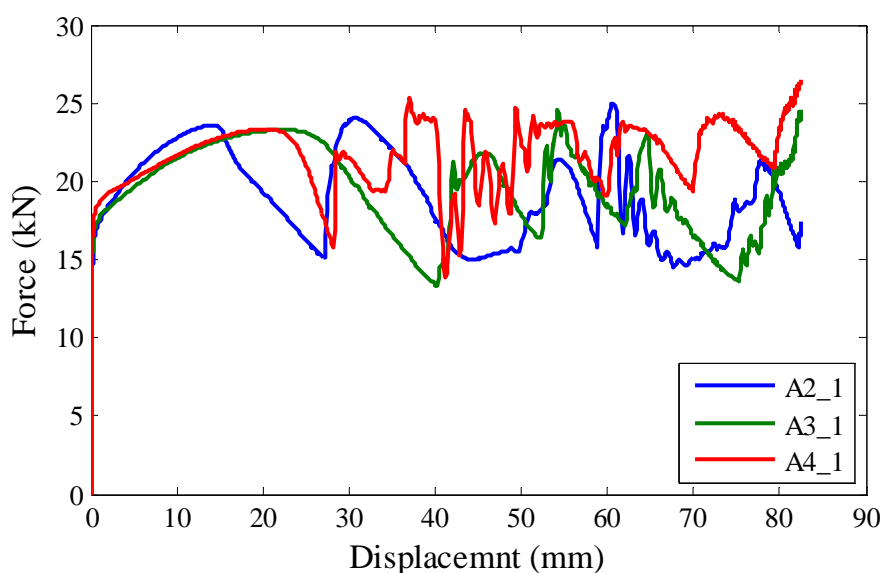


Fig. 4.17 Force vs displacement curves of A2\_1, A3\_1, and A4\_1.

In summary, it is found that for a square origami tube



- The critical value of  $2\theta$  that is just able to trigger the complete diamond mode depends on  $M$ , and this value decreases with  $M$  when  $M$  is no less than the number of lobes formed in the corresponding conventional square tube axially. In other words, a larger amount of pre-folding is needed to induce the complete diamond mode as more modules are put on a tube.
- When the complete diamond mode is triggered, increasing  $2\theta$  leads to increase in  $P_m$  provided that  $M$  remains the same, and increasing  $M$  results in increase in  $P_m$  provided that  $2\theta$  is unchanged. Therefore generally less pre-folding and more modules help to improve the energy absorption of a square origami tube.
- In the optimum case, as much as a 92.1% increase in  $P_m$  is achieved.

#### 4.4.3.2 Ratio $b / t$

As mentioned in Chapter 2, ratio  $b / t$  is an important factor that influences the failure mode of a thin-walled square tube. Different failure modes can be triggered when  $b / t$  varies, resulting in different energy absorption capabilities.

Seven tubes, A7\_1 – A7\_7, are analyzed. All of the tubes have identical geometry with that of A1\_1 except that  $t$  varies from 0.6 mm to 2.0 mm, which covers the range of  $b / t$  practically used in energy absorption devices. Numerical results show that within  $30 \leq b / t \leq 100$ , the crushing process of the tube is not noticeably affected by  $b / t$  and the complete diamond mode is consistently obtained. Thus it seems that the failure mode of a properly designed origami tube is independent of  $b / t$  within the practical range, which is desirable for an energy absorption device.

#### 4.4.4 Effects of tube profile

##### 4.4.4.1 Rectangular cross section

Rectangular tubes are frequently used in practice. Theoretically, the complete diamond mode triggered by the pattern does not depend on cross-sectional aspect ratio  $a / b$ .

However, since inclined plastic hinge lines travel away from tube corners during the collapse of a tube, a proper distance between adjacent corners is required in order to leave enough space for them to travel and deform material in the corner areas.

Four rectangular origami tubes, B1 – B4, are analyzed. B1 and B2 have identical  $c/l$ ,  $M$ , and surface area with those in A1\_1, and B3 and B4 have identical  $c/l$ ,  $M$ , and surface area with those in A2\_1. Numerical results show that the initial buckling of the tubes is not noticeably changed by  $a/b$ . However, merging of adjacent lobes is observed in the subsequent folding of B1 and B2. For instance, it can be seen from the crushing process of B2, Fig. 4.18, that after the tube buckles, the travelling plastic hinge lines from adjacent corners quickly cross each other, and then the merged lobes are gradually folded until the tube is completely crushed. This mode can also be categorized as the incomplete diamond mode. In contrast, B3 and B4 show no sign of lobe merging and collapse very similarly to A2\_1, i.e., in the complete diamond mode.

The numerical data are listed in Table 4.3. It can be seen that  $P_m$  of B1 and B2 are lower than that of A1\_1. The larger  $l/b$ , the lower  $P_m$ . This phenomenon can be attributed to the fact that as  $l/b$  reaches a certain value, the distance between adjacent corners becomes not large enough for the lobes from the two corners to develop independently. As a result, they join and interfere the folding of each other before the tube is completely crushed, leading to reduced energy absorption.  $P_m$  of B3 and B4, on the other hand, are found to be almost identical to that of A2\_1, confirming that  $a/b$  itself has little effect on the energy absorption.



Fig. 4.18 Crushing process of B2.

In summary, it is found that both the failure mode and energy absorption properties of a rectangular origami tube are independent of  $a/b$  provided that  $l/b$  is below a critical value to ensure that the distance between adjacent corners is large enough to prevent lobe merging. No attempts have been made to find the exact critical value, but it seems that  $a/b$  has negligible effect when  $l/b \leq 1$ .

#### 4.4.4.2 Polygonal cross section

A polygonal cross section can be seen as a trade-off between a square one and a circular one. The energy absorption of conventional polygonal tubes increases with  $N$  until when  $N$  is so large that a polygonal tube virtually becomes a circular one.

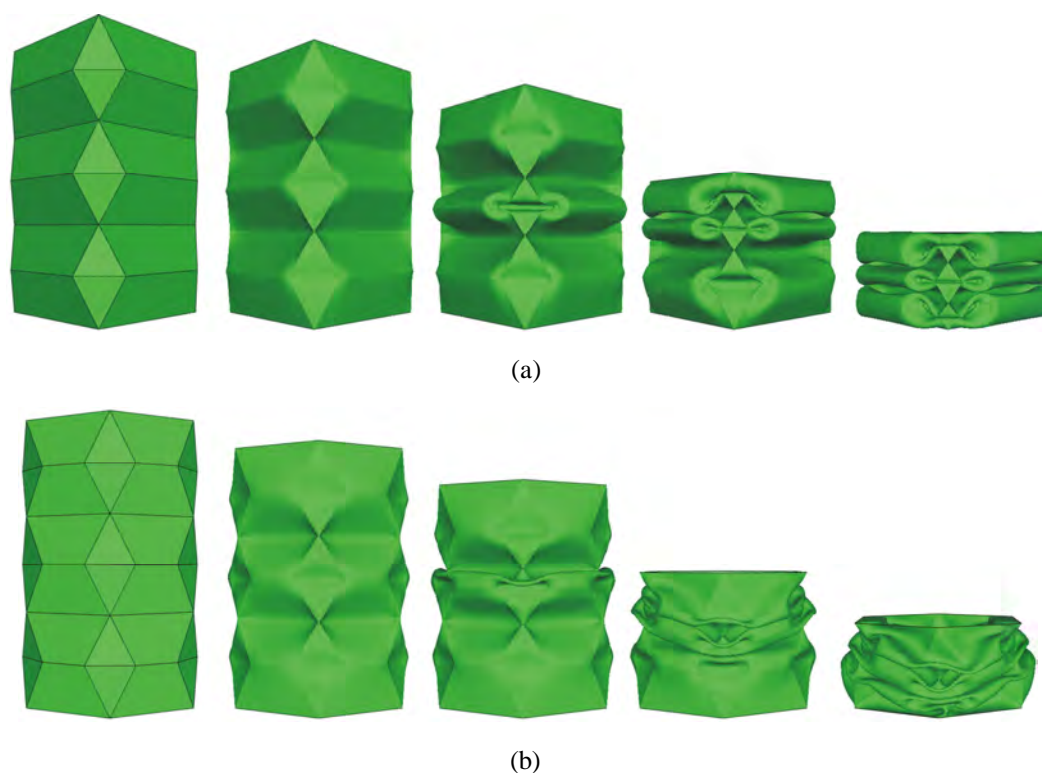


Fig. 4.19 Crushing processes of (a) C1, and (b) C3.

Three origami tubes, C1, C2, and C3, which possess identical  $c/l$ ,  $M$ , and surface area with those in A2\_1 but have 3, 5, and 6 sides, respectively, are analyzed. The crushing process of the triangular origami tube C1 is shown in Fig. 4.19(a). It can be seen that the lobe development and the overall failure mode are similar to those in A2\_1, with

the only exception that 3 lobes rather than 4 are formed in the circumferential direction of C1. The pentagonal origami tube C2 also shows a similar complete diamond mode. When  $N$  reaches 6, the axial crushing process of the hexagonal origami tube C3, Fig. 4.19(b), shows that the origami pattern is no longer well followed and the failure mode becomes somewhat irregular. This result indicates that a larger magnitude of pre-folding is needed for the pattern to be followed well, which can be realized by selecting a larger  $c/l$ .

The force vs displacement curves of C1, C2, and C3 are plotted together with that of A2\_1 in Fig. 4.20, and the numerical data are given in Table 4.3. As expected, both  $P_{\max}$  and  $P_m$  increase with  $N$ . The irregularity of the failure mode of C3 is also reflected in the numerical data: the increase in  $P_m$  from C2 to C3 is quite small. This result again suggests the strong correlation between failure mode and energy absorption.

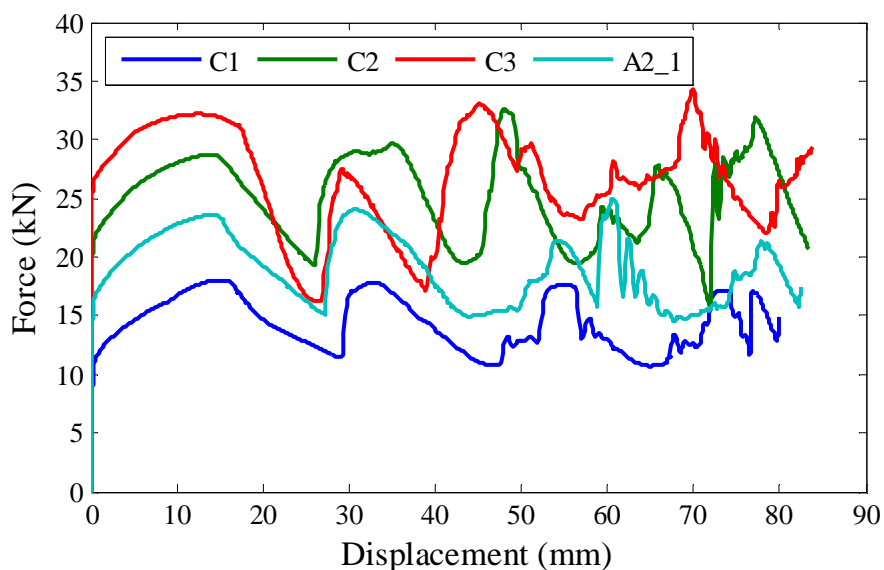


Fig. 4.20 Force vs displacement curves of C1, C2, C3, and A2\_1.

#### 4.4.4.3 Tapered shape

Tapered tubes have wide practical applications in the design of thin-walled energy absorption devices due to two main reasons: first of all, tapered tubes produce more

stable and consistent failure modes than straight ones when subjected to eccentric or oblique loads; and secondly, in such applications as automobile frontal bumpers, a device is often required to connect two members with different cross sectional dimensions, in which situation tapered tubes are an obvious choice.

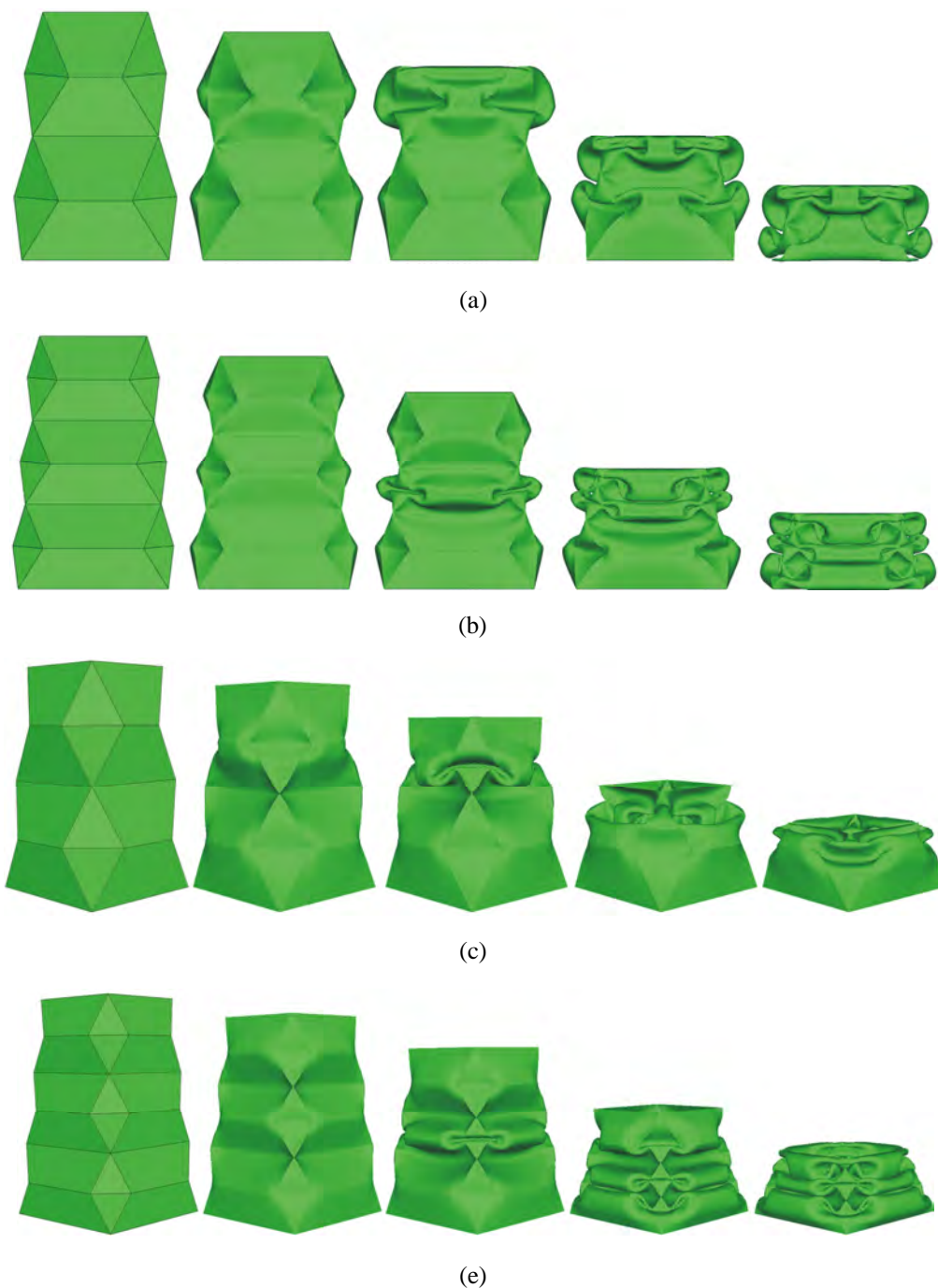


Fig. 4.21 Crushing processes of (a) D1, (b) D3, (c) D5, and (d) D7.

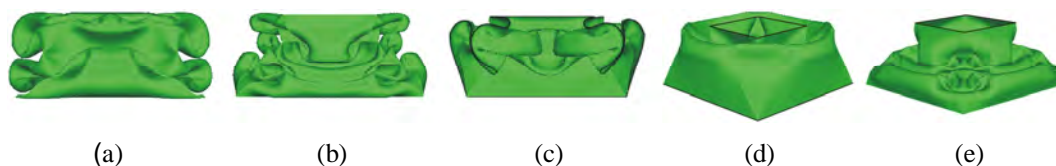


Fig. 4.22 Crushed configurations of (a) D2, (b) D4, (c) D5, (d) D6, and (e) D8.

Four type I tapered tubes, D1 - D4, and four type II tapered tubes, D5 - D8, are analyzed here. D1, D2, D5, and D6 have identical  $c/l$  and  $M$  with those in A1\_1, and D3, D4, D7, and D8 have identical  $c/l$  and  $M$  with those in A2\_1.

For type I tapered tubes, the axial crushing process of D1 is first presented in Fig 4.21(a). It can be observed that the pattern is well followed during the crushing process, indicating that the failure mode is not significantly changed by the tapered shape. However, the upper module of the tube shows some sign of lobe merging due to the relative large value of  $l/a_1$  which is equivalent to  $l/b$  in straight tubes. A similar phenomenon is also observed from D2 in Fig. 4.22(a). When  $l$  is reduced from 60 mm to 40 mm, it can be seen from the crushing process of D3, Fig. 4.21(b), that no lobe merging occurs any more, leading to the complete diamond mode. D4, Fig. 4.22(b), also shows the same failure mode. These results once more indicate that an appropriate distance between adjacent corners is needed for the complete diamond mode to be formed.

The force vs displacement curves of D1, D2, D3, and D4 are plotted in Fig. 4.23, and the numerical data are compiled in Table 4.3. Three observations can be made from the results. First of all, the forces of D1 and D2 which have different values of  $a_1/a_2$  match quite well and so do those of D3 and D4, indicating that the energy absorption of type I tapered tubes is no very sensitive to the degree of tapering within the range studied here. Secondly,  $P_m$  of D3 and D4 are larger than those of D1 and D2, further confirming that lobe merging results in reduced energy absorption. And finally,  $P_{max}$  of D3 and D4 without lobe merging are very close to that of A2\_1, and the differences in their  $P_m$  are also negligible. Therefore it can be concluded that type I tapered shape

does not significantly affect the energy absorption of the origami tube provided that a proper pattern geometry is selected.

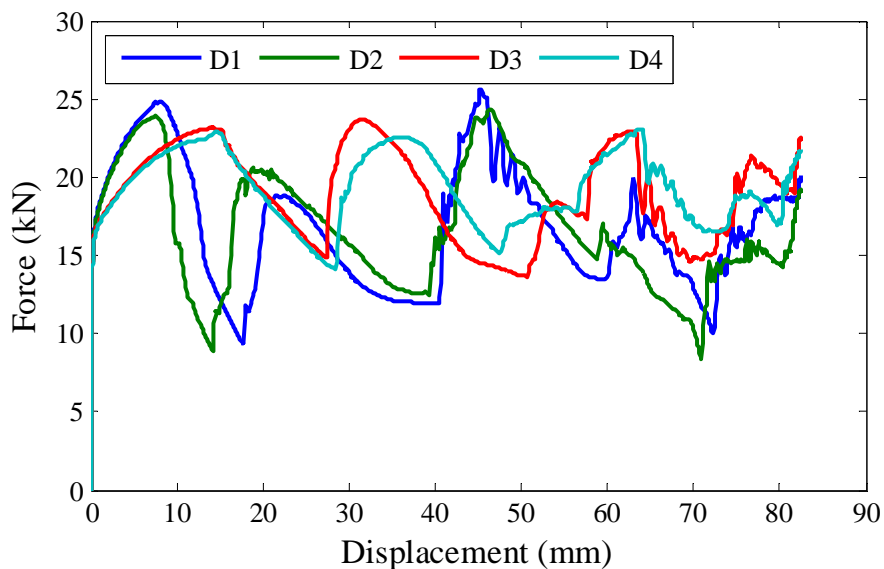


Fig. 4.23 Force vs displacement curves of D1 - D4.

For type II tapered tubes, the axial crushing process of D5 is first shown in Fig. 4.21(c). It can be seen that the lobes in the upper module develop at the early stage of crushing. Subsequently tube inversion is generated and the folded upper module goes inside the lower one, which hinders the development of the lobes in the lower one. The tube inversion deformation can be seen more clearly from the sectional view of the crushed configuration of D5 shown in Fig. 4.22(c). As a result, a hybrid failure mode combining the complete diamond mode and tube inversion is finally attained. When  $M$  increases from 2 to 3, the crushing process of D7, Fig. 4.21(d), shows that tube inversion is eliminated and the complete diamond mode is eventually achieved. A similar failure mode switch is also observed by comparing D6 and D8 presented in Fig. 4.22(d) and (e), respectively.

The force vs displacement curves of D5, D6, D7, and D8 are plotted in Fig. 4.24. It can be seen that D5 and D6 have relatively smooth curves compared with those of D7 and D8, which is due to the tube inversion deformation in D5 and D6. The numerical results of the four tubes are presented in Table 4.3. Comparison of  $P_m$  of D5 and D7

indicates that the energy absorption capabilities of the hybrid failure mode and the complete diamond mode are very close. This conclusion is further supported by comparing  $P_m$  of D6 and D8.  $P_m$  of D5 and D7 are higher than those of D6 and D8, suggesting that the energy absorption of type II tapered tubes, unlike type I tubes, increases with  $a_1 / a_2$  within the range studied here. In other words, the less tapered a tube is, the more energy it can absorb.

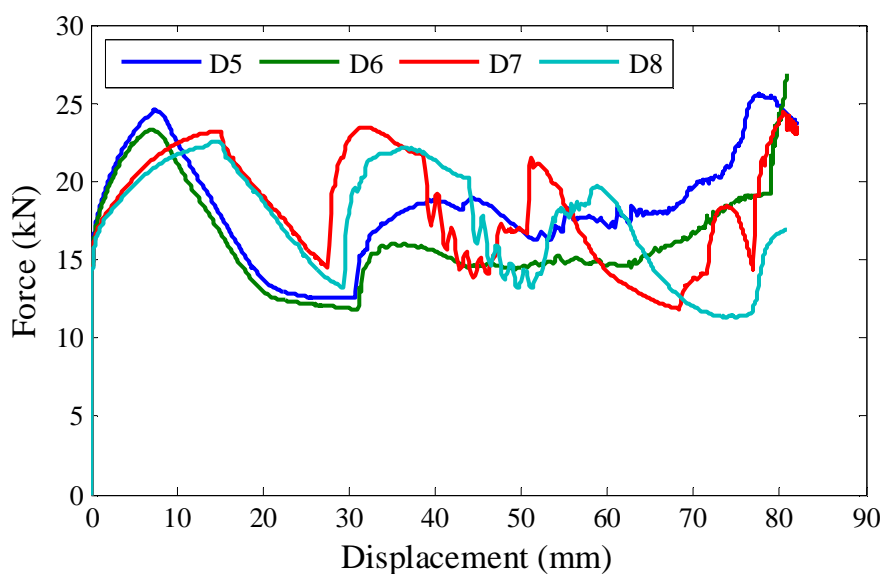


Fig. 4.24 Force vs displacement curves of D5 - D8.

## 4.5 Other Factors Influencing the Performance of the Origami Tube

### 4.5.1 Boundary condition

Pinned-pinned boundary conditions have been considered in Section 4.4. However, real world thin-walled energy absorption devices could be subjected to various boundary conditions depending on the way they are installed. Figure 4.25 shows two automobile crashcans. For the Range Rover crashcan in Fig. 4.25(a), two opposite sides of the lower end are connected to the mounting plate through spot-welding, and two opposite sides of the upper end are bolted to a bumper beam (not included in the



figure). This can be treated as pinned-pinned boundary conditions. For the BMW crashcan in Fig. 4.25(b), the lower end is welded to the mounting plate and the upper end to the bumper beam. This can be treated as fixed-fixed boundary conditions. In addition, crashcans are usually attached to the longitudinal members of a vehicle which could also deform upon impact.

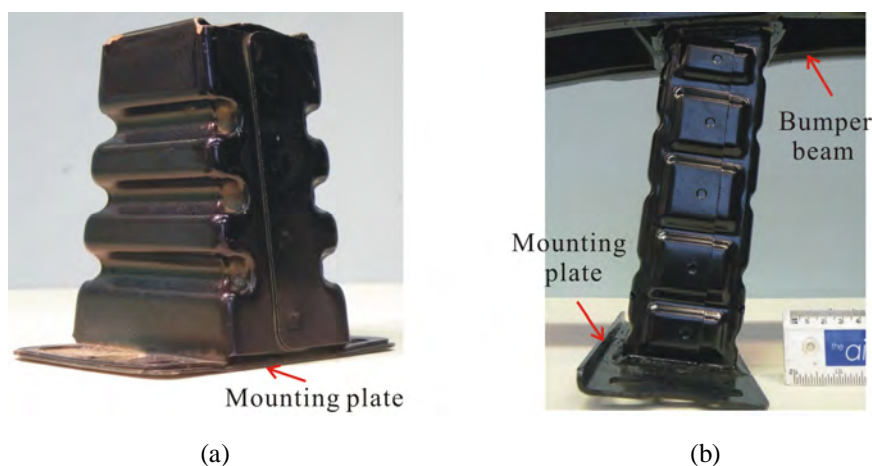


Fig. 4.25 (a) Range Rover crashcan, and (b) BMW crashcan.

To investigate the effect of boundary condition on the performance of the origami tube, A1\_1 was reanalyzed under three types of boundary conditions: free-free, fixed-fixed, and pinned on the end of impact and rigidly attached to a supporting square tube on the other end. The geometry of the supporting tube was chosen as  $b = 60$  mm,  $H = 120$  mm, and  $t = 2.0$  mm. Note that the supporting tube was designed to be stiffer than A1\_1 to ensure that A1\_1 would fail first.

The crushed configurations of A1\_1 subjected to the three types of boundary conditions are presented in Fig. 4.26. It can be seen that the complete diamond mode is invariably triggered irrespective of boundary condition. The force vs displacement curves generated under the three types of boundary conditions are plotted in Fig. 4.27 together with that under the pinned-pinned boundary conditions obtained in Section 4.4. All of the curves are found to have similar shape and comparable force level. Therefore the complete diamond mode is not sensitive to boundary condition. In other words, the origami tube can perform well under practical boundary conditions.

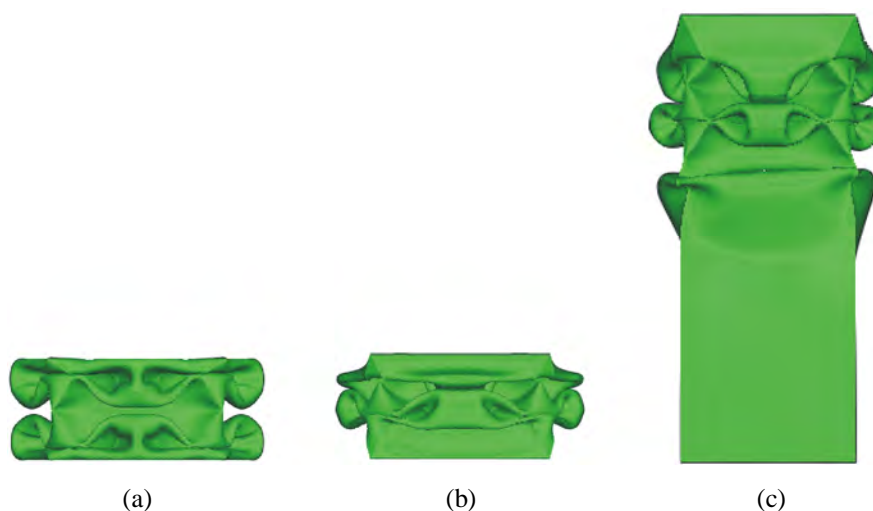


Fig. 4.26 Crushed configurations of A1\_1 subjected to different boundary conditions. (a) Free, (b) fixed, and (c) with supporter.

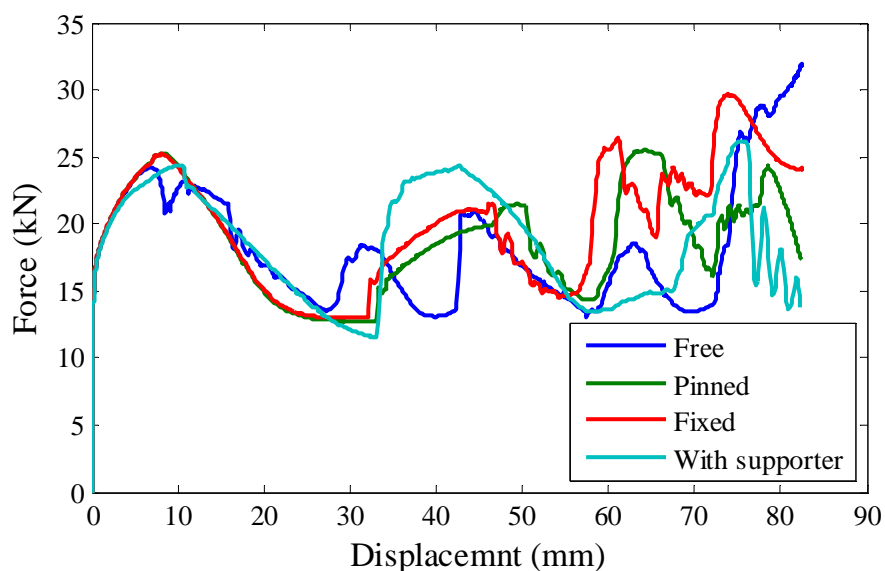


Fig. 4.27 Force vs displacement curves of A1\_1 subjected to different boundary conditions.

#### 4.5.2 Material mechanical properties

The concept of the origami tube presented in this chapter is purely structural, so we expect that the complete diamond mode can be triggered in a tube made of any ductile material. To further confirm the independence of the behaviour of the origami tube from material mechanical properties, another two commonly used materials for thin-walled energy absorption devices, i.e., high strength steel and aluminium alloy, were

respectively assigned to A0 and A1\_1 and the axial crushing analysis was re-conducted. The mechanical properties of the two materials are listed in Table 4.4, and the engineering stress vs strain curves are plotted in Fig. 4.28.

Table 4.4 Mechanical properties of high strength steel and aluminium alloy

Material	$\rho$ (Kg/m <sup>3</sup> )	$E$ (GPa)	$\nu$	$\sigma_y$ (MPa)	$\sigma_u$ (MPa)	$\epsilon_u$
High strength steel	7800	210	0.3	406	819.6	17.6%
Aluminium alloy	2700	68.2	0.3	80	173	17.3%

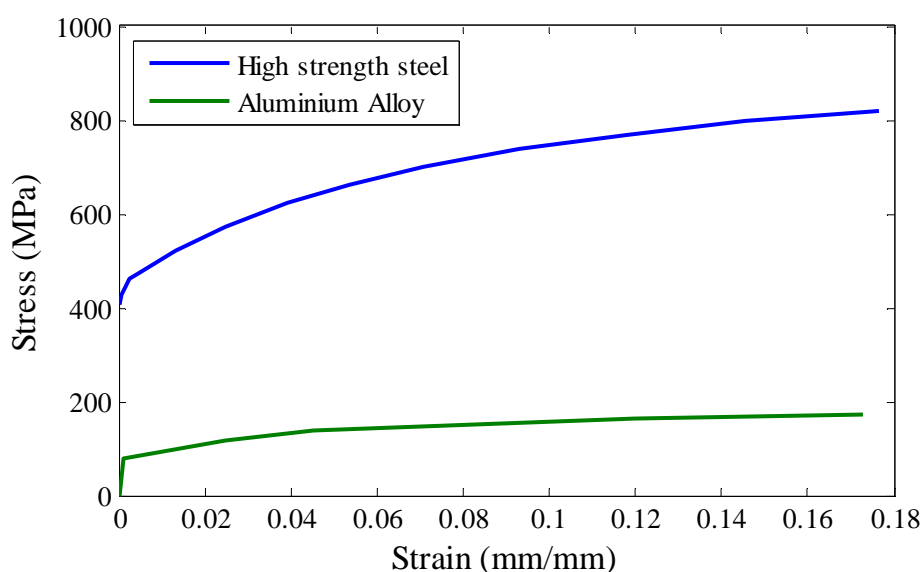


Fig. 4.28 Engineering stress vs strain curves of high strength steel and aluminium alloy.

The crushed configurations of A1\_1 made of high strength steel and aluminium alloy, respectively, are presented in Fig. 4.29. It can be seen that the complete diamond mode is successfully triggered in both cases. These results indicate that the complete diamond mode is also not sensitive to material mechanical properties, further demonstrating the ability of the origami pattern to trigger the complete diamond mode in a stable manner.



Fig. 4.29 Crushed configurations of A1\_1 made of (a) high strength steel, and (b) aluminium alloy.

The force vs displacement curves of A0 and A1\_1 made of high strength steel are plotted in Fig. 4.30, and those of A0 and A1\_1 made of aluminium alloy are plotted in Fig. 4.31. The numerical data are summarized in Table 4.5. As expected, substantial  $P_{\max}$  reduction and  $P_m$  increase are achieved in both cases, indicating that the origami pattern is applicable to tubes with other ductile materials.

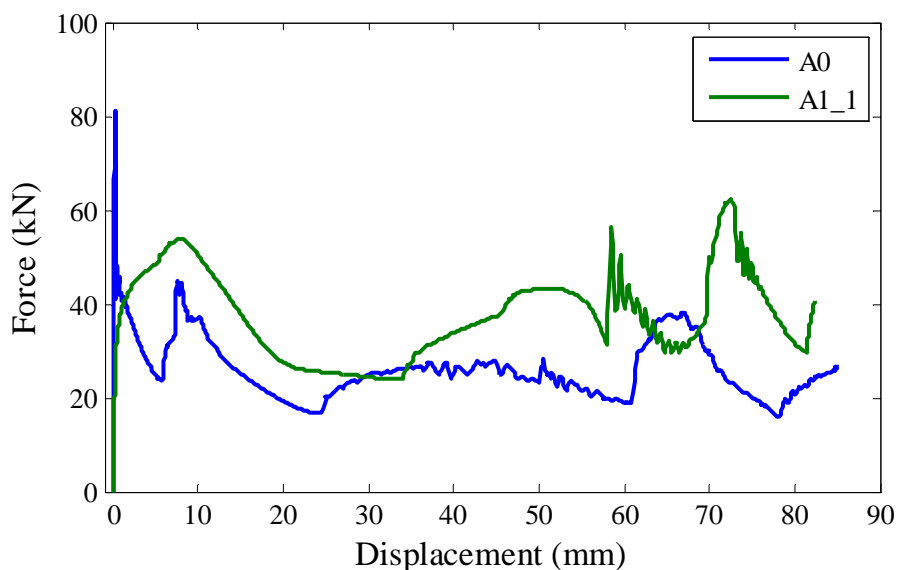


Fig. 4.30 Force vs displacement curves of A0 and A1\_1 made of high strength steel.

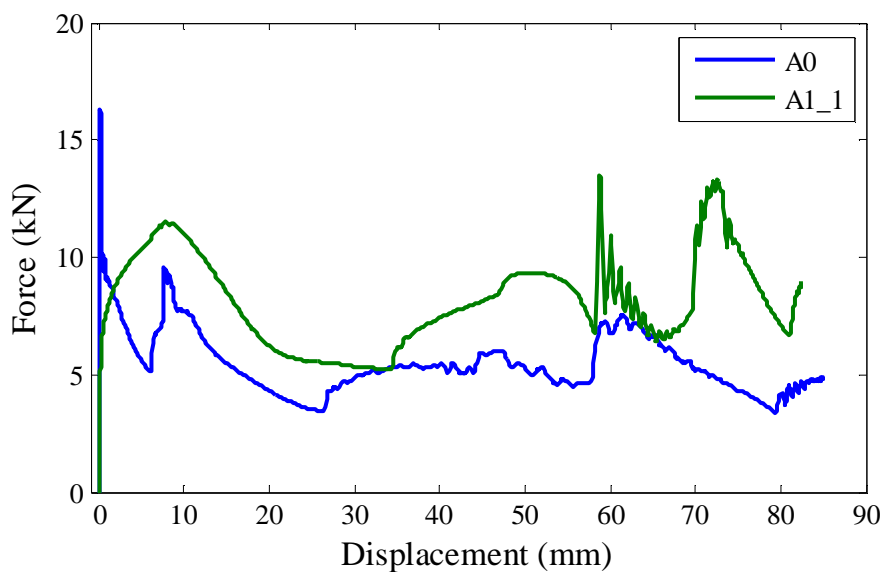


Fig. 4.31 Force vs displacement curves of A0 and A1\_1 made of aluminium alloy.

Table 4.5 Numerical results of A0 and A1\_1 made of high strength steel and aluminium alloy

Material	Model	$P_{\max}$ (kN)	$P_{\max}$ reduction	$P_m$ (kN)	$P_m$ increase
High strength steel	A0	80.90	-	25.94	-
	A1_1	62.24	23.1%	37.38	44.1%
Aluminium alloy	A0	16.33	-	5.45	-
	A1_1	13.46	17.6%	8.14	49.4%

### 4.5.3 Reinforcement

Multi-cell cross sections have also been applied in the design of thin-walled energy absorption devices, among which double-cell cross sections, i.e., box sections reinforced by centre webs, are occasionally adopted in practice when single cell cross sections are not able to meet certain design objectives. To study the effect of reinforcement on the failure mode and energy absorption of the origami tube, tubes A0\_R and A3\_1\_R, obtained by reinforcing A0 and A3\_1 with centre webs, respectively, were built and axially crushed. The centre web of A0\_R was a straight plate, whereas that of A3\_1\_R was a corrugated plate like the sides of A3\_1. The thickness of both centre webs was chosen as 1.0 mm.

The crushed configurations of the two tubes are shown in Fig. 4.32. Due to the introduction of the centre web, the folding wavelength of A0\_R is significantly reduced compared with that of A0. As a result, four lobes are formed axially. For A3\_1\_R, on the other hand, the pattern is still well followed as in the case of A3\_1 without being noticeably affected by the centre web, and the complete diamond mode is obtained.

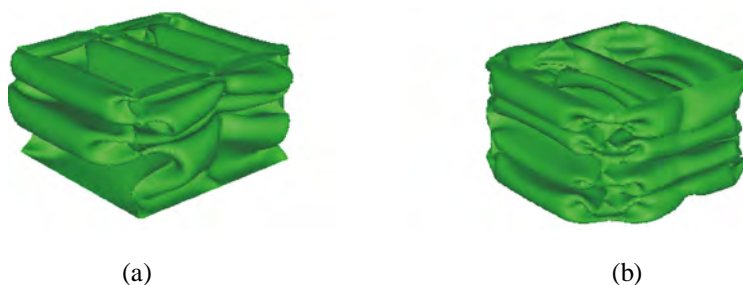


Fig. 4.32 Crushed configurations of (a) A0\_R, and (b) A3\_1\_R.

The force vs displacement curves of the two tubes are plotted in Fig. 4.33 and the numerical results are summarized in Table 4.6. A substantial reduction in  $P_{\max}$  is still obtained for A3\_1\_R compared with that of A0\_R.  $P_m$  increase of A3\_1\_R, on the other hand, is not as pronounced as in the case of no centre web, with 26.0% being achieved. The reason for the relatively low energy absorption improvement can be explained as follows. The centre web of A0\_R helps to increase the energy absorption in two ways. First, it absorbs energy through its own plastic deformation. Second, it reduces the folding wavelength so that the tube can absorb more energy through axial folding. The centre web of A3\_1\_R, however, does not noticeably change the failure mode, and thus contributes to the total energy absorption mainly through plastic deformation in itself. As a result, the centre web of A0\_R is more effective at improving the energy absorption of the whole structure, leading to reduced energy absorption difference between the two tubes. Despite that, the advantage of the origami tube is still evident, indicating that it is also worthwhile to apply the origami pattern on tubes with centre webs.

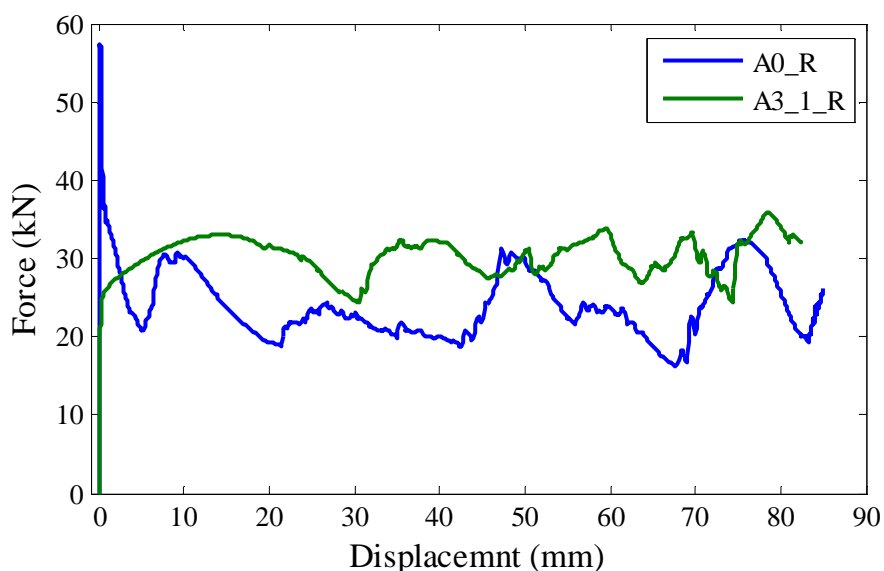


Fig. 4.33 Force vs displacement curves of A0\_R and A3\_1\_R.

Table 4.6 Numerical results of A0\_R and A3\_1\_R

Model	$P_{\max}$ (kN)	$P_{\max}$ reduction	$P_m$ (kN)	$P_m$ increase
A0_R	57.23	-	24.07	-
A3_1_R	35.88	37.3%	30.32	26.0%

#### 4.5.4 Bending capacity and torsion capacity

In addition to high energy absorption under axial compression, a good energy absorption device also needs to possess reasonable bending capacity and torsion capacity because of two reasons. First of all, some devices not only dissipate kinetic energy in the event of a collision but also function as structural components in normal working conditions, so they are required to be reasonably stiff to ensure sound all-around performance of the whole structure. Secondly, the real loading applied to a device in an impact event is rarely a perfect axial compression. In most cases it is a combination of compression, bending, and sometime torsion. Therefore if a device is not rigid enough to resist bending and torsion, the axial failure mode could be severely distorted, leading to weakened energy absorption capability.

When subjected to large deformation, the origami tube is expected to have lower bending capacity and torsion capacity than those of “perfect” conventional tubes without any form of pre-manufactured imperfection because of the origami pattern on the surface of the origami tube which replaces straight corners with lobes. However, “perfect” conventional tubes are rarely used as energy absorption devices due to the excessively high initial buckling force, so it is more meaningful to compare the origami tube with “imperfect” conventional tubes which are intentionally weakened to reduce the initial buckling force. To evaluate the bending capacity and torsion capacity of the origami tube, six square origami tubes, A1\_1, A1\_3, A2\_1, A2\_3, A3\_1, and A3\_3, one “perfect” and one “imperfect” conventional square tubes were bent and twisted, respectively. Both conventional tubes had identical geometry with that of A0, and dents were introduced on the surface of the “imperfect” one. The configuration of the “imperfect” tube is shown in Fig. 4.34.

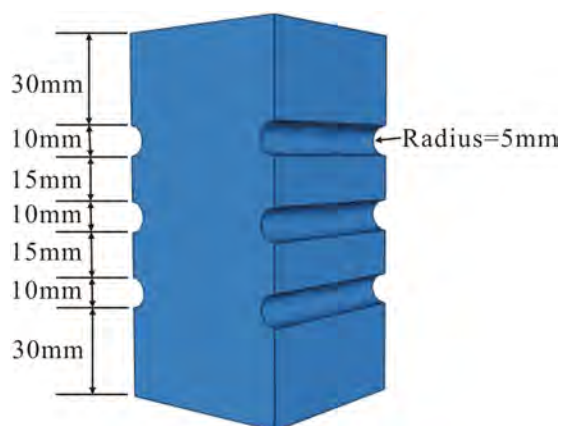


Fig. 4.34 The “imperfect” square tube.

Abaqus/Standard (SIMULIA Corp., USA) was employed to conduct the static numerical simulations. In the bending analysis, only a half of each tube shown in Fig. 4.35(a) was built due to symmetry. One end of the tube was tied to a stationary rigid panel by six degrees of freedom and the other to a moving one. The stationary rigid panel was completely fixed in space. Only the translational degree of freedom of the moving rigid panel in  $y$  direction was not constrained, to which a displacement of 2 mm in negative  $y$  direction was applied.

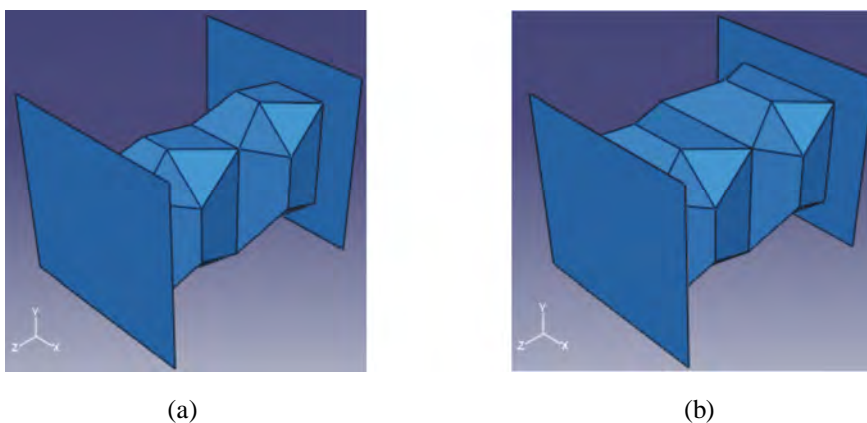


Fig. 4.35 Loading scenarios of (a) bending analysis, and (b) twisting analysis.

In the twisting analysis, the whole tube shown in Fig. 4.35(b) was modelled in each case. The two ends of the tube were tied to a stationary rigid panel and a moving one, respectively, by six degrees of freedom. The stationary rigid panel was completely fixed, whereas all of the degrees of freedom of the moving one were constrained



except for the rotational degree of freedom about  $z$  axis. A rotation of  $1^\circ$  about  $z$  axis was assigned to the free degree of freedom of the moving rigid panel.

The bending capacity of the tubes is first evaluated. The force vs displacement curves are plotted in Fig. 4.36. Unsurprisingly, the curve of the “perfect” tube is the highest among all of the tubes. The curves of the six origami tubes stay close to that of the “imperfect” tube, indicating that a properly designed origami tube can offer reasonable bending capacity.

If the origami tubes are sorted according to the force in ascending order, the sequence listed in Table 4.7 can be obtained. It is observed that the bending capacity of a square origami tube is affected by two parameters:

- $c/l$ : the bending capacity increases with reducing  $c/l$ .
- $l/b$ : the bending capacity increases with reducing  $l/b$ .

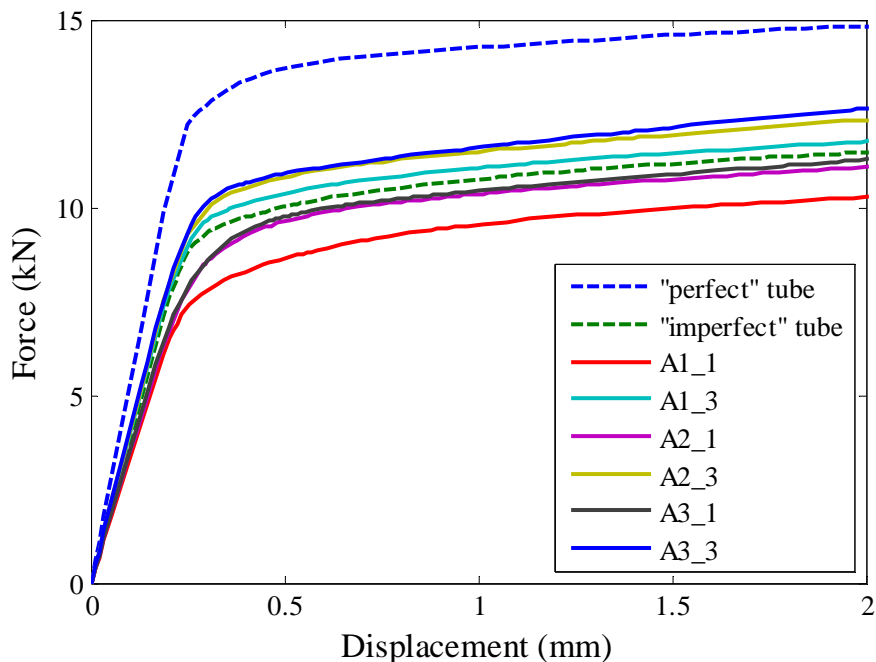


Fig. 4.36 Force vs displacement curves of the tubes under bending.

Table 4.7 Ranking of the bending capacity and torsion capacity of the origami tubes

Model	$c$ (mm)	$l$ (mm)	$c/l$	$l/b$	Bending	Twisting
A1_1	30	60	0.5	1	1st	1st
A1_3	20	60	0.33	1	4th	3rd
A2_1	20	40	0.5	0.67	2ed	2ed
A2_3	13.3	40	0.33	0.67	5th	5th
A3_1	15	30	0.5	0.5	3rd	4th
A3_3	10	30	0.33	0.5	6th	6th

Subsequently the torsion capacity of the tubes is assessed. The torque vs rotation curves are plotted in Fig. 4.37. It can be seen that the origami tubes have relatively low torsion capacity, with the curves of four of them staying below that of the “imperfect” tube. So special attention should be paid to the design if an origami tube is required to resist large torsion. Sorting the origami tubes according to the torque in ascending order, the sequence also shown in Table 4.7 can be obtained. Two parameters are found to influence the torsion capacity of a square origami tube:

- $c$ : the torsion capacity increases with reducing  $c$ .
- $l/b$ : the torsional capacity increases with increasing  $l/b$ .

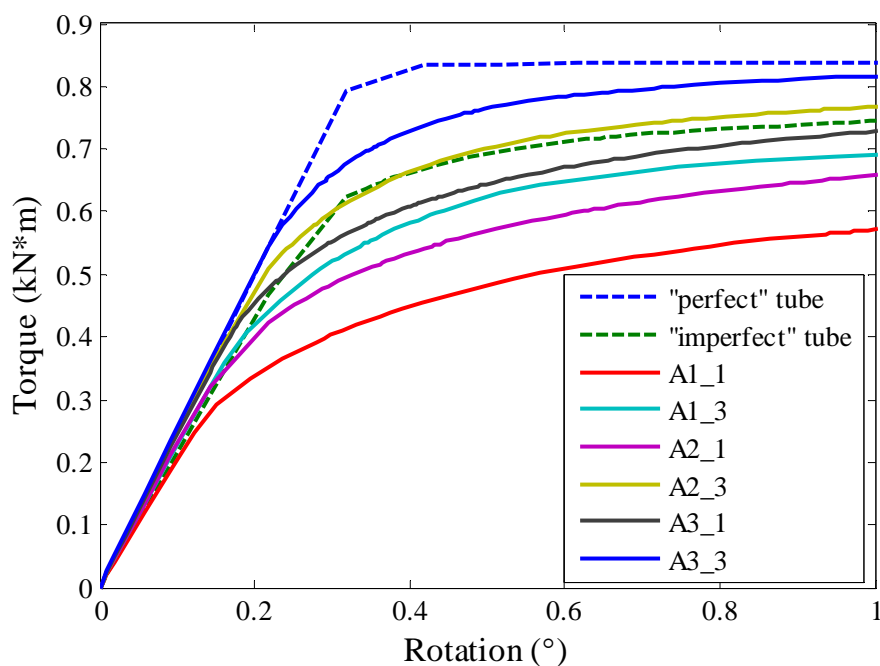


Fig. 4.37 Torque vs rotation curves of the tubes under twisting.

### 4.5.5 Dynamic axial crushing

The response of an energy absorption device subjected to dynamic loading is crucial for the device to perform in a realistic impact event. In order to investigate dynamic effects on the performance of the origami tube, a conventional tube,  $C_c$ , and an origami one,  $O_c$ , were built. Both tubes had the structural profile of a type I tapered shape and identical surface area. The configurations of the tubes are listed in Table 4.8.

Table 4.8 Configurations of the tubes

Model	$a_1$ (mm)	$a_2$ (mm)	$b$ (mm)	$c$ (mm)	$l$ (mm)	$M$	$t$ (mm)
$C_c$	60	90	60	-	-	-	2.0
$O_c$	60	90	60	22.5	45	4	2.0

It was mentioned in Chapter 2 that the dynamic response of a thin-walled tube was mainly affected by inertia and material strain rate sensitivity. To comprehensively evaluate the effects of each factor and a combination of the two, respectively, the tubes were crushed under four conditions. The material density, material strain rate sensitivity, loading rate, and target factors to be studied in each condition are listed in Table 4.9.

Table 4.9 Axial crushing conditions for the tubes

Condition	Density	Strain rate sensitivity	Loading rate	Target factors
I	original	No	quasi-static	-
II	original	No	20 m/s	inertia
III	1 / 1000 of original	Yes	20 m/s	strain rate sensitivity
IV	original	Yes	20 m/s	inertia and strain rate sensitivity

The material model and finite element simulation approach used in Section 4.3.2 were adopted for the axial crushing analysis here, with the following changes being made.

- Fixed-fixed boundary conditions were applied to each tube.

- Geometric imperfection in terms of a linear combination of the first eight buckling modes was introduced on  $C_c$  to ensure a stable and progressive crushing.
- Material strain rate sensitivity was considered through the Cowper-Symonds equation (2.19) in Chapter 2, with material constants  $C_r$  and  $q_r$  being chosen as  $6844 \text{ s}^{-1}$  and 3.91, respectively (Abramowicz and Jones, 1984a).

The crushed configurations of the tubes under four conditions are shown in Fig. 4.38.  $C_c$  fails in the typical symmetric mode under conditions I - III, but in a mode exhibiting both symmetric folding and circumferential extension under condition IV see Fig. 4.38(a). These results indicate that the combined effects of inertia and strain rate sensitivity associated with high speed impacts can lead to a change in failure mode for conventional tubes.  $O_c$ , on the other hand, demonstrates the complete diamond mode under all four conditions, see Fig. 4.38(b). This consistent and predictable response of the origami tube can be attributed to the effectiveness of the origami pattern at controlling the axial collapse route of the tube, which outweighs inertia and strain rate effects.

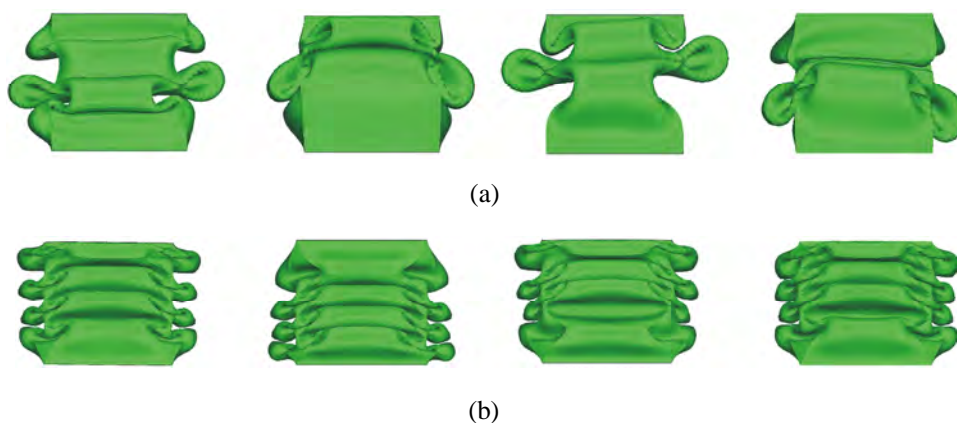
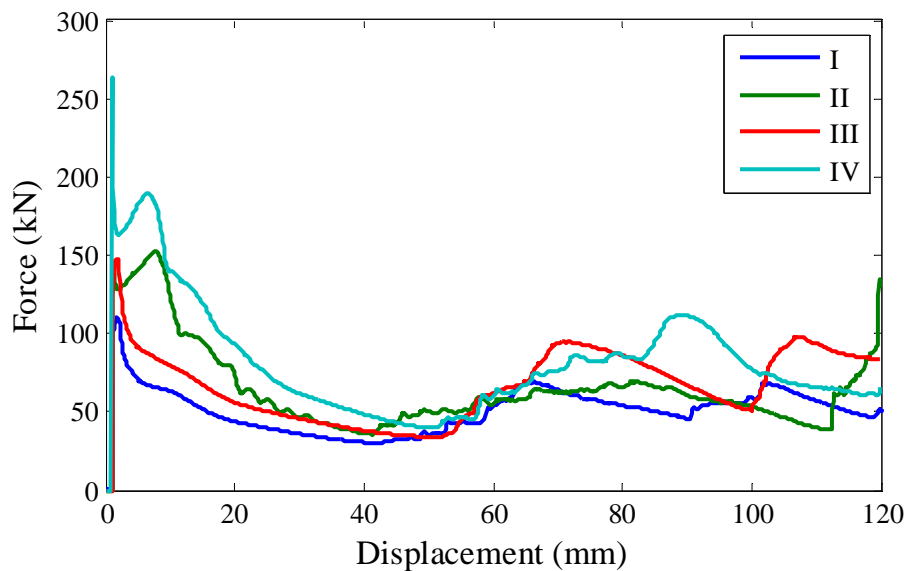
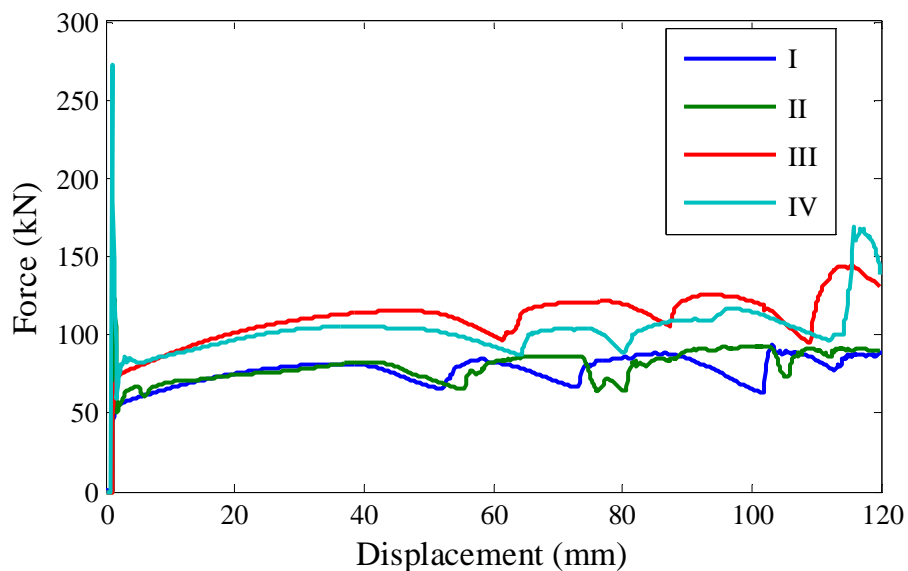


Fig. 4.38 Crushed configurations of (a)  $C_c$ , and (b)  $O_c$  under conditions I - IV (from left to right).

The force vs. displacement curves of  $C_c$  under all four conditions and those of  $O_c$  are plotted in Fig. 4.39(a) and (b), respectively. The numerical results are presented in Table 4.10. Three observations can be made from the results.



(a)



(b)

 Fig. 4.39 Force vs displacement curves of (a)  $C_c$ , and (b)  $O_c$  under four conditions.

Table 4.10 Numerical results of the tubes under four conditions

Condition	$C_c$		$O_c$			
	$P_{\max}$ (kN)	$P_m$ (kN)	$P_{\max}$ (kN)	$P_{\max}$ reduction	$P_m$ (kN)	$P_m$ increase
I	110.30	50.77	93.55	15.2%	76.73	51.1%
II	152.03	64.47	122.98	19.1%	79.36	23.1%
III	148.00	66.74	144.38	2.4%	110.49	65.6%
IV	263.30	81.86	272.27	-3.4%	103.37	26.3%

First of all, both  $P_{\max}$  and  $P_m$  of  $C_c$  under condition II are noticeably higher than those under condition I. By contrast, only  $P_{\max}$  of  $O_c$  under condition II is significantly increased in comparison with that under condition I, whereas  $P_m$  of  $O_c$  under both conditions are quite close to each other. This phenomenon can be explained as follows. Inertia effects tend to preserve the unbuckled shape of a tube when subjected to a high speed impact. For  $C_c$ , the inertia effects delay initiation of local folding, leading to a prolonged high force at the beginning of the crushing process which can be seen from Fig. 4.39(a). As a result, both  $P_{\max}$  and  $P_m$  of  $C_c$  increase considerably. For  $O_c$ , on the other hand, the origami pattern works as a type of geometric perturbation which favours immediate strain localization. The effect of the origami pattern outweighs the inertia effects, and therefore local folding happens immediately after loading, resulting in a sharp drop in force which can be seen from Fig. 4.39(b). After the force drop, the inertia effects become insignificant, and therefore the forces under the two conditions nearly overlap. As a result, only  $P_{\max}$  of  $O_c$  is raised considerably whereas  $P_m$  remains almost the same.

Secondly, both  $P_{\max}$  and  $P_m$  of  $C_c$  under condition III are noticeably higher than those under condition I, and a similar result is also obtained for  $O_c$ . This observation indicates that strain rate sensitivity has similar effects on both types of tubes. The reason is that strain rate effects are associated with plastic strain rate, and are therefore obvious during the entire crushing process.

Finally, when both inertia and strain rate sensitivity are considered, as in the case of condition IV,  $P_{\max}$  of the two tubes are quite close.  $P_m$  of  $O_c$ , on the other hand, is still considerably higher than that of  $C_c$ , which demonstrates the superior energy absorption capability of the origami tube.

## 4.6 Summary

A family of novel origami patterns have been proposed to design a type of high-performance energy absorption device known as the origami tube in this chapter. The origami pattern pre-manufactured on the surface of the tube has the dual functions of a geometric imperfection to reduce the initial buckling force and of a mode inducer to trigger a failure mode that is more efficient in terms of absorbing energy in a collision. Hence the origami tube is able to meet the twin design objectives of high SEA and low load uniformity.

An extensive numerical study has been conducted on four groups of origami tubes with various configurations to investigate their failure modes and energy absorption properties when subjected quasi-static axial crushing. The results show that, a new failure mode, referred to as the complete diamond mode, which resembles the diamond mode typical of thin-walled circular tubes, can be successfully triggered in square, rectangular, polygonal, and tapered origami tubes over a wide range of pattern geometries. Peak force reduction by about 30% and mean crushing force increase by over 50% are consistently achieved for the origami tube compared with those of a conventional square tube with identical surface area and wall thickness.

Compared with existing thin-walled tube designs, the origami tube has several important advantages. First of all, both high SEA and low load uniformity are unified in a single tube design. This desirable result is achieved due to the new design approach. In a typical design approach if the objective is to increase the energy absorption of a tube, the tube is strengthened in some way, e.g., by replacing a single-cell cross section with a cellular cross section or by introducing circumferential reinforcement along the tube. The design approach applied here, however, is to increase the energy absorption of a tube through replacing its original failure mode with a new mode by means of application of origami patterns. It is now possible to increase the energy absorption of a tube by first weakening it, since any perturbation of the initially straight walls of a conventional square tube will reduce its peak loading at the beginning of the crushing. As a result, the problem of high initial buckling force is solved automatically. It should be mentioned that square tubes with pyramid patterns on the surface are also able to

achieve both low initial buckling force and high energy absorption simultaneously (Ma, 2008). But the difficulty is how to consistently trigger the octagonal mode, as mentioned in Chapter 3. Secondly, the geometry of the origami pattern can be flexibly adjusted to ensure that the complete diamond mode is triggered in a stable manner. It has been shown in Section 4.4 that  $c/l$  is crucial in determining the failure mode of the origami tube. As long as  $c/l$  is sufficiently large, the complete diamond mode is bound to occur. Of course, an excessively large  $c/l$  would lead to reduction in the energy absorption efficiency. Therefore an optimum value needs to be determined to maximize energy absorption efficiency. Note that one of the shortcomings of the pyramid pattern is that the geometry of the pattern cannot be easily adjusted to ensure the forming of the octagonal mode. Thirdly, the origami pattern is developable, meaning that the origami tube can be made out of a flat sheet of material with little in-plane stretching. This property thus provides a convenient and accurate manufacturing technique to construct the origami tube without substantial cost increment. By contrast, the commonly applied dents on existing thin-walled energy absorption devices unavoidably introduce material stretching during the manufacturing process. The same is true for the pyramid pattern.

In addition to the energy absorption performance, some other factors, crucial for the origami tube to be used as an energy absorption device, have also been investigated through a series of case studies, from which five conclusions can be drawn:

- The complete diamond mode is quite robust under a variety of practical boundary conditions, indicating that the origami tube can perform well under realistic scenarios.
- The performance of the origami tube shows no obvious dependence on material mechanical properties provided that ductile material is used. Therefore the material of the origami tube can be flexibly selected based on practical requirements.
- Reinforcing the origami tube with a centre web can still preserve its superior energy absorption performance.
- As long as a proper pattern geometry is chosen, the bending and torsional performances of an origami tube become comparable to those tubes with pre-



manufactured dents on the surface. In other words, the origami tube integrates well under both bending and twisting.

- The response of the origami tube subjected to dynamic axial crushing is consistent and predictable. The energy absorption of the origami tube is also superior to that of conventional tubes.

Various properties that influence the performance of the origami tube as a practical energy absorption device have been discussed in this chapter when it is subjected to axial compression. However, the tube often is subjected to off-axial or inclined loading in practice. There are two ways to consider the real world scenario. The first is to treat the origami tube as a stand-alone structure subjected to an off-axial impact. An oblique impact load can be applied to the origami tube, and the focus is to investigate in what range of impact angle the complete diamond mode can be maintained. The second is to integrate the origami tube into a structural system such as an automobile frontal bumper. The behaviour of the origami tube is then obtained from the impact analysis of the bumper. The second is chosen in the dissertation, and the results will be presented in Chapter 7.

# CHAPTER 5

## THE ORIGAMI TUBE: THEORETICAL ANALYSIS AND EXPERIMENTS

The superior energy absorption properties of the origami tube were clearly demonstrated via an extensive numerical study in Chapter 4. In this chapter theoretical and experimental studies on the origami tube will be presented.

In Section 5.1 a basic folding element is proposed to describe the complete diamond mode and a theoretical formula is derived to estimate the mean crushing force of a square origami tube with specified geometry and material properties. Section 5.2 presents quasi-static axial crushing tests on several square origami tube samples. Two manufacturing approaches are developed to construct tube samples with different wall thicknesses. Numerical simulations of the test samples are also conducted and the numerical results are compared with the experimental data. Finally a summary is given in Section 5.3.

### **5.1 Theoretical Prediction of the Mean Crushing Force**

It was shown in Chapter 4 that the origami patterns could trigger the complete diamond mode in origami tubes with a wide range of pattern geometries and tube profiles. From the viewpoint of design, it would be desirable to have a simple mathematical formula to estimate the energy absorption of an origami tube with specified geometry and

material, or to roughly determine the size of an origami tube if the material used to construct the tube is chosen and the energy required to be absorbed is known. To this end, a theoretical analysis on the crushing of the origami tube is conducted. Square origami tubes which have the smallest number of independent geometric parameters are selected for the study. The three-step procedure outlined in Chapter 2 is adopted to derive the mean crushing force.

### **5.1.1 Basic folding element**

Before building a basic folding element, let us start with a detailed analysis of the folding process of square origami tubes. Tube model A2\_2 in Chapter 4, consisting of three modules which are referred to as module I – III from top to bottom, is selected as an example. The front and side views of the crushing process of a quarter of A2\_2, each of which includes eight typical configurations, are shown in Fig. 5.1(a) and (b), respectively, and the corresponding equivalent plastic strain (PEEQ) contour at each configuration is plotted in Fig. 5.1(c). At the beginning of the crushing process, module II first starts to fold. The second configuration in Fig. 5.1(a) indicates that two pairs of travelling plastic hinge lines are formed along the four sides of the lobe in module II. This observation is also reflected in the second PEEQ contour in Fig. 5.1(c), which shows that large plastic deformation occurs along the four sides. Subsequently, two pairs of inclined stationary plastic hinge lines, as can be observed from the third configuration in Fig. 5.1(a), appear in the lobe area of module II. The third PEEQ contour in Fig. 5.1(c) also shows that large plastic strain takes place at the locations of those hinges. In addition, two horizontal stationary plastic hinge lines are formed near the upper and lower ends of module II, respectively. Those hinges are not exactly along the ends of module II but at locations inside the module, which can be seen from the third configurations in Fig. 5.1(b) and the third PEEQ contour in Fig. 5.1(c). As a result, module II is not completely flattened but has a residual height. The horizontal stationary plastic hinge line in the middle of module II, which is initiated at the beginning of the crushing process, is completely folded at this point. As the tube is compressed further, modules I and III are folded one after another in a similar manner.

Another observation that can be made from the PEEQ contours in Fig. 5.1(c) is that large plastic deformation is limited to the area swept by the travelling plastic hinge lines and the neighbourhood of the stationary plastic hinge lines, whereas the remaining panels undergo very small plastic deformation. This observation indicates that no circumferential membrane deformation of a large magnitude is activated in the tube, and therefore the deformation mode can be practically treated as circumferentially inextensible.

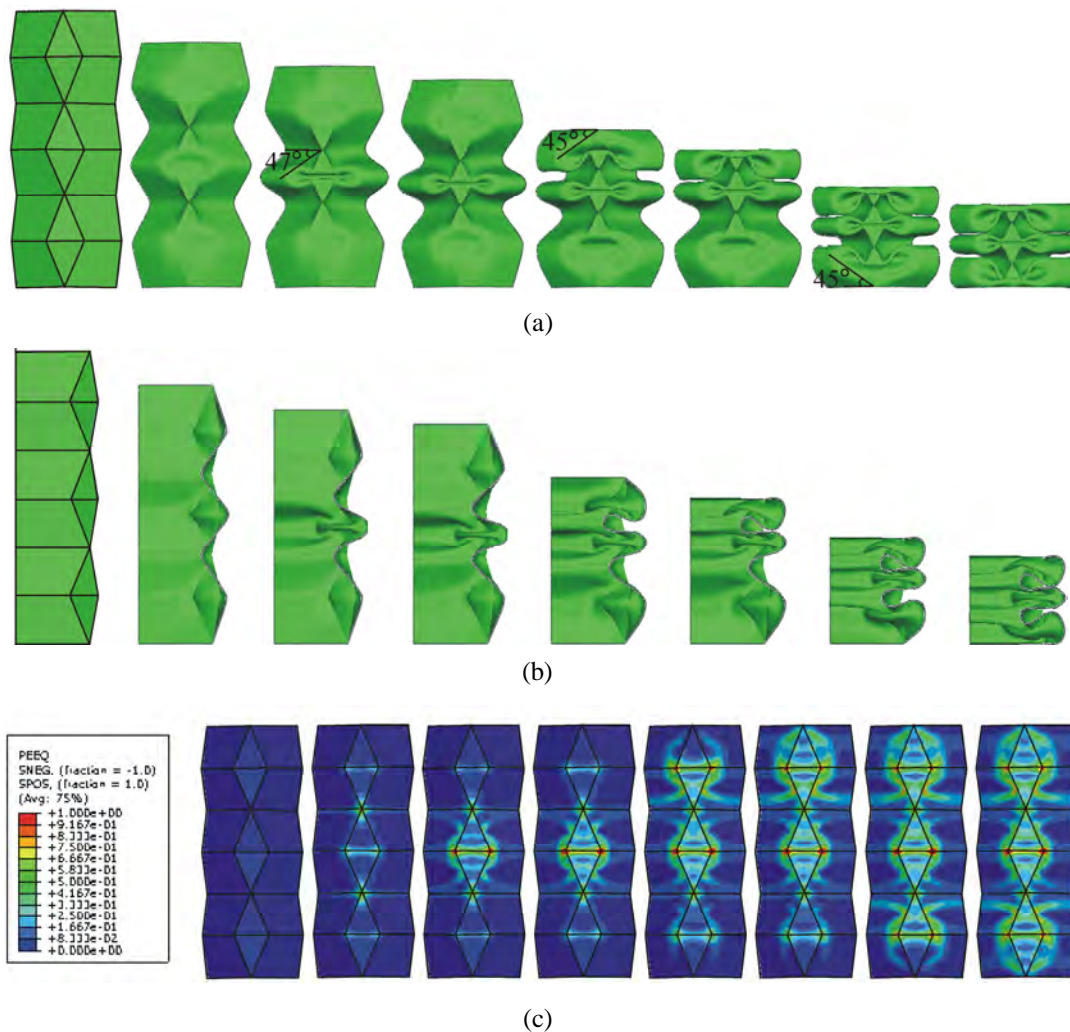


Fig. 5.1 Crushing process of a quarter of A2\_2. (a) Front view, (b) side view, and (c) PEEQ contour.

Now consider one quarter of a module of a square origami tube with tube width  $b$ , module length  $l$ , and corner width  $c$  as a basic folding element. Based on the numerical

results presented in Chapter 4, the crushing process of the basic folding element can be approximately divided into two stages.

At stage I,  $CA_1$ ,  $CB_1$ ,  $EA_1$ , and  $EB_1$ , highlighted by thick lines in Fig. 5.2(a), become travelling plastic hinge lines and move away from the corner as the element is being crushed until they reach  $CA$ ,  $CB$ ,  $EA$ , and  $EB$ , respectively. The value of  $\alpha$  measured from the numerical models is around  $\pi/4$ . For instance, the angles formed in the three modules of A2\_2 are approximately  $45^\circ$ ,  $47^\circ$ , and  $45^\circ$ , respectively. Meanwhile, a circumferential stationary plastic hinge line, also highlighted by thick lines, is formed in the middle of the element and bent as the travelling plastic hinge lines propagate to keep the element geometrically compatible. The configuration of the element at the end of Stage I is shown in Fig. 5.2(b). Note that the element is only slightly shortened at this time.

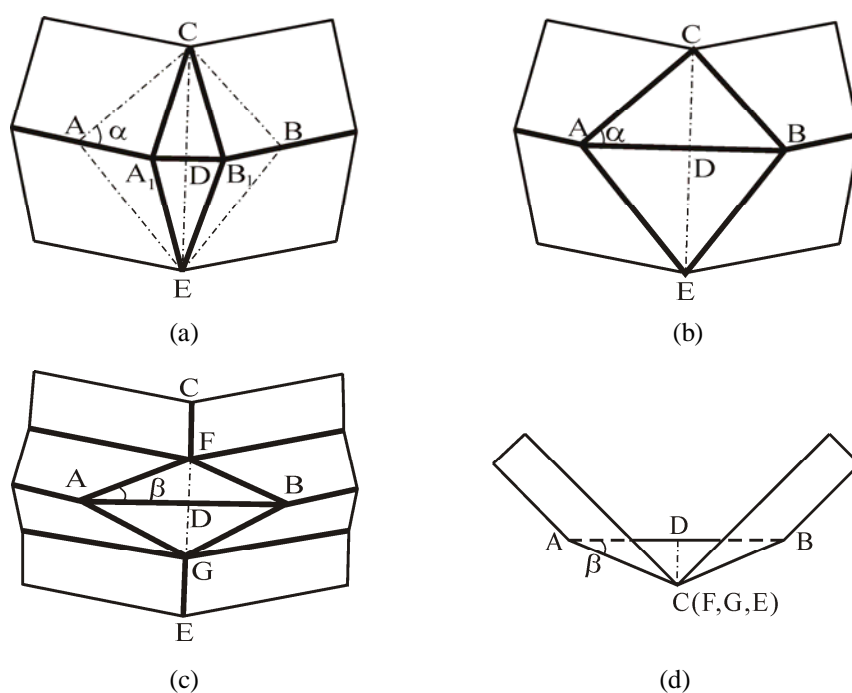


Fig. 5.2 Crushing process of the basic folding element. (a) perspective view of the initial configuration, (b) perspective view of the configuration at the end of Stage I, (c) perspective view of a partially crushed configuration at Stage II, and (d) top view of the fully crushed configuration.

Subsequently Stage II starts, during which the element is substantially shortened to its final configuration. If the entire element were to be perfectly folded to flat, the four

travelling hinge lines would have to move further until  $\alpha$  reduces to  $\pi/8$  which can be readily obtained from a simple geometric analysis. However, no such movement is observed from the numerical analysis. Here a geometrically compatible folding route as follows is assumed. Four inclined stationary plastic hinge lines, FA, FB, GA, and GB, two vertical ones, FC and GE, and two circumferential ones passing points F and G, respectively, all of which are highlighted by thick lines in Fig. 5.2(c), are formed and continuously bent until the basic folding element is crushed completely. Angle  $\beta$  is  $\pi/8$ , and the final crushing distance of the element is  $l \tan(\pi/8)$ . The completely folded configuration of the element is shown in Fig. 5.2(d).

The material is assumed to be rigid-perfectly plastic and strain rate insensitive with a suitably chosen plastic flow stress to take the strain-hardening of the material into consideration (Wierzbicki and Abramowicz, 1983).

With the basic folding element above, the total energy absorption can then be calculated as the summation of the energies absorbed at stages I and II.

### **5.1.2 Energy absorption at Stage I**

Previous research (Meng *et al.*, 1983) indicated that when a travelling plastic hinge line swept an area, the material was bent to a radius  $r$  and then unbent again to flat. Wierzbicki and Abramowicz (1983) pointed out that in-plane deformation existed in the localized zone around the intersecting point of two travelling plastic hinge lines, e.g.,  $A_1$  and  $B_1$  in Fig. 5.2(a). Therefore the total energy absorption at this stage consists of three parts: the energies absorbed by the circumferential stationary plastic hinge line, the inclined travelling plastic hinge lines, and the in-plane deformation. The energy absorption of the stationary plastic hinge line will be considered at stage II since it is continuously being bent during the entire crushing process.

To obtain the energy absorption of the travelling plastic hinge lines, first consider hinge line  $CA_1$  only, see Fig. 5.2(a). According to the basic folding element,  $CA_1$  travels from

its original position until it reaches CA, sweeping the area of triangle ACA<sub>1</sub>. For simplicity, it is assumed that the bending and unbending radius  $r$  is constant and  $r \ll b$ . Thus, the energy absorbed by CA<sub>1</sub> is (Meng *et al.*, 1983)

$$E_{CA_1} = \frac{2S_{ACA_1}}{r} M_p = \frac{l(l-c)}{4r} M_p \quad (5.1)$$

in which  $S_{ACA_1}$  is the area of triangle ACA<sub>1</sub> and  $M_p$  is the full plastic bending moment per unit length

$$M_p = \frac{\sigma_0 t^2}{4} \quad (5.2)$$

Since there are four such travelling plastic hinge lines in the element, the energy absorbed by this part can be calculated as

$$E_1 = 4E_{CA_1} = \frac{l(l-c)}{r} M_p \quad (5.3)$$

For the energy absorption of the in-plane deformation, the energy dissipated at one intersecting point is (Wierzbicki and Abramowicz, 1983)

$$E_e = 16I_1 \frac{lr}{2t} M_p \quad (5.4)$$

where  $I_1$  is a numerical integral and can be calculated as

$$I_1\left(\frac{c}{l}\right) = \frac{4}{3 \tan(\pi/8)} \int_{\arcsin\left(\frac{c}{l} \tan\frac{\pi}{8}\right)}^{\arcsin\left(\tan\frac{\pi}{8}\right)} \cos x \left\{ \begin{array}{l} \sin \frac{\pi}{8} \sin \left[ \frac{3}{4} \arctan\left(\frac{\tan x}{\sin(\pi/8)}\right) \right] + \cos \frac{\pi}{8} \\ - \cos \frac{\pi}{8} \cos \left[ \frac{3}{4} \arctan\left(\frac{\tan x}{\sin(\pi/8)}\right) \right] \end{array} \right\} dx \quad (5.5)$$

Since there are two intersecting points in the element, the energy absorbed by this part is

$$E_2 = 2E_e = 16I_1 \frac{lr}{t} M_p \quad (5.6)$$

### 5.1.3 Energy absorption at Stage II

The energy absorption at this stage can be obtained by adding up the energies absorbed by the three circumferential stationary plastic hinge lines, four inclined ones, and two vertical ones, all of which are highlighted by thick lines in Fig. 5.2(c).

The three circumferential hinge lines have identical length  $b$ , and their angles of rotation from top to bottom are  $\pi/2$ ,  $2 \arccos[(\sqrt{2}-1)c/l]$ , and  $\pi/2$ , respectively. So the energy absorbed by this part is

$$E_3 = \left[ \pi + 2 \arccos \frac{(\sqrt{2}-1)c}{l} \right] b M_p \quad (5.7)$$

The total length of the four inclined hinge lines is

$$l_i = \frac{2l}{\cos(\pi/8)} \quad (5.8)$$

And their angle of rotation is  $\pi$ , so the energy absorbed by this part is

$$E_4 = \frac{2\pi l}{\cos(\pi/8)} M_p \quad (5.9)$$

The total length of the two vertical hinge lines is

$$l_v = (1 - \tan \frac{\pi}{8}) l \quad (5.10)$$

And their angle of rotation is  $\pi/2$ , so the energy absorbed by this part is

$$E_5 = \frac{1}{2} (1 - \tan \frac{\pi}{8}) \pi l M_p \quad (5.11)$$

### 5.1.4 Mean crushing force

Having obtained the energy absorptions at the two stages, the mean crushing force can now be calculated by applying the balance between external work and internal plastic



dissipation. Considering that there are four basic folding elements in a module, the following equation can be obtained

$$P_m l \tan(\pi / 8) = 4(E_1 + E_2 + E_3 + E_4 + E_5) \quad (5.12)$$

Substituting Eqs. (5.3), (5.6), (5.7), (5.9), and (5.11) into Eq. (5.12) yields

$$P_m = \left\{ 9.66 \frac{l-c}{r} + 154.51 I_1 \frac{r}{t} + 9.66 \left[ \pi + 2 \arccos \frac{(\sqrt{2}-1)c}{l} \right] \frac{b}{l} + 74.56 \right\} M_p \quad (5.13)$$

It is reasonable to assume that  $r$  should be so chosen as to make  $P_m$  a minimum. Differentiate Eq. (5.13) with respect to  $r$

$$\frac{dP_m}{dr} = 0 \quad (5.14)$$

which yields

$$-9.66 \frac{l-c}{r^2} + 154.51 I_1 \frac{1}{t} = 0 \quad (5.15)$$

Solving  $r$  from Eq. (5.15) gives

$$r = 0.25 I_1^{-1/2} (l-c)^{1/2} t^{1/2} \quad (5.16)$$

Substituting Eqs. (5.2) and (5.16) into Eq. (5.13), we obtain

$$P_m = \sigma_0 \left\{ 19.31 I_1^{1/2} (l-c)^{1/2} t^{3/2} + \left[ \frac{7.57b}{l} + \frac{4.82b}{l} \arccos \frac{(\sqrt{2}-1)c}{l} + 18.64 \right] t^2 \right\} \quad (5.17)$$

In Eq. (5.17), both terms in the brace depend only on tube geometry. For a square origami tube with fixed  $b$  and  $t$ , reducing  $c$  results in increase in both terms, whereas increasing  $l$  leads to increase in the first one and reduction in the second one.

In the case that  $l/b = 1$  and  $c/l = 0.5$ ,  $I_1(0.5) = 0.21$  and the mean crushing force is

$$P_m = \sigma_0(6.29b^{1/2}t^{3/2} + 32.80t^2) \quad (5.18)$$

The theoretical prediction of  $P_m$  calculated from Eq. (5.18) and the numerical data of A1\_1 and A7\_1 – A7\_7 in Chapter 4 are plotted against  $t$  in Fig. 5.3. It can be seen that a good agreement between the theoretical prediction and the numerical results is obtained. Therefore Eq. (5.18) can be used to estimate the mean crushing force of a square origami tube with given geometry and material.

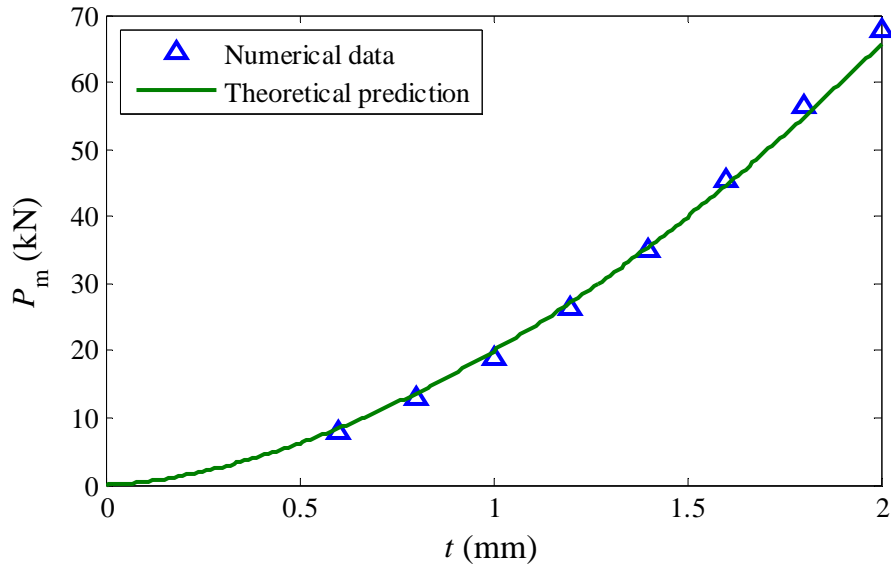


Fig. 5.3 Comparison of theoretical prediction of  $P_m$  and numerical results.

Dividing Eq. (5.18) by Eq. (2.17) in Section 2.1.2 of Chapter 2 which gives the mean crushing force of conventional square tubes, the following equation can be obtained

$$p_m = 0.94 + 4.91(b/t)^{-1/2} \quad (5.19)$$

in which  $p_m$  is the ratio of  $P_m$  of square origami tubes to that of conventional square tubes.

Equation (5.19) indicates that  $P_m$  improvement of square origami tubes in comparison of conventional square tubes decreases with  $b/t$ . In other words, the larger  $b/t$ , the closer the energy absorption of a square origami tube is to that of a conventional one. The reason is that as  $b/t$  increases, the second term in Eq. (5.18), which corresponds to the energy absorption of stationary plastic hinge lines, accounts for a smaller portion of the total energy absorption, leading to a reduced  $P_m$  difference between a square origami tube and a conventional one.

Despite the satisfactory agreement with numerical results, the theoretical analysis fails to capture the realistic final crushing distance of square origami tubes. The final crushing distance of the basic folding element, 41% of its original length, is considerably smaller than that of the numerical models which is typically about 70%. A more advanced basic folding element needs to be developed in order to conduct a more accurate analysis.

The mean crushing force derived based on square origami tubes can also be used to estimate the energy absorption of rectangular and tapered ones. Recall that the energy absorption of a rectangular or tapered origami tube can be very close to that of a square origami tube with identical surface area and wall thickness provided that suitable pattern geometries are selected. Therefore the mean crushing force of a rectangular or tapered origami tube can be roughly estimated as that of the corresponding square tube, which considerably extends the scope of application of Eq. (5.18).

## **5.2 Axial Crushing Tests**

### **5.2.1 Sample preparation and experimental setup**

It was mentioned in Chapter 4 that the origami tube had a developable surface and thus could be made out of a flat sheet of material with little in-plane stretching. Therefore the method of folding a steel sheet following the pre-manufactured origami pattern on

it was applied to construct origami tube samples. As it was difficult to fold a single sheet into a complete tubular shape, two half-tubes were first formed and then connected by welding. Consequently, a three-step procedure was used to construct tube samples.

- Stamping the origami pattern on a steel sheet. A pair of male and female moulds, Fig. 5.4(a), was designed for the stamping process. They were made of hard steel and had protruded steel bars and corresponding rubber strips on the surface to define the geometry of the pattern. Two types of channel were machined on the moulds, i.e., that for rubber strips which was 5 mm wide and 3 mm deep, and that for steel bars which was 2 mm wide and 1 mm deep. The width and thickness of the rubber strips were 5 mm and 3 mm, respectively, whereas the radius of the steel bars was 1 mm. As seen in Fig. 5.4(b), the hill and valley creases could be well formed on the sheet by stamping.

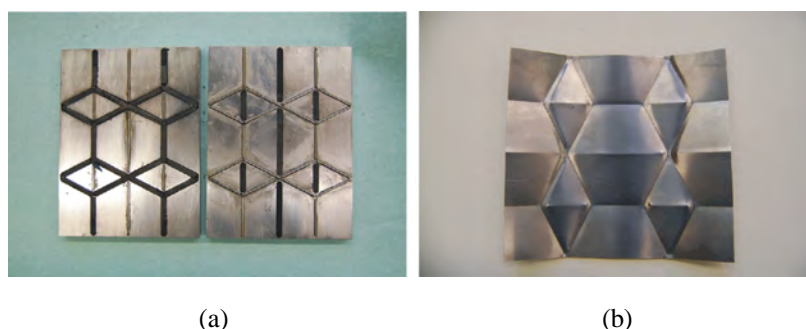


Fig. 5.4 (a) Moulds for stamping, and (b) a stamped steel sheet.

- Folding the stamped sheet along the creases to form a half-tube shown in Fig. 5.5. This step was finished by hand, which made the final product rather crude. Geometric imperfection in the form of out-of-plane deformation was found to be unevenly distributed on the tube walls.
- Forming a complete tube by connecting two half-tubes using spot-welding. The width of the overlapped regions of two half-tubes was 10 mm, along which eight welding spots were evenly lined.



Fig. 5.5 A half-tube folded out of a stamped sheet.

Considering the brittle nature of very thin steel sheets, they were annealed at  $600^{\circ}\text{C}$  for one hour and then slowly cooled down in oven before stamping in order to avoid micro cracks along the creases. The same heat treatment procedure was also conducted on the origami tube samples for the sake of relieving heat effects caused by spot-welding.

It should be pointed that this extremely simple manufacturing approach has its limitations. Only very thin tubes with wall thickness around 0.5 mm can be constructed and tubes built in this way are not of high quality. However, it will be shown next that even those relatively poorly constructed samples are capable of demonstrating the advantages of the origami tube.

Three tube samples, including one conventional square tube and two square origami tubes, were built using mild steel sheets with  $t = 0.5$  mm. Sample N was a conventional tube made through connecting two channel sections by spot-welding. The tube width and height of N were 60 mm and 120 mm, respectively. Samples O1 and O2 were two origami tubes with  $b = 60$  mm,  $c = 30$  mm,  $l = 60$  mm, and  $M = 2$ . Note that the three samples were so designed that they had identical surface area.

The axial crushing tests were conducted on an Instron machine with the upper loading limit of 100 kN. During the crushing process the tube stood on a thick plate while the cross head connected to the load cell moved downward to compress the tube. Both ends of the tube were free of constraints. Displacement control was applied in the tests

and the loading rate was chosen as 5 mm / min to avoid dynamic effects. The final crushing distance was chosen as 80 mm which was about 70% of the tube height.

### 5.2.2 Material tensile tests

Material tensile tests were conducted on three steel sheet specimens which were subjected to identical heat treatment with the tube samples at 0.5 mm / min loading rate to characterize the material properties. The averaged mechanical properties obtained were:  $E = 220.8$  GPa,  $\sigma_y = 245.6$  MPa,  $\sigma_u = 369.2$  MPa, and  $\epsilon_u = 25.0\%$  . A typical engineering stress vs strain curve is plotted in Fig. 5.6.

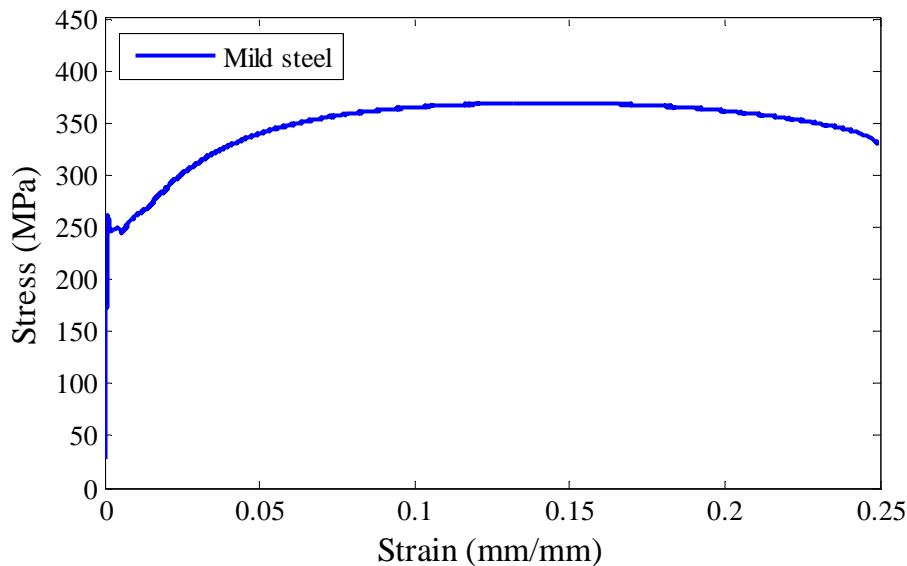


Fig.5.6 Material engineering stress vs strain curve.

### 5.2.3 Experimental results

The conventional square tube sample N is first analyzed. Previous research (Reid *et al.*, 1986) indicated that the non-compact mode was most likely to appear in a square tube with  $b/t=120$  . This mode is clearly observed from the test with N, Fig. 5.7(a), suggesting the effectiveness of the experimental setup at yielding reliable results.

Subsequently the axial crushing processes of origami tube samples O1 and O2 are shown in Fig. 5.7(b) and (c), respectively. It can be seen that both samples collapse one module after another following the predefined folding route, leading to a stable and progressive complete diamond mode. Stationary plastic hinge lines are formed along the horizontal creases and gradually bent during the crushing process, while travelling plastic hinge lines originate from the corners and move away to deform the material in the corner zones. The only evident difference between the crushing processes of the two samples is that the lower module of O1 is first folded whereas the upper one of O2 collapses first. This discrepancy is probably attributed to the geometric imperfection on the tube samples.

Compared with the complete diamond mode of the numerical models in Chapter 4, the failure mode of the physical samples seems somewhat irregular, e.g., the lobes in the same module of O1 are not folded exactly simultaneously. This phenomenon could also be caused by the geometric imperfection on the tube samples.

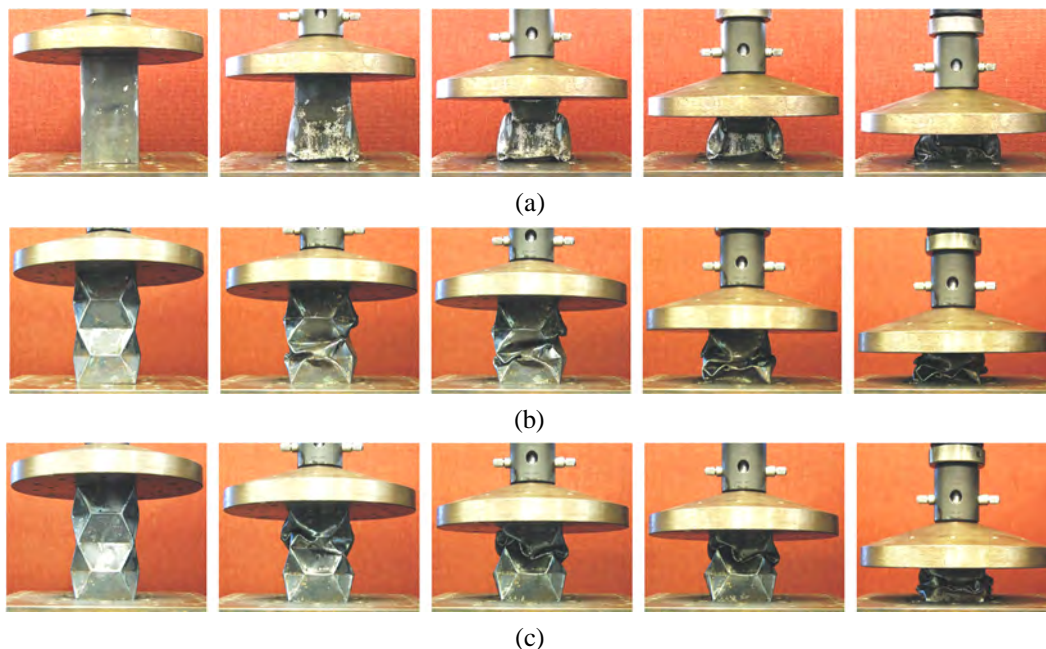


Fig. 5.7 Crushing processes of (a) N, (b) O1, and (c) O2.

The force vs displacement curves of all of the three samples are plotted in Fig. 5.8 and the experimental results are summarized in Table 5.1. It can be seen that the curves of

O1 and O2 are relatively smooth compared with that of N and stay above of it during most of the crushing process. The introduction of the origami pattern leads to  $P_{\max}$  reduction of more than 40%. The improvement in  $P_m$ , on the other hand, is not as remarkable, with only about 20% increase being achieved.

Three conclusions can be drawn from the experiments.

- The ability of the origami pattern to trigger the complete diamond mode in square origami tubes is verified. And both low  $P_{\max}$  and high  $P_m$  are obtained.
- The  $P_m$  enhancement of very thin origami tubes tested here is not as pronounced as that of tubes with moderate thickness analyzed in Chapter 4. This observation is accordance with the trend reflected by Eq. (5.19). However, very thin tubes are rarely used in the design of energy absorption devices, and thus the usefulness of the origami design is not greatly compromised by this shortcoming.
- The complete diamond mode is not very sensitive to geometric imperfection and local material variation, since the rather crude samples can still fail in the complete diamond mode. This feature would greatly reduce the requirement of accuracy in the manufacturing process, making the origami tube suitable for industrial mass production.

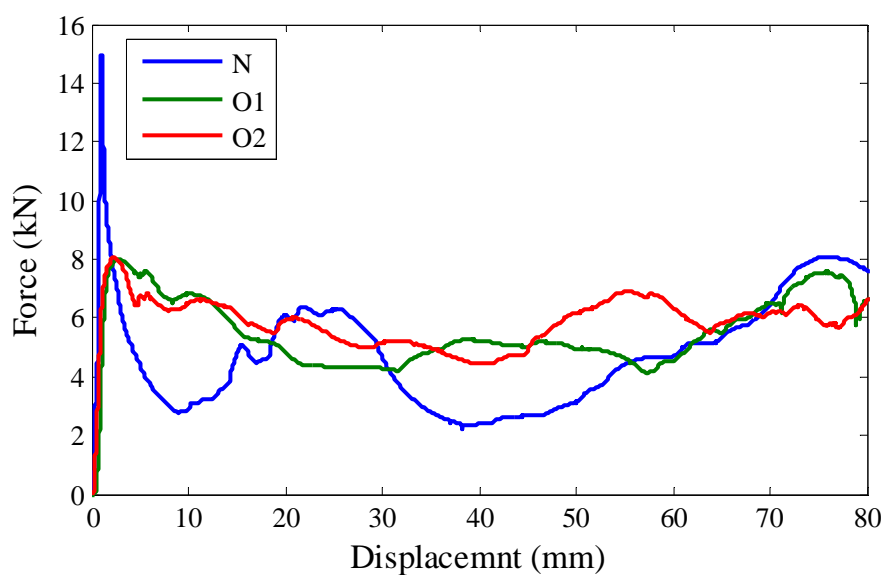


Fig. 5.8 Force vs displacement curves of N, O1, and O2.



Table 5.1 Axial crushing test results of N, O1, and O2

Sample	$P_{\max}$ (kN)	$P_{\max}$ reduction	$P_m$ (kN)	$P_m$ increase
N	14.95		4.78	
O1	7.99	46.6%	5.50	15.1%
O2	8.07	46.0%	5.84	22.2%

#### 5.2.4 Numerical simulation of the axial crushing tests

The experiments conducted in this chapter report much lower energy absorption improvement than that obtained from the numerical analysis in Chapter 4. To further verify the reliability of the finite element modelling approach employed in Chapter 4, the same approach was reapplied to simulate the axial crushing tests.

Several modifications were made to simulate the experiments realistically. First of all, considering that the physical samples were constructed by spot-welding two halves, both a half-tube model and a whole-tube model were built. The former was identical to that used before, whereas the latter was implemented by connecting two halves through the mesh-independent fastener technique built in Abaqus (SIMULIA Corp., USA). Secondly, free-free boundary conditions were applied to the numerical tube model in accordance with the boundary conditions in the experiments. Finally, the material properties obtained from the tensile tests in Section 5.2.2 were assigned to the numerical model. The material density and Poisson ratio were  $\rho = 7800 \text{ kg/m}^3$  and  $\nu = 0.3$ .

The axial crushing processes of the two models are presented in Fig. 5.9(a) and (b), respectively. It can be seen that both models show the complete diamond mode, which agrees reasonably well with the experimental results. The failure mode of the numerical models is quite regular compared with that of the physical samples, with all of the lobes in one module being folded simultaneously.

The numerical results of the two models are summarized in Table 5.2.  $P_{\max}$  of both models are found to be higher than those of O1 and O2 listed in Table 5.1. Geometric imperfection on the physical samples might well be responsible for this discrepancy.  $P_m$  of the whole-tube model is very close to those obtained experimentally. The half-tube model, on the other hand, slightly underestimates  $P_m$ . This underestimation is most likely to be due to that the extra material in the overlapped area of the physical samples and the spot welds were not taken into consideration in the half-tube model. Despite that, a reasonable agreement between the numerical value and the experimental value is still obtained.

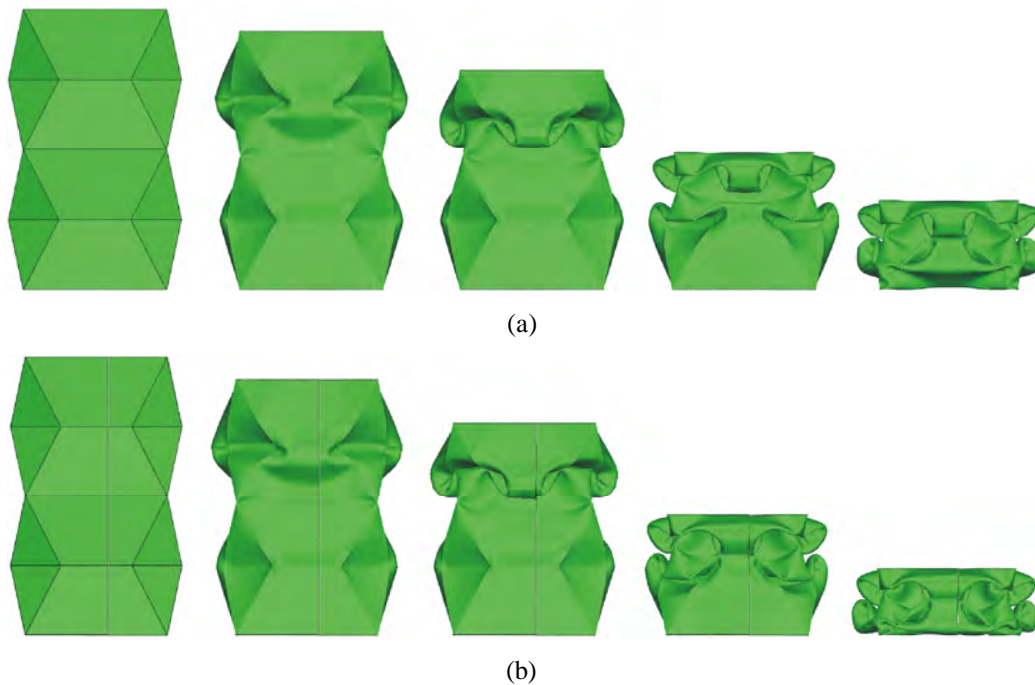


Fig. 5.9 Crushing processes of (a) half-tube model, and (b) whole-tube model.

Table 5.2 Numerical simulation results

Model	$P_{\max}$ (kN)	$P_m$ (kN)
Half-tube model	9.95	5.42
Whole-tube model	10.04	5.62

In summary, the above results further confirm that the finite element modelling approach used in Chapter 4 can reasonably simulate the crushing of the origami tube and yield reliable results.

### **5.2.5 Refined manufacturing approach**

The crude manufacturing approach presented in Section 5.2.1 has the merit of simplicity but can only be used to construct very thin origami tubes and the quality of the samples is low. Casting and hydroforming are possible alternatives but the manufacturing cost can be prohibitively high for small number of prototypes. Therefore a cost-effective manufacturing approach needs to be developed to construct origami tubes using thick materials.

A commonly adopted approach in the manufacturing of commercial tubular energy absorption devices is to construct a tube by joining two halves through spot-welding. Pre-manufactured geometric imperfection on the tube such as indentation is usually formed by stamping. The same can be used for the origami tube. To keep the manufacturing cost low, the procedure of first stamping a steel sheet into a half-tube and then joining two halves by spot-welding to form a complete one was preserved, but a new way of stamping was developed to improve accuracy. Foreseeing the difficulty in forming a half-tube out of a steel sheet in one punch because of its complicated three-dimensional configuration, a set of moulds, Fig. 5.10, was designed. The set is composed of six individual parts named from A to F. The sizes and shapes of the parts are determined by the geometry of the origami tube to be manufactured. The bars in Part A and the corresponding holes in the others are used to align the parts during the stamping process. The three steps to form a half-tube using the moulds are as follows

- Putting a steel sheet on the surface of Part A, and then placing Part B on the sheet through bars 1 and 2 in the middle of Part A and compressing Part B to stamp the pattern on one side.

- Placing Parts C and D on the sheet through bars 3 and 4, and bars 5 and 6, respectively, and compressing them to form the lobes at the two corners.
- Placing Parts E and F on the sheet through bars 7 and 8, and bars 9 and 10, respectively, and compressing them to stamp the pattern on the other two sides.

A set of moulds, Fig. 5.11(a), was manufactured and applied to construct prototypes. Threads were machined on the bars and the stamping compressive force was generated by turning nuts placed on the threaded bars. One of the prototypes which possesses identical geometry with that of O1 and O2 but has 1.0 mm wall thickness is shown in Fig. 5.11(b). Compared with O1 and O2, the tube sample constructed by the new approach is much better in terms of quality.

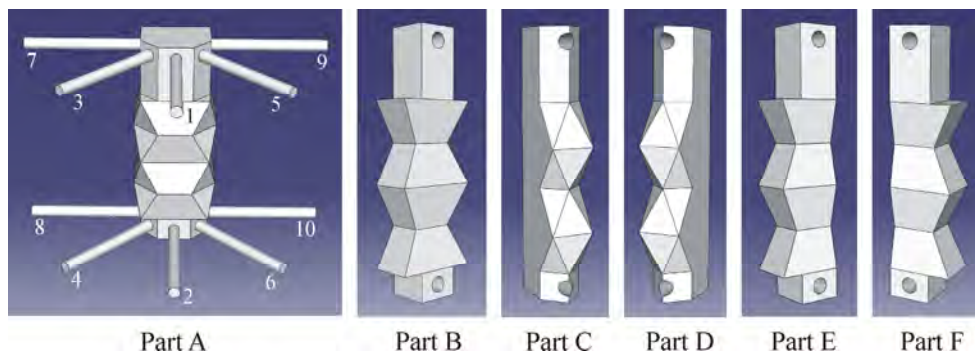


Fig. 5.10 Moulds to form a half-tube.

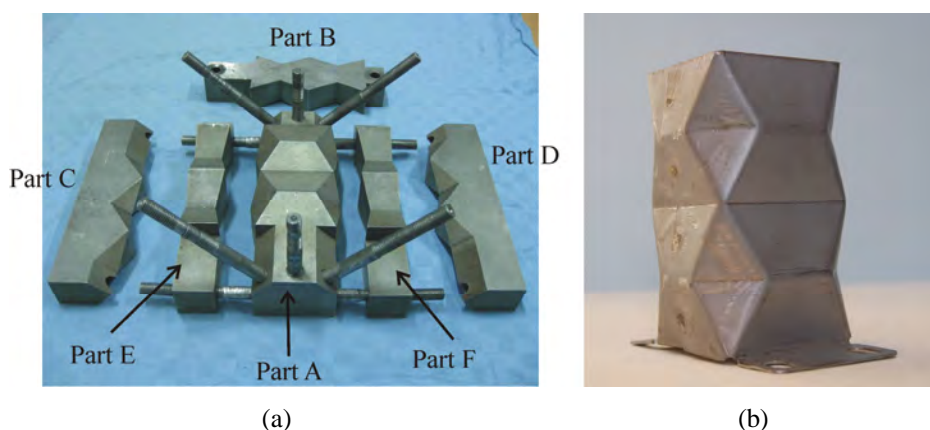


Fig. 5.11 (a) Steel moulds, and (b) prototype origami tube.

This manufacturing approach can also be used to produce origami tubes with other profiles which also have a developable surface. Therefore it can be taken as a universal

solution to the fabrication of the origami tube. In addition, since this approach is similar to that used in industry, the manufacturing cost of the origami tube is also comparable to that of conventional ones with dents.

### 5.3 Summary

Both theoretical and experimental research on the novel origami tube proposed in Chapter 4 has been presented in this chapter.

In the theoretical part, a basic folding element has been developed to describe the folding process of square origami tubes. Three main sources of energy absorption in the basic folding element have been identified and the energy absorption from each source has been calculated. Applying the balance between external work and internal plastic deformation energy, a simple mathematical formula of the mean crushing force including only tube geometry and material mechanical properties has been derived. A reasonable agreement between theoretical prediction of the mean crushing force and numerical data is observed. Furthermore, although the formula is derived for square origami tubes, it can also be used to give a rough estimate of the mean crushing forces of rectangular or tapered origami tubes.

In the experimental part, the following work has been conducted.

First, a simple manufacturing approach has been developed to construct square origami tubes and quasi-static axial crushing tests have been conducted. In spite of the relatively low quality of the tube samples because of the crude manufacturing approach, the complete diamond mode is still observed from the experiments. In addition, both peak force reduction and mean crushing force increase are achieved in comparison with those of conventional square tubes. The experimental results demonstrate the usefulness of the origami pattern in triggering the complete diamond mode. It is also

indicated that the complete diamond mode triggered by the origami pattern is quite robust and not very sensitive to geometric imperfection and local material variation.

Second, the finite element modelling approach developed in Chapter 4 has been reapplied to simulate the axial crushing tests. A good overall agreement between the numerical results and the experimental results in terms of failure mode and mean crushing force is achieved.

Finally, a refined manufacturing approach has been developed to construct relatively thick square origami tubes of high quality. A set of moulds has been designed to gradually fold a sheet of material with thickness up to 2 mm into a half-tube. High quality prototypes have been constructed using the refined manufacturing approach, demonstrating that the seemingly geometrically complicated origami tube can be produced at a cost comparable to that of commercial energy absorption devices. Due to the fact that all of the origami tubes are made of developable surface, this approach can be regarded as a universal solution for the construction of origami tubes with various profiles.

To this point, the design and analysis of the origami tube subjected to quasi-static axial crushing have been completed.

## CHAPTER 6

# THE ORIGAMI BEAM

Thin-walled beams are another type of commonly used structural form for energy absorption devices. Practical applications include automobile bumper beams and the beam components of roll-over and falling object protective structures (ROPS and FOPS). A typical failure mode of thin-walled beams subjected to lateral loading is the forming of localized plastic hinges along the beam. The lateral bending collapse mode of thin-walled beams is not as efficient as the axial folding mode of thin-walled tubes in terms of energy absorption because large plastic deformation concentrates near those plastic hinges whereas the rest of the beam undergoes only small deformation.

The focus here is curved beams which are commonly used in automobile bumpers. Inspired by the origami tube, the origami technique is also applied to beams to alter their failure mode. A failure mode involving extensive plastic deformation along the entire beam instead of only in the neighbourhood of localized plastic hinges could be desirable from the perspective of energy absorption. Particularly, in the case of curved beams, if some sort of longitudinal folding of beam walls can be induced during the lateral bending collapse, high energy absorption might be attained.

Two requirements are to be satisfied in order to realize this objective. First, longitudinal folding deformation of curved beams needs to be made to as easy as lateral bending so that it would occur during the crushing process. Second, an efficient longitudinal folding mode in terms of energy absorption needs to be induced so that a

large amount of energy can be absorbed. As the novel origami patterns presented in Chapter 4 are able to trigger an efficient failure mode in terms of energy absorption in a thin-walled tube subjected to axial compression, high energy absorption can be achieved if the same can be transplanted to curved beams.

In this chapter a type of curved beam with an origami pattern on the surface, known as the *origami beam*, is presented. The geometry of the origami pattern which is slightly different from those in Chapter 4 is first introduced in Section 6.1. Subsequently in Section 6.2 a series of origami beams with various configurations are designed and analyzed using finite element modelling approach. The numerical results are presented and discussed in Section 6.3. A summary is given in Section 6.4.

## 6.1 Origami Pattern Geometry

A module of the origami pattern for curved thin-walled beams is shown in Fig. 6.1. It can be seen that the pattern is very similar in shape to that for square origami tubes. Because of the curved profile of the beams to which the pattern is applied, however, the surface of the pattern has to be adjusted and therefore is no longer developable. Note that this undesirable property of nondevelopable surface is not caused by the pattern since the surface of a conventional curved beam is also not developable. Without the restriction of developable surface, there is much greater flexibility in the design of the pattern. However, different pattern designs lead to different levels of material in-plane stretching during the forming process if an origami beam is to be manufactured through stamping out of a conventional curved beam.

The pattern geometry is as follows. For an origami module with cross section length  $a$  and width  $b$ , radius of curvature  $R_b$ , and module length  $l$ , five geometric parameters, i.e., dihedral angle  $2\theta$  and crease lengths  $d_1$ ,  $d_2$ ,  $d_3$ , and  $d_4$ , shown in Fig. 6.1, are used to describe its configuration. Note that  $d_1$ ,  $d_2$ ,  $d_3$ , and  $d_4$  are related to  $a$ ,  $b$ ,  $R_b$ ,  $l$ , and  $2\theta$  through the following equations



$$d_1 = a - \frac{(\sqrt{2} + 1)(R_b + b/2)l}{R_b \tan \theta} \quad (6.1)$$

$$d_2 = a - \frac{(\sqrt{2} + 1)(R_b - b/2)l}{R_b \tan \theta} \quad (6.2)$$

$$d_3 = \frac{b}{2} - \frac{(\sqrt{2} + 1)(R_b + b/2)l}{2R_b \tan \theta} \quad (6.3)$$

$$d_4 = \frac{b}{2} - \frac{(\sqrt{2} + 1)(R_b - b/2)l}{2R_b \tan \theta} \quad (6.4)$$

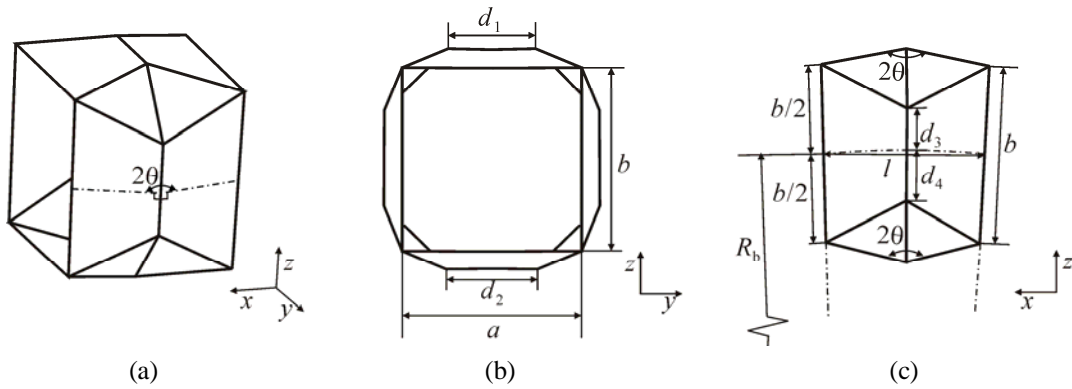


Fig. 6.1 A module of the origami pattern for curved thin-walled beams. (a) Perspective view, (b) projection on  $y$ - $z$  plane, and (c) projection on  $x$ - $z$  plane.

Among all of the geometric parameters, only five of them, e.g.,  $a$ ,  $b$ ,  $R_b$ ,  $l$ , and  $2\theta$ , are independent. Should a square cross section be used, the number of independent geometric parameters can be further reduced to four because  $a = b$ .

## 6.2 Numerical Modelling

### 6.2.1 Arrangement of origami modules

A series of square-sectional curved beams, including one conventional beam and fourteen origami ones, were designed to investigate the failure mode and energy

absorption properties of the origami beam. The conventional beam P0, shown in Fig. 6.2, had the profile of an arc with the following geometry: beam length  $L_b = 776.8$  mm, radius of curvature  $R_b = 1592$  mm, cross section width  $b = 60$  mm, wall thickness  $t = 2.0$  mm.

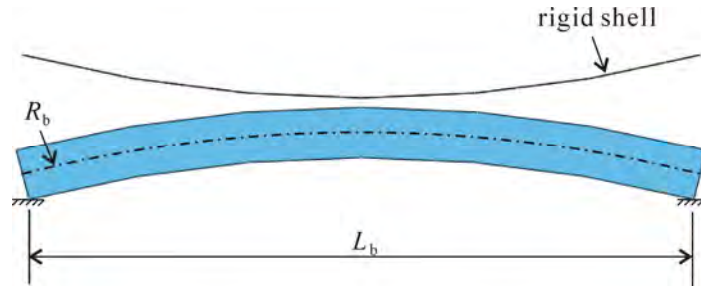


Fig. 6.2 Configuration and loading scenario of P0.

Fourteen origami beams, all of which had identical  $L_b$ ,  $R_b$ ,  $b$ , and  $t$  with those of P0, were also built. The beam was divided into  $M$  equal modules, each of which could be an origami module or one without origami pattern. Beams P1\_1, P2\_1, P3\_1 - P3\_5, and P4\_1 had origami modules along the entire length, whereas beams P1\_2 - P1\_7, on the other hand, had only a few origami modules. The arrangement of origami modules on these six beams are depicted through the schematic diagrams shown in Fig. 6.3. In the diagrams, a box denotes an origami module, and a line denotes a group of modules without pattern the number of which is specified by the figure below the line. Since a group of modules without pattern is actually a conventional beam segment, non-integral figures are also permissible. The arrangement of origami modules was considered for the reason that unlike the origami tube, the origami beam was expected to undergo relatively small longitudinal folding deformation, and thus it might not be the most effective way to place origami modules along the entire beam. Parameters  $l$  and  $2\theta$  were varied among the origami beams to investigate the effect of pattern geometry. The configurations of the beams are listed in Table 6.1 where  $S$  denotes the surface area of a beam.

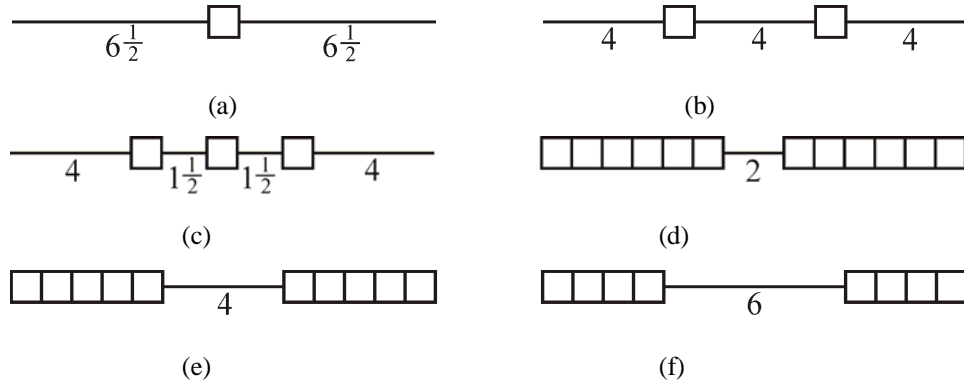


Fig. 6.3 Arrangements of origami modules on (a) P1\_2, (b) P1\_3, (c) P1\_4, (d) P1\_5, (e) P1\_6, and (f) P1\_7.

Table 6.1 Configurations of the beams and numerical results.

Model	$2\theta$ ( $^{\circ}$ )	$l$ (mm)	$M$	$S$ ( $10^5 \text{mm}^2$ )	$P_{\max}$ (kN)	$P_{\max}$ reduction	$P_m$ (kN)	$NSEA$
P0	-	-		1.920	23.82	-	14.91	1
P1_1	156	57.15	14	1.963	20.16	15.4%	16.21	1.063
P1_2	156	57.15	14	1.923	20.56	13.7%	11.58	0.775
P1_3	156	57.15	14	1.926	23.64	0.8%	16.28	1.088
P1_4	156	57.15	14	1.929	20.40	14.4%	12.21	0.815
P1_5	156	57.15	14	1.957	18.77	21.2%	16.29	1.072
P1_6	156	57.15	14	1.951	21.34	10.4%	17.06	1.126
P1_7	156	57.15	14	1.945	21.62	9.2%	15.37	1.018
P2_1	164	57.15	14	1.939	20.30	14.8%	17.41	1.156
P3_1	168	57.15	14	1.931	21.01	11.8%	17.99	1.200
P3_2	168	44.44	18	1.930	23.17	2.7%	18.55	1.238
P3_3	168	50.00	16	1.930	20.75	12.9%	18.52	1.236
P3_4	168	66.66	12	1.930	21.69	8.9%	17.93	1.196
P3_5	168	79.99	10	1.930	21.98	7.7%	16.21	1.082
P4_1	170	57.15	14	1.936	21.68	9.0%	16.28	1.083

Furthermore, considering that the surface areas of the beams are not identical due to varying pattern geometries, the mean crushing force cannot be directly used to compare their energy absorption capabilities. Therefore a weighted factor known as the

normalized specific energy absorption (*NSEA*) is introduced in the analysis, which is calculated by the following equation

$$NSEA_i = \frac{P_{m,i}S_0}{P_{m,0}S_i} \quad (6.5)$$

where  $NSEA_i$ ,  $P_{m,i}$ , and  $S_i$  are the normalized specific energy absorption, mean crushing force, and surface area of beam  $i$ , respectively, and  $P_{m,0}$  and  $S_0$  are the mean crushing force and surface area of  $P_0$ , respectively.

### 6.2.2 Finite element modelling

Abaqus/Explicit (SIMULIA Corp., USA) was adopted to simulate the quasi-static crushing of the beam. The crushing scenario was modelled as a rigid shell moving downward to crumple the beam. The rigid shell, shown in Fig. 6.2, had identical radius of curvature with that of the beam. Due to the symmetry of beam geometry and loading condition, only a half of the beam was modelled to reduce computational time. Four node shell elements S4R were mainly employed to mesh the beam, supplemented by a few triangular elements to avoid excessively small or distorted elements. The lower edge of each end of the beam was clamped as shown in Fig. 6.2, and the longitudinal edges of the beam on the plane of symmetry were subjected to symmetric boundary conditions. All the degrees of freedom of the rigid shell were constrained except for the translational one in the vertical direction. Prescribed downward displacement of 75 mm was assigned to the free translational degree of freedom of the rigid shell, and smooth magnitude built in Abaqus (SIMULIA Corp., USA) was applied to control the loading rate. Self-contact was defined to model the contact among different parts of the beam, whereas surface-to-surface contact was adopted to model the contact between the beam and the rigid shell. Friction was considered for both types of contacts and the friction coefficient  $\mu$  was chosen as 0.25.

Mild steel used in Chapter 4 was applied in the numerical simulations. The mechanical properties are:  $\rho = 7800 \text{ Kg/m}^3$ ,  $E = 210 \text{ GPa}$ ,  $\sigma_y = 200 \text{ MPa}$ ,  $\sigma_u = 400 \text{ MPa}$ ,  $\varepsilon_u = 20.0\%$ ,  $\nu = 0.3$ , and  $n = 0.34$ .

Convergence tests with respect to mesh density and analysis time, respectively, were conducted on Beam P1\_1 prior to the analysis. It was found that a global mesh size of 2 mm and an analysis time of 0.08s were able to yield satisfactory results.

## 6.3 Results and Discussions

### 6.3.1 Crushing of conventional beam

The conventional beam P0, chosen as a baseline to assess the performance improvement of the origami beam, is first analyzed. Numerical simulation results show that P0 fails in the typical lateral bending collapse mode. It can be seen from Fig. 6.4(a) that as the beam is being crushed, local buckling first occurs in the mid-span of the beam where the bending moment is at the maximum, followed by the forming of a localized plastic hinge. Subsequently, the beam segments on the left hand side and the right hand side rotate about the plastic hinge up to the completion of the crushing process.

The force vs displacement curve of the beam is plotted in Fig. 6.5. It can be seen that a high peak force appears at the beginning of the crushing and is followed by a steady drop. Subsequently the force rises again as the plastic hinge is squeezed until the crushing process ends. The numerical results indicate that more than 50% of the energy absorption of the beam comes from the neighbourhood of the plastic hinge. This high degree of concentration is also reflected from the Mises stress contour plots in Fig. 6.4(a) which clearly show that the stress level is among the highest in the vicinity of the plastic hinge.

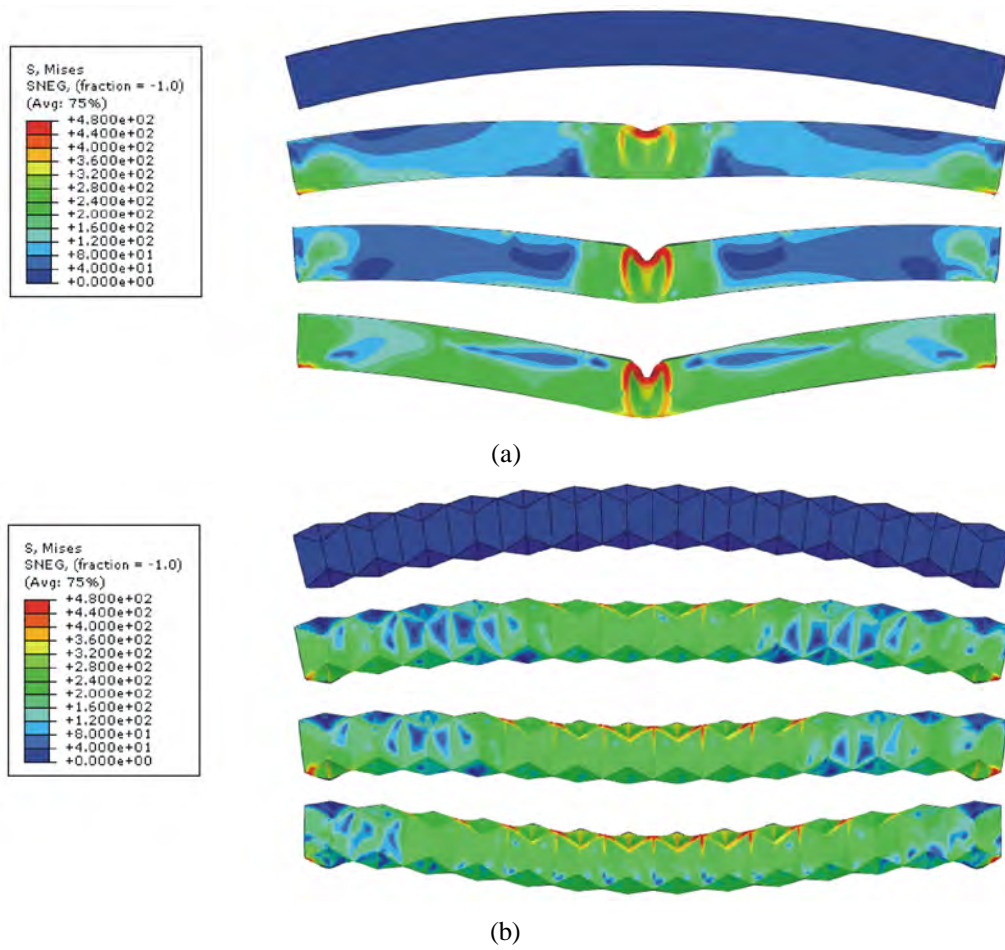


Fig. 6.4 Crushing processes of (a) P0, and (b) P1\_1.

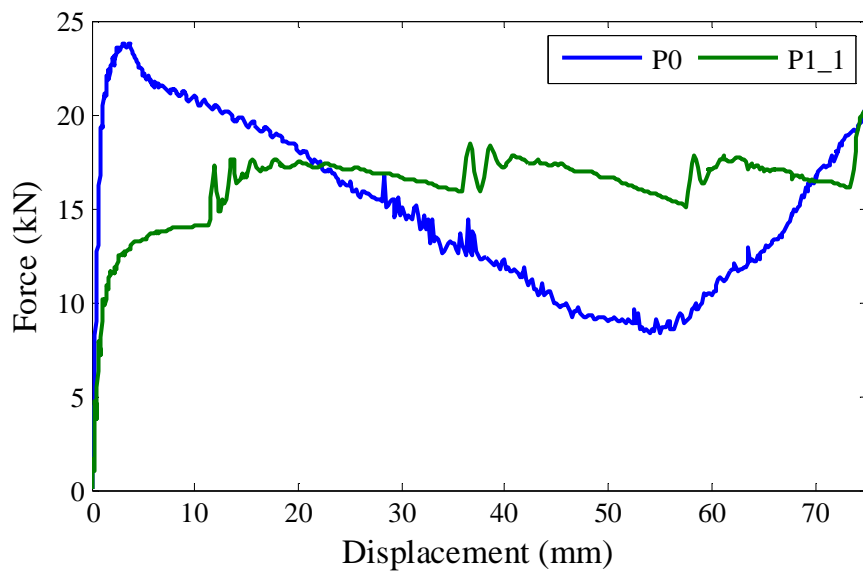


Fig. 6.5 Force-displacement curves of P0 and P1\_1.

### 6.3.2 Crushing of origami beam

The crushing process of origami beam P1\_1 which has origami modules along the entire length is presented in Fig. 6.4(b) as a representative. It can be seen that P1\_1 has a failure mode clearly different from that of P0. First of all, no localized plastic hinge is formed in the beam. Instead, plastic deformation is distributed along the entire beam. Furthermore, folding of beam walls in the longitudinal direction occurs during the crushing process. Specifically, the longitudinal length of the beam undergoes a process of shortening followed by elongation, which is realized mainly through the axial folding and unfolding of the origami modules. Due to the relatively small curvature of the beam, nevertheless, the longitudinal folding of beam walls is not as pronounced as the folding of the origami tube. This new failure mode is referred to as the *longitudinal folding mode*. A qualitative explanation of the occurrence of this new failure mode is as follows. A beam without pattern is rather stiff longitudinally, allowing little deformation, and therefore it can only fail through the forming of a localized plastic hinge. The origami pattern, however, makes it easier for the beam to deform in the longitudinal direction. As a result, longitudinal folding of beam walls occurs at the beginning of the crushing process, which in turn prevents any localized plastic hinge from being formed, leading to the new failure mode with globally distributed deformation.

The force vs displacement curve of P1\_1 is also plotted in Fig. 6.5. A quite smooth curve is obtained, which is a desirable feature as it means that the energy dissipation rate is rather stable. The numerical results presented in Table 6.1 show that compared with those of P0, P1\_1 achieves a  $P_{\max}$  reduction of 15.4% and a *NSEA* increase of 6.3%. Therefore while confirming that the longitudinal folding mode is more efficient in terms of energy absorption than the lateral bending collapse mode, these results suggest that further optimization of pattern geometry is required to obtain substantial energy absorption improvement.

### 6.3.3 The dihedral angle

The numerical analysis of P1\_1 shows that a new failure mode featuring longitudinal folding of beam walls can be successfully triggered by the origami pattern, but the energy absorption improvement is only marginal. One method of enhancing the energy absorption of the origami beam is to make it more difficult for the beam walls to be folded, which can be realized by choosing a larger dihedral angle  $2\theta$  so that the beam is folded less initially.

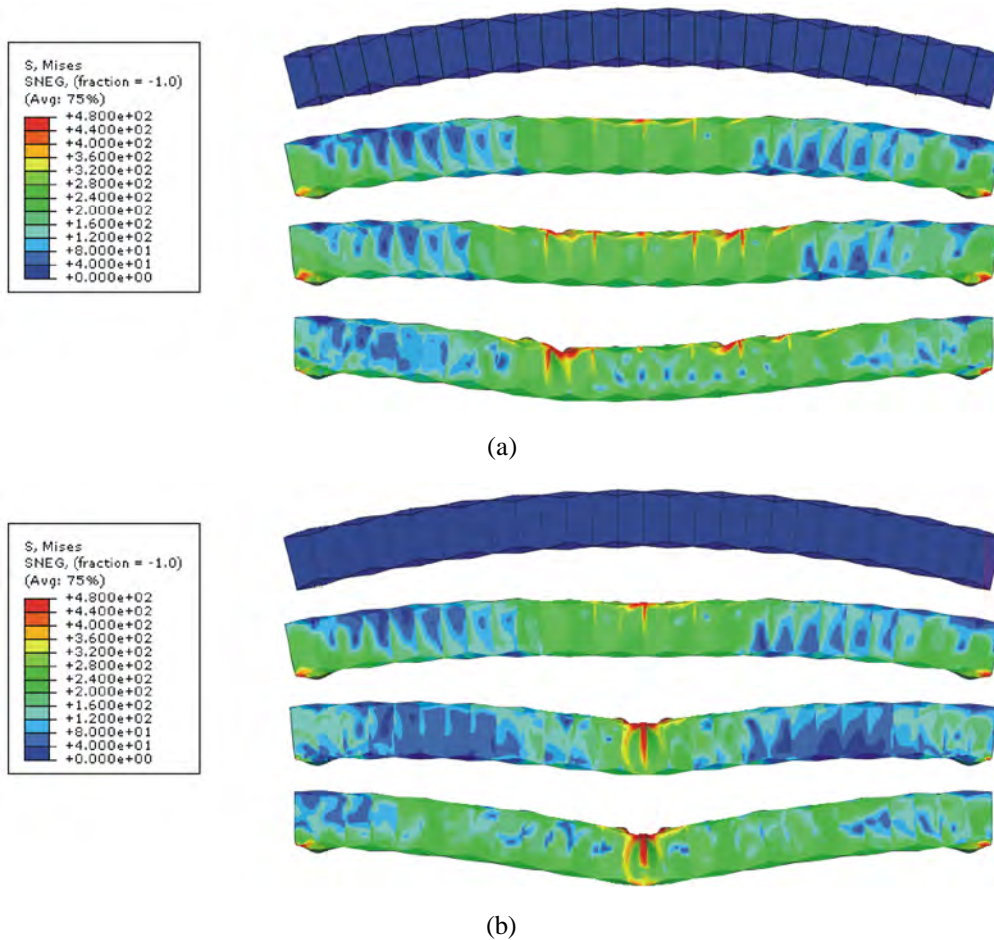


Fig. 6.6 Crushing processes of (a) P3\_1, and (b) P4\_1.

Three beams, P2\_1, P3\_1, and P4\_1, which have identical  $M$  with P1\_1 but monotonically increasing  $2\theta$ , are analyzed. Two types of failure modes are observed from the numerical simulations. When  $2\theta$  is relatively small, P2\_1 and P3\_1 show failure modes similar to that of P1\_1. Only the crushing process of P3\_1 is shown in



Fig. 6.6(a). In addition, comparison of the failure modes of P1\_1 and P3\_1 reveals that as  $2\theta$  increases, the deformation becomes less uniform along the beam. For instance, the sixth module of P3\_1 from left to right undergoes much larger deformation than the others at the end of the crushing, whereas no such noticeable deformation concentration is observed in P1\_1. When  $2\theta$  increases further, however, the crushing process of P4\_1, Fig. 6.6(b), shows that longitudinal folding of beam walls is no longer obvious and a localized plastic hinge is clearly formed in the mid-span of the beam. As a result, the failure mode of P4\_1 returns to the lateral bending collapse mode. This is understandable because when  $2\theta$  reaches a certain value, folding along the pattern is no longer easier than forming a localized plastic hinge, and consequently the origami beam reduces back to a conventional beam.

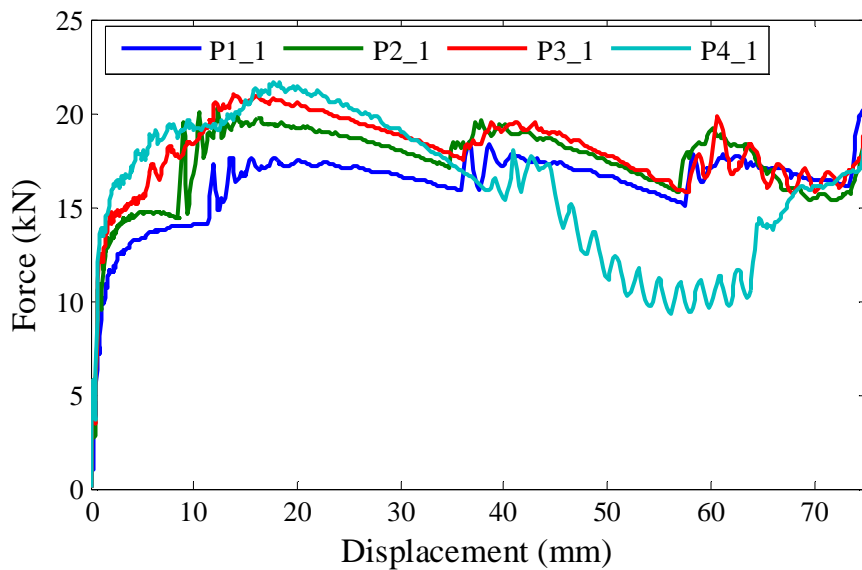


Fig. 6.7 Force vs displacement curves of P1\_1, P2\_1, P3\_1, and P4\_1.

The force vs displacement curves of P2\_1, P3\_1, and P4\_1 are plotted along with that of P1\_1 in Fig. 6.7. Two observations can be made from the curves. First of all, for P1\_1, P2\_1 and P3\_1 which show similar failure modes, the overall force is elevated as  $2\theta$  becomes larger, indicating that increasing  $2\theta$  is successful in making longitudinal folding of the origami beam consume more energy. The side effect of a large  $2\theta$ , however, is that the curve is less smooth because of the increasingly non-uniform deformation in the beam. Secondly, the curve of P4\_1 is similar to that of P0

in shape, both of which feature an obvious force drop, although  $P_{\max}$  of P4\_1 is still slightly reduced by the origami modules.

Table 6.1 gives  $P_{\max}$ ,  $P_m$ , and  $NSEA$  of each beam. It is shown that  $P_{\max}$  increases monotonically with  $2\theta$ .  $NSEA$ , on the other hand, initially increases with  $2\theta$  and subsequently drops when the longitudinal folding mode fails to be triggered.  $NSEA$  increase of P3\_1 can reach as much as 20.0%, while  $P_{\max}$  is still reduced by 11.8%, which indicates that adjusting  $2\theta$  is effective at improving the energy absorption of the origami beam.

### 6.3.4 The number of modules

The number of modules  $M$  is another parameter that can be varied in the design of the origami beam with origami modules along the entire length. From the perspective of manufacturing, it is desirable to have as few modules as possible in order to keep the beam geometry simple. On the other hand, a small number of modules might not be able to trigger the desired longitudinal folding mode. Therefore a suitable value of  $M$  needs to be chosen to balance the mutually contradicting requirements of simple geometry and high energy absorption.

Four origami beams, P3\_2 - P3\_5, which possess identical  $2\theta$  with that in P3\_1 but have 18, 16, 12, and 10 origami modules along the entire length, respectively, are analyzed. Figure 6.8 presents the crushed configurations of P3\_2, P3\_3, and P3\_4. It can be seen that all of the three beams collapse in the longitudinal folding mode. When  $M$  reduces to 10, however, the crushing process of P3\_5, Fig. 6.9, shows that a localized plastic hinge is formed at the mid-span of the beam, and the lateral bending collapse mode is finally obtained.

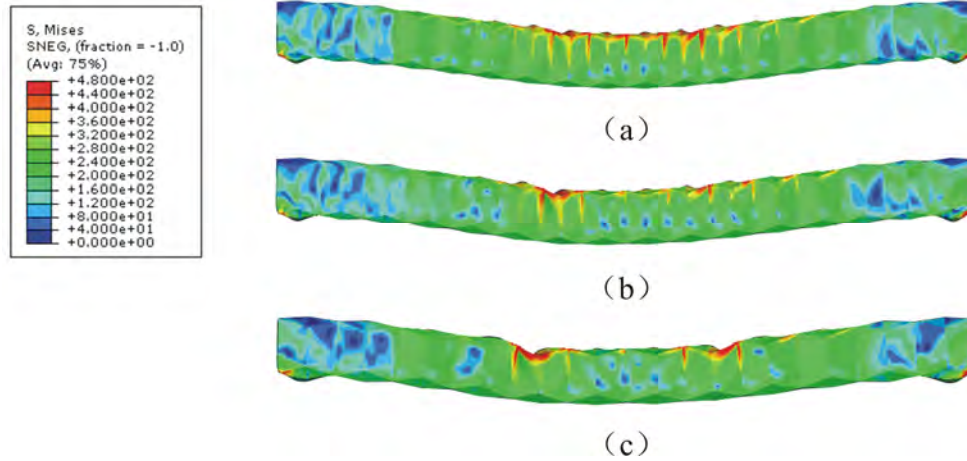


Fig. 6.8 Crushed configurations of (a) P3\_2, (b) P3\_3, and (c) P3\_4.

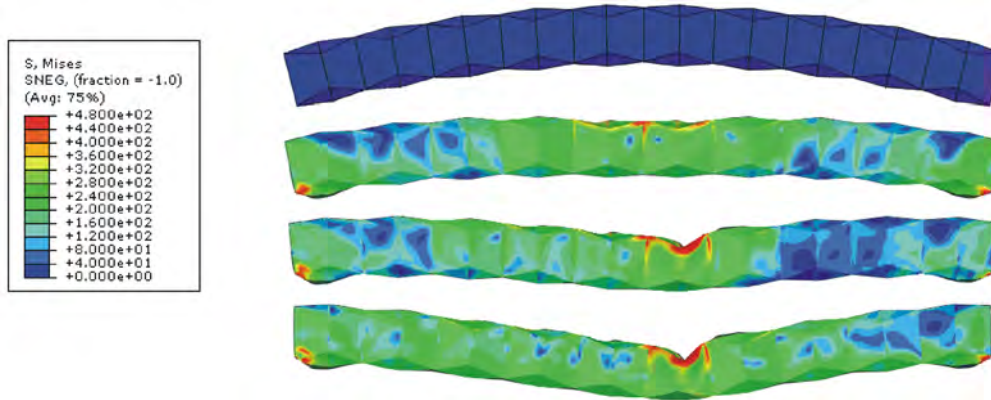


Fig. 6.9 Crushing process of P3\_5.

The force vs displacement curves of the four beams as well as P3\_1 are plotted in Fig. 6.10. The curves of P3\_1 - P3\_4 are found to have similar shapes, whereas that of P3\_5 shows large magnitude fluctuation as in the case of P0.  $P_{\max}$ ,  $P_m$ , and  $NSEA$  of each beam are given in Table 6.1. It can be seen that  $NSEA$  of P3\_5 is the lowest among the five beams. In cases where the longitudinal folding mode is successfully triggered,  $NSEA$  increases with  $M$ , but the effectiveness of using a large  $M$  to improve the energy absorption seems only moderate since  $NSEA$  difference between P3\_2 with  $M = 18$  and P3\_4 with  $M = 12$  is not substantial. In addition, the energy absorption of the origami beam can eventually saturate when  $M$  takes a relatively large value, for  $NSEA$  of P3\_2 with  $M = 18$  is very close to that of P3\_3 with  $M = 16$ .

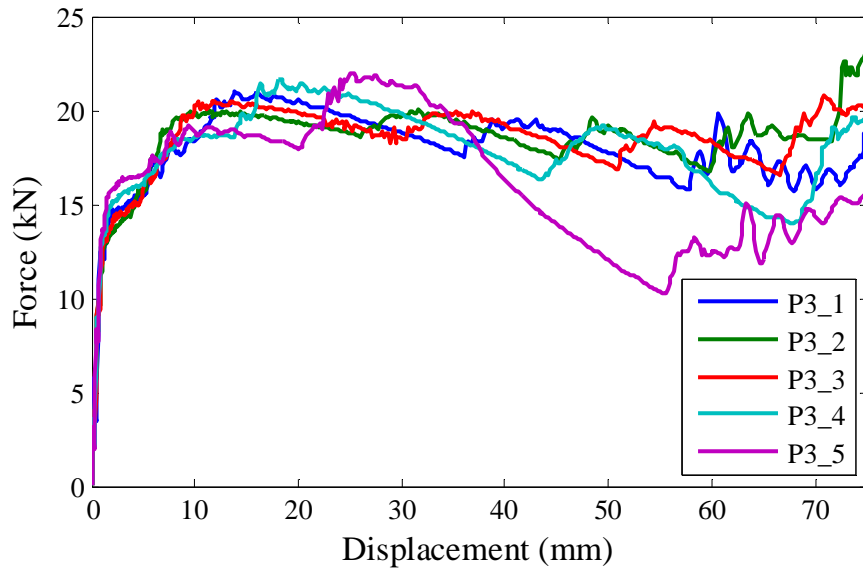


Fig. 6.10 Force vs displacement curves of P3\_1 - P3\_5.

### 6.3.5 Arrangement of origami modules

First of all, three origami beams, P1\_2, P1\_3, and P1\_4, which have one, two, and three origami modules discretely placed in the beam, respectively, are analyzed. The crushed configurations of the three beams are given in Fig. 6.11. All of the three beams fail in the lateral bending collapse mode with a localized plastic hinge in the middle of the beam, regardless of whether an origami module is placed there. The origami module in the mid-span of the beam, as in the cases of P1\_2 and P1\_4, only slightly affects the configuration of the plastic hinge.

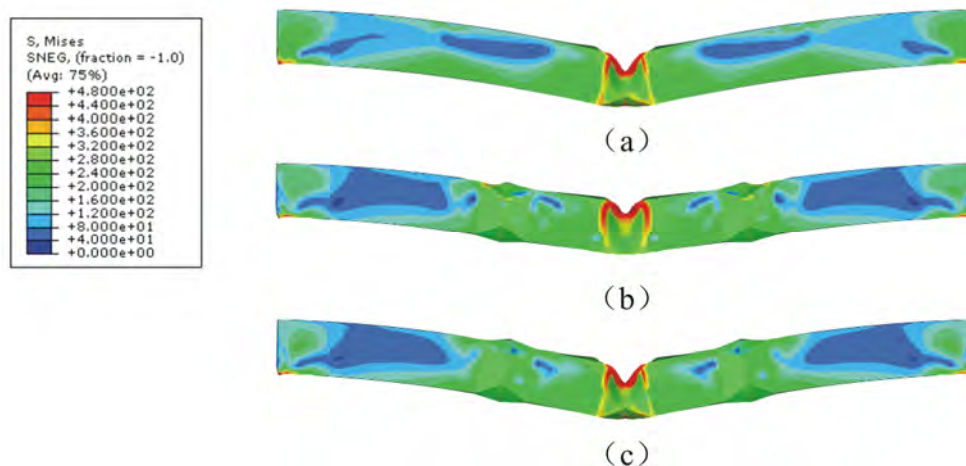


Fig. 6.11 Crushed configurations of (a) P1\_2, (b) P1\_3, and (c) P1\_4.

The force vs displacement curves of the three beams are plotted in Fig. 6.12. All of the three curves are similar in shape to that of the conventional beam P0. The curves of P1\_2 and P1\_4 with an origami module in the mid-span are below that of P1\_3. The numerical results given in Table 6.1 show that both P1\_2 and P1\_4 have lower *NSEA* than that of P0, which implies that the origami module actually compromises the energy absorption capability of the localized plastic hinge. *NSEA* of P1\_3, on the other hand, is 8.8% higher than that of P0, suggesting that even two origami modules in the beam can help to induce some longitudinal folding deformation and thus increase the energy absorption.

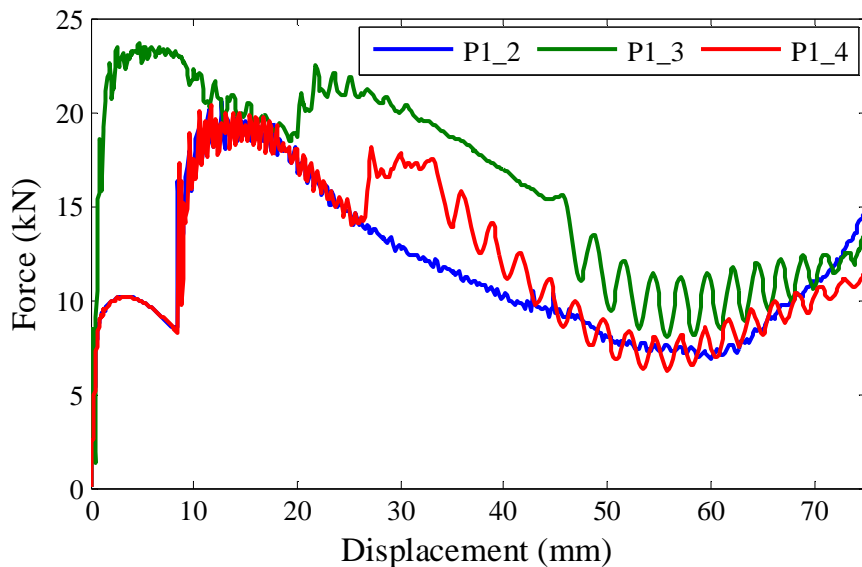


Fig. 6.12 Force vs displacement curves of P1\_2, P1\_3, and P1\_4.

Now let us examine the scenario when both a plastic hinge and longitudinal folding of beam walls occur together. It is conjectured that it may lead to high energy absorption. To achieve this goal, a suitable arrangement of origami modules and modules without pattern needs to be worked out. Having known that an origami module in the middle of a beam actually impairs the energy absorption, it is desirable to place origami modules near the two ends in a beam and modules without pattern in the middle.

Three origami beams, P1\_5, P1\_6, and P1\_7, which have identical pattern geometry with that of P1\_1 but increasing number of modules without pattern, are analyzed.

Numerical results show that by appropriately choosing the number of modules without pattern in the middle of a beam, both a localized plastic hinge and longitudinal folding of the beam can be formed. The crushing process of P1\_6 which contains this new failure mode is shown in Fig. 6.13. At the early stage of the crushing, an obvious sign of longitudinal folding is observed, which is supported by the relatively uniform stress distribution along the beam. As P1\_6 is deformed further, a localized plastic hinge is formed in the middle of the beam and is continuously bent up to the end of the crushing process. This new failure mode is referred to as the *mixed mode*. When the number of modules without pattern is too small, it can be seen from the crushed configuration of P1\_5, Fig. 6.14(a), that although longitudinal folding deformation is still maintained, no localized plastic hinge is formed in the middle of the beam where no origami module is placed. When, on the other hand, the number of modules without pattern is too large, as can be seen from the crushed configuration of P1\_7 in Fig. 6.14(b), the central plastic hinge dominates the crushing process. Therefore the key of the origami beam design seems to achieve a balanced energy absorption between plastic hinge bending and beam walls folding. This can be realized by varying the number of the two types of modules.

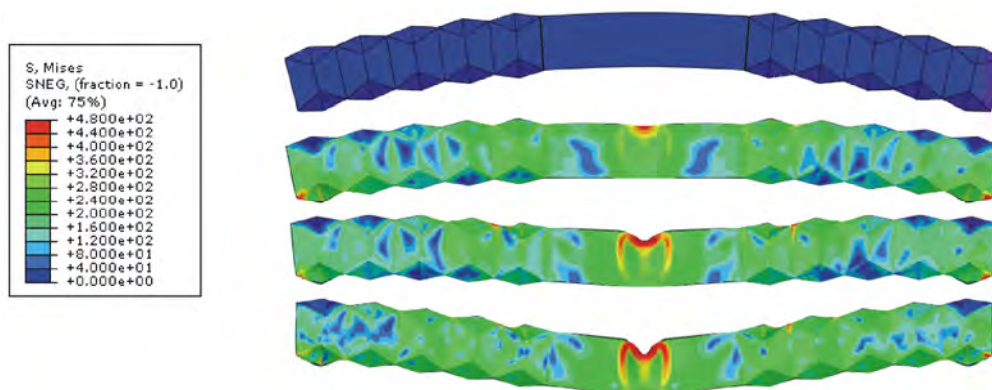


Fig. 6.13 Crushing process of P1\_6.

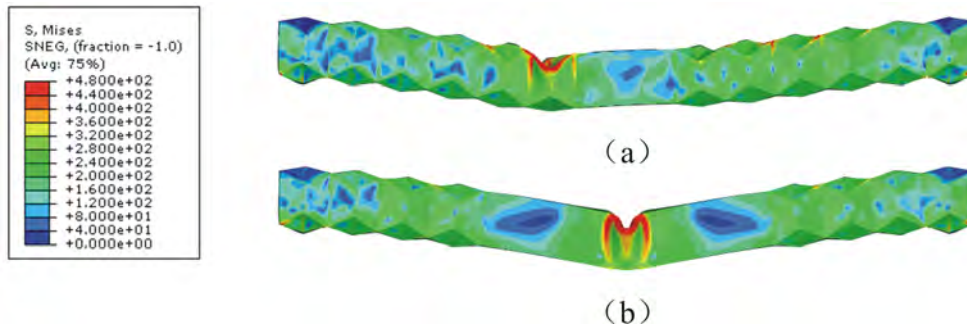


Fig. 6.14 Crushed configurations of (a) P1\_5, and (b) P1\_7.

The force vs displacement curves of the three beams together with P1\_1 are plotted in Fig. 6.15. A transition in curve shape from being relatively smooth to featuring an obvious force drop can be clearly observed from the figure. The numerical data in Table 6.1 show that *NSEA* of P1\_6, which fails in the mixed mode, is the highest among the four beams. These results suggest that the mixed mode is the most efficient in terms of energy absorption among the three main failure modes that have been investigated so far.

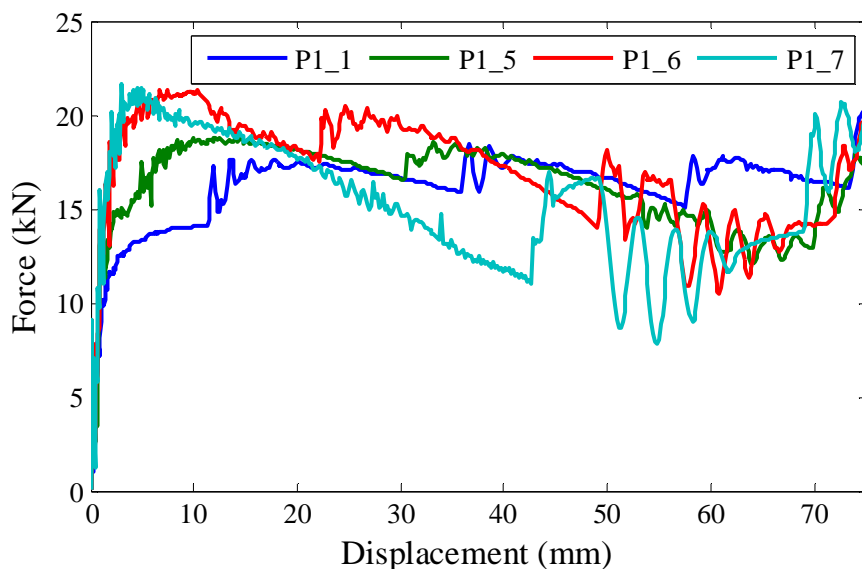


Fig. 6.15 Force vs displacement curves of P1\_1, P1\_5, P1\_6, and P1\_7.

## 6.4 Summary

The failure modes and energy absorption capabilities of a series of curved origami beams subjected to quasi-static lateral crushing have been studied numerically in this chapter. A modified version of the origami patterns developed in Chapter 4 has been applied on curved thin-walled beams to trigger more efficient failure modes in terms of energy absorption than the lateral bending collapse mode typical of conventional curved beams.

Numerical simulation has demonstrated that two new failure modes, namely, the longitudinal folding mode and the mixed mode, can be triggered in the origami beam. If origami modules are placed along the entire length of a beam, the longitudinal folding mode which features folding of beam walls in the longitudinal direction can be obtained provided that the pattern geometry is properly designed. The effects of dihedral angle and number of modules on the failure mode and energy absorption of the origami beam have been investigated. A *NSEA* increase of as much as 23.6% can be achieved, whilst a peak force reduction by 12.9% is also obtained in the same beam.

If, on the other hand, origami modules are placed only near both ends of a beam, the mixed mode involving both longitudinal folding of beam walls and bending of a central plastic hinge can be triggered by choosing an appropriate combination of origami modules and modules without pattern. The mixed mode is found to be most efficient in terms of energy absorption among all of the three failure modes. An origami beam collapsing in the mixed mode is geometrically simpler than one in the longitudinal folding mode and thus can be manufactured more conveniently.

For this type of geometrically complicated origami structure, manufacturing is a very important issue. Different from the origami tube, the surface of the origami beam is not developable due to the nondevelopable nature of curved beam surface. On one hand, removal of the restriction of developability allows more flexibility in the design of the origami pattern. On the other hand, the nondevelopable surface implies that material in-plane stretching is unavoidable during the forming process of the origami beam if it is to be made out of a conventional beam. In this chapter a simple pattern geometry has



been proposed as a compromise to ensure the surface area variation from a conventional beam to the corresponding origami beam being very small. It is typically below 2% as seen from Table 6.1, which indicates that only a small magnitude of material stretching would incur if the origami beam is manufactured by means of stamping the origami pattern on a conventional beam. Considering that the surface area change caused by stamping dents on the surface of thin-walled tubes is much larger than 2%, no great difficulty is expected in constructing the origami beam.

# CHAPTER 7

## THE COMPLETE BUMPER

Chapters 4, 5, and 6 showed that new failure modes that were efficient in terms of energy absorption could be triggered in thin-walled tubes and beams by pre-folding their surfaces with origami patterns. Both low peak force and high energy absorption were achieved.

Only idealized load cases have been considered so far, whereas energy absorption devices in practice are most likely to be subjected to more complex loading. How the origami structures perform under practical loading scenarios remains unclear. In fact, the analysis of structures subjected to realistic loading has been a missing element in most of the literatures on thin-walled energy absorption structures.

In this chapter the performances of the two types of origami structures subjected to practical loading are addressed through the design and analysis of a number of automobile frontal bumpers using the origami tube and the origami beam as key components. A brief introduction of automobile frontal bumpers and relevant impact tests to evaluate the performance of a bumper are first outlined in Section 7.1. Section 7.2 focuses on the design and analysis of four bumpers subjected to three impact tests. In Section 7.3 the numerical results are presented and discussed. And finally a summary is given in Section 7.4.

## 7.1 Introduction of Automobile Frontal Bumpers

The idea of crumple zone was first introduced by Mercedes-Benz engineer Béla Barényi on the 1959 Mercedes-Benz "*Fintail*"<sup>1</sup> and has since become one of the most important concepts in the area of auto safety. A typical crumple zone design is an automobile frontal bumper. It is normally composed of one cross beam and two crashcans attached on each end of the beam and is designed to deform and absorb kinetic energy during a low speed collision in order to reduce damage to the main structure of a vehicle.

A vehicle could be hit from different angles at different speeds in a real world car crash. Therefore a frontal bumper needs to pass a number of impact tests to ensure a sound all-around performance. Four main impact test standards are currently adopted to evaluate the performance of a bumper subjected to low speed impacts. In Europe, the United Nations Economic Commission for Europe (UNECE) has designed a test procedure, known as ECE 42 (UNECE, 1980), which vehicle manufacturers have to comply with. In the full overlap test, a bumper is hit by a pendulum at 4 km/h (2.5 mph). Corner tests are also conducted at 2.5 km/h (1.6 mph). In the United States, the National Highway Traffic Safety Administration (NHTSA) has established a similar test procedure for passenger cars, known as Part581 Bumper Standard (NHTSA, 1999), which includes a series of car-into-barrier tests conducted at 2.5 mph on the full-width of a bumper and at 1.5 mph on the corner of a bumper. Note that the crashcans in a bumper are usually not initiated in these low speed tests.

In addition, the Research Council for Automobile Repairs (RCAR) has developed a structural test protocol to determine the damageability and reparability features of vehicles. The test is a 40% overlap frontal impact into an angled barrier at 15 km/h (9.3 mph) (RCAR, 2006). Note that this test is currently used by the Motor Insurance Repair

---

<sup>1</sup> Source: [http://www.dpma.de/ponline/erfindergalerie/e\\_bio\\_barenyi.html](http://www.dpma.de/ponline/erfindergalerie/e_bio_barenyi.html)

Research Centre, Thatcham, U.K., to rate vehicles for insurance pricing. The counterpart of the RCAR structural test protocol in the United States is a test protocol developed by the Insurance Institute for Highway Safety (IIHS) to assess bumper designs based on how easily a vehicle can be repaired after impact (IIHS, 2009). The protocol includes a full overlap test at 10 km/h (6.2mph) and front and rear corner tests at 5 km/h (3.1mph). In these tests, both the bumper beam and the crashcans in a bumper are expected to be crushed, but the main vehicle structure is not severely damaged.

When subjected to high speed impacts, the main task of a bumper is to absorb as much kinetic energy as possible and transmit the loading to the main vehicle structure in a stable manner. The UNECE regulates bumper designs at high speed impacts through ECE 94 (UNECE, 2007). The procedure of conducting a 40% overlap frontal impact at 56 km/h (34.8 mph) is depicted in the standard. The European New Car Assessment Program (Euro NCAP) has also developed a testing procedure to evaluate the performance of a bumper subjected to high speed impacts based on ECE 94 but at 64 km/h (40 mph)<sup>2</sup>. Both the entire bumper system and the main vehicle structure are likely to undergo damage in these tests.

It can be clearly seen from the above introduction that designing an effective frontal bumper is a challenging task and requires multiple impact tests at different speeds. Therefore frontal bumpers provide an ideal platform to evaluate the performances of the two types of origami structures for two reasons. First of all, both the origami tube and the origami beam can be collectively integrated in one bumper as crashcan and cross beam, respectively. Secondly, a frontal bumper needs to be tested through a series of impact scenarios, and therefore the two types of origami structures subjected to practical complex loading conditions can be evaluated.

---

<sup>2</sup> Source: <http://www.euroncap.com/tests/frontimpact.aspx>

## 7.2 Design of Bumpers and Finite Element Modelling

### 7.2.1 Design of bumpers

A total of four bumpers were designed to investigate the performances of the origami tube, also referred to as the origami crashcan in this chapter as it is called in automobile industry, and the origami beam.

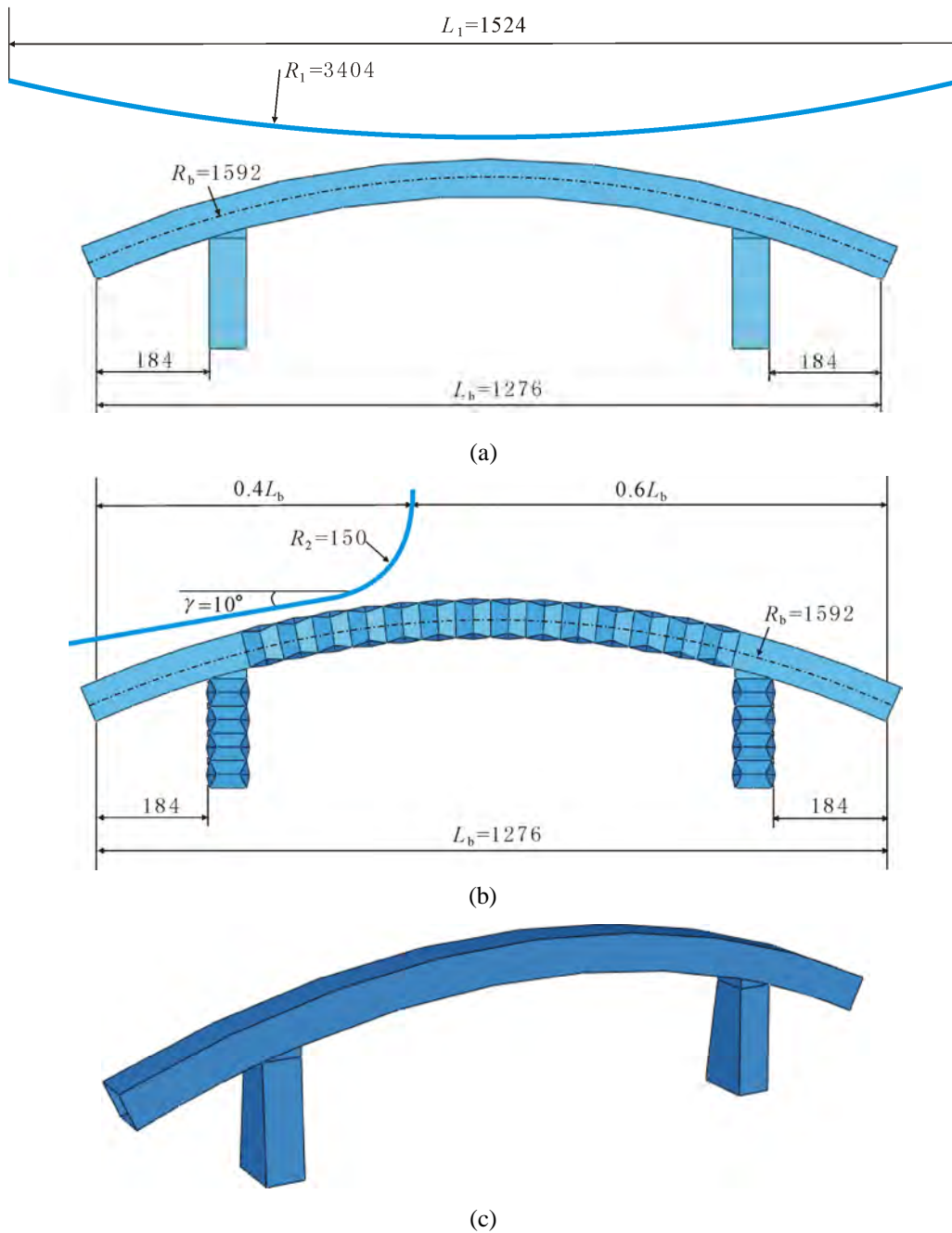


Fig. 7.1 (a) Front view of CC, (b) front view of OO, and (c) perspective view of CC.

Two cross beams, a conventional one,  $C_b$ , shown in Fig. 7.1(a), and an origami one,  $O_b$ , shown in Fig. 7.1(b), were built.  $C_b$  had the profile of a shallow curved beam with a square cross section, and  $O_b$  possessed identical overall size with that of  $C_b$  but had origami modules along the entire beam segment between two crashcans. The beam length  $L_b$ , radius of curvature  $R_b$ , cross section width  $b$ , wall thickness  $t$ , and surface area  $S$  of both beams, and the dihedral angle  $2\theta$ , module length  $l$ , and number of modules  $M$  of the origami beam are listed in Table 7.1.

The two type I tapered tubes designed in Section 4.5.5 of Chapter 4, the conventional one  $C_c$  and the origami one  $O_c$ , were adopted here as crashcans. The configurations of the two crashcans are reproduced in Table 7.2.

With all of the components being designed, four bumpers were attained by combining the cross beams and the crashcans in various ways. The relative positions of the two crashcans and the cross beam in a bumper is shown in Fig. 7.1(c). Small transitional plates were introduced between the beam and each crashcan to join them rigidly. The configurations of the bumpers are listed in Table 7.3.

Table 7.1 Configurations of the cross beams

Model	$L_b$ (mm)	$R_b$ (mm)	$b$ (mm)	$t$ (mm)	$S$ ( $10^5\text{mm}^2$ )	$2\theta$ ( $^\circ$ )	$l$ (mm)	$M$
$C_b$	1276	1592	60	2.0	3.216	-	-	-
$O_b$	1276	1592	60	2.0	3.227	168	57.15	14

Table 7.2 Configurations of the crashcans

Model	$a_1$ (mm)	$a_2$ (mm)	$b$ (mm)	$t$ (mm)	$c$ (mm)	$l$ (mm)	$M$
$C_c$	60	90	60	2.0	-	-	-
$O_c$	60	90	60	2.0	22.5	45	4

Table 7.3 Configurations of the bumpers

Model	Beam	Crashcans
CC	C <sub>b</sub>	C <sub>c</sub>
CO	C <sub>b</sub>	O <sub>c</sub>
OC	O <sub>b</sub>	C <sub>c</sub>
OO	O <sub>b</sub>	O <sub>c</sub>

### 7.2.2 Design of impact tests

It has been mentioned in Section 7.1 that a variety of impact tests are required to be conducted on a bumper to evaluate its performances under practical loading conditions. Specifically, two main impact scenarios, the full overlap impact and the 40% overlap impact, are frequently applied in low speed impacts, whereas the 40% overlap impact is mainly employed in high speed impacts. In addition, the impact speed for low speed impacts is usually below 9.3 mph, and that for high speed impacts is no larger than 40 mph. To comprehensively evaluate the performances of the bumpers, three impact tests were considered.

- The full overlap impact test at 5 m/s (11.2 mph) constant loading speed. The barrier, shown in Fig. 7.1(a), was designed based on the IIHS Bumper Test Protocol (Version VII) (IIHS, 2009) with the following geometry: barrier length  $L_1 = 1524$  mm, and radius of curvature  $R_1 = 3404$  mm.
- The 40% overlap impact test at 5 m/s constant loading speed. The barrier, shown in Fig. 7.1(b), had identical shape with that in the RCAR structural test protocol (RCAR, 2006). The geometry of the barrier was: corner radius of curvature  $R_2 = 150$  mm, and barrier angle  $\gamma = 10^\circ$ .
- The 40% overlap impact test at 20 m/s (44.7 mph) constant loading speed. The barrier design was identical to that in the 40% overlap impact test at 5 m/s.

### 7.2.3 Finite element modelling

The impact scenario was simulated as a rigid barrier moving downward to compress a bumper fixed in space. Due to the symmetry of bumper geometry and loading condition, only a half of the bumper was analyzed to reduce computational time. The rigid barrier was modelled as a rigid shell and meshed with 4-node 3D rigid quadrilateral elements R3D4. Quadrilateral shell elements with reduced integration S4R were mainly employed to mesh the bumper, supplemented by a small number of triangular elements to avoid excessively small or distorted elements. The lower ends of the two crashcans in the bumper were fixed and symmetric boundary conditions were applied to the edges of the bumper on the plane of symmetry. All of the degrees of freedom of the rigid barrier were constrained except for the translational one in the vertical direction. Downward velocity boundary condition was assigned to the free degree of freedom of the rigid barrier to control the crushing process. The final crushing distance was chosen as 250 mm in the full overlap impact tests and 200 mm in the 40% overlap impact tests. Two types of contacts were defined in the analysis: self-contact among different parts of the bumper and surface-to-surface contact between the rigid barrier and the bumper. Friction was also taken into consideration and the friction coefficient  $\mu$  was selected as 0.25 for both types of contacts.

Mild steel used in Chapters 4 and 6 was also selected as the material. The mechanical properties are:  $\rho = 7800 \text{ Kg/m}^3$ ,  $E = 210 \text{ GPa}$ ,  $\nu = 0.3$ ,  $\sigma_y = 200 \text{ MPa}$ ,  $\sigma_u = 400 \text{ MPa}$ ,  $\epsilon_u = 20.0\%$ , and  $n = 0.34$ . Material strain rate effects were considered through the Cowper-Symonds equation (2.19) in Chapter 2. The material constants  $C_r$  and  $q_r$  were chosen as  $6844 \text{ s}^{-1}$  and 3.91, respectively (Abramowicz and Jones, 1984a).

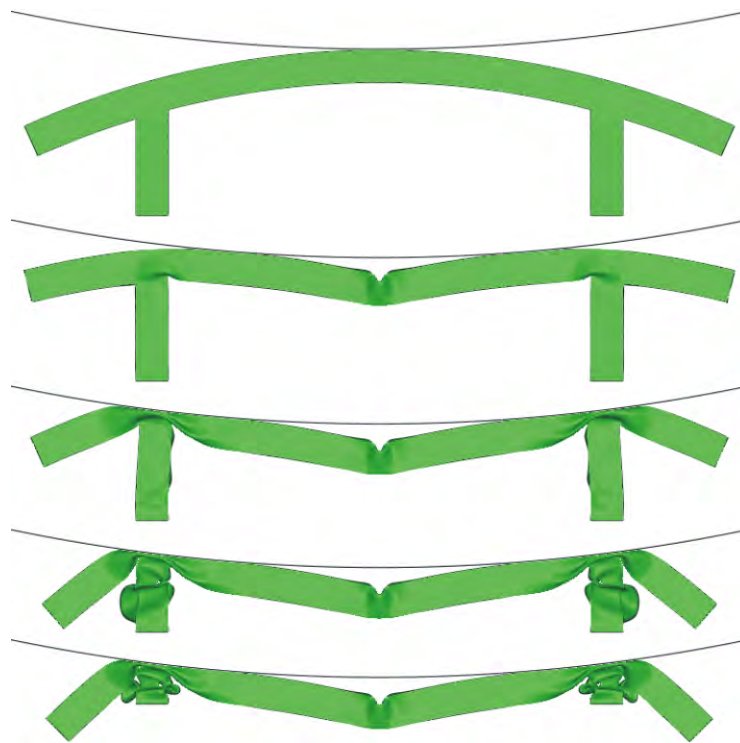
## **7.3 Results and Discussions**

### **7.3.1 Full overlap impact at 5 m/s**

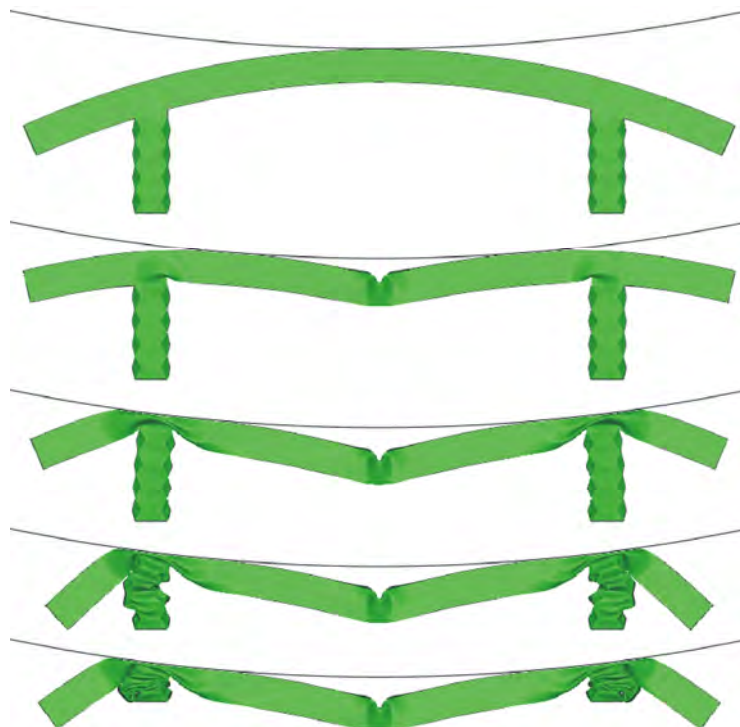
The crushing processes of the four bumpers subjected to this test are shown in Fig. 7.2, and their force vs displacement curves are plotted in Fig. 7.3. The mean crushing force,



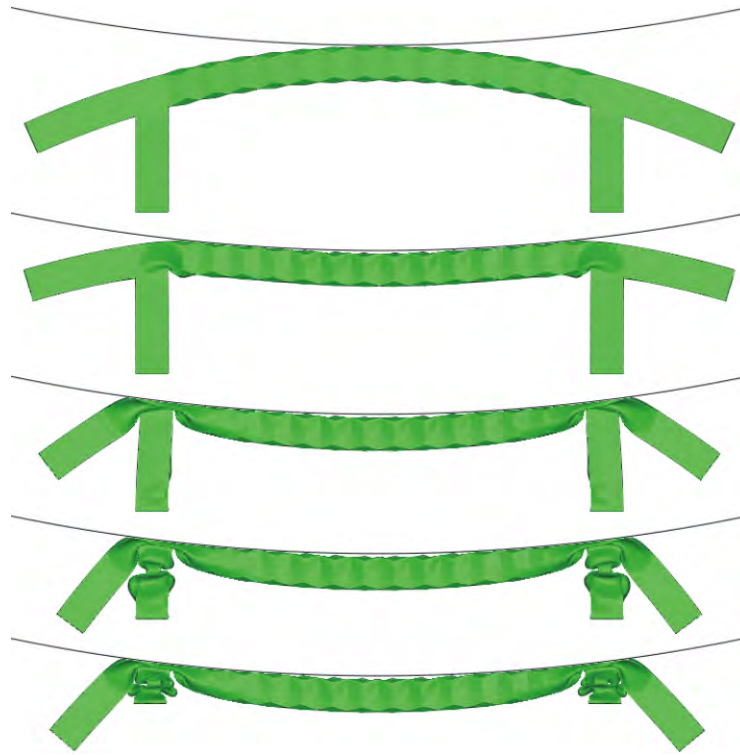
$P_m$ , energy absorption of the beam,  $E_b$ , and energy absorption of the crashcan,  $E_c$ , of the four bumpers are listed in Table 7.4.



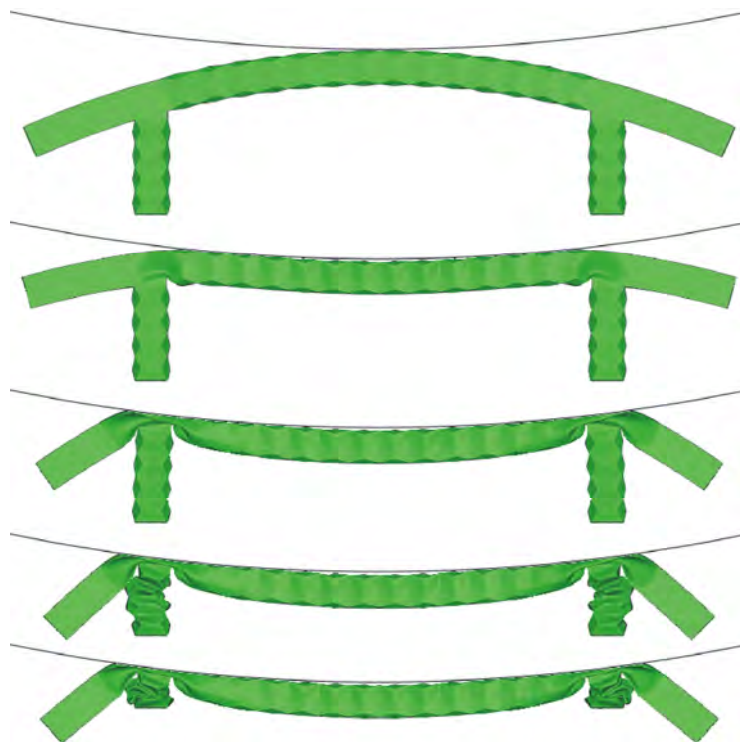
(a)



(b)



(c)



(d)

Fig. 7.2 Full overlap crushing processes at 5 m/s of (a) CC, (b) CO, (c) OC, and (d) OO.

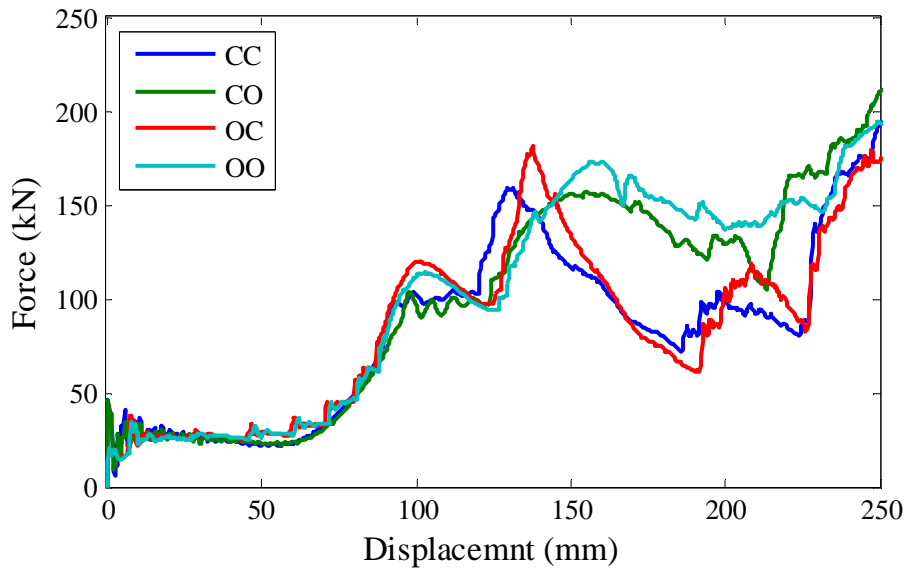


Fig. 7.3 Force vs displacement curves of the bumpers subjected to the full overlap impact at 5 m/s.

Table 7.4 Numerical results of the bumpers subjected to the full overlap impact at 5 m/s

Model	$P_m$ (kN)	$P_m$ increase	$E_b$ (kJ)	$E_b$ increase	$E_c$ (kJ)	$E_c$ increase
CC	83.21	-	7.32	-	6.30	-
CO	98.12	19.6%	7.35	0.4%	8.12	28.9%
OC	84.85	2.0%	8.04	9.8%	6.20	-1.6%
OO	102.17	23.4%	8.50	16.1%	8.11	28.7%

### 7.3.1.1 Performance of the origami crashcan

Bumpers CC and CO, consisting of an identical conventional beam but different types of crashcans, are analyzed here to investigate the performance of the origami crashcan as a bumper component. The crushing process of CC, Fig. 7.2(a), shows that the conventional beam first fails in the lateral bending collapse mode, followed by the crushing of the two conventional crashcans in the symmetric mode. Bending deformation is clearly observed in the crashcans. The crushing process of CO is shown in Fig. 7.2(b). It can be seen that the conventional beam fails in a similar way to that in CC. The two origami crashcans collapse following the patterns on their surfaces, indicating that they integrate well with the conventional beam. However, only some of

the lobes at the corners of the origami crashcans are well folded because of the large bending deformation during the crushing process, resulting in the incomplete diamond mode being formed in the end.

The force vs displacement curves of the two bumpers are plotted in Fig. 7.3. The two curves almost overlap up to the displacement of about 120 mm during which only the beams are substantially deformed, and subsequently the curve of CO rises on top of that of CC as the crashcans start to fold. The numerical results in Table 7.4 show that  $E_b$  of the two bumpers are very close to each other, which is reasonable because both beams collapse in an identical failure mode.  $E_c$  of CO, on the other hand, is 28.9% higher than that of CC, which clearly demonstrates the advantage of the origami crashcan design. Mainly because of the high energy absorption of the origami crashcans in CO,  $P_m$  of CO is increased by 19.6% compared with that of CC.

#### *7.3.1.2 Performance of the origami beam*

Bumper OC is analyzed and compared with CC, both of which consist of conventional crashcans but different types of beams, in order to investigate the performance of the origami beam as a bumper component. The crushing process of OC is shown in Fig. 7.2(c). It can be seen that the origami beam collapses before the conventional crashcans, and the longitudinal folding failure mode reported in Chapter 6 is induced in the beam. This indicates that the origami beam works well with the conventional crashcans. After the collapse of the beam, both conventional crashcans fold in the symmetric mode as those in CC.

The force vs displacement curve of OC is also plotted in Fig. 7.3 along with that of CC. By looking into the curves in detail, the entire crushing process of each bumper can be roughly divided into three stages based on displacement.

- Stage I (0 – 70 mm): the main deformation mechanism is the collapse of the beam segment between two crashcans.

- Stage II (70 – 120 mm): the main deformation mechanism is the flattening of the localized zones of the beam in the neighbourhood of the two crashcans.
- Stage III (120 – 250 mm): the main deformation mechanism is the crushing of the two crashcans.

At Stage I, the pattern induces the longitudinal folding mode in the origami beam in OC. If only the deformation at this stage is considered,  $P_{\max}$  and  $E_b$  of CC and OC, listed in Table 7.5, show that a  $P_{\max}$  reduction of 17.5% and an  $E_b$  increase of 18.0% are obtained for OC, which agree reasonably well with the outcomes obtained in Chapter 6. Therefore it can be concluded that the pattern on the origami beam in OC functions well in this loading scenario.

Table 7.5 Numerical results of CC and OC subjected to the full overlap impact at 5 m/s at Stage I

Model	$P_{\max}$ (kN)	$P_{\max}$ reduction	$E_b$ (kJ)	$E_b$ increase
CC	45.84	-	1.50	-
OC	37.84	17.5%	1.77	18.0%

At Stage II, however, the pattern on the origami beam in OC appears to have little effect on the localized flattening deformation, and therefore does not help to improve the energy absorption. As a result,  $E_b$  of OC shown in Table 7.4, which accounts for the deformation at all three stages, is only 9.8% higher than that of CC.  $P_m$  of OC is only increased by 2.0% compared with that of CC, indicating the limited effect of the origami beam.

In summary, while confirming the effectiveness of the origami pattern at triggering the longitudinal folding mode in the origami beam, the results indicate that there is still room for further improvement of the origami beam design in order to achieve higher energy absorption.

### 7.3.1.3 Combination of the origami crashcan and the origami beam

It has been shown that both the origami crashcan and the origami beam are able to increase the energy absorption of a bumper. In this section bumper OO, consisting of an origami beam and two origami crashcans, is analyzed to determine the effect of combining the two types of origami structures.

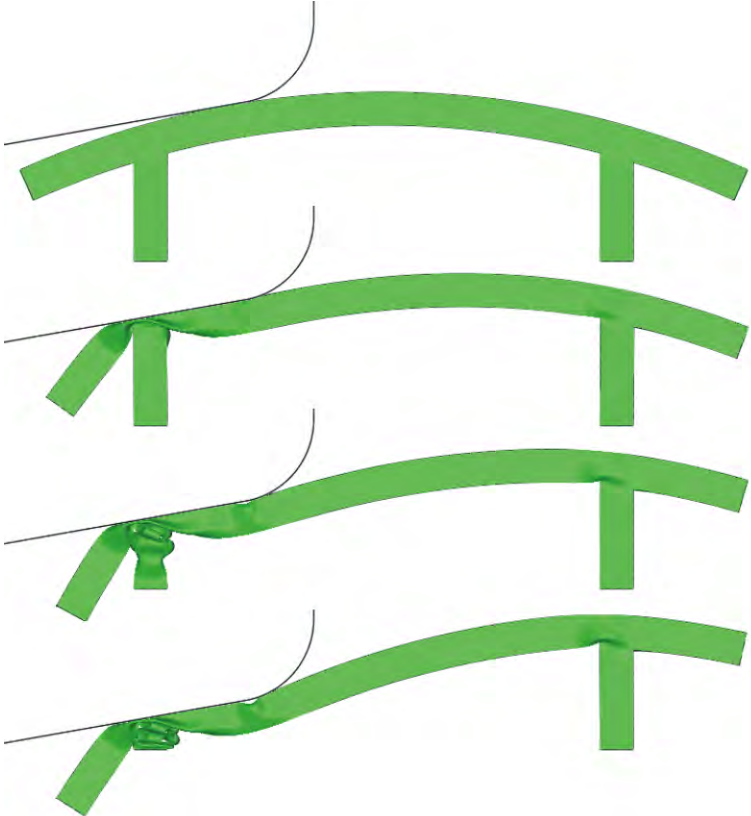
The crushing process of OO is shown in Fig. 7.2(d). Both the origami beam and the origami crashcans collapses following the patterns on their surfaces, suggesting that the two types of origami structures work well together. In addition, obvious bending deformation is again observed in the crashcans. The force vs displacement curve of OO is plotted in Fig. 7.3 along with those of CC, CO, and OC, and the numerical results are given in Table 7.4. It can be seen that the curve of OO is among the highest during the entire crushing process.  $P_m$  of OO is higher than those of the other three bumpers, with an increase of 23.4% being obtained compared with that of CC. Therefore it can be concluded that combining the two types of origami structures can lead to the most efficient bumper design in this loading scenario.

### **7.3.2 40% overlap impact at 5 m/s**

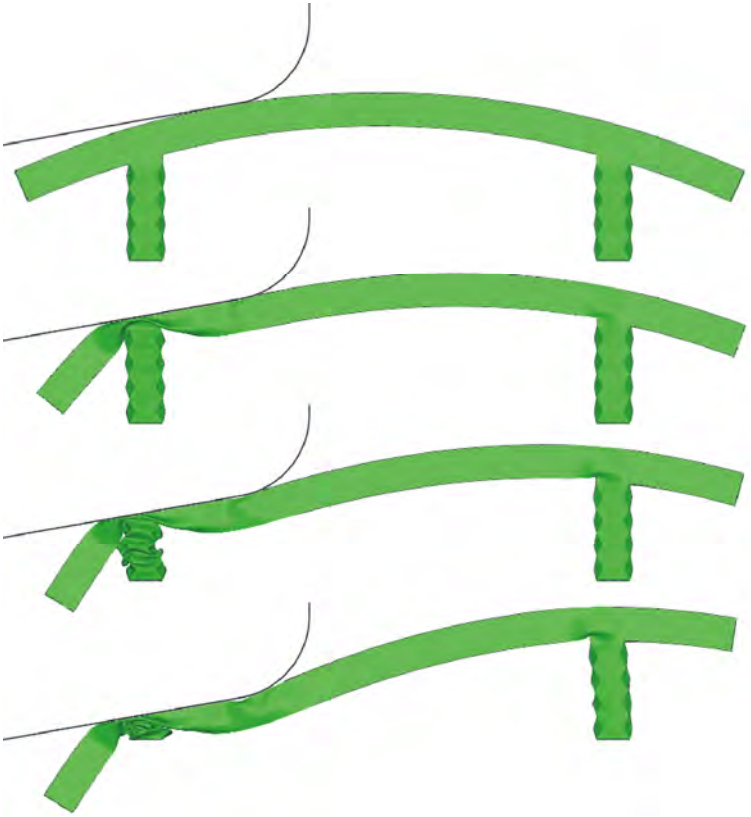
The crushing processes of the four bumpers subjected to this test are shown in Fig. 7.4 and their force vs displacement curves are plotted in Fig. 7.5. The numerical results are summarized in Table 7.6. Note that  $E_c$  in the table denotes the energy absorption of the crashcan on the side of impact.

#### *7.3.2.1 Performance of the origami crashcan*

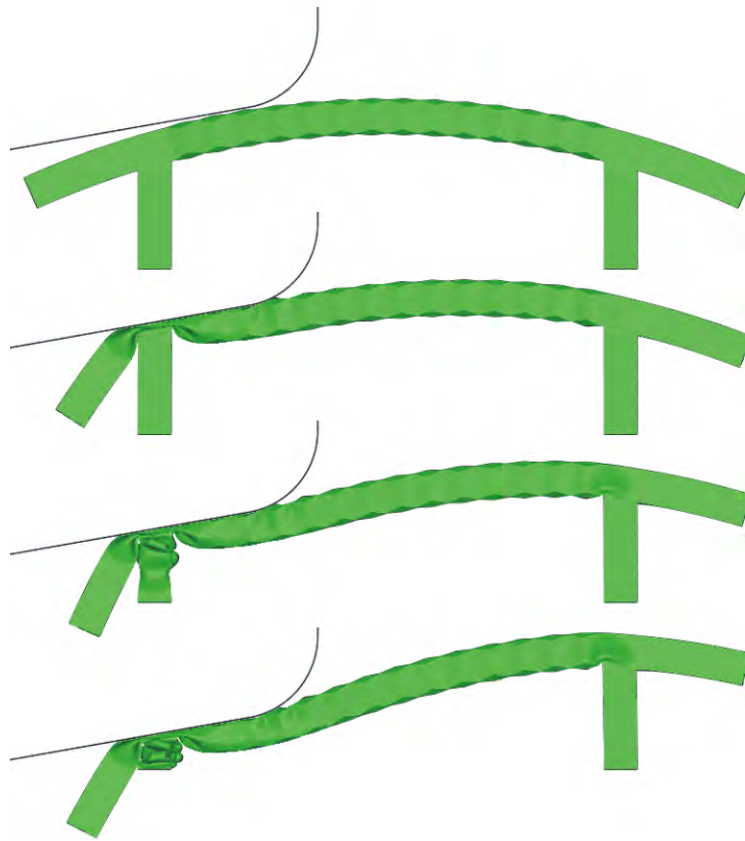
The responses of bumpers CC and CO, both of which are composed of an identical conventional beam but different types of crashcans, are presented here in order to evaluate the performance of the origami crashcan subjected to the 40% overlap impact at 5 m/s. The crushing processes of the two bumpers are shown in Fig. 7.4(a) and (b), respectively.



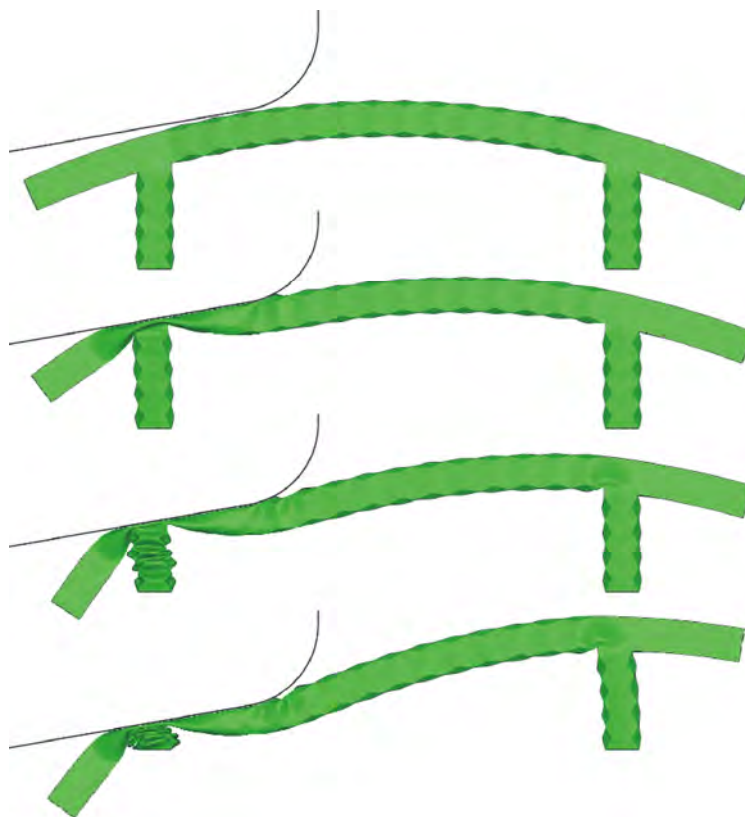
(a)



(b)



(c)



(d)

Fig. 7.4 40% overlap crushing processes at 5 m/s of (a) CC, (b) CO, (c) OC, and (d) OO.



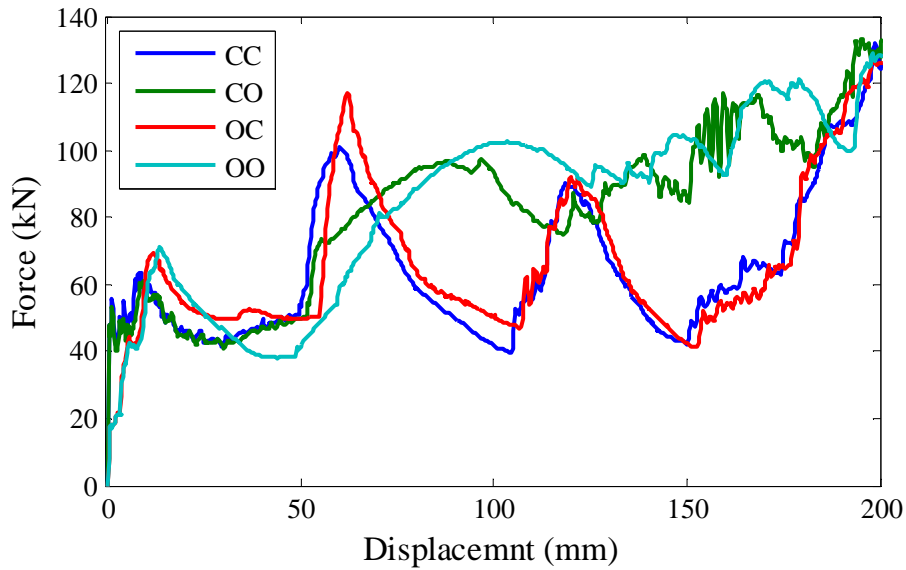


Fig. 7.5 Force vs displacement curves of the bumpers subjected to the 40% overlap impact at 5 m/s.

Table 7.6 Numerical results of the bumpers subjected to the 40% overlap impact at 5 m/s

Model	$P_m$ (kN)	$P_m$ increase	$E_b$ (kJ)	$E_b$ increase	$E_c$ (kJ)	$E_c$ increase
CC	64.58	-	3.97	-	8.21	-
CO	82.15	27.2%	3.96	-0.3%	11.47	39.7%
OC	65.95	2.1%	4.20	5.8%	8.16	-0.6%
OO	83.21	28.8%	3.83	-3.5%	12.15	48.0%

Four observations can be made from the crushing of the two bumpers. First, the conventional beam in each bumper fails mainly by localized flattening in the neighbourhood of the crashcan on the side of impact. This mode is referred to as the *localized flattening mode*. Second, only the crashcan on the side of impact is completely crushed in each case, whereas the other one undergoes quite small deformation. Third, the conventional crashcan in CC collapses in the symmetric mode, whereas the origami one in CO in the complete diamond mode. This observation indicates that the origami crashcan also integrates well with the conventional beam in this loading scenario. Finally, bending deformation is quite small in both types of crashcans.

The force vs displacement curves of the two bumpers are plotted in Fig. 7.5. Different from the curve of CC which shows a high degree of fluctuation, the curve of CO is quite smooth, which is a desirable feature because it can deliver a relatively constant deceleration in an impact. The numerical results in Table 7.6 show that  $E_c$  increase of CO reaches 39.7% in comparison with that of CC, which is considerably higher than that obtained in the full overlap impact at 5 m/s. This performance improvement is because the relatively small bending deformation makes the pattern followed better, leading to the complete diamond mode being formed in the origami crashcan in CO.  $E_b$  of the two bumpers, on the other hand, are very close due to the identical failure mode of their respective beams.  $P_m$  of CO is 27.2% higher than that of CC primarily because of the superior performance of the origami crashcan in CO.

### 7.3.2.2 Performance of the origami beam

The response of OC is presented and compared with that of CC, both of which are composed of identical conventional crashcans but different types of beams, in order to examine the behaviour of the origami beam subjected to the 40% overlap impact at 5 m/s. The crushing process of OC is shown in Fig. 7.4(c). It can be seen that the conventional crashcan on the side of impact still fails in the symmetric mode. The origami beam, however, shows no obvious sign of longitudinal folding following the pattern, and collapses in the localized flattening mode as in the case of the conventional beam in CC.

The force vs displacement curves of the two bumpers plotted in Fig. 7.5 show that the entire crushing process of each bumper can be approximately broken down into two stages based on displacement.

- Stage I (0 – 50 mm): the main deformation mechanism is the localized flattening of the beam segment in the neighbourhood of the crashcan on the impact side.
- Stage II (50 mm – 200 mm): the main deformation mechanism is the crushing of the crashcan on the impact side.

The pattern on the origami beam in OC does not make a significant difference at either stage. As a result,  $E_b$  of OC, listed in Table 7.6, is very close to that of CC, and the difference in the  $P_m$  of them is also negligible.

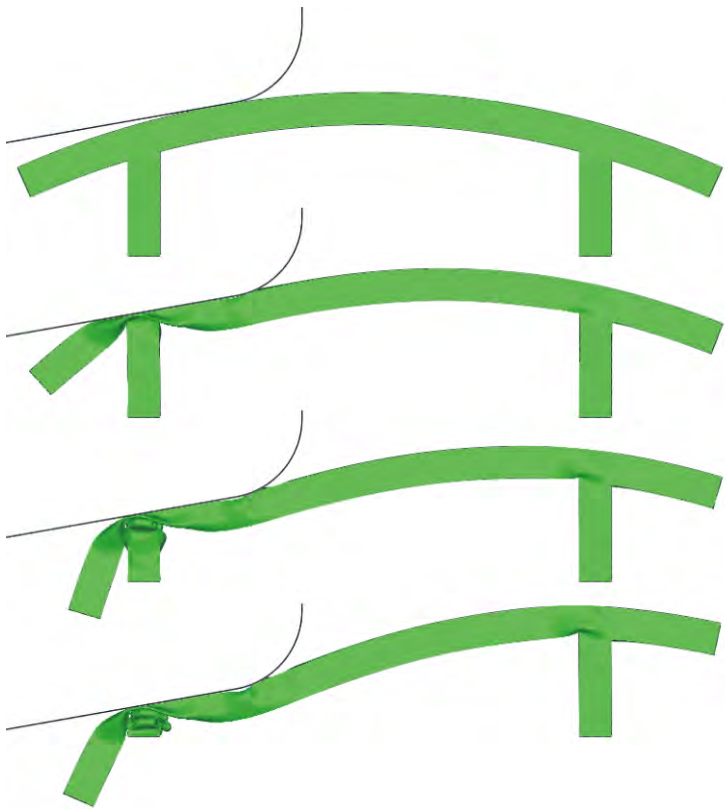
### 7.3.2.3 *Combination of the origami crashcan and the origami beam*

The crushing process of bumper OO, which is composed of an origami beam and two origami crashcans, is presented in Fig. 7.4(d). It can be seen that the origami crashcan on the impact side fails in the complete diamond mode. No severe distortion by bending deformation is observed. The origami beam still collapses in the localized flattening mode. Therefore it is indicated that the collapses of the two types of origami structures are not noticeably affected by each other in the 40% overlap impact at 5 m/s.

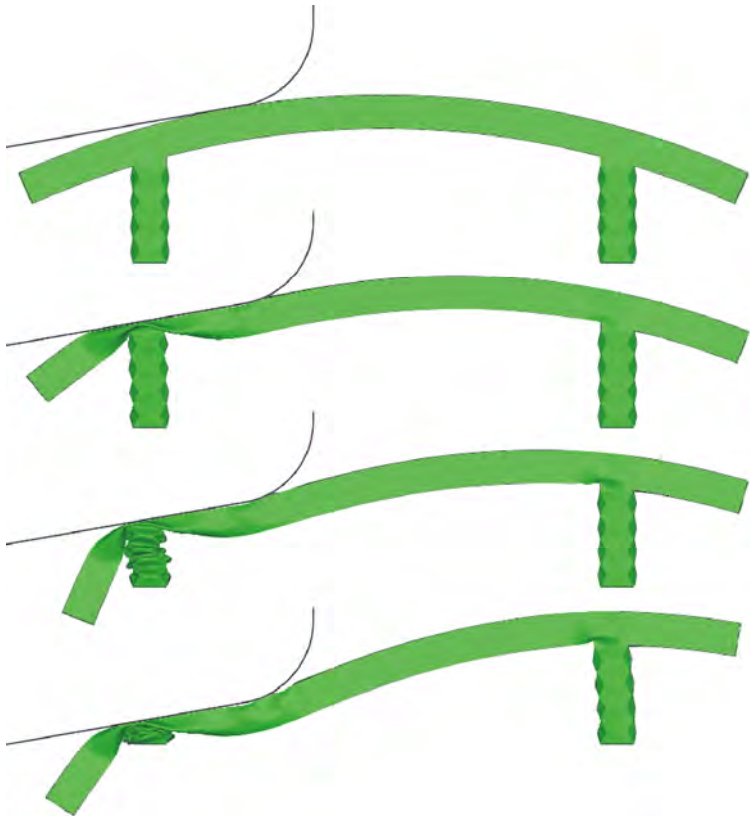
The force vs displacement curves plotted in Fig. 7.5 show that the curve of OO stays close to that of OC when the origami beam is crushed, and subsequently jumps to the neighbourhood of that of CO when the origami crashcan is folded. The numerical results in Table 7.6 show that an  $E_c$  increase of 48.0% is achieved for OO, whereas no  $E_b$  increase is attained in the same bumper. Despite the less satisfactory performance of the origami beam in OO,  $P_m$  of OO is the highest among the four bumpers, with an increase of 28.8% being obtained compared with that of CC. Therefore it can be concluded that OO is the most efficient design in terms of energy absorption in this loading scenario.

The results presented above and in Section 7.3.2.2 indicate that the origami beam does not help to significantly improve the energy absorption of a bumper subjected to the 40% overlap impact at 5 m/s. This is mainly due to the localized flattening mode of the origami beam on which the influence of the pattern is negligible.

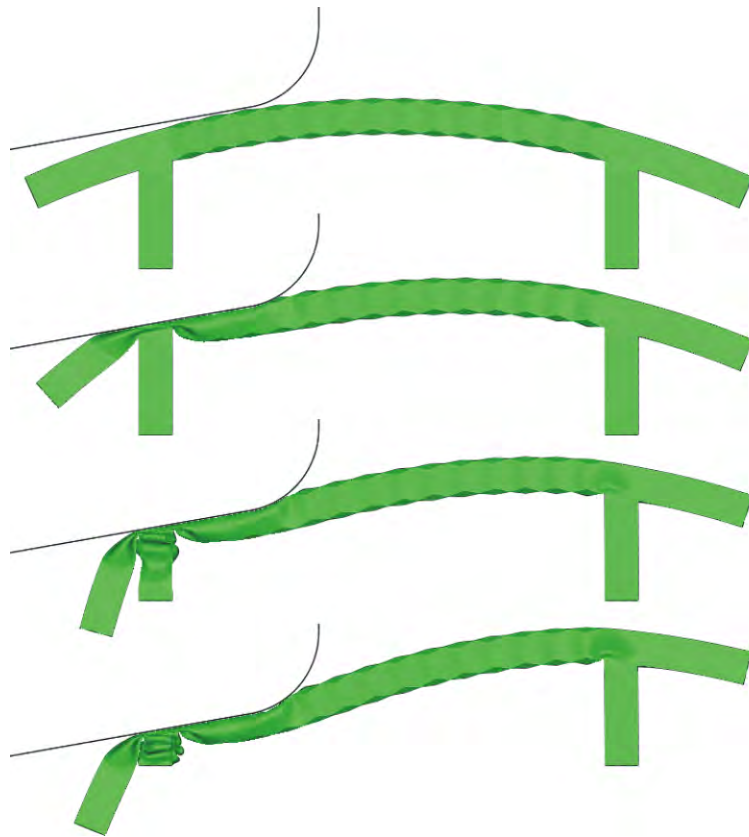
### **7.3.3 40% overlap impact at 20 m/s**



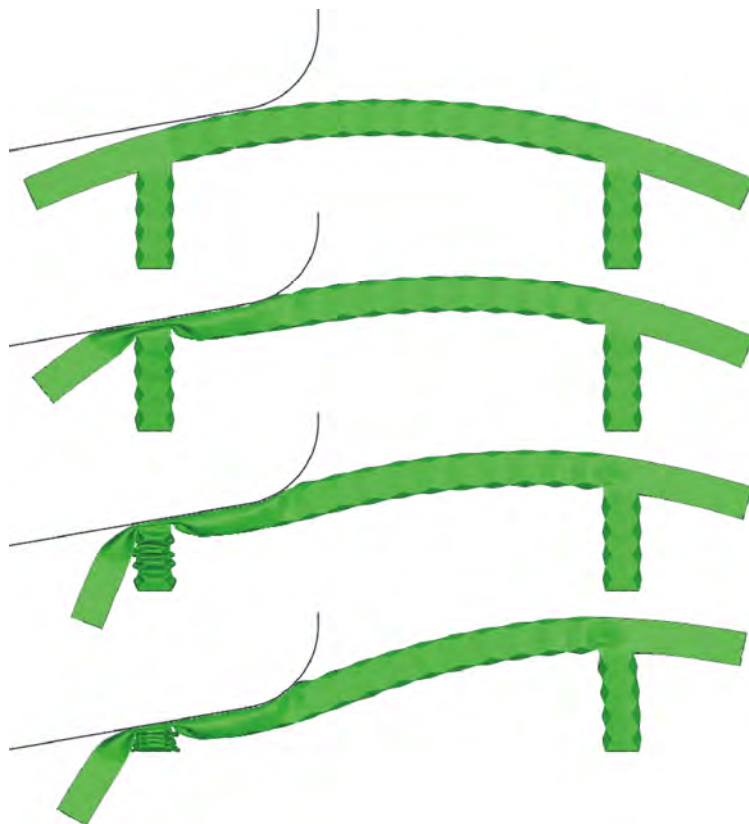
(a)



(b)



(c)



(d)

Fig. 7.6 40% overlap crushing processes at 20 m/s of (a) CC, (b) CO, (c) OC, and (d) OO.

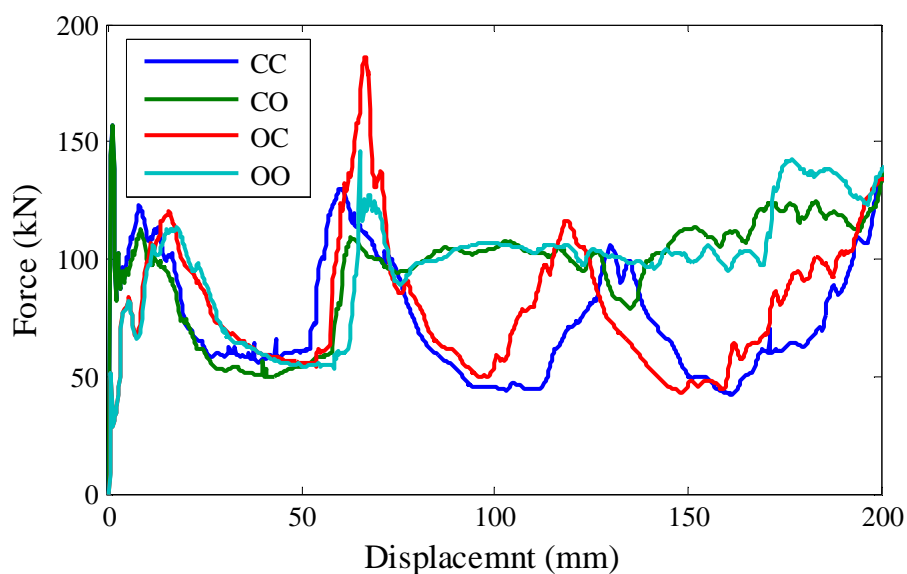


Fig. 7.7 Force vs displacement curves of the bumpers subjected to the 40% overlap impact at 20 m/s.

Table 7.7 Numerical results of the bumpers subjected to the 40% overlap impact at 20 m/s

Model	$P_m$ (kN)	$P_m$ increase	$E_b$ (kJ)	$E_b$ increase	$E_c$ (kJ)	$E_c$ increase
CC	74.13	-	5.15	-	8.39	-
CO	95.20	28.4%	4.69	-8.9%	13.14	56.6%
OC	79.88	7.8%	5.28	2.5%	9.27	10.5%
OO	97.47	31.5%	4.71	-8.5%	13.48	60.7%

The crushing processes of the four bumpers subjected to this test are shown in Fig. 7.6 and their force vs displacement curves are plotted in Fig. 7.7. The numerical results are compiled in Table 7.7.

All of the four bumpers show failure modes very close to those obtained from the 40% overlap impact at 5 m/s. However, the bending deformation in both types of crashcans is less obvious than that in the 40% overlap impact at 5 m/s, leading to that the crashcans fold as though loaded by an axial compression. The results in Tables 7.6 and 7.7 show that  $P_m$  of all of the bumpers are noticeably increased when the loading speed

rises from 5 m/s to 20 m/s. The reduced bending deformation and the strain rate effects are considered to be the main causes of the increase in energy absorption.

An  $E_c$  increase of over 50% is obtained for both CO and OO in comparison with that of CC, whereas  $E_b$  of OC and OO are close to that of CC. In addition, OO remains the most efficient bumper design in terms of energy absorption, with a  $P_m$  increase of 31.5% being achieved in comparison with that of CC. This result once again demonstrates the usefulness of the origami structures.

## 7.4 Summary

Four bumpers, CC consisting of a conventional beam and two conventional crashcans, CO consisting of a conventional beam and two origami crashcans, OC consisting of an origami beam and two conventional crashcans, and OO consisting of an origami beam and two origami crashcans, have been designed and analyzed in this chapter to investigate the failure modes and energy absorptions of the origami tube and the origami beam, developed in Chapters 4, 5, and 6, when subjected to complex loading. Three realistic impact tests, the full overlap impact at 5 m/s, the 40% overlap impact at 5 m/s, and the 40% overlap impact at 20 m/s, have been conducted on each bumper.

The numerical results show that the origami crashcan, adopted in bumpers CO and OO, integrates well with either a conventional beam or an origami one. The performances of the origami crashcan subjected to the three impact tests are summarized in Table 7.8. It can be seen that the origami crashcan performs quite well except for in the full overlap impact at 5 m/s. The less satisfactory performance in this loading scenario is caused by the large bending deformation in the origami crashcan during the crushing process which makes it fail in the less efficient incomplete diamond mode. This result indicates that the energy absorption of the origami crashcan is reduced when subjected to a large bending moment in addition to an axial force, which is undesirable for an energy absorption device. Increasing the number of modules in the origami crashcan,

which was reported in Chapter 4 to have the effect of improving the bending capacity of the origami crashcan, can be used to improve the energy absorption in this loading scenario.

Table 7.8 Performances of the origami crashcan subjected to the three impact tests

Impact test	Failure mode	$E_c$ increase*	
		CO	OO
Full overlap at 5 m/s	Incomplete diamond mode	28.9%	28.7%
40% overlap at 5 m/s	Complete diamond mode	39.7%	48.0%
40% overlap at 20 m/s	Complete diamond mode	56.6%	60.7%

\*  $E_c$  increase is calculated in comparison with that of CC.

The origami beam, adopted in bumpers OC and OO, is also found to work well with either conventional crashcans or origami ones. The performances of the origami beam under the three impact tests are summarized in Table 7.9. The results indicate that the origami beam only significantly improves the energy absorption in the full overlap impact at 5 m/s, and could even slightly reduce the energy absorption in the 40% overlap impacts when combined with origami crashcans. This main reason for the inability of the origami beam to perform well in the 40% overlap impacts is that local flattening deformation dominates the collapse of the beam, and therefore the desirable longitudinal folding mode cannot be triggered. Reinforcing the regions of the bumpers where the beam connects the crashcans is one approach to improving the overall structural performance. Despite that, the current origami beam design can still have some merit in terms of balancing the responses of a bumper in different loading scenarios. It has been shown that the energy absorption improvement of the origami crashcan in the full overlap impact at 5 m/s is lower than those in the 40% overlap impacts at 5 m/s and 20 m/s. The energy absorption increase of the origami beam in the full overlap impact at 5 m/s, on the other hand, is higher than those in the 40% overlap impacts at 5 m/s and 20 m/s. Therefore the relatively high energy absorption of the origami beam can to some extent compensate for the relatively low energy



absorption of the origami crashcan in the full overlap impact at 5 m/s, resulting in a balanced performance of the bumper in different impact scenarios.

Table 7.9 Performances of the origami beam subjected to the three impact tests

Impact test	Failure mode	$E_b$ increase*	
		OC	OO
Full overlap at 5 m/s	Longitudinal folding mode	9.8%	16.1%
40% overlap at 5 m/s	Localized flattening mode	5.8%	-3.5%
40% overlap at 20 m/s	Localized flattening mode	2.5%	-8.5%

\*  $E_b$  increase is calculated in comparison with that of CC.

The mean crushing forces of the four bumpers subjected to the three impact tests are summarized in Table 7.10. It can be seen that bumper OO has the highest mean crushing force in all three impact tests. Therefore combining both types of origami structures in one bumper can lead to the most efficient design in terms of energy absorption.

Table 7.10 Mean crushing forces of the bumpers subjected to the three impact tests\*

Impact test	CC	CO	OC	OO
Full overlap at 5 m/s	83.21	98.12	84.85	102.17
40% overlap at 5 m/s	64.58	82.15	65.95	83.21
40% overlap at 20 m/s	74.13	95.20	79.88	97.47

\* The unit of the data in the table is kN.

To this point, it is clear that the origami crashcan satisfies all of the main requirements for a good energy absorption device: low peak force, high energy absorption, stable and predictable failure mode under realistic loading scenarios, reasonable bending and torsion capacity, and low cost. Therefore, it can be concluded that the origami crashcan has great potential as a high-performance energy absorption device. For the origami beam, while the results in this chapter show that the longitudinal folding mode is also stable and efficient in terms of energy absorption, further design modification is

required to improve the performance of the origami beam if it is to be used as a bumper component.

# CHAPTER 8

## FINAL REMARKS

### 8.1 Main Achievements

This dissertation is concerned with the design and analysis of thin-walled structures with pre-folded origami patterns on their surface as high-performance energy absorption devices. The principal achievements are summarized in the following paragraphs.

First, an experimental study of a type of previously reported thin-walled square tube with pre-fabricated pyramid patterns on the surface has been conducted. A simple manufacturing approach has been developed to construct tube samples with two different designs. Quasi-static axial crushing tests on these samples reveal that the octagonal mode, despite being proven numerically to be efficient in terms of energy absorption, cannot be consistently triggered. This shortcoming has led us to seek new origami patterns to improve the energy absorption of thin-walled tubes.

A new type of thin-walled tubular energy absorption device known as the origami tube which also has origami pattern pre-manufactured on the surface has been developed and analyzed. A family of origami patterns, including a basic one for square tubes and several modifications for rectangular tubes, polygonal tubes, and two types of tapered tubes have been worked out and a set of independent geometric parameters for each pattern has been identified. The origami pattern on the surface of the origami tube acts

as a form of geometric imperfection to reduce the initial buckling force and, more importantly, as a failure mode inducer to trigger the complete diamond mode in a tube which is more efficient in terms of energy absorption because it doubles the number of travelling plastic hinge lines at each corner of the tube. In addition, those origami patterns have several additional properties. They are designed in a modular way so that origami tubes of various sizes can be easily obtained by changing the number of modules axially. The surface of the tube with origami patterns is developable so that the origami tube can be conveniently and accurately constructed out of a flat sheet of material with little in-plane stretching.

An extensive numerical study of the performances of origami tubes with various configurations when subjected to quasi-static axial crushing has been carried out. The results show that the complete diamond mode can be successfully induced in a square origami tube, and both low peak force and high energy absorption are achieved in a single tube with the new design. A parametric study has been conducted on square origami tubes to investigate the effects of a series of geometric parameters. It is found that by properly selecting the pattern geometry, the mean crushing force can be increased by over 80% in comparison with that of a conventional square tube with identical surface area and wall thickness, whilst a peak force reduction by more than 30% can still be reached. Furthermore, the axial crushing of origami tubes with rectangular cross sections, polygonal cross sections, and two types of tapered shape has also been analyzed. The results demonstrate that the complete diamond mode can always be triggered in origami tubes with those profiles provided that a proper pattern geometry is selected, leading to both low peak force and high mean crushing force.

The axial crushing behaviour of a square origami tube made of mild steel and subjected to four types of boundary conditions, free on both ends, pinned on both ends, clamped on both ends, pinned on one end and rigidly connected to a deformable supporting structure on the other, respectively, have been obtained via numerical simulation and compared. The results indicate that the complete diamond mode is not sensitive to boundary conditions on the ends. Subsequently, a simply supported square

origami tube made of three commonly used metallic materials, mild steel, high strength steel, and aluminium alloy, respectively, has been axially crushed. It is found that the complete diamond mode is also independent of material mechanical properties provided that ductile materials are used. A square origami tube reinforced by a centre web has been analyzed. Both reduced peak force and increased mean crushing force are attained compared with those of a reinforced conventional square tube. Furthermore, the bending capacity and torsion capacity of six square origami tubes have been examined. The results indicate that the origami tube has comparable bending capacity and torsion capacity with those of the commonly used conventional tubes with dents. Finally, a type I tapered origami tube has been axially crushed at 5 m/s and 20 m/s, respectively. A consistent and predictable response is observed in the origami tube, and substantial energy absorption is achieved in comparison with that of conventional ones.

In addition to numerical analysis, a theoretical study of the axial crushing of square origami tubes has been conducted. A simplified basic folding element has been established to describe the complete diamond mode. Three main sources of energy absorption have been identified, and the energy dissipated from each source has been calculated. Applying the upper bound theory, a concise mathematical formula has been derived to calculate the mean crushing force of a square origami tube with specified geometry and material properties. Comparison between theoretical prediction and numerical results shows a good agreement. Since properly designed rectangular origami tubes and tapered ones have energy absorption close to that of square ones with identical surface area and wall thickness, the theoretical formula can also be used to approximately estimate the mean crushing forces of origami tubes with those two profiles.

Quasi-static axial crushing experiments on several square origami tube samples have been carried out. A simple manufacturing procedure has been developed to construct the samples. The experimental results show that the complete diamond mode is formed in the samples and both peak force reduction and mean crushing force increase are

attained. Furthermore, the simple manufacturing procedure has been further refined and high quality prototype tubes have been constructed.

A new type of curved thin-walled beam with pre-manufactured origami pattern on the surface, known as the origami beam, has been designed and analyzed for the purpose of energy absorption. The origami pattern for square origami tubes has been slightly modified to suit the curved surface of the origami beam. Similar to that for the origami tube, the pattern has the effect of inducing new failure modes, which are efficient in terms of energy absorption, in the origami beam subjected to quasi-static lateral bending. Two types of pattern arrangements on the origami beam have been proposed. One is to apply origami pattern along the entire beam. Numerical simulation results show that a new failure mode known as the longitudinal folding mode, which features folding of beam walls in the longitudinal direction during the crushing process, can be triggered in the origami beam, leading to reduced peak force and increased overall energy absorption. As much as 23.6% specific energy absorption increase can be attained while the peak force is still reduced by 12.9%. The alternative is to apply origami pattern near both ends of a beam while leaving the middle part intact. The numerical results indicate that an origami beam designed in this way fails in a new mode, referred to as the mixed mode, which features both longitudinal folding of beam walls and bending of a localized plastic hinge. The mixed mode is found to be even more efficient than the longitudinal folding mode in terms of energy absorption.

Finally, both the origami tube and the origami beam are used to form four automobile frontal bumpers. Three impact tests, the full overlap impact at 5 m/s, the 40% overlap impact at 5 m/s, and the 40% overlap impact at 20 m/s, have been respectively conducted on each bumper. Numerical results show that the origami tube integrates well with either a conventional beam or an origami one, and can substantially improve the energy absorption of the bumper in all three loading scenarios. The origami beam, on the other hand, helps to significantly increase the energy absorption of the bumper only in the full overlap impact at 5 m/s, regardless of working with conventional crashcans or origami ones. However, the origami beam can still be useful through

balancing the performances of a bumper in different loading scenarios. The bumper designed by combining the two types of origami structures is found to be most efficient in terms of energy absorption.

## 8.2 Future Work

The novelty and feasibility of utilizing origami patterns to improve the performance of thin-walled energy absorption devices have been established in this dissertation. The research reported here opens up many new research opportunities.

A thorough theoretical analysis of the complete diamond mode of the origami tube can be conducted. Two important questions are to be answered. One is how to determine the exact amount of pre-folding that can take the origami tube to the complete diamond mode without reversing back to other principle failure modes. For instance, the corner width of the origami pattern is crucial in the design of the origami tube. It would be desirable if the critical value of the corner width can be calculated analytically. The other is how to accurately estimate the energy absorption of the origami tube failing in the complete diamond. The simple formula derived in Chapter 5, while agreeing well with numerical results, does not capture all of the main features of the complete diamond mode observed from the numerical analysis. A more advanced basic folding element is to be built, and a suitable approach to quantify the extension and shear deformation in the origami tube is to be developed.

The successful application of origami patterns in the design of thin-walled energy absorption structures with closed cross sections raises the question of whether the same approach also work for thin-walled structures with open cross sections, i.e., whether corrugated shells with origami patterns on the surface can bear some useful properties from the perspective of energy absorption. This type of thin-walled structure is not only widely applied as cores of sandwich plates, but could also provide a solution to the sub-skin structures of passenger car bonnets which, as the main cause of pedestrian

head injuries (Crandall *et al.*, 2002), are facing great difficulty in complying with the newly launched EU regulation.



## APPENDIX I:

A detailed geometric analysis of the origami patterns for two types of tapered tubes presented in Chapter 4 is conducted here.

### 1. Pattern for Type I Tapered Tube

Figure A.1 shows the pattern design for type I tapered tube. Five geometric parameters, i.e.,  $a_1$ ,  $a_2$ ,  $b$ ,  $c$ , and  $l$ , are required to completely define the pattern. Due to the symmetric nature, only a quarter of the pattern is analyzed below.

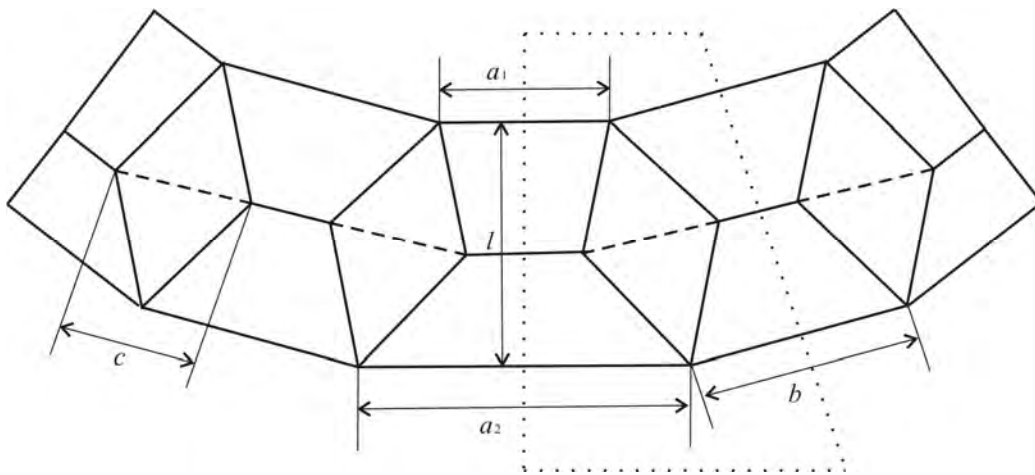


Fig. A.1 Pattern for type I tapered tube.

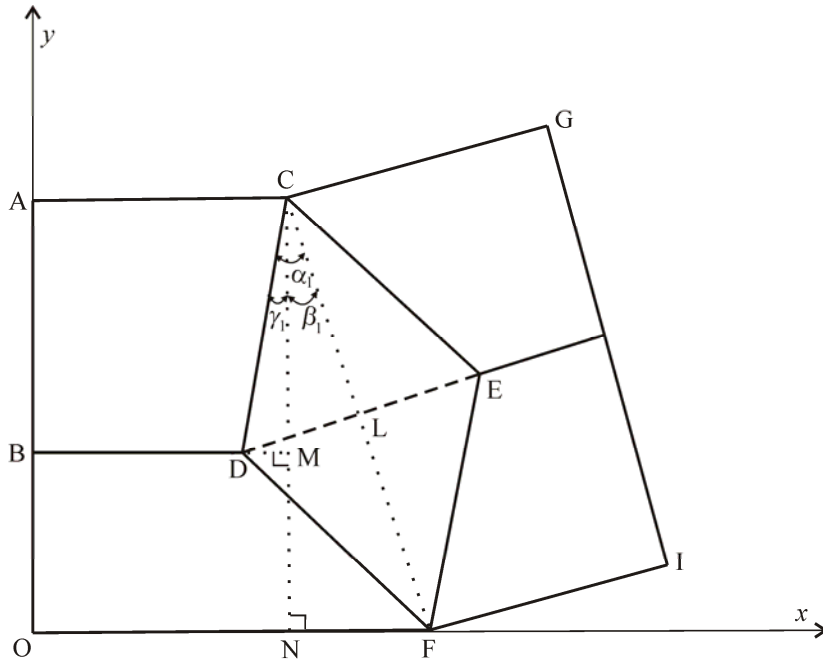


Fig. A.2 A quarter of the pattern for type I tapered tube in the developed configuration.

For a quarter of the pattern presented in Fig. A.2, the lengths of the following creases are known:

$$\left\{ \begin{array}{l} l_{AC} = \frac{a_1}{2} \\ l_{OF} = \frac{a_2}{2} \\ l_{AO} = l \\ l_{CG} = l_{FI} = \frac{b}{2} \\ l_{DE} = c \end{array} \right. \quad (\text{A.1})$$

And the following geometric relationships are also known:

$$\left\{ \begin{array}{l} l_{CD} = l_{DF} = l_{FE} = l_{EC} \\ l_{GH} = l_{HI} \end{array} \right. \quad (\text{A.2})$$

Then the task is to calculate the lengths of AB, BO, BD, CD, EH, and GH in order to determine the positions of all of the nodes of the pattern. The lengths of EH, GH, and CD are first calculated:

$$\left\{ \begin{array}{l} l_{EH} = \frac{l_{LH} - l_{LE}}{2} = \frac{b - c}{2} \\ l_{CF} = d_1 = \sqrt{l_{CN}^2 + l_{NF}^2} = \sqrt{l^2 + \left(\frac{a_2 - a_1}{2}\right)^2} \\ l_{GH} = \frac{l_{CF}}{2} = \frac{d_1}{2} \\ l_{CD} = e_1 = \sqrt{l_{DL}^2 + l_{CL}^2} = \frac{1}{2} \sqrt{c^2 + d_1^2} \end{array} \right. \quad (A.3)$$

in which  $d_1$  and  $e_1$  denote the lengths of CF and CD, respectively.

To calculate the lengths of BD, AB, and BO, first introduce three angles  $\alpha_1$ ,  $\beta_1$ , and  $\gamma_1$

$$\left\{ \begin{array}{l} \alpha_1 = \arctan \frac{l_{DL}}{l_{CL}} = \arctan \frac{c}{d_1} \\ \beta_1 = \arctan \frac{l_{NF}}{l_{CN}} = \arctan \frac{a_2 - a_1}{2l} \\ \gamma_1 = \alpha_1 - \beta_1 \end{array} \right. \quad (A.4)$$

Then the lengths of BD, AB, and BO can be calculated as

$$\left\{ \begin{array}{l} l_{BD} = \frac{f_1}{2} = l_{BM} - l_{DM} = \frac{a_1}{2} - e_1 \sin \gamma_1 \\ l_{AB} = l_1 = l_{CD} \cos \gamma_1 = e_1 \cos \gamma_1 \\ l_{BO} = l_2 = l_{AO} - l_{AB} = l - l_1 \end{array} \right. \quad (A.5)$$

in which  $f_1 / 2$ ,  $l_1$ , and  $l_2$  denote the lengths of BD, AB, and BO, respectively.

With the lengths of all of the creases being obtained, the position of each node of the pattern can be calculated, and the layout of the pattern can then be completely determined.

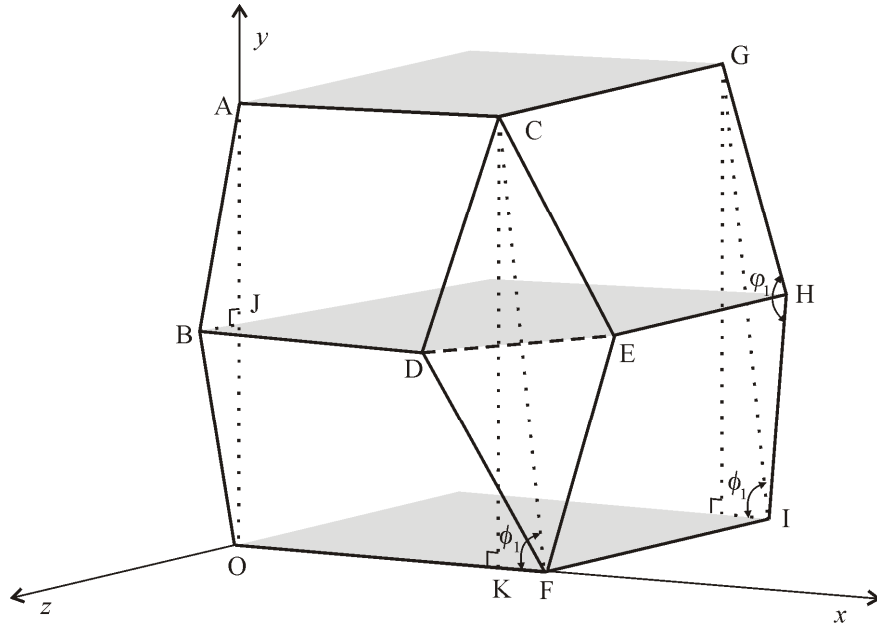


Fig. A.3 A quarter of the pattern for tapered tube I in the folded configuration.

If we fold the pattern in Fig. A.2 along the creases, a quarter of a tapered tube as shown in Fig. A.3 can be obtained. Two more parameters, i.e., the lengths of AJ and JO, are needed to determine when the folding process should be finished. Let  $h_1$  and  $h_2$  denote the lengths of AJ and JO respectively and introduce two more angles  $\phi_1$  and  $\phi_2$ , the following geometric relationships can be obtained

$$\left\{ \begin{array}{l} l_{CF} = g_1 = \sqrt{l_{CK}^2 + l_{KF}^2} = \sqrt{(h_1 + h_2)^2 + \left(\frac{a_2 - a_1}{2}\right)^2} \\ l_{BJ} = n_1 = \sqrt{l_{AB}^2 - l_{AJ}^2} = \sqrt{l_{BO}^2 - l_{OJ}^2} = \sqrt{l_1^2 - h_1^2} = \sqrt{l_2^2 - h_2^2} \\ \phi_1 = \arctan \frac{l_{CK}}{l_{KF}} = \arctan \frac{2(h_1 + h_2)}{a_2 - a_1} \\ \phi_2 = \arccos \frac{l_{GH}^2 + l_{HI}^2 - l_{GI}^2}{2l_{GH}l_{HI}} = \arccos \frac{d_1^2 - 2g_1^2}{d_1^2} \end{array} \right. \quad (A.6)$$

in which  $g_1$  and  $n_1$  denote the lengths of CF and BJ, respectively.

Then the coordinate of points D and E can be worked out:

$$\begin{cases} \text{D} \left( \frac{f_1}{2}, h_2, n_1 \right) \\ \text{E} \left( \frac{a_1}{2} + \frac{d_1}{2} \sin\left(\frac{\varphi_1}{2} + \phi_1\right), \frac{d_1}{2} \cos\left(\frac{\varphi_1}{2} - \phi_1\right), -\frac{c}{2} \right) \end{cases}$$

Note that  $l_{DE} = c$ , i.e.

$$\left[ \frac{a_1}{2} + \frac{d_1}{2} \sin\left(\frac{\varphi_1}{2} + \phi_1\right) - \frac{f_1}{2} \right]^2 + \left[ \frac{d_1}{2} \cos\left(\frac{\varphi_1}{2} - \phi_1\right) - h_2 \right]^2 + \left( -\frac{c}{2} - n_1 \right)^2 = c^2 \quad (\text{A.7})$$

Now  $h_1$  and  $h_2$  can be calculated by solving Eqs. (A.6) and (A.7) simultaneously. No close-form solutions can be obtained due to the existence of transcendental functions in Eq. (A.6), so that  $h_1$  and  $h_2$  have to be calculated numerically. When  $h_1$  and  $h_2$  are worked out, all of the nodes of the pattern in 3D space can be readily obtained, and the shape of the tube can then be completely determined.

## 2. Pattern for Type II Tapered Tube

The pattern design for type II tapered tube, which can be completely determined by four geometric parameters, i.e.,  $a_1$ ,  $a_2$ ,  $c$ , and  $l$ , is shown in Fig. A.4. This pattern also has symmetric property and therefore only a quarter is analyzed below.

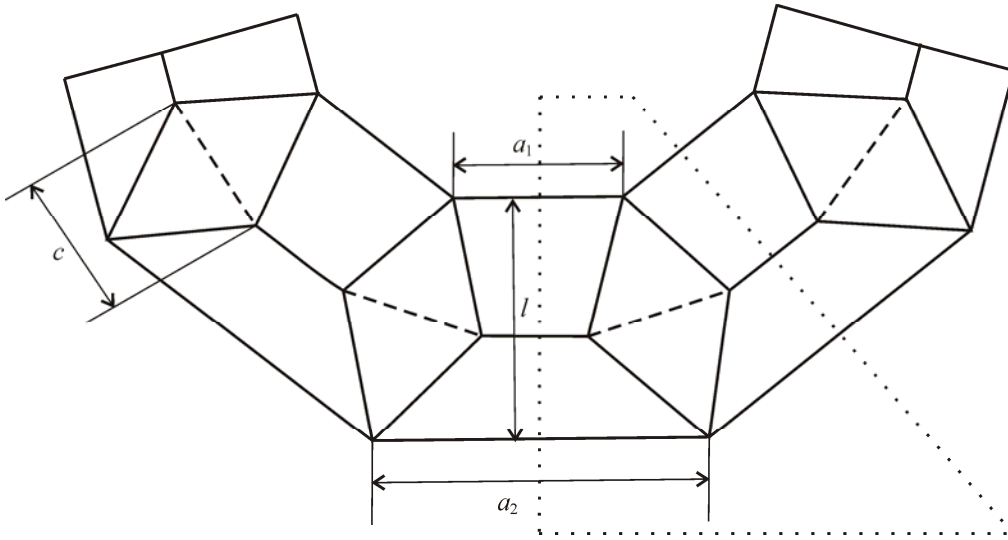


Fig. A.4 Pattern for type II tapered tube.

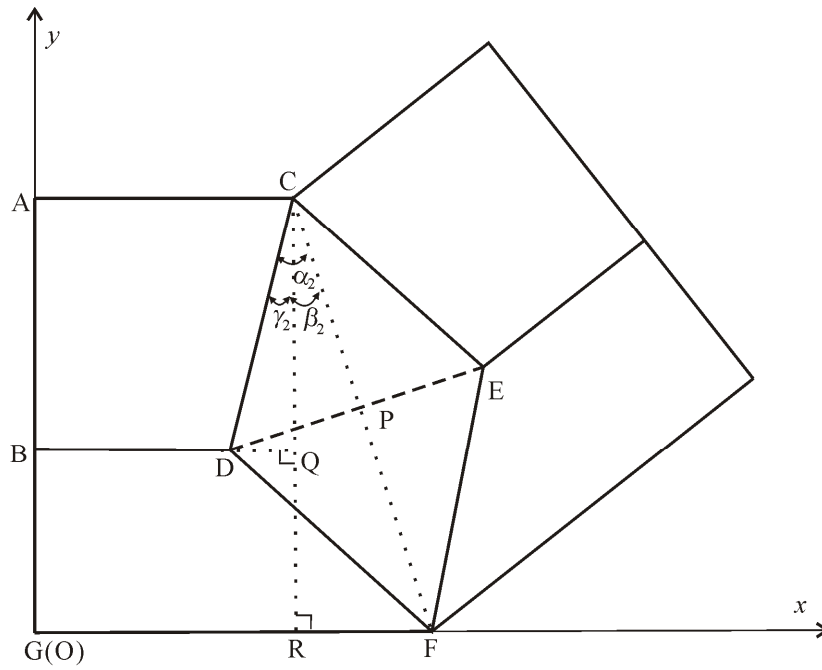


Fig. A.5 A quarter of the pattern for type II tapered tube in the developed configuration.

The lengths of the following creases of the pattern are known

$$\left\{ \begin{array}{l} l_{AC} = \frac{a_1}{2} \\ l_{GF} = \frac{a_2}{2} \\ l_{AG} = l \\ l_{DE} = c \end{array} \right. \quad (A.8)$$

And the following geometric relationships are also known:

$$l_{CD} = l_{DF} = l_{FE} = l_{EC} \quad (\text{A.9})$$

Then the position of all of the nodes of the pattern can be obtained by calculating the lengths of AB, BG, BD, and CD.

The length of CF, denoted as  $d_2$ , can be calculated as

$$l_{CF} = d_2 = \sqrt{l^2 + \left(\frac{a_2 - a_1}{2}\right)^2} \quad (\text{A.10})$$

Then the length of CD, denoted as  $e_2$ , is

$$l_{CD} = e_2 = \frac{1}{2} \sqrt{c^2 + d_2^2} \quad (\text{A.11})$$

To calculate the lengths of BD, AB, and BG, we first calculate three angles  $\alpha_2$ ,  $\beta_2$ , and  $\gamma_2$

$$\begin{cases} \alpha_2 = \arctan \frac{l_{DP}}{l_{CP}} = \arctan \frac{c}{d_2} \\ \beta_2 = \arctan \frac{l_{RF}}{l_{CR}} = \arctan \frac{a_2 - a_1}{2l} \\ \gamma_2 = \alpha_2 - \beta_2 \end{cases} \quad (\text{A.12})$$

Then the lengths of BD, AB, and BG are

$$\begin{cases} l_{BD} = \frac{f_2}{2} = l_{BQ} - l_{DQ} = \frac{a_1}{2} - e_2 \sin \gamma_2 \\ l_{AB} = l_3 = l_{CD} \cos \gamma_2 = e_2 \cos \gamma_2 \\ l_{BG} = l_4 = l_{AG} - l_{AB} = l - l_3 \end{cases} \quad (\text{A.13})$$

in which  $f_2 / 2$ ,  $l_3$ , and  $l_4$  denote the lengths of BD, AB, and BG, respectively.

Now the positions of all of the nodes of the pattern can be readily calculated from the lengths of the creases, and the layout of the pattern can then completely determined.

A quarter of a tapered tube as shown in Fig. A.6 can be obtained by folding the pattern in Fig. A.5 along the creases. In order to determine when the folding process should cease, the lengths of AH and HI, respectively denoted by  $h_3$  and  $h_4$ , need to be calculated.

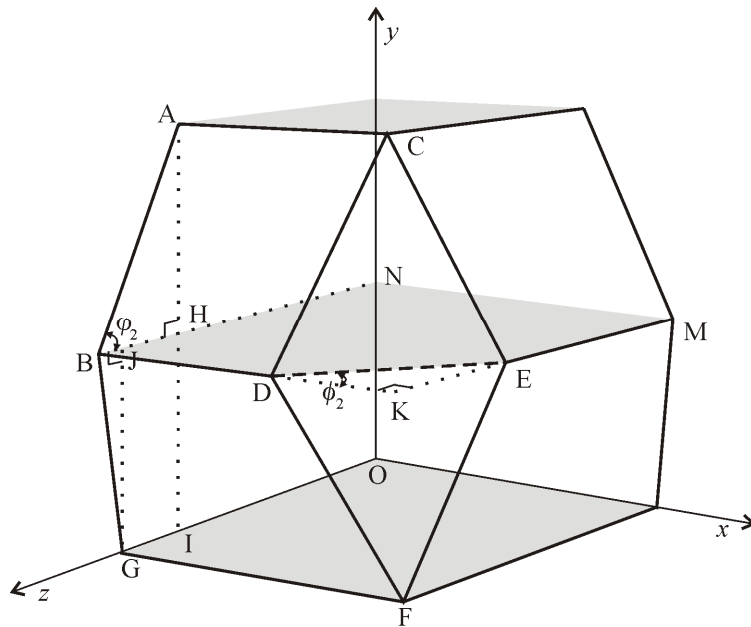


Fig. A.6 A quarter of the pattern for type II tapered tube in the folded configuration.

To start with, the following geometric relationships can be obtained due to symmetry of the pattern:

$$\begin{cases} l_{BD} = l_{ME} \\ l_{DK} = l_{EK} \\ \phi_2 = \frac{\pi}{4} \end{cases} \quad (\text{A.14})$$



Therefore

$$l_{DK} = l_{EK} = \frac{\sqrt{2}}{2}c \quad (\text{A.15})$$

Then the lengths of BN and KM can be calculated

$$\begin{cases} l_{BN} = l_{BH} + l_{HN} = l_3 \cos \varphi_2 + \frac{a_1}{2} \\ l_{KM} = l_{KE} + l_{EM} = \frac{\sqrt{2}}{2}c + e_2 \end{cases} \quad (\text{A.16})$$

Note that  $l_{BN} = l_{KM}$ , i.e.

$$l_3 \cos \varphi_2 + \frac{a_1}{2} = \frac{\sqrt{2}}{2}c + e_2 \quad (\text{A.17})$$

Solving Eq. (A.17) for  $\varphi_2$

$$\varphi_2 = \arccos \frac{e_2 + \sqrt{2}c - a_1}{2l_3} \quad (\text{A.18})$$

Now  $h_3$  and  $h_4$  can be calculated as

$$\begin{cases} h_3 = l_{AB} \sin \varphi_2 = l_3 \sin \varphi_2 \\ h_4 = \sqrt{l_{BG}^2 - l_{BJ}^2} = \sqrt{l_4^2 - (l_3 \cos \varphi_2 + \frac{a_1}{2} - \frac{a_2}{2})^2} \end{cases} \quad (\text{A.19})$$

With  $h_3$  and  $h_4$  being attained, the coordinates of all of the nodes of the pattern in the folded configuration can be readily obtained, and the shape of the tube in 3D space can then be completely determined.

## APPENDIX II

The following publications are related to the work presented in this dissertation.

Ma, J., You, Z., Wang, B., and Cheng, G. (2009), *Origami Crashcan*, China Patent Application No. : 200910013553.X (pending).

Ma, J., Le, Y., and You, Z. (2010), Axial crushing tests of thin-walled steel square tubes with pyramid patterns, *51st AIAA/ASME/ASCE/AHS/ASC Structures, Structural Dynamics, and Materials Conference*, Orlando, FL, USA, April 12-15.

Ma, J. and You, Z. (2010), The origami crash box, *5th International Conference on Origami in Science, Mathematics and Education and Folding Convention*, Singapore, July 13 – 17.

Ma, J. and You, Z. (2010), A novel thin-walled tube with origami patterns as energy absorption device, *ASME International Mechanical Engineering Congress and Exposition*, Vancouver, BC, Canada, November 12-18.

You, Z. and Ma, J. (2010), Energy absorption of thin-walled tubes with origami patterns, *IASS 2010 "Spatial Structures – Permanent and Temporary"*, Shanghai, China, November 8-12.

# REFERENCES

*Abaqus*, Version 6.7, SIMULIA Corp., Providence, RI, USA.

AASHTO (1995), *A guide to standardized highway barrier hardware*, Washington, D.C.

Abramowicz, W. (1983), The effective crushing distance in axially compressed thin-walled metal columns, *International Journal of Impact Engineering*, **1**(3), 309-317.

Abramowicz, W. and Jones, N. (1984a), Dynamic axial crushing of square tubes, *International Journal of Impact Engineering*, **2**(2), 179-208.

Abramowicz, W. and Jones, N. (1984b), Dynamic axial crushing of circular tubes, *International Journal of Impact Engineering*, **2**(3), 263-281.

Abramowicz, W. and Jones, N. (1986), Dynamic progressive buckling of circular and square tubes, *International Journal of Impact Engineering*, **4**(4), 243-270.

Abramowicz, W. and Wierzbicki, T. (1988), Axial crushing of foam-filled columns, *International Journal of Mechanical Sciences*, **30**(3-4), 263-271.

Abramowicz, W. and Wierzbicki, T. (1989), Axial crushing of multicorner sheet metal columns, *Journal of Applied Mechanics* **56**(1), 113-120.

Adachi, T., Tomiyama, A., Araki, W. and Yamaji, A. (2008), Energy absorption of a thin-walled cylinder with ribs subjected to axial impact, *International Journal of Impact Engineering*, **35**(2), 65-79.

Airoldi, A., Gerardus, J., Bergamelli, C. and Sanvito, M. (2006), *Triggering system for the plastic collapse of a metal structural element*, US 2006/0208134 A1.

Airoldi, A. and Janszen, G. (2005), A design solution for a crashworthy landing gear with a new triggering mechanism for the plastic collapse of metallic tubes, *Aerospace Science and Technology*, **9**(5), 445-455.

Alexander, J. M. (1960), An approximate analysis of the collapse of thin cylindrical shells under axial loading, *The Quarterly Journal of Mechanics and Applied Mathematics* **13**(1), 10-15.

Alghamdi, A. A. A. (2001), Collapsible impact energy absorbers: An overview, *Thin-Walled Structures*, **39**(2), 189-213.

Aljawi, A. A. N. and Alghamdi, A. A. A. (1999), *Investigation of axially compressed frusta as impact energy absorbers*, Computational methods in contact mechanics iv, Edited by Gaul, L. and Brebbia, A. A., WIT Press, Southampton, 431-443.

Aljawi, A. A. N. and Alghamdi, A. A. A. (2000), *Inversion of frusta as impact energy absorbers*, Current advances in mechanical design and production vii, Edited by Hassan, M. F. and Megahed, S. M., Pergamon, New York, 511-519.

Allan, T. (1968), Experimental and analytical investigation of the behaviour of cylindrical tubes subject to axial compressive forces, *Journal of Mechanical Sciences* **10**(2), 182-197.

Amano, K., Suzuki, Y. and Kozuma, H. (2005), *Bumper beam for automobiles*, US Patent, 6,893,062.

Andrews, K. R. F., England, G. L. and Ghani, E. (1983), Classification of the axial collapse of cylindrical tubes under quasi-static loading, *International Journal of Mechanical Sciences*, **25**(9-10), 687-696.

Bambach, M. R. and Elchalakani, M. (2007), Plastic mechanism analysis of steel SHS strengthened with CFRP under large axial deformation, *Thin-Walled Structures*, **45**(2), 159-170.

Bambach, M. R., Elchalakani, M. and Zhao, X. L. (2009a), Composite steel-CFRP SHS tubes under axial impact, *Composite Structures*, **87**(3), 282-292.

Bambach, M. R., Jama, H. H. and Elchalakani, M. (2009b), Static and dynamic axial crushing of spot-welded thin-walled composite steel-CFRP square tubes, *International Journal of Impact Engineering*, **36**(9), 1083-1094.

Bardi, F. C. and Kyriakides, S. (2006), Plastic buckling of circular tubes under axial compression-part I: Experiments, *International Journal of Mechanical Sciences*, **48**(8), 830-841.

Barker, R. G. P. and Guest, S. D. (1998), Inflatable triangulated cylinders, *IUTAM-IASS Symposium on Deployable Structures: Theory and Applications*, Cambridge, U.K., 6-9 September 1998.

Carpenter, R. A. (1990), *Vehicle bumper system*, US Patent, 4,961,603.

Chen, W. and Wierzbicki, T. (2001), Relative merits of single-cell, multi-cell and foam-filled thin-walled structures in energy absorption, *Thin-Walled Structures*, **39**(4), 287-306.

Cheon, S. S., Choi, J. H. and Lee, D. G. (1995), Development of the composite bumper beam for passenger cars, *Composite Structures*, **32**(1-4), 491-499.

Connelly, R., Sabitov, I. and Walz, A. (1997), The bellows conjecture, *Beiträge zur Algebra und Geometrie*, **38**(1), 1-10.

Crandall, J. R., Bhalla, K. S. and Madeley, N. J. (2002), Designing road vehicles for pedestrian protection, *BMJ*, **324**(7346), 1145-1148.

Cumming, D. M., Gabbianelli, G., Mellis, J. J. and Uchiyama, H. (2005), *Multiple material bumper beam*, US Patent, 6,923,482.

Daneshi, G. H. and Hosseinipour, S. J. (2002), Grooves effect on crashworthiness characteristics of thin-walled tubes under axial compression, *Materials & Design*, **23**(7), 611-617.

Farley, G. and Jones, R. (1992), Crushing characteristics of continuous fiber-reinforced composite tubes, *Journal of Composite Materials*, **26**, 37-50.

Guest, S. D. (1994), *Deployable structures: Concepts and analysis*, D.Phil. dissertation, University of Cambridge.

Guest, S. D. and Pellegrino, S. (1994a), The folding of triangulated cylinders, part I: Geometric considerations, *ASME Journal of Applied Mechanics*, **61**, 773-777.

Guest, S. D. and Pellegrino, S. (1994b), The folding of triangulated cylinders, part II: The folding process, *ASME Journal of Applied Mechanics*, **61**, 777-783.

Guest, S. D. and Pellegrino, S. (1996), The folding of triangulated cylinders, part III: Experiments, *ASME Journal of Applied Mechanics*, **63**, 77-83.

Hanefi, E. H. and Wierzbicki, T. (1996), Axial resistance and energy absorption of externally reinforced metal tubes, *Composites Part B: Engineering*, **27**(5), 387-394.

Hanssen, A. G., Langseth, M. and Hopperstad, O. S. (2000a), Static and dynamic crushing of square aluminium extrusions with aluminium foam filler, *International Journal of Impact Engineering*, **24**(4), 347-383.

Hanssen, A. G., Langseth, M. and Hopperstad, O. S. (2000b), Static and dynamic crushing of circular aluminium extrusions with aluminium foam filler, *International Journal of Impact Engineering*, **24**(5), 475-507.

Hanssen, A. G., Langseth, M. and Hopperstad, O. S. (2001), Optimum design for energy absorption of square aluminium columns with aluminium foam filler, *International Journal of Mechanical Sciences*, **43**(1), 153-176.

Hosseinipour, S. J. (2003), Mathematical model for thin-walled grooved tubes under axial compression, *Materials & Design*, **24**(6), 463-469.

Hosseinipour, S. J. and Daneshi, G. H. (2003), Energy absorption and mean crushing load of thin-walled grooved tubes under axial compression, *Thin-Walled Structures*, **41**(1), 31-46.

IIHS (2009), Bumper Test Protocol (Version VII).

Jones, N. and Abramowicz, W. (1985), Static and dynamic axial crushing of circular and square tubes, *Metal Forming and Impact Mechanics*, 225-247.

Jonsson, M. (2003), *Lightweight beam*, US Patent, 6,554,345.

Jonsson, M. and Juntti, M. (2005), *Bumper beam for a vehicle and a method of adapting a bumper beam to various vehicle models*, US Patent, 6,863,321.

Karagiozova, D. (2004), Dynamic buckling of elastic-plastic square tubes under axial impact-I: Stress wave propagation phenomenon, *International Journal of Impact Engineering*, **30**(2), 143-166.

Karagiozova, D., Alves, M. and Jones, N. (2000), Inertia effects in axisymmetrically deformed cylindrical shells under axial impact, *International Journal of Impact Engineering*, **24**(10), 1083-1115.

Karagiozova, D. and Jones, N. (2001), Influence of stress waves on the dynamic progressive and dynamic plastic buckling of cylindrical shells, *International Journal of Solids and Structures*, **38**(38-39), 6723-6749.

Karagiozova, D. and Jones, N. (2002), On dynamic buckling phenomena in axially loaded elastic-plastic cylindrical shells, *International Journal of Non-Linear Mechanics*, **37**(7), 1223-1238.

Karagiozova, D. and Jones, N. (2004), Dynamic buckling of elastic-plastic square tubes under axial impact-II: Structural response, *International Journal of Impact Engineering*, **30**(2), 167-192.

Karagiozova, D., Nurick, G. N. and Chung Kim Yuen, S. (2005), Energy absorption of aluminium alloy circular and square tubes under an axial explosive load, *Thin-Walled Structures*, **43**(6), 956-982.

Kim, H.-S. (2002), New extruded multi-cell aluminum profile for maximum crash energy absorption and weight efficiency, *Thin-Walled Structures*, **40**(4), 311-327.

Kokkula, S., Hopperstad, O. S., Lademo, O. G., Berstad, T. and Langseth, M. (2006a), Offset impact behaviour of bumper beam-longitudinal systems: Numerical simulations, *International Journal of Crashworthiness*, **11**(4), 317-336.

Kokkula, S., Langseth, M., Hopperstad, O. S. and Lademo, O. G. (2006b), Offset impact behaviour of bumper beam-longitudinal systems: Experimental investigations, *International Journal of Crashworthiness*, **11**(4), 299-316.

Kuribayashi, K. (2004), *A novel foldable stent graft*, University of Oxford.

Lee, K. S., Kim, S. K. and Yang, I. Y. (2008), The energy absorption control characteristics of al thin-walled tube under quasi-static axial compression, *Journal of Materials Processing Technology*, **201**(1-3), 445-449.

Lee, S., Hahn, C., Rhee, M. and Oh, J.-E. (1999), Effect of triggering on the energy absorption capacity of axially compressed aluminum tubes, *Materials & Design*, **20**(1), 31-40.

Lu, G. (1993), A study of the crushing of tubes by two indenters, *International Journal of Mechanical Sciences*, **35**(3-4), 267-278.

Lu, G. and Yu, T. X. (2003), *Energy absorption of structures and materials*, CRC Press, Woodhead, Cambridge.

Lundquist, E. E. (1933), *Strength tests of thin-walled duralumin cylinders in compression*, NACA Report 473.

Ma, J. (2008), *Design of thin-walled tubes with patterns*, Transfer Report, University of Oxford.

Mamalis, A. G. and Johnson, W. (1983), The quasi-static crumpling of thin-walled circular cylinders and frusta under axial compression, *International Journal of Mechanical Sciences*, **25**(9-10), 713-732.

Mamalis, A. G., Manolakos, D. E., Baldoukas, A. K. and Viegelaan, G. L. (1991), Energy dissipation and associated failure modes when axially loading polygonal thin-walled cylinders, *Thin-Walled Structures*, **12**(1), 17-34.

Mamalis, A. G., Manolakos, D. E., Demosthenous, G. A. and Ioannidis, M. B. (1996), Analysis of failure mechanisms observed in axial collapse of thin-walled circular fibreglass composite tubes, *Thin-Walled Structures*, **24**(4), 335-352.

Mamalis, A. G., Manolakos, D. E., Demosthenous, G. A. and Ioannidis, M. B. (1997), The static and dynamic axial crumpling of thin-walled fibreglass composite square tubes, *Composites Part B: Engineering*, **28**(4), 439-451.

Mamalis, A. G., Manolakos, D. E., Ioannidis, M. B. and Kostazos, P. K. (2000), Axial collapse of hybrid square sandwich composite tubular components with corrugated core: Experimental, *International Journal of Crashworthiness*, **5**(3), 315-332.

- Mamalis, A. G., Manolakos, D. E., Ioannidis, M. B. and Kostazos, P. K. (2001), Axial crushing of hybrid square sandwich composite vehicle hollow bodysHELLS with reinforced core: Experimental, *International Journal of Crashworthiness*, **6**(3), 363-376.
- Mamalis, A. G., Manolakos, D. E., Ioannidis, M. B. and Kostazos, P. K. (2003a), Crushing of hybrid square sandwich composite vehicle hollow bodysHELLS with reinforced core subjected to axial loading: Numerical simulation, *Composite Structures*, **61**(3), 175-186.
- Mamalis, A. G., Manolakos, D. E., Ioannidis, M. B., Kostazos, P. K. and Dimitriou, C. (2003b), Finite element simulation of the axial collapse of metallic thin-walled tubes with octagonal cross-section, *Thin-Walled Structures*, **41**(10), 891-900.
- Mamalis, A. G., Manolakos, D. E., Ioannidis, M. B., Kostazos, P. K. and Kastanias, S. N. (2003c), Numerical modelling of the axial plastic collapse of externally grooved steel thin-walled tubes, *International Journal of Crashworthiness*, **8**(6), 583-590.
- Mamalis, A. G., Manolakos, D. E., Ioannidis, M. B., Kostazos, P. K. and Papapostolou, D. P. (2002a), Axial collapse of hybrid square sandwich composite tubular components with corrugated core: Numerical modelling, *Composite Structures*, **58**(4), 571-582.
- Mamalis, A. G., Manolakos, D. E., Ioannidis, M. B. and Papapostolou, D. P. (2005), On the response of thin-walled cfrp composite tubular components subjected to static and dynamic axial compressive loading: Experimental, *Composite Structures*, **69**(4), 407-420.
- Mamalis, A. G., Manolakos, D. E., Ioannidis, M. B., Papapostolou, D. P., Kostazos, P. K. and Konstantinidis, D. G. (2002b), On the compression of hybrid sandwich composite panels reinforced with internal tube inserts: Experimental, *Composite Structures*, **56**(2), 191-199.
- Mamalis, A. G., Manolakos, D. E., Saigal, S., Viegelnahn, G. and Johnson, W. (1986a), Extensible plastic collapse of thin-wall frusta as energy absorbers, *International Journal of Mechanical Sciences*, **28**(4), 219-229.
- Mamalis, A. G., Manolakos, D. E. and Viegelnahn, G. L. (1989), The axial crushing of thin pvc tubes and frusta of square cross-section, *International Journal of Impact Engineering*, **8**(3), 241-264.
- Mamalis, A. G., Manolakos, D. E., Viegelnahn, G. L., Vaxevanidis, N. M. and Johnson, W. (1986b), On the inextensional axial collapse of thin PVC conical shells, *International Journal of Mechanical Sciences*, **28**(5), 323-335.



Mamalis, A. G., Viegelaahn, G. L., Manolakos, D. E. and Johnson, W. (1986c), Experimental investigation into the axial plastic collapse of steel thin-walled grooved tubes, *International Journal of Impact Engineering*, **4**(2), 117-126.

Martinez, E., Tyrell, D. and Perlman, A. B. (2004), Development of crash energy management designs for existing passenger rail vehicles, *2004 ASME International Mechanical Engineering Congress and Exposition*, Anaheim, CA, USA, November 13-19.

Mayville, R., Johnson, K. N., Stringfellow, R. G. and Tyrell, D. C. (2003), The development of a rail passenger coach car crush zone, *IEEE/ASME Joint Rail Conference*, Chicago, Illinois, USA, April 22-24.

Meguid, S. A., Attia, M. S., Stranart, J. C. and Wang, W. (2007), Solution stability in the dynamic collapse of square aluminium columns, *International Journal of Impact Engineering*, **34**(2), 348-359.

Meng, Q., Al-Hassani, S. T. S. and Soden, P. D. (1983), Axial crushing of square tubes, *International Journal of Mechanical Sciences*, **25**(9-10), 747-773.

Miscow F, P. C. and Al-Qureshi, H. A. (1997), Mechanics of static and dynamic inversion processes, *International Journal of Mechanical Sciences*, **39**(2), 147-161.

Murase, K. and Wada, H. (2004), Numerical study on the transition of plastic buckling modes for circular tubes subjected to an axial impact load, *International Journal of Impact Engineering*, **30**(8-9), 1131-1146.

Nagel, G. M. and Thambiratnam, D. P. (2005), Computer simulation and energy absorption of tapered thin-walled rectangular tubes, *Thin-Walled Structures*, **43**(8), 1225-1242.

NHTSA (1999), Part 581 Bumper Standard.

Pitarresi, G., Carruthers, J. J., Robinson, A. M., Torre, G., Kenny, J. M., Ingleton, S., Velecela, O. and Found, M. S. (2007), A comparative evaluation of crashworthy composite sandwich structures, *Composite Structures*, **78**(1), 34-44.

Pugsley, A. (1960), The large-scale crumpling of thin cylindrical columns, *The Quarterly Journal of Mechanics and Applied Mathematics* **13**(1), 1-9.

Pugsley, A. G. (1979), On the crumpling of thin tubular struts, *The Quarterly Journal of Mechanics and Applied Mathematics* **32**(1), 1-7.

RCAR (2006), The Procedure for Conducting a Low Speed 15 km/h Offset Insurance Crash Test to Determine the Damageability and Repairability Features of Motor Vehicles.

- Reddy, T. Y. and Reid, S. R. (1980), Phenomena associated with the crushing of metal tubes between rigid plates, *International Journal of Solids and Structures*, **16**(6), 545-562.
- Reddy, T. Y. and Reid, S. R. (1986), Axial splitting of circular metal tubes, *International Journal of Mechanical Sciences*, **28**(2), 111-131.
- Reddy, T. Y. and Wall, R. J. (1988), Axial compression of foam-filled thin-walled circular tubes, *International Journal of Impact Engineering*, **7**(2), 151-166.
- Reid, J., Rohde, J. and Sicking, D. (2002), Box-beam bursting energy absorbing terminal, *Journal of Transportation Engineering*, **128**(3), 287-294.
- Reid, S. R. and Reddy, T. Y. (1986), Static and dynamic crushing of tapered sheet metal tubes of rectangular cross-section, *International Journal of Mechanical Sciences*, **28**(9), 623-637.
- Reid, S. R., Reddy, T. Y. and Gray, M. D. (1986), Static and dynamic axial crushing of foam-filled sheet metal tubes, *International Journal of Mechanical Sciences*, **28**(5), 295-322.
- Robertson, A. (1928), The strength of tubular struts, *Proceedings of the Royal Society of London. Series A, Containing Papers of a Mathematical and Physical Character* **121**(788), 558-585.
- Rothmund, P. W. K. (2006), Folding DNA to create nanoscale shapes and patterns, *Nature*, **440**(7082), 297-302.
- Roussel, T., Cavillon, T. and Bouguedra, D. (2003), *Motor vehicle bumper beam, and a bumper fitted with such a beam*, US Patent, 6,669,252.
- Santosa, S. and Wierzbicki, T. (1998), Crash behavior of box columns filled with aluminum honeycomb or foam, *Computers & Structures*, **68**(4), 343-367.
- Santosa, S. P., Wierzbicki, T., Hanssen, A. G. and Langseth, M. (2000), Experimental and numerical studies of foam-filled sections, *International Journal of Impact Engineering*, **24**(5), 509-534.
- Schwartz, R. and Ramoo, R. (1999), *Energy absorbing bumper*, US Patent, 6,007,123.
- Shuler, S. and Trappe, A. (2006), *Integrated solitary bumper beam*, US Patent, 6,994,384.
- Singace, A. A. (1999), Axial crushing analysis of tubes deforming in the multi-lobe mode, *International Journal of Mechanical Sciences*, **41**(7), 865-890.

- Singace, A. A. and El-Sobky, H. (1997), Behaviour of axially crushed corrugated tubes, *International Journal of Mechanical Sciences*, **39**(3), 249-268.
- Singace, A. A., Elsobky, H. and Reddy, T. Y. (1995), On the eccentricity factor in the progressive crushing of tubes, *International Journal of Solids and Structures*, **32**(24), 3589-3602.
- Sogame, A. and Furuya, H. (1998), Conceptual study on cylindrical deployable space structures, *IUTAM-IASS Symposium on Deployable Structures: Theory and Applications*, Cambridge, U.K., 6-9 September 1998.
- Song, H.-W., Wan, Z.-M., Xie, Z.-M. and Du, X.-W. (2000), Axial impact behavior and energy absorption efficiency of composite wrapped metal tubes, *International Journal of Impact Engineering*, **24**(4), 385-401.
- Timoshenko, S. (1961), *Theory of elastic stability*, McGraw-Hill.
- Tsunoda, H. and Senbokuya, Y. (2002), Rigidizable membranes for space inflatable structures, *43rd AIAA/ASME/ASCE/AHS/ASC Structures, Structural Dynamics, and Materials Conference*, Denver, Colorado, USA, Apr. 22-25, 2002
- Tyrell, D., Jacobsen, K., Martinez, E. and Perlman, A. B. (2006), A train-to-train impact test of crash energy management passenger rail equipment: Structural results, *2006 ASME International Mechanical Engineering Congress and Exposition*, Chicago, Illinois, USA, November 5-10.
- UNECE (1980), Regulation No.42.
- UNECE (2007), Regulation No.94.
- Weissenborn, M. (2003), *Bumper system with face-abutting energy absorber* US Patent, 6,575,510.
- WHO (2004), *World report on road traffic injury prevention*.
- Wierzbicki, T. and Abramowicz, W. (1983), On the crushing mechanics of thin-walled structures, *Journal of Applied Mechanics*, **50**(4), 727-734.
- Wierzbicki, T., Bhat, S. U., Abramowicz, W. and Brodtkin, D. (1992), Alexander revisited-a two folding elements model of progressive crushing of tubes, *International Journal of Solids and Structures*, **29**(24), 3269-3288.
- Yamashita, M., Gotoh, M. and Sawairi, Y. (2003), Axial crush of hollow cylindrical structures with various polygonal cross-sections: Numerical simulation and experiment, *Journal of Materials Processing Technology*, **140**(1-3), 59-64.

Yoshimura, Y. (1955), *On the mechanism of buckling of a circular cylindrical shell under axial compression*, NACA TM 1390.

You, Z. and Cole, N. (2006), Self-locking bi-stable deployable booms, *47th AIAA/ASME/ASCE/AHS/ASC Structures, Structural Dynamics, and Materials Conference*, Newport, Rhode Island, 1 - 4 May 2006.

Zhang, X., Cheng, G., You, Z. and Zhang, H. (2007), Energy absorption of axially compressed thin-walled square tubes with patterns, *Thin-Walled Structures*, **45**(9), 737-746.

Zhang, X., Cheng, G. and Zhang, H. (2006), Theoretical prediction and numerical simulation of multi-cell square thin-walled structures, *Thin-Walled Structures*, **44**(11), 1185-1191.

Zhang, X. W., Su, H. and Yu, T. X. (2009), Energy absorption of an axially crushed square tube with a buckling initiator, *International Journal of Impact Engineering*, **36**(3), 402-417.